Savannah River National Laboratory™

OPERATED BY SAVANNAH RIVER NUCLEAR SOLUTIONS

Savannah River National Laboratory

2017 LDRD

Laboratory Directed Research and Development Program

Environmental Stewardship

Nuclear Materials Management

National Security

Clean Energy

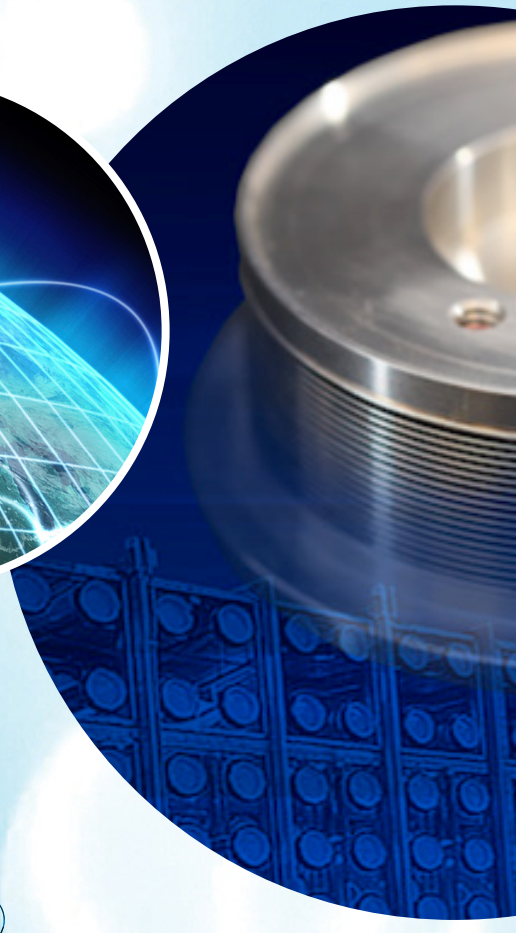

2017 LDRD ANNUAL REPORT

DISCLAIMER

SRNL-STI-2018-00143

TABLE OF CONTENTS

MESSAGE FROM **THE LAB DIRECTOR**

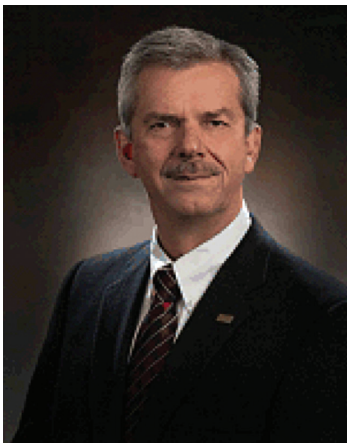

At Savannah River National Laboratory (SRNL) our Laboratory Directed Research and Development (LDRD) plays an important role in positioning the laboratory for future growth in key mission areas, truly serving as the lifeblood of the lab. The LDRD program provides opportunities for early exploration and exploitation of innovative ideas that will enhance the ability of the lab to support the critical Department of Energy (DOE) missions in environmental stewardship, national security, clean energy, and nuclear materials management. As the global manufacturing sector is undergoing a transformation not seen since the onset of the industrial revolution, a host of revolutionary technologies are allowing the industrial sector to re-think almost every aspect of how work is done. SRNL has taken a strategic direction focused on developing and adapting the best science and technology for the chemical and materials manufacturing needs of DOE and the National Nuclear Security Administration (NNSA). With this objective in mind our FY17 LDRD program included a focus on innovative steps to obtain digital tools and data needed to fuel advances in manufacturing, including projects related to process intensification, process imaging, additive manufacturing, and cyber security.

Another important role that LDRD plays is sustaining staff excellence by providing the opportunity to nurture existing and grow emerging core competencies. The LDRD program also provides an avenue to forge strategic partnerships with not only other national labs, but also universities and commercial companies. SRNL's university partnerships are especially valuable as they not only allow for fruitful collaborations, but also provide links with the next generation of scientists and engineers as students and post-doctoral researchers working on cutting-edge R&D programs.

This report reflects the execution of our LDRD program within the objectives and guidelines outlined by the DOE through the DOE Order 413.2C. The projects described herein reflect the innovation required to fulfill SRNL's strategic vision and program plans, and they provide great value to the DOE and the nation. The diversity exhibited in the research and development projects underscores the DOE Office of Environmental Management (DOE-EM) mission and enhances that mission by developing the technical capabilities and human capital necessary to support future DOE-EM national needs.

On behalf of the SRNL Senior Management team, I would like to congratulate those members of the SRNL staff, and their collaborators for their accomplishments and the quality of their work. Their efforts create a product that continues to demonstrate the importance of SRNL's competencies to the nation. ■

Dr. Terry A. Michalske
Laboratory Director
Savannah River National Laboratory

2017 OVERVIEW

Savannah River National Laboratory's (SRNL)
Laboratory Directed Research and Development Program (LDRD)

Fiscal Year (FY) 2017 marked the twelfth year of Savannah River National Laboratory's (SRNL's) Laboratory Directed Research and Development (LDRD) program and the largest year to date. When the program began in FY06, just two years after SRNL becoming the DOE's 17th national lab, it began with a modest authorized collection rate of just under 1.5%. It grew from there each year, reaching 4% in FY11. FY17 marked the first increase in the authorized collection rate since FY11, increasing from 4% to 5%. This increase highlights the value placed on this important program, which provides the discretionary funding needed to develop ideas for future programmatic growth in our key business areas of environmental stewardship, national security, nuclear materials management, and secure energy manufacturing, as well as develop and maintain our core competencies. The LDRD program leverages the unique capabilities of SRNL to yield foundational scientific research and development (R&D) essential to our core business areas, while aligning optimally and continuously with SRNL's Strategic Plan and providing long-term benefits to DOE and the National Nuclear Security Administration (NNSA), other customers, and stakeholders. As can be seen in the "By the Numbers" summary, this program also plays an important role in sustaining staff excellence with high participation by students, post-docs, and early-career staff. Over 75% of the projects in FY17 included contributions from early-career or post-doctoral staff.

FY17 LDRD PROGRAM FOCUS AREAS:

The FY17 LDRD Program included focus areas in each of our three main business areas, as well as encouraging proposals supporting the themes of the Advanced Manufacturing Collaborative (AMC).

ENVIRONMENTAL STEWARDSHIP AND NUCLEAR MATERIALS MANAGEMENT

Unique concepts that lead to new approaches and options for critical EM risk reduction challenges and also reduce the life cycle in processing high activity liquid waste and nuclear materials, remediating contaminated soil, groundwater and facilities, as well as validating long-term remediation strategies.

NATIONAL SECURITY

Unique concepts that address national security mission area needs that are currently underserved by the DOE Lab system. Game-changing innovations and tools that advance the national security agenda for the United States Government, including monitoring, nonproliferation, and deterrence.

CLEAN ENERGY

Advanced research in the development, demonstration, and deployment of clean energy technologies and clean energy manufacturing; innovative technologies to assure the future utilization of clean, reliable energy or dramatically improve the energy efficiency of industrial, manufacturing, transportation, and building technologies, plus strengthen SRNL's Core Competencies.

ADVANCED MANUFACTURING COLLABORATIVE (AMC)

Themes of the AMC include additive manufacturing, process intensification, virtual reality, process modeling, computational chemistry, smart manufacturing, robotics, and cyber security.

The pie chart below shows the distribution of FY17 projects, both new starts and continuation projects, among the three program areas, as well as those supporting the Advanced Manufacturing Collaborative theme. Note that Environmental Stewardship also includes Nuclear Materials Management.

FY17 PORTFOLIO BY PROGRAM AREA + AMC

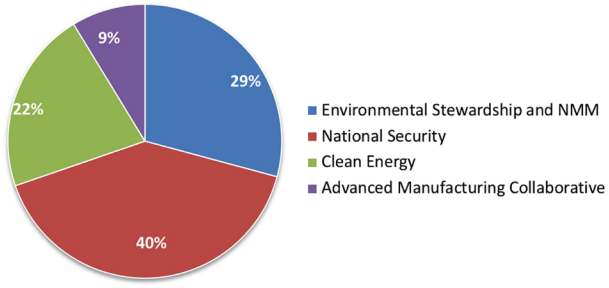

BY THE NUMBERS

TOTAL PROGRAM COST

$9.5M

TOTAL NUMBER OF PROJECTS

35

AVERAGE PROJECT COST

$265K

TANGIBLE ACCOMPLISHMENTS RESULTING FROM PERSISTENT TECHNICAL EFFORTS IN FY17 INCLUDE:

SCIENTIFIC PRODUCTIVITY

Research efforts supported by the LDRD program led to securing intellectual property and peer reviewed publications which included:

- ✔ **5 invention disclosures were submitted during FY17**
- ✔ **3 patents granted related to prior year LDRD efforts**
- ✔ **7 publications in peer reviewed journals.**

POST-DOCTORAL & STUDENT INVOLVEMENT

12 post-doctoral researchers were members of 10 LDRD supported research teams in FY17, 10 performed research at SRNL.

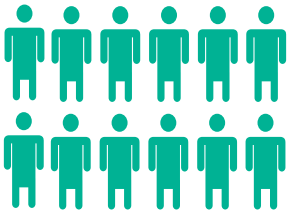

OVER 40% OF ALL SRNL POST-DOCS WERE SUPPORTED (AT LEAST 10% OF THEIR TIME) BY LDRD PROJECTS.

Additional research performed, both on and off-site for LDRD projects included:

7 graduate students

and 10 undergraduate students

SUSTAINING **STAFF EXCELLENCE**

26%
Percent of the FY17 projects were led by early career staff (terminal degree within the past 10 years)

6
New hires in FY17 were attributed to the LDRD program

26%
Percent of hours charged to LDRD projects in FY17 were by new staff (< 2 years of service)

77%
Percent of FY17 projects involved post-docs or early career professionals (terminal degree within the past 10 years)

FORGING **STRATEGIC PARTNERSHIPS**

31
FY17 Projects Included

31
Collaborations

UNIVERSITIES	COMPANIES	NATIONAL LABS
8	4	5

2017 **TOTAL COLLABORATIONS**

8 Universities, 4 Companies, 5 National Labs

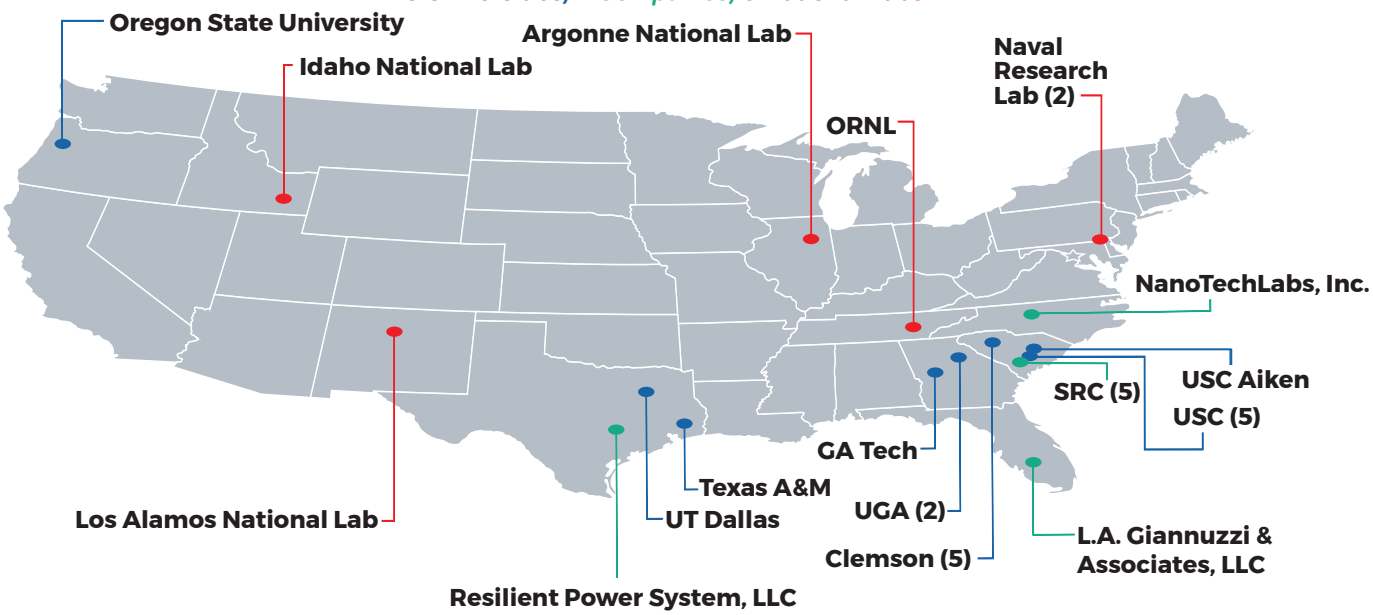

ENVIRONMENTAL STEWARDSHIP

UNIQUE CONCEPTS THAT LEAD TO NEW APPROACHES AND OPTIONS FOR CRITICAL EM RISK REDUCTION CHALLENGES AND ALSO REDUCE THE LIFE CYCLE IN PROCESSING HIGH ACTIVITY LIQUID WASTE AND NUCLEAR MATERIALS, REMEDIATING CONTAMINATED SOIL, GROUNDWATER AND FACILITIES, AS WELL AS VALIDATING LONG-TERM REMEDIATION STRATEGIES.

DEVELOPMENT OF LIQUID PHASE WATER DETRITIATION TECHNOLOGY

Project Team: Steve Xiao (PI), P. Beaumont, L. Angelette, A.B. Thompson

Thrust Area: Environmental Stewardship

Project Start Date: 10/1/14

Project End Date: 9/30/17

The potential of hydration based materials was investigated through material synthesis, characterization, performance evaluation and recipe optimization during FY17. Development of a hydration based material followed two tracks, using ion-exchange resin and alumina as starting materials. The best HDO/H_2O separation performance over the hydration material doubled deuterium removal capacity of the "Optimized" surface hydroxyl group material but did not have orders of magnitude improvements as anticipated. It is likely that the surface hydroxyl group material, when wet, has enough water capacity already, so that further improvements are limited. In other words, this LDRD development confirmed that the current wet column material is almost optimized.

FY2017 OBJECTIVES

TASK ONE

Development of hydration based column material for water isotope separation

INTRODUCTION

An efficient water detritiation process, if fully developed, could have broad impacts to heavy water from SRS legacy moderator, TVA (Tennessee Valley Authority) cooling water, nuclear power industry, and environmental remediations, etc. Until now, no technology existed to remove low levels of tritium contamination economically. The potential for a direct isotope separation of water molecules is of considerable interest. Molecular Separation Inc. (MSI) reported tritium data on an ion-exchange resin loaded with aluminum sulfate **[1].** An independent evaluation **[2]** confirmed significant reduction in the tritium concentration in wastewater samples. Aluminum sulfate can have up to 18-hydration waters, $Al_2(SO_4)_3 \cdot 18H_2O$. It is believed that its hydration water has a greater affinity for tritiated water (HTO) over light water (HOH). The property could be used for water detritiation if the aluminum sulfate is anchored with a solid substrate since the salt is highly soluble in water. The SRNL 3-step concept **[3]** for water isotope separation has been achieved with positive and encouraging results, including separation of HDO/H_2O and HTO/H_2O experimentally (Figure 1.) Development of a hydration based material could further improve the capacity of the current surface hydroxyl group based column material for water isotope separation. The potential of hydration based materials was investigated through material synthesis, characterization, performance evaluation and recipe optimization during the FY17 LDRD performance period.

Figure 1. SRNL 3-step water detritiation process with no secondary contaminated streams

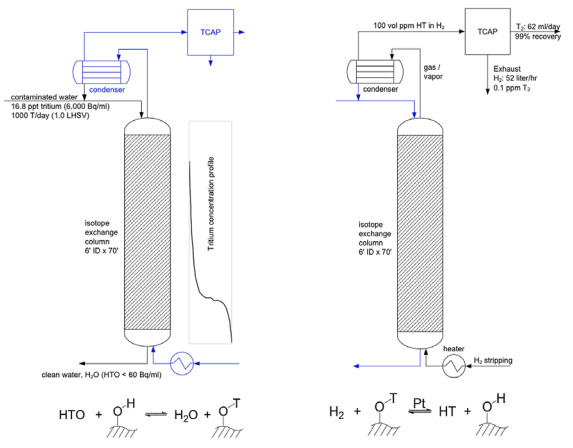

a) Water Isotope Exchange **b)** Catalytic Isotope Exchange

APPROACH

The hydration material development followed two tracks, as seen in Figure 2a and Figure 2b, using ion-exchange resin and alumina as starting materials. The ion-exchange resin was loaded with $Al_2(SO_4)_3$ solution in a burette (Figure 2c). Qualitative analysis on the collected eluent was periodically performed, monitoring for the concentration of Al^{3+} in order to quantify the uptake of Al^{3+} onto the resin. The treated resin was collected via vacuum filtration and washed with DI water to remove excess $Al_2(SO_4)_3$ and air dried overnight. The alumina sphere was treated with H_2SO_4 solution at various concentrations, followed by drying and calcination. Surface $Al_2(SO_4)_3$ were formed in situ while still preserving a good portion of surface area of the Al_2O_3 support. The samples were characterized by SEM and surface area if applicable, then evaluated for water isotope separation, which provided feedback to adjust recipes in the following material synthesis.

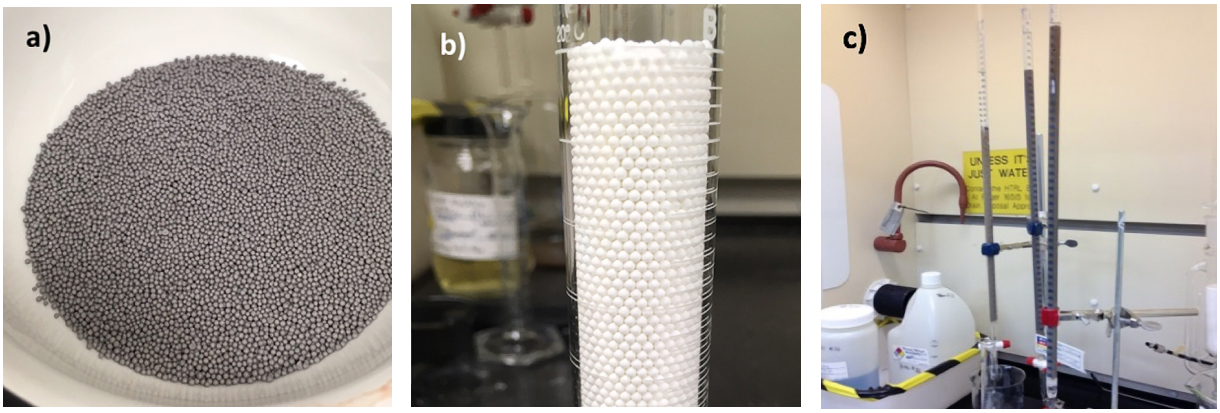

Figure 2. Untreated **a)** Resin #1, **b)** alumina, **c)** burette experimental setup

RESULTS/DISCUSSION

The $Al_2(SO_4)_3$ treated ion-exchange resin was analyzed by SEM/EDS. Figure 3 shows morphology of a resin particle and confirmed even distribution of Al over the particle analyzed. The Al/S ratio was consistent with theoretical values.

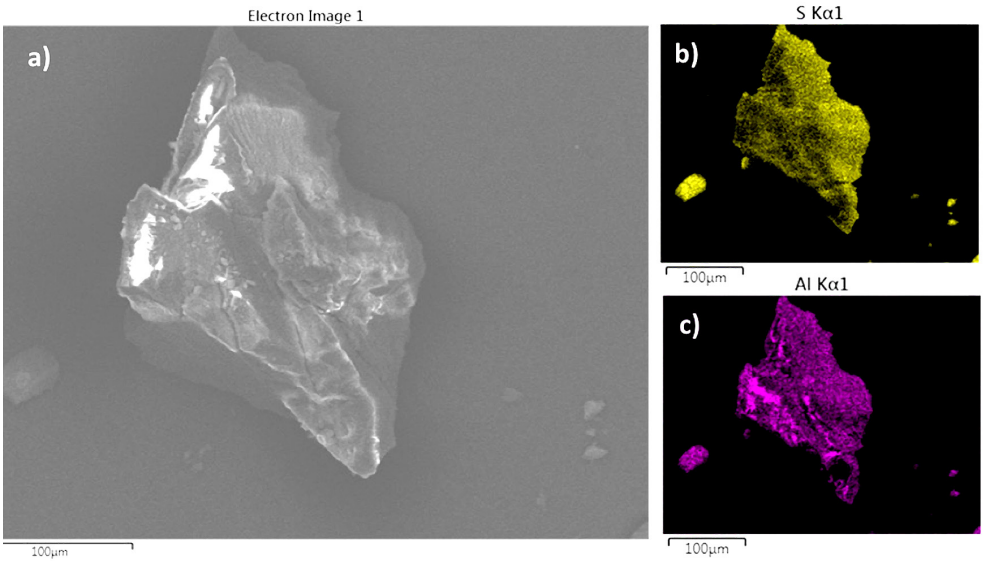

Figure 3. Resin depicting **a)** SEM, and EDS elemental analysis for **b)** sulfur, **c)** aluminum

The HDO/H_2O water isotope separation performance of the $Al_2(SO_4)_3$ treated ion-exchange resin (Hydration Water) was compared with the surface hydroxyl group based column materials (Beginning, Optimized in Figure 4). The treated resin showed excellent deuterium removal. It matched the performance of the "Optimized" surface hydroxyl group material but did not have anticipated further improvements by orders of magnitude. It is noted that the "Optimized" surface hydroxyl group material already has 9X improvement over the early benchmark "Beginning" material, including 3X from material screening and 3X with column wetting. It is likely that the surface hydroxyl group material, when wet, has water capacity comparable to the hydration material, so that no further improvements could be realized. In other words, the hydration material development under this LDRD confirmed that the previous wet column material had similar capacity as the hydration material. The improvement of this hydration material was about an order of magnitude better over the early benchmark "Beginning" material but not the "Optimized" surface hydroxyl group material.

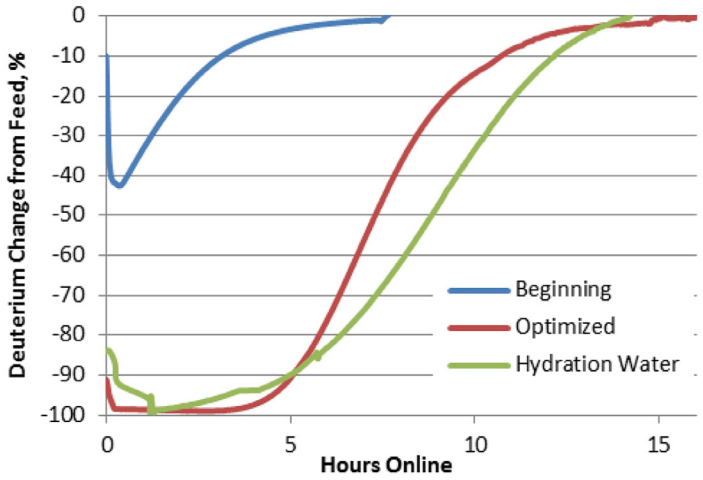

Figure 4. Performance of hydration material vs. surface hydroxyl group based column materials

Sample Name	Sample Description	Surface Area (m^2/g)
A	Untreated base alumina	193.73
A-1a	0.7 M H_2SO_4 – 10 min soak	193.06
A-1b	0.7 M H_2SO_4 – 15 min soak	195.09
A-1c	0.7 M H_2SO_4 – 120 min soak	198.78
A-2a	1 M H_2SO_4 – 40 min soak	181.14
A-2b	1 M H_2SO_4 – 240 min soak	182.87
A-2c	1 M H_2SO_4 – 370 min soak	175.06
A-3a	4.5 M H_2SO_4 – 30 min soak	68.78
A-3b	4.5 M H_2SO_4 – 60 min soak	53.87
A-3c	4.5 M H_2SO_4 – 120 min soak	74.79
A-4a	9 M H_2SO_4 – 30 min soak	10.34
A-4b	9 M H_2SO_4 – 60 min soak	10.93
A-4c	9 M H_2SO_4 – 120 min soak	12.15
A-5a	1 M H_2SO_4 – 30 min soak – 1 °C/min heat ramp	193.96
A-5b	1 M H_2SO_4 – 60 min soak – 1 °C/min heat ramp	195.23
A-5c	1 M H_2SO_4 – 120 min soak – 1 °C/min heat ramp	190.35
A-6a	4.5 M H_2SO_4 – 30 min soak – 1 °C/min heat ramp	130.50
A-6b	4.5 M H_2SO_4 – 60 min soak – 1 °C/min heat ramp	127.46
A-6c	4.5 M H_2SO_4 – 120 min soak – 1 °C/min heat ramp	103.37
A-7a	4.5 M H_2SO_4 – 30 min soak – 1 M NH_4OH	179.21
A-7b	4.5 M H_2SO_4 – 60 min soak – 1 M NH_4OH	173.58
A-7c	4.5 M H_2SO_4 – 120 min soak – 1 M NH_4OH	155.33
A-8	Repeat of A-3c	50.36
A-9	No Pre-Calcination – 1 M H_2SO_4 – 60 min soak	204.11
A-10	No Pre-Calcination – 4.5 M H_2SO_4 – 60 min soak	69.16
A-11	No Pre-Calcination – Repeat of A-3c	18.46

A large number of $Al_2(SO_4)_3$ treated ion-exchange resin and sulfated alumina samples were synthesized. Table 1 shows the list of the sulfated alumina samples being investigated. The best HDO/H_2O separation performance over the hydration material doubled deuterium removal capacity of the "Optimized" surface hydroxyl group material.

Table 1. Samples of sulfated alumina and surface areas

FY2017 ACCOMPLISHMENTS

- Hydration-based material was successfully synthesized, and the water isotope separation over this type of material was confirmed.
- The development also concluded that the surface hydroxyl group material previously developed, when tested in a wet column, could have comparable water isotope removal capacity to the hydration material, so that further improvements would be limited.
- During this LDRD performance period a DOE proposal (LAB 16-1588) developed with Clemson University has been selected for FY18 & FY19 funding ($920k total, $588k SRNL).
- LDRD project (LDRD-2018-00105) "Develop Isotopic Enriched Separations of Tritiated Water from Air" was selected due to development of LDRD-2015-00002.

FUTURE DIRECTIONS

- Continue investigation on hydrogen isotope fractionation using graphene and related 2-D materials under scope of DOE LAB 16-1588.
- Support LDRD project LDRD-2018-00105 on Isotopic Enriched Separations of Tritiated Water from Air.

REFERENCES

1. L. E. Furlong, S. L. Stockinger, G. B. Collins, "Method for Separating Heavy isotopes of Hydrogen from Water", US Patent 6,632,367 (2003)

2. P. Snead, S. Bushart, M. Naughton, R. Kohlmann, L. Furlong, Evaluation of a Low Level Waste Technology – "A Media Based Tritium Removal Process", EPRI, Palo Alto, CA, and Progress Energy, Raleigh, NC: 2002. 1006710

3. X. Xiao, "Decontamination of Tritiated Water", US Patent Application Number No. 15/034,611

ACRONYMS

DI Deionized Water
DOE Department of Energy
EDS Electron Dispersive Spectroscopy
LDRD Laboratory Directed Research and Development
MSI Molecular Separation Inc.
SEM Scanning Electron Microscope
SRNL Savannah River National Laboratory
SRS Savannah River Site
TVA Tennessee Valley Authority

TOTAL NUMBER OF POST-DOCTORAL RESEARCHERS

1. Paul Beaumont joined this project as postdoc, and has since been hired as SRNL employee during this LDRD performance period

PROBLEMATIC CONTAMINANTS (Tc-99, Hg) FOR TANK WASTE TREATMENT AND DISPOSAL

Project Team: M. M. Reigel (Primary), T. B. Peters, S. H. Reboul, D. P. DiPrete, T. A. DeVol, and A. F Seliman
Subcontractor: Clemson University (T. A. DeVol and A. F. Seliman)
Thrust Area: Environmental Stewardship
Project Start Date: 10/26/15
Project End Date: 9/30/17

Processing and retention of problematic contaminants (Tc-99, Hg) in high-level tank waste has been an issue throughout the DOE complex, due to the inherent mobility of these contaminants in environmental media and the associated environmental risks. The goal of this project is to design improved processes for removing the contaminants from tank-waste and/or retaining the contaminants in the final waste form (such as in the Saltstone waste form at SRS). Synthesis, evaluation and testing of novel extractant media for removing technetium from salt tank waste was performed. Testing showed polystyrene (PS) based methyldioctylamine (MDOA) and PS tributylamine (TBA) resins can remove significantly more Tc from salt simulant than the best commercially-available Tc extraction resin (TEVA®). The resins were incorporated into simulant Saltstone waste form samples to determine if the resins act as improved Tc-99 retention agents under oxic conditions. The results show that the PS based MDOA had the highest Tc-99 retention.

FY2017 OBJECTIVES

TASK ONE
Synthesis of polymethacrylate (PM) MDOA resin and PS tributylamine (TBA) resin

TASK TWO
Extended duration (0-72 hours) batch contact testing of Tc-99 decontamination under salt simulant conditions utilizing PS MDOA, PM MDOA, silica MDOA, and PS TBA resins

TASK THREE
Tc-99 retention testing in the Saltstone waste form using PS, PM, and silica MDOA resins

INTRODUCTION

At DOE waste sites, Tc-99 is typically a primary environmental risk driver owing to its high fission yield, high mobility, and long half-life. Performance Assessments performed at the Savannah River Site identified Tc-99 as a principal radionuclide contributing potential long-term beta-dose, both from stabilized waste residue remaining after tank cleaning and from stabilized salt waste immobilized in the cement-based waste form (Saltstone). At the Hanford reservation, research has proceeded in the area of technetium removal, in an effort to reduce concentrations of Tc-99 in existing waste, and ultimately to reduce potential releases of Tc-99 into the environment after disposition and closure.

PHOTO: DOE

At the Hanford reservation, research has proceeded in the area of technetium removal, in an effort to reduce concentrations of Tc-99 in existing waste, and ultimately to reduce potential releases of Tc-99 into the environment after disposition and closure.

Most of the tested technetium extraction agents are either eluted or back-extracted after capture, with the objective of regenerating the extraction medium for further repeated use. An alternative is to use an extraction agent that has such high affinity for technetium that it retains it over the long-term and can double as a binding agent within the final stable waste form. Recent research[1] has identified tertiary amines that hold promise for such potential use—methyldioctylamine (MDOA) and triethylamine (TEA). Another potentially effective amine is tributylamine (TBA). Initial results suggest that the extraction efficiencies of the MDOA, TEA, and TBA are high relative to other established extractants, and that moderately high concentrations of acid and base (4 M nitric acid and 4 M sodium hydroxide) have little impact on the holding power of the extractant. In this LDRD project, the MDOA, TEA, and TBA extractants were incorporated into solid phase resins (PS, PM, and silica resins), and then the technetium removal/retention efficiencies of the resins were evaluated, using simulated salt waste solution and the simulated SRS Saltstone waste form.

The science being investigated in this project has potential applications to multiple DOE waste sites and to environmental remediation efforts associated with damaged nuclear reactor facilities such as those at Fukushima and Chernobyl. Development of a superior technetium removal strategy (and/or waste form retention strategy) utilizing MDOA, TEA, and/or TBA would be potentially marketable to such applications. Following successful demonstration of the strategy, external funding will be targeted via facility-specific proposals. Decontamination of SRS/Hanford aqueous waste streams, improved binding of technetium within SRS Saltstone grout, and remediation of contaminated saltwater near the Fukushima reactor are examples of promising applications.

APPROACH

MDOA, TEA, and TBA extractants were incorporated into polystyrene (PS) resins via amination, to facilitate solid-liquid phase extraction testing. The MDOA extractant was also incorporated into a polymethacrylate (PM) resin and a silica resin. Alkaline salt simulant containing Tc-99 was prepared and used to evaluate the technetium decontamination efficacies of the MDOA, TEA, and TBA resins against those of Eichrom TEVA® resin (the "gold standard" of technetium removal resins) and conventional anion exchange (IX) resin. Batch contact decontamination tests were conducted over time periods ranging from 1-72 hours, with sampling and analysis performed on salt simulant aliquots removed intermittently during those periods. The salt simulant aliquots were analyzed for Tc-99 and other key constituents, to quantify constituent decontamination factors as a function of time.

The PS, PM and silica MDOA resins were also tested in a simulant Saltstone waste form to determine the Tc-99 retention efficiencies. The same alkaline salt solution simulant that was used in the removal testing was used in the Saltstone formulation. Saltstone dry feed materials (portland cement, blast furnace slag, and fly ash) were also used. The test matrix included resin addition techniques (adding to liquid or dry feed), ratios of resin to salt solution, and varying resin types. Each Saltstone sample was cured for at least 28 days under oxic conditions prior to performing leaching studies on the crushed Saltstone. The crushed Saltstone was tumbled with a leachate (SRS artificial ground water) for seven days prior to filtering and analysis of the leachate. Distribution ratio (Rd) and solubility calculations were performed to determine the effectiveness of the resins at retaining Tc-99 in the waste form.

RESULTS/DISCUSSION

Technetium decontamination factors (DFs) for the salt simulant tests are plotted as a function of contact time in Figures 1, 2, and 3. Figure 1 contains the comparison of DFs for PS MDOA, TEVA®, PS TEA, and IX; Figure 2 contains the comparison of DFs for PS MDOA, PM MDOA, and silica MDOA; and Figure 3 contains the comparison of DFs for PS TBA and PS MDOA. As shown in the figures, at contact times greater than or equal to four hours, the PS MDOA and PS TBA resins removed significantly more technetium than the other resins, including the "gold standard" TEVA® resin. At a contact time of twenty-four hours, the DF for the PS MDOA resin was about twice that of the TEVA® resin, about three times that of the PS TEA resin, and about seven times that of the conventional anion exchange resin (Figure 1). The kinetics of the PS MDOA resin reactions were slower than those of the other resins, as evidenced by the fact that the MDOA DF was highest at twenty-four hours and lowest at one hour, while the DFs of the other resins were relatively constant over the range from one to twenty-four hours. In contrast, the PS MDOA resin was about twice as effective as the PM MDOA resin, and at least an order of magnitude more effective than the silica MDOA resin (Figure 2). The low effectiveness of the silica MDOA resin is not surprising, given the tendency for silica to dissolve in the caustic salt simulant. Comparison of the DFs of the PS TBA with the DFs of the PS MDOA shows both similarities and differences (Figure 3). At contact times of 1-4 hours, the PS TBA is significantly more effective than the PS MDOA, while at contact times of 24-72 hours, the effectiveness of the PS TBA is approximately equivalent to that of the PS MDOA. Clearly, the kinetics of the PS TBA are better than those of the PS MDOA, as indicated by the higher relative DFs at contact times ≤ 4 hours.

Figure 1. Removal of Tc-99 from Simulated Salt Waste - Comparison of PS MDOA, TEVA®, PS TEA, and IX

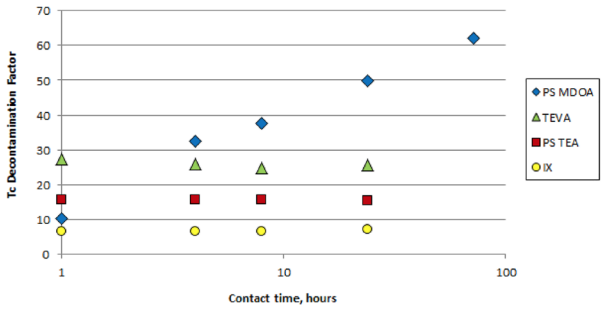

Figure 2. Removal of Tc-99 from Simulated Salt Waste - Comparison of PS MDOA, PM MDOA, Silica MDOA

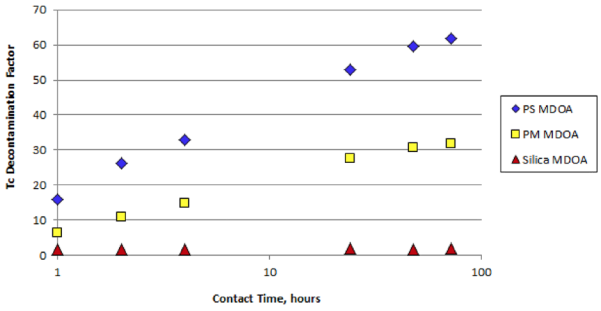

Figure 3. Removal of Tc-99 from Simulated Salt Waste - Comparison of PS TBA and PS MDOA

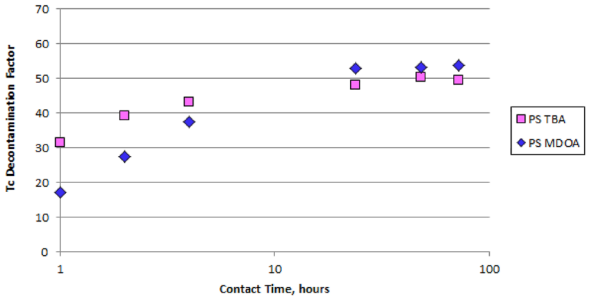

Saltstone Waste form Retention Test	Resin Addition Method	Rd	Solubility (mol/L)
Saltstone Control Sample	--	37	1.5E-06
Saltstone with 2.2g silica	dry feed	92	7.0E-07
Cement & fly ash with 2.2g silica	dry feed	8	3.9E-06
Saltstone with 2.2g silica	liquid	140	3.1E-07
Saltstone with 4.4g PM	liquid	130	3.3E-07
Saltstone with 11g PM	liquid	120	3.5E-07
Saltstone with 2.2g PM	liquid	160	2.7E-07
Saltstone with 2.2g PS	liquid	430	1.1E-07

Table 1. Results of Saltstone Waste form Retention Tests

The results of the Saltstone retention tests are shown in Table 1. Both the Rd and solubility results show that the PS MDOA resin was the most effective at retaining Tc-99 in the waste form. Rd is a ratio of the analyte of interest in the leachate compared to the amount of the anlalyte that remains in the solid. Therefore, the higher the Rd number, the more analyte remains in the waste form. Solubility numbers show how soluble the analyte is in the leachate, therefore, the lower the solubility value, the higher the retention in the waste form. Table 1 also shows that adding the resin to the salt solution prior to batching the Saltstone provides more effective retention in the waste form. The cement and fly ash test was to determine if the resin could replace blast furnace slag in the waste form. The initial results show that with silica MDOA resin, blast furnace slag still needs to be incorporated into the Saltstone formulation. However, based on the PS MDOA results, future work can be done to determine if the amount of blast furnace slag can be reduced when PS MDOA resin is included in the Saltstone formulation. The high Rd observed for the PS resin (Rd = 430) is indicative of its apparent superior performance.

FY2017 ACCOMPLISHMENTS

- ✔ Fabrication of PM MDOA and PS TBA technetium extraction resins (Clemson).
- ✔ Extended duration technetium decontamination tests with PS MDOA, PM MDOA, silica MDOA, PS TBA resins (the PS MDOA and silica MDOA resins were fabricated in FY16). Results showed that the PS MDOA and the PS TBA resins removed significantly more technetium than any of the other applicable resins, including the TEVA® resin, considered the “gold” standard of technetium extraction resins.
- ✔ Performed MDOA-based resin tests in the simulated Saltstone waste form. Investigated the retention of Tc-99 using different resin types, resin addition mechanisms, and varying the ratio of resin to salt solution.
- ✔ The results of the Saltstone retention tests with MDOA based resins showed that adding 2.2 g of polystyrene based MDOA resin to 240 g Saltstone increased Tc-99 retention under oxic conditions by a factor of 11.5.

FUTURE DIRECTIONS

This project was not renewed for a third year. However, the proposed future scope of work is:

- ✔ Identify tank waste sample to use in resin and Saltstone testing
- ✔ Resin selection based on results of FY17 testing
- ✔ Perform testing in acidic conditions and elevated temperature to mimic potential use in DWPF feed
- ✔ Investigate scale-up of resin formulation with Clemson
- ✔ Develop implementation plan in facilities based on Tc-99 testing results
- ✔ Referred publication in open literature

FY 2017 PUBLICATIONS/PRESENTATIONS

Submitted abstract to Waste Management Symposia 2018.

REFERENCE

1. Sleiman, A. F., A. Samadhi, S. M. Hasson, E. H. Bora, and T. A. Devol, *"Preparation of Polymer-Coated, Scintillating Ion-Exchange Resins for Monitoring of 99Tc in Groundwater,"* Anal. Chem. 83, 4759-4766, 2011.

ACRONYMS

DF	Decontamination Factor
DWPF	Defense Waste Processing Facility
IX	Ion-exchange
MDOA	Methyldioctylamine
PM	Polymethacrylate
PS	Polystyrene
Rd	Distribution Ratio
SRS	Savannah River Site
TBA	Tributylamine
TEA	Triethylamine

INTELLECTUAL PROPERTY

SRS Invention Disclosure: SRS-17-006 "Use of Novel Resin for Removing Technetium from DOE Tank Waste"

DEVELOPMENT OF A METHOD FOR MEASURING MERCURY (Hg) SPECIES USING Hg-DIFFUSIVE GRADIENTS IN THIN FILM (DGT) TECHNOLOGY

Project Team: Michael Paller, Brian Looney, Anna Knox, Dennis Jackson, Nancy Halverson, Wendy Kuhne (SRNL), Michele Harmon (USCA)

Subcontractor: University of Georgia

Thrust Area: Environmental Stewardship

Project Start Date: 10/1/16

Project End Date: 9/30/17

DGT is a type of passive sampler that consists of a gel-layer that selectively binds to contaminants and a diffusion gel that admits molecules that are available and toxic to organisms. DGT has potential to improve environmental monitoring of surface and ground water on DOE sites by reducing labor and analytical costs and providing better data for calculating risks. Research in 2017 included two projects, one concerning the measurement of bioavailable metals by DGT and the other concerning the development of methods for measuring mercury using DGT. We found that metal concentrations measured by DGT probes were correlated with metal toxicity to an aquatic invertebrate suggesting that DGT can serve as a surrogate for aquatic organisms. DGT can enhance risk assessment accuracy by improving the measurement of metal fractions that are bioavailable to aquatic organisms, but it does not fully account for all factors that affect bioavailability. We also developed a novel reactive DGT probe that measures only methymercury, potentially making it possible to assess Hg speciation more efficiently and economically than currently used techniques. The reactive probe adds a chemical reaction to the diffusion pathway of the DGT probe that chemically modifies and collects inorganic mercury, thereby preventing it from reaching the DGT collection gel. The reactive DGT concept represents an advancement in DGT technology that may be useful for other environmental contaminants besides mercury.

FY2017 OBJECTIVES

TASK ONE
Determine if DGT can accurately predict the effects of water quality on the bioavailability of metals to an aquatic organism.

TASK TWO
Develop a protocol for using DGT to measure and discriminate between inorganic mercury (InHg) and organic mercury (methylmercury, MeHg) in water.

INTRODUCTION

What is DGT?

Environmental sampling on the SRS and elsewhere within the Department of Energy (DOE) complex relies on labor intensive traditional approaches. However, passive samplers are efficient and costeffective alternatives to traditional methods. They rely on the unassisted molecular diffusion of analytes through a diffusive surface onto an adsorbent because of differences in concentration between the two media. They use no electricity, have no moving parts, and are simple to use. The adsorbed analytes are desorbed off the adsorbent and analyzed; e.g., by inductively coupled plasma mass spectrometry. wDiffusive Gradients in Thin Films (DGT) is a type of passive sampler that consists of an absorbent gel that selectively binds to specific contaminants and a diffusion gel that selectively admits analyte molecules (Davison and Zhang 1994, Van der Veeken et al. 2010) (Figure 1). DGT probes are exposed in surface waters, ground waters, submerged sediments, and saturated soils for hours to days to measure metals and other contaminants. Following exposure, the DGT absorbent gel is removed from the probe and analyzed to determine the concentration of the analyte (or analytes) of interest. Computations based on Fick's law are then used to determine the average concentrations of the analyte during the period of deployment based on its concentration in the absorbent gel, probe configuration, analyte diffusion coefficient, deployment time, and other factors.

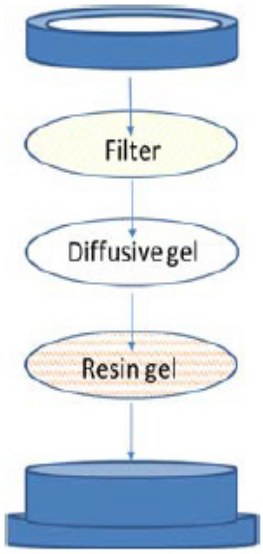

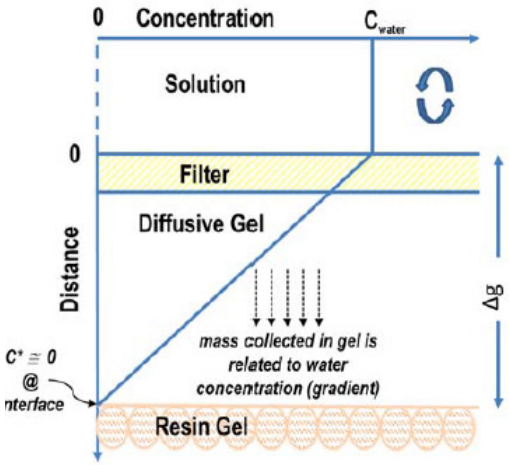

Figure 1. (Above) DGT water probe. **(Below)** Schematic cross-section shows a steady state concentration gradient between an analyte in solution and the probe collection resin that assimilates the analyte.

Measurement of Bioavailability

It is well known that metals and other contaminants exist in various forms that differ in bioavailability – the degree to which chemicals are absorbed or metabolized by human or ecological receptors or are available for biological interactions (ISO, 2005). Metal bioavailability, hence bioaccumulation and toxicity, is strongly affected by water chemistry. Key factors include dissolved organic matter, which can bind with metals to reduce their bioavailability and the ions associated with water hardness (primarily calcium and magnesium), which can affect the uptake of metals by the gills of aquatic organisms. This has led to an interest in analytical methods and/or sampling devices that predict the metal fraction that is bioavailable. Some believe that DGT mimics uptake by biota (Davison and Zhang, 1994) because it measures bioavailable dissolved and labile metal species that pass through the diffusion gel but excludes relatively unavailable metals, such as those bound to large organic molecules. However, metal toxicity to aquatic organisms is affected by cations associated with water hardness that compete with metals for binding sites on respiratory surfaces as well as by metal-ligand (e.g., metal-organic matter) interactions that reduce free ion activity (Di Toro 2001). The former mechanism may not influence the passage of metal through the diffusion gel nor metal uptake by the binding gel/resin, hence could represent a factor affecting bioavailability that is not measured by DGT. Metal species measured by DGT and their relationships with bioavailability need to be assessed more fully, and DGT needs to be compared with conventional measurement methods to identify conditions under which the two may differ.

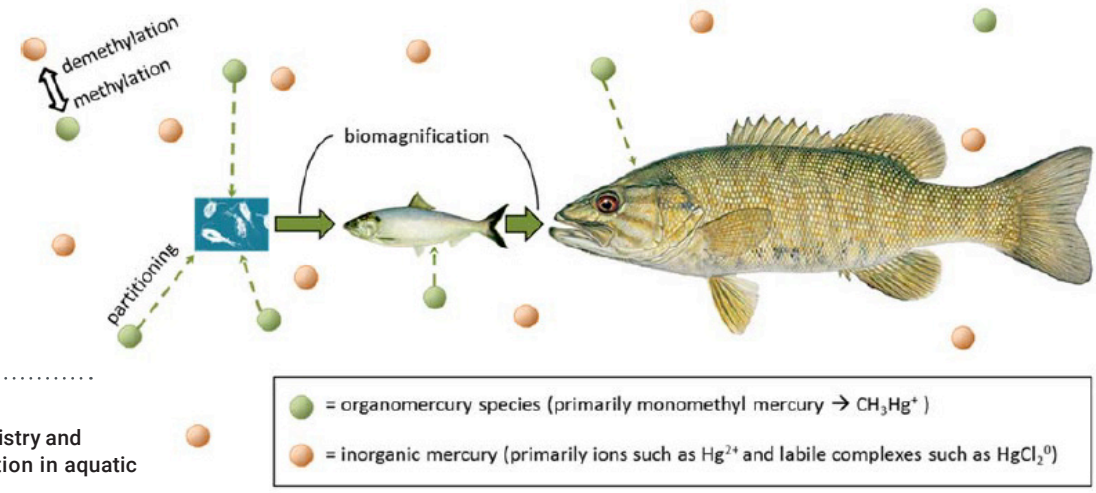

Figure 2.
Mercury chemistry and biomagnification in aquatic environments

Measurement of Mercury Speciation

Effective DGT probes have been developed for the measurement of most metals and a variety of other contaminants but not for mercury (Hg), an important persistent, bioaccumulative, and toxic element. Mercury measurement is difficult and expensive because the speciation of Hg is complex and unusual. The chemical speciation of mercury determines its toxicity. Organic mercury, of which methylmercury (MeHg) is the most commonly occurring form, is the most harmful species of Hg in aquatic environments because it is neurotoxic and bioaccumulates in fish (Figure 2). Currently available DGT probes cannot discriminate between inorganic Hg (InHg) and organic Hg making it difficult to accurately assess the environmental and human health risks posed by water pollution with Hg. Development of a DGT probe that accurately measures MeHg and discriminates it from inorganic Hg in aqueous media could provide a quick and simple method of measuring organic Hg that would result in significant cost savings and better protection of the environment.

Research conducted under LDRD-2016-00048 in 2017 included two related projects, one concerning the measurement of bioavailable metals by DGT and the other concerning the development of methods for measuring Hg using DGT. These are designated as Task 1 and Task 2, discussed separately on the following pages.

APPROACH

TASK 1: Determine if DGT can accurately predict the effects of water quality on the bioavailability of metals to an aquatic organism

We used standard bioassay procedures to calculate 48-hr LC50s for copper (Cu) and zinc (Zn) to Ceriodaphnia dubia, a small crustacean used for toxicity testing, in four types of water that differed in dissolved organic carbon (DOC) content and water hardness. The LC50 is the concentration that kills half of the test organism population in 48 hrs.

The four water types were:

1. Low hardness (10-13 mg/L as $CaCO_3$) and low (<detection limit) DOC,

2. Low hardness and high DOC (5 mg C/L).

3. High hardness (80-100 mg/L as $CaCO_3$) and low DOC (<DL)

4. High hardness water (80-100 mg/L as $CaCO_3$) and high DOC (5 mg C/L).

Each water type was made by adding reagent grade chemicals to untreated well water purified by passage through a Nanopure ultra purification system. DOC consisted of BorreGRO HA-1™.

The static acute toxicity tests were performed according to protocols described by ASTM (1993) in temperature- and light-controlled environmental chambers at the University of South Carolina at Aiken (USCA) (Figure 3). Separate toxicity tests were conducted for Cu and Zn. Test organisms obtained from cultures maintained at USCA were exposed to a control treatment and an ascending series of metal concentrations prepared by adding appropriate volumes of concentrated metal solution to the test water. Two replicates, each containing ten organisms, were prepared for each concentration. Replicates consisted of 250-ml glass beakers, each containing 100 ml of test solution. Test water without added metals served as the control.

Total metal levels in water were measured by Inductively Coupled Plasma Mass Spectrometry (ICP MS) at the beginning and end of each 48-hr bioassay. ICP MS measurements were generally in agreement with the calculated (from metal stock solution dilutions) metal levels for each treatment, averaging about 4% higher for Cu and about 2% lower for Zn. A water DGT probe (polyacrylamide gel cross-linked with an agarose derivative diffusive gel and Chelex binding layer) was deployed in each beaker for the duration of each test. Metals were removed from the DGT binding layers by acid extraction, analysed by ICP MS, and compared with metal levels in water measured by ICP MS.

Figure 3. Toxicity testing in climate controlled test chamber at the University of South Carolina (Aiken); Dark beaker contains water with DOC (BorreGRO HA-1™) - colorless beaker without DOC

The following hypotheses were tested under Task 1:

Hypothesis 1: DGT-DGT-based LC50s and water-based (i.e., total metal-based) LC50s will be more similar in low DOC water than in high DOC water because DGT will exclude Cu bound to DOC that does not contribute to toxicity in high DOC water.

Hypothesis 2: The effects of DOC on the relationship between DGT measurements and water measurements by ICP MS will be greater for Cu than Zn because Zn is less likely than Cu to form strongcomplexes with organic matter that will be excluded by DGT.

Hypothesis 3: Water hardness (i.e., calcium and magnesium ions) will strongly affect metal toxicity because of interactions at the respiratory surfaces of organisms but will have less effect on DGT measurements of metal concentrations because hardness will not strongly affect the uptake of metals by DGT.

RESULTS/DISCUSSION

Metal Levels in Water Measured by ICP MS and by DGT

DOC strongly influenced the measurement of Cu by DGT. Cu concentrations measured by DGT were much lower than Cu concentrations measured in water when DOC was high but only slightly lower when DOC was low (Figure 6). The relationship between DGT and water measurements was strong (R2 = 0.92-0.98) across all Cu concentrations and water types as indicated by linear regression; however, regression slopes differed greatly among water types (0.14 – 1.14) (Figure 7). In high DOC water, relatively low slopes (0.14-0.25) indicated that DGT consistently measured less Cu than was actually present. Much higher slopes in low DOC water (0.74-1.14) indicated that DGT measured most of the Cu in the water. The effects of hardness were smaller, resulting in a slope difference of 0.11 in high DOC water and 0.40 in low DOC water.

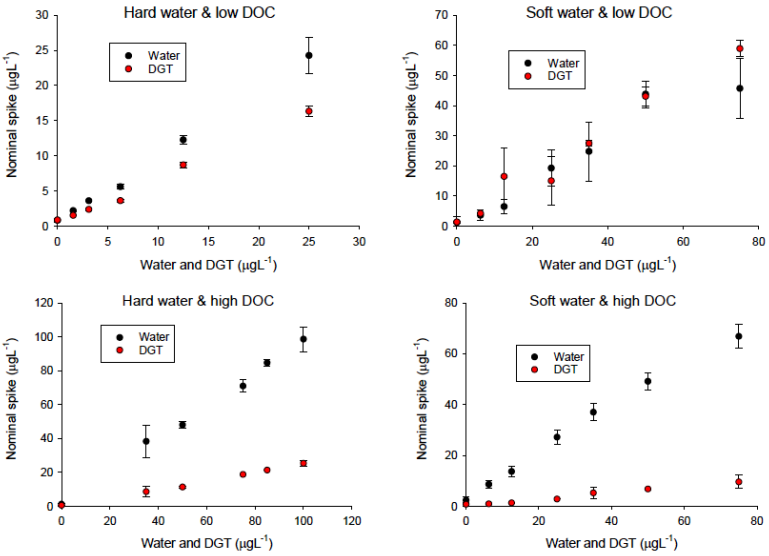

Figure 4. Copper concentrations in different types of water (hard and soft, high and low dissolved organic carbon) measured by DGT and ICP-MS

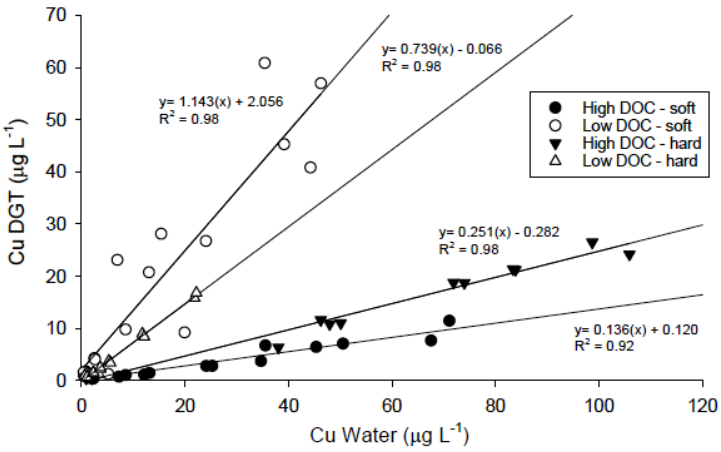

Figure 5. Linear regressions showing the relationships between Cu levels in water and DGT Cu in each treatment

In low DOC water, Zn concentrations measured by DGT were similar to or slightly lower than total Zn concentrations measured by ICP MS (Figure 8). In high DOC water Zn concentrations measured by DGT were lower than total Zn concentrations measured by ICPMS but the difference was less than observed with Cu (Figures 6 and 8). Linear regression indicated strong relationships between total Zn levels in water (as measured by ICP MS) and DGT-measured Zn (R2 = 0.92-0.99) (Figure 9). Regression slopes describing the relationship between total Zn measured by ICP MS and Zn measured by DGT were fairly similar across treatments (0.65 -0.82, Figure 9) indicating that water quality affected the measurement of Zn by DGT less than it affected the measurement of Cu by DGT, which exhibited highly variable slopes (Figure 7). These results generally support hypothesis 2: the effects of DOC on the relationship between DGT measurements and aqueous measurements will be greater for Cu than for Zn because Zn is less likely than Cu to form strong complexes with organic matter that will be excluded by DGT.

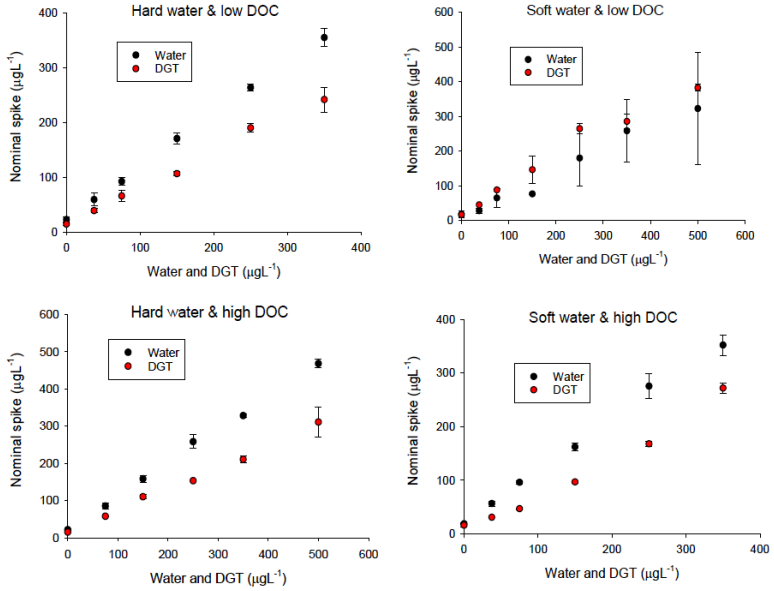

Figure 6. Zinc concentrations in different types of water (hard and soft, high and low dissolved organic carbon) measured by DGT and ICP-MS

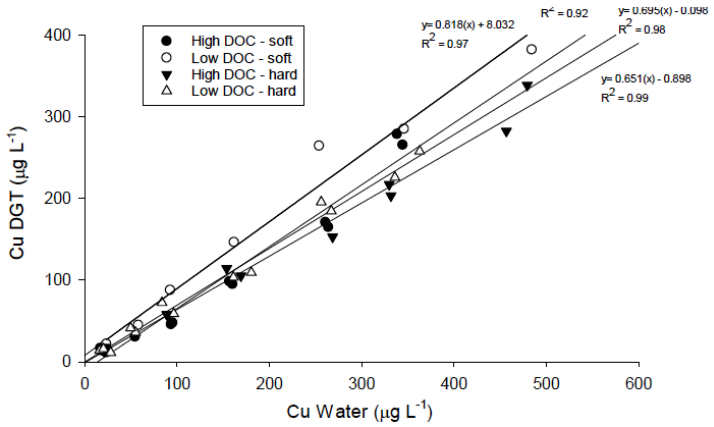

Figure 7. Linear regressions showing the relationships between Zn levels in water and DGT Zn in each treatment

Relationship Between Toxicity and Metal Concentrations Measured by DGT

Copper toxicity, as indicated by 48 hr LC50s for Ceriodaphnia dubia, was strongly affected by DOC. DGTbased LC50s for Cu were much lower than water-based LC50s (hereafter referred to as actual LC50s) in high DOC water (Figure 10). The difference between actual and DGT-based LC50s in low DOC water was smaller than in high DOC water, although LC50s could only be calculated for low DOC water with high hardness, as explained more fully later. The ratio of the actual LC50 to the DGT-based LC50 was 1.5 in water with low DOC compared with 3.8 – 6.6 in water with high DOC (Figure 10). These results support hypothesis 1: Differences between DGT-based LC50s and actual LC50s will be smaller in low DOC water than in high DOC water. LC50s based on total Cu levels in water were higher than DGT-based LC50s in high DOC water because total Cu included non-bioavailable Cu complexed with organic matter that contributed minimally to toxicity. These Cu-organic matter complexes were likely excluded by DGT because they did not readily pass through the DGT diffusion gel.

DOC had smaller effects on Zn toxicity than on Cu toxicity: actual LC50s for Zn were only 1.7-1.9 times higher than DGT-based LC50s in high DOC water compared with 3.8-6.6 for Cu. Presumably, this difference occurred because Zn did not form strong complexes with organic matter that reduced bioavailability and toxicity as well as uptake by DGT. The lack of such complexes is supported by the previously described comparisons of total Zn in water with Zn uptake by DGT (Figures 8 and 9).

Hardness strongly affected Cu toxicity in low DOC water. The actual LC50 in moderately hard water with low DOC was 9 ppb but could not be calculated in soft water with low DOC because all tested concentrations (including those <5 ppb) resulted in complete mortality of the test organisms (Figure 10). The effects of hardness were less prominent in high DOC water: actual LC50s were about 60% higher in moderately hard water than in soft water indicating less toxicity in the former. Hardness affected Zn toxicity, but the effects were less than with Cu. At low levels of DOC, actual LC50s were about 40% higher in moderately hard water than in soft water. At high levels of DOC, Zn LC50s were actually higher in soft water than in moderately hard water.

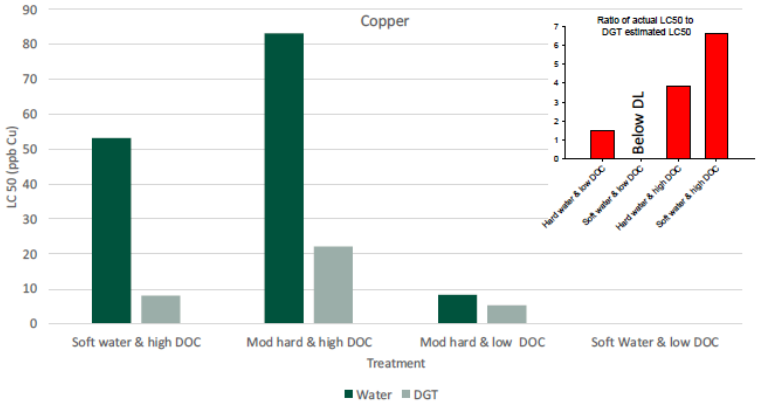

Figure 8. Effects of dissolved organic carbon (DOC) and hardness on copper toxicity to Ceriodaphnia dubia; Copper levels were below the detection limit (DL) in soft water with low DOC

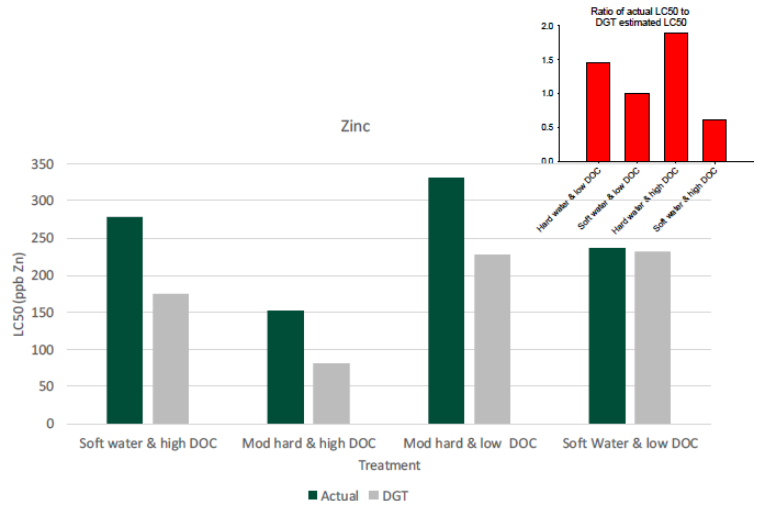

Figure 9. Effects of dissolved organic carbon (DOC) and hardness on zinc toxicity to *Ceriodaphnia dubia*

The preceding results can be interpreted in terms of hypothesis 3: water hardness (i.e., calcium and magnesium ions) will strongly affect metal toxicity because of interactions at the respiratory surfaces of aquatic organisms but will have less effect on DGT measurements of metal concentrations because hardness will not strongly affect the uptake of metals by DGT. This was partly true for Cu. Hardness strongly affected Cu toxicity when DOC was low (Figure 10) but only moderately affected the measurement of Cu by DGT. The latter was indicated by comparing regressions of DGT-Cu on ICP MS-Cu (i.e., total water Cu) between soft and hard water, which differed in slope (0.74-1,14, Figure 7), but to a proportionally smaller degree than differences in toxicity (which varied from 9 ppb to below detection limits). When DOC was high, the effects of hardness on Cu toxicity were less pronounced than when DOC was low (as indicated by differences between LC50s, Figure 10) and roughly proportional to the difference between DGT and ICP MS measurements of Cu. LC50s differed by about 60% and regression slopes by 78% between hard and soft water. Hypothesis 3 was largely true for Zn: large differences in hardness had minimal effects on the measurement of Zn

by DGT, as indicated by comparing regressions of DGT measurements on ICP MS measurements of Zn between soft and hard water, which diffed by <17%-19% (Figure 9). However, effects on toxicity were greater as indicated by LC%50s that differed by 40-80% between hard and soft water.

This study showed that DOC, which occurs naturally in most surface waters in variable amounts, can strongly affect the measurement of some metals by DGT. Copper concentrations recorded by DGT were significantly lower than actual Cu concentrations in high DOC water, presumably because the organic compounds in high DOC water combined with Cu to form a complex that was unable to pass through the DGT diffusion gel. Such complexes are also unlikely to be bioavailable. Thus, in high DOC water, DGT is likely to provide a better estimate of bioavailable Cu than conventional water measurements because it excludes non-bioavailable Cu bound to DOC. DGT-based LC50s under such circumstances will be lower than actual LC50s because they include only bioavailable Cu while the latter includes bioavailable and non-bioavailable (i.e., non-toxic) Cu. Therefore, DGT measurements of Cu can be combined with water measurements to estimate the total Cu fraction that is toxic, or compared directly with toxicity thresholds to provide a more realistic estimate than total water measurements of the likelihood of environmental impacts caused by metal toxicity. DGT may be useful, in this context, with other metals besides Cu that readily bind with organic matter.

Hardness had substantial effects on the toxicity of Cu and Zn (especially in soft water for the former) but relatively weak effects on the uptake of these metals by DGT. This probably occurred because hardness influences toxicity at the gill surfaces of aquatic organisms by mechanisms that do not have a commensurate effect on the uptake of metals by DGT. In summary, DGT can enhance risk assessment accuracy by improving the measurement of metal fractions that are bioavailable to aquatic organisms. However; it does not completely account for all factors that affect bioavailability.

TASK 2: Develop a protocol for using DGT to measure and discriminate between inorganic mercury (InHg) and organic (methyl) mercury (MeHg) in water

This task consisted of four subtasks, referred to as campaigns, with different approaches and hypotheses (Figure 12). Campaigns 1 and 2 tested the ability of DGT probes designed for measuring organic compounds to measure methyl mercury (MeHg). We thought this might be possible because octanol-water partitioning coefficients reported for MeHg are similar to those of some organic compounds that are measurable by DGT probes with collection gels specifically designed for organic compounds. Campaign 1 tested a commercially available DGT probe with XAD18 collection resin, referred to as “probe type 2”, designed to measure antibiotics in solution. Campaign 2 tested a commercially available DGT probe with an HLB binding layer, referred to as “probe type 3”, designed to measure pesticides and personal care products. Probe types 2 and 3 will hereafter be referred to as hydrophobic probes.

Campaigns 3 and 4 involved the design and testing of novel reactive DGT probes for collecting MeHg only (Figure 12). The reactive probes added a chemical reaction to the diffusion pathway of the DGT probe to chemically modify and collect InHg in the DGT, thereby preventing it from reaching the collection gel. Specifics will not be disclosed herein because the reactive Hg DGT probe design is proprietary and the subject of an SRNL patent disclosure.

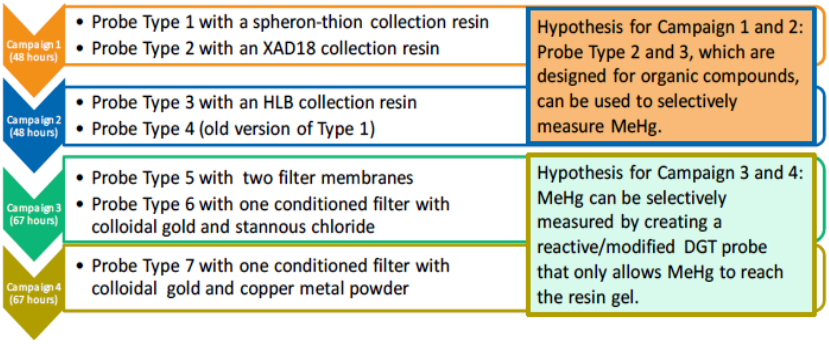

Figure 10. Study design for testing DGT probes for the measurement of methyl mercury

Campaigns 1 and 2 compared probes types 2 and 3 with commercially available Hg DGT probes, referred to as "probe type 1" and "probe type 4." Probe type 1 contained a spheron-thiol resin designed to collect both inorganic Hg (InHg) and MeHg. Probe type 4 was similar to probe type 1 but represented an older probe model. Campaigns 3 and 4 evaluated the abilities of different types of reactive DGT probes, referred to as "probe types 5, 6, and 7", to selectively collect MeHg. In all campaigns, the DGT probes were tested by placing them for 48 hours in 5 l beakers containing artificial stream water spiked with one of the following: 1) sufficient InHg to produce a concentration of 1200 ng/l of InHg, and 2) sufficient MeHg to produce a concentration of 1200 ng/l of MeHg (Figure 13). In some trials, a combination of 50% InHg and 50% MeHg sufficient to produce a concentration of 1200 ng/l of total Hg was also employed. Each treatment was replicated (i.e., represented by two beakers), and all beakers were stirred continually. The resin gels were extracted and analyzed by pyrolysis in a Lumex Mercury Analyzer following retrieval of the DGT probes. Water samples were collected from each beaker before and after DGT deployment, preserved with bromine monochloride, and taken to an SRNL laboratory for Hg analysis using standard methods. Mercury in the water samples was compared with calculated Hg uptake by the DGT probes.

Figure 11. Experimental apparatus for testing HgDGT probes

The following are hypotheses for the campaigns:

Hypothesis for Campaigns 1 and 2: DGT probes for measuring organic compounds (probe types 2 and 3) will selectively collect and measure MeHg and exclude inorganic Hg (InHg). Hg concentrations calculated from these probe types will be about 1200 ng/l for beakers with MeHg solution, 0 ng/l for beakers with InHg solutions, and 600 ng/l for beakers with 50% InHg and 50% MeHg (Figure 4).

Hypothesis for Campaigns 3 and 4: It is possible to construct a novel reactive DGT probe that only allows MeHg to reach the resin (collection) gel, thereby measuring MeHg only. Hg concentrations calculated with a successful reactive Hg probe will be about 1200 ng/l for beakers with MeHg solution, 0 ng/l for beakers with InHg solutions, and 600 ng/l for beakers with 50% InHg and 50% MeHg.

RESULTS/DISCUSSION

Probe types 1 and 4 (commercially available Hg probes) collected InHg, MeHg, and the combination of InHg and MeHg in approximately equal quantities, as indicated by Lumex Mercury Analyzer absorbance values (Figure 14). These results show that spheron-thiol collection resins are unsuitable for discriminating between InHg and MeHg. The hydrophobic probe evaluated in campaign 1 exhibited limited ability to differentiate between Hg species and had relatively low affinity for all forms of Hg compared with the commercial spheron-thiol probe (probe type 1) (Figure 14). The results of campaign 2 showed that hydrophobic probe type 3 (not shown) were similar to those for hydrophobic probe type 2 evaluated in campaign 1. These data show that DGT probes with hydrophobic collection resins used to measuring organic compounds are not suitable for the measurement of MeHg and assessment of Hg speciation.

Probe types 5 and 6 represent initial efforts to develop reactive DGT probes that selectively collected MeHg by preventing the passage of InHg through the DGT diffusion gel (Figure 14). Probe type 5 evaluated in campaign 3 preferentially collected MeHg but also collected some InHg. Probe type 6 successfully excluded InHg from the DGT collection resin but produced a precipitate that leached out of the DGT probe. Probe type 7 (evaluated in campaign 4) overcame the preceding difficulties resulting in a reactive DGT probe that selectively measured MeHg and excluded InHg (Figure 15).

The reactive DGT (rDGT) developed as part of this LDRD project has the unique capability of selectively measuring MeHg. It has potential to facilitate the assessment of Hg speciation in surface or groundwater and may represent a substantial contribution to the science of measuring Hg in aquatic environments. Hg speciation could be assessed by deploying a reactive Hg DGT probe that selectively measures MeHg together with a conventional Hg DGT probe that measures total mercury (i.e., the sum of MeHg and InHg). Upon retrieval, the DGT collection resins of each probe could be removed and analyzed with an automated system for direct Hg analysis to quickly provide estimates of environmental concentrations of both total Hg and MeHg, as needed for accurate rick analysis and environmental assessment. This approach is simpler, faster, and more economical than existing wet chemistry methods that are laborious and time-consuming. It should also be noted that the reactive DGT concept represents an advancement in DGT technology that may be useful for the accurate and cost-effective analysis of other environmental contaminants besides Hg.

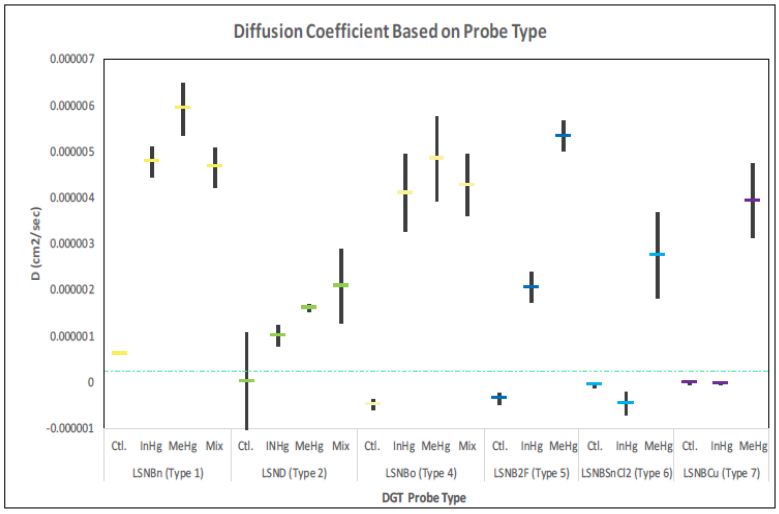

Figure 12. Spectrophotometric absorbance values for methyl mercury (MeHg), inorganic mercury (InHg) and a combination of 50% methyl mercury and 50% inorganic mercury (Mix) generated by analyzing the mercury collection resins of six types of DGT probes following 48 hours of immersion in mercury test solutions; Absorbance values are proportional to Hg masses collected by each probe. Probe types are described in the text.

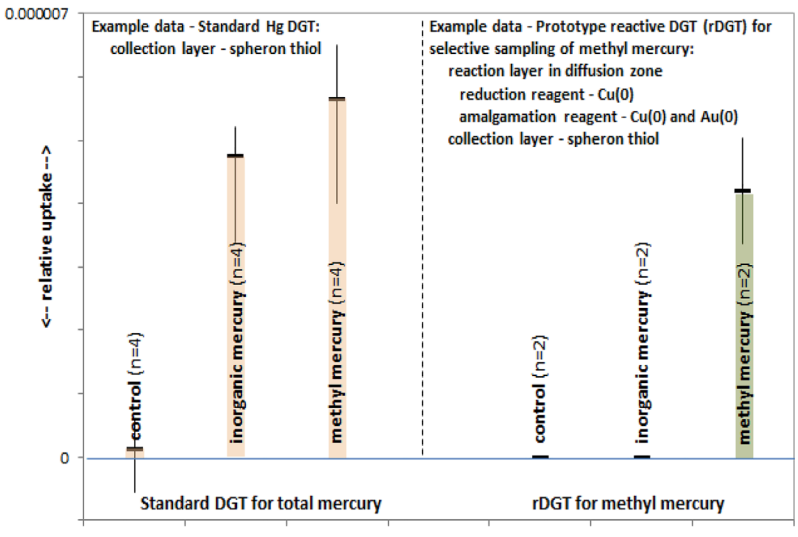

Figure 13. Comparison of the relative abilities of a standard DGT probe and novel reactive DGT probe to selectively measure methyl mercury

FY2017 ACCOMPLISHMENTS

- We found that metal concentrations measured by DGT probes were correlated with metal toxicity to an aquatic invertebrate suggesting that DGT probes may serve as surrogates for aquatic organisms.
- We found that DGT can enhance risk assessment accuracy by improving the measurement of metal fractions that are bioavailable to aquatic organisms, but it does not account for all factors that affect bioavailability.
- We developed a novel reactive DGT probe that measures only methylmercury potentially making it possible to assess Hg speciation quickly, simply, and economically. The reactive DGT concept represents an advancement in DGT technology.

FUTURE DIRECTIONS

- Identify optimal reductant for MeHg reactive DGT (rDGT)
- Modify DGT resin by incorporating a reductant
- Test reactive DGT shelf life, effective deployment time, and effects of variations in pH and dissolved organic carbon concentration on MeHg measurements
- Assess viability of measuring mercury with DGT technology as a low cost rapid assessment monitoring technique for SRS and elsewhere

PRESENTATIONS/PUBLICATIONS

1. Presentation at ICOBTE 2017: "Effects of water quality on the measurement of bioavailable metal fractions by diffusive gradients in thin films (DGT)"

REFERENCES

1. ASTM (1993a) Standard Guide for Conducting Three-Brood, Renewal Toxicity Tests with *Ceriodaphnia dubia*, ASTM Standards on Aquatic Toxicology and Hazard Evaluation, Designation E-1295-89. American Society for Testing and Materials, Philadelphia, PA

2. Davison, W., Zhang, H. 1994. In situ speciation measurements of trace components in natural waters using thin-film gels. Nature 367: 546-548.

3. Di Toro DM, Allen HE, Bergman HL, Meyer JS, Paquin PR, Santore RC. 2001. Biotic Ligand Model of the Acute Toxicity of Metals. I. Technical Basis. Environmental Toxicology and Chemistry 20: 2383–2396.

4. ISO. 2005. 11074: Soil-quality-Vocabulary. ISO, Geneva, Switzerland.

5. Van der Veeken, P.L.R., Van Leeuwen, H.P., 2010. DGT/DET gel partition features of humic acid/metal species. Environ. Sci. Technol., 44: 4253-4257.

ACRONYMS

CaCO3: Calcium Carbonate
Cu: Copper
DOC: Dissolved Organic Carbon
DOE: Department of Energy
DGT: Diffusive Gradients in Thin Films
Hg: Mercury
Hg-DGT: Mercury-Diffusive Gradients in Thin Films
ICP MS: Inductively Coupled Plasma Mass Spectrometry
LC50: Lethal Concentration 50
MeHg: Methylmercury
rDGT: Reactive DGT
SRS: Savannah River Site
Zn: Zinc

INTELLECTUAL PROPERTY

Patent disclosure submitted: "Mercury Speciation using Reactive Diffusive Gradient in Thin-Film (rDGT) Sampler."

TOTAL NUMBER OF STUDENTS

3 Students

MERCURY REMOVAL & STABILIZATION IN THE SUBSURFACE USING VAPOR PHASE SULFUR

Project Team: Dennis G. Jackson (Primary), Miles E. Denham, and Carol Eddy-Dilek

Subcontractor:
Clemson University – Ron Falta

Thrust Area: Environmental Stewardship

Project Start Date: 10/1/15

Project End Date: 9/30/18

Along with Clemson University the operational strategies related to thermal heating of elemental mercury with gas injection were evaluated. These simulations were performed with the DOE developed code TOUGH2/TMVOC. Dr. Ronal Falta, a developer of this code directed a Master's candidate in the performance of these simulations. The TOUGH2/TMVOC library of thermophysical parameters was updated with relative properties for elemental mercury. Benchmark simulations were performed specific to laboratory results and simulation output from a proprietary software package. Simulations representative of a practical field problem were performed to determine the effect of moisture and air injection requirements to facilitate removal of elemental mercury. Simulations were performed by a Master's student.

FY2017 OBJECTIVES

TASK ONE

Partnered with Clemson University to model the multiphase processes that occur during heating and cooling of subsurface porous media and evaluate the effectiveness for removal of elemental mercury.

INTRODUCTION

The Oak Ridge Y-12 National Security Complex (Y-12) used large amounts of elemental mercury from the early 1950's through the 1970's. This mercury serves as a source of contamination to groundwater and surface waters that exit the reservation. Remediation of mercury contaminated soils and building materials is a high priority technical challenge that needs to be resolved to support decommissioning activities within the Y-12 complex. In this research our team is evaluating the remediation of elemental mercury from the subsurface using in-situ thermal remediation coupled with a novel in-situ stabilization mechanism.

Thermal remediation is a mature technology that has been used for two decades in the remediation of organic contaminants such as benzene, toluene, trichloroethylene and tetrachloroethylene from soils. All of these compounds have boiling points on the order of (80 to 125 °C). In thermal remediation, heat is used to increase the vapor pressure of the contaminant allowing removal using soil vapor extraction. Conventional thermal remediation involves heating the subsurface to temperatures near the boiling point of the target contaminant (357 °C for elemental mercury). Our team is exploring the unique properties of elemental mercury to evaluate and develop a remediation strategy at operating temperatures consistent with current in-situ remediation technology. For large-scale applications that involve thermal removal of elemental mercury, the use of lower treatment temperatures will translate directly to lower implementation and operational costs compared to baseline costs.

To ensure long-term compliance with the treatment standards, our remediation strategy incorporates a sequestration mechanism to address residual mercury that remains after the heating campaign. This research develops an SRNL technology (US #8,770,891) designed to stabilize elemental mercury in the subsurface. The technology uses residual heat present following thermal treatment to deliver elemental sulfur vapor as a sequestering agent. Sulfur combines with mercury to form mercury sulfide compounds, a more stable, less leachable form of mercury. Our goal is to establish an operating paradigm that couples thermal mass removal with this process to stabilize residual contamination in place.

APPROACH

The basis for our treatment paradigm exploits the unique behavior of mercury volatilization from soils during heating to develop a thermal remediation strategy specific to elemental mercury. This strategy is based upon the "thermograms" for various species of mercury that are presented in Figure 1. These thermograms illustrate the volatilization (removal) of various mercury species from soils during controlled pyrolysis. Our team is using the unique temperature window of each of the different mercury species and compounds to develop remediation strategy technologies specific to elemental mercury. The results from these controlled pyrolysis studies indicate that relatively low temperatures (80 to 125 °C) are sufficient to liberate elemental mercury from soils. These observations are being used to identify and develop specific technologies for the remediation of elemental mercury.

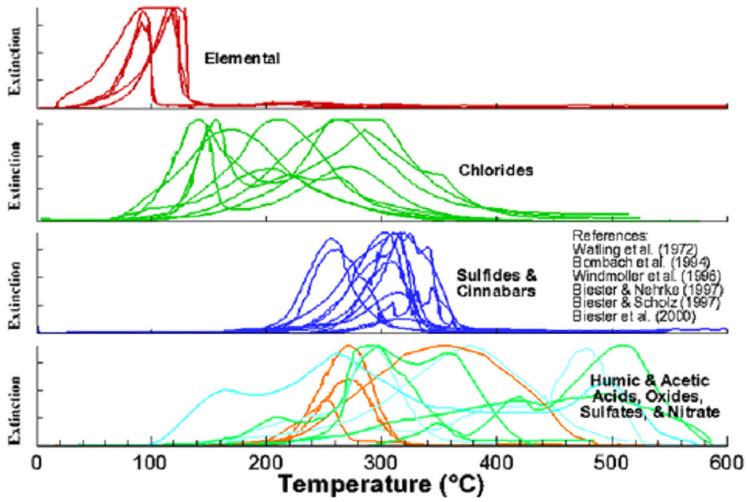

Figure 1. "Thermograms" depicting the removal of mercury species during controlled pyrolysis

Since elemental mercury is so reactive with very low environmental thresholds, any in-situ remedy will need to provide a stabilization component to address any residual material left in the subsurface following thermal extraction. SRNL technology (US #8,770,891) provides a mechanism to stabilize elemental mercury in the subsurface. The patented technology uses residual heat present in the subsurface following thermal treatment to aid in the delivery of elemental sulfur for use as a sequestering agent. Our approach is to evaluate mercury and sulfur reactions in the subsurface as a function of temperature. We note that in the thermograms, mercury sulfides require temperatures in the 200 to 350 °C range to decompose. This indicates a more recalcitrant species versus the more soluble elemental mercury and the chloride species. Chemical equilibrium modeling was used to evaluate effectiveness of the treatment and assess secondary reactions associated with formation of stable mercury compounds.

RESULTS/DISCUSSION

In FY2017 Clemson University performed numerical simulations to evaluate the viability of the removal of elemental mercury from soils using thermal heating and augmented with air injection. This work was performed using the DOE developed TOUGH2/TMVOC software.

Validation of TOUGH2/TMVOC software for Application: Previously reported laboratory experiments and numerical simulations using the proprietary STARS software package were duplicated. Kunkel's one-dimensional thermal desorption experiments performed at 244 °C[1] were simulated using TOUGH2/TMVOC. The TOUGH2/TMVOC model entails four parts [1] establishing the initial conditions within the column, [2] injecting the elemental mercury into the column, [3] redistribution of the elemental mercury post injection, and [4] air flooding for the removal of elemental mercury.

The first part of the simulation was to create a grid mesh and establish the initial conditions within the TOUGH2/TMVOC model. Both the STARS and TOUGH2/TMVOC models were setup to allow air to be injected at the bottom of the column and collected from the top. A three-dimensional Cartesian grid was constructed in TOUGH2/TMVOC to match the grid created in STARS[1]. The vapor pressure of mercury at 244 °C (0.085 atm) is exceeded by the 1 atm in the column and the initial conditions are sufficient to transfer mercury into the gas phase. The column contains only air at the initial stages of the simulation. Both models contain 24 horizontal layers but have a variable numbers of grid blocks in each layer. The STARS model contains 64 gridblocks in each of the 24 layers, while the TOUGH2/TMVOC model contains one gridblock in each of the 24 layers (Figure 2).

Elemental mercury was created and added to the VOC library in the TOUGH2/TMVOC simulation. The physical and chemical properties of mercury that were used to create the mercury VOC are listed in reference 2. Vapor pressure was calculated in each grid block in the TOUGH2/TMVOC simulation using Antoine's equation[3]. Vapor pressure constants were obtained from the NIST database and were used to calculate the vapor pressure of the mercury in each gridblock at each time step. Capillary pressure and relative permeability are calculated using three phase estimation methods modified from Lenhard & Parker[4], Stone[5], and Pruess & Battistelli[3]. Dynamic viscosity was calculated as a function of temperature using the Van Velzen et al. equation[3,6].

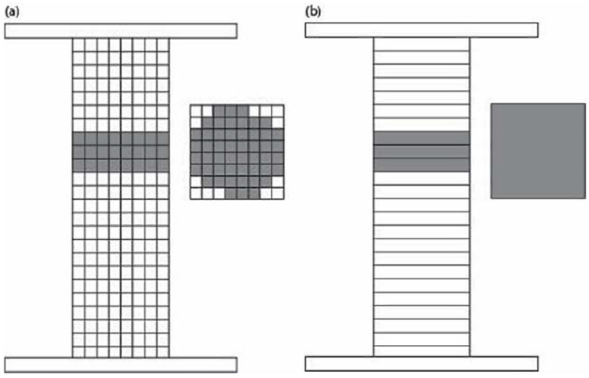

Figure 2. Modified from Kunkel et al.[1] **(a) illustrates the DNAPL distribution in the three dimensional Cartesian grid used in the STARS simulation. (b) Illustrates the DNAPL distribution in the TOUGH2/TMVOC simulation.**

The second part of the simulation involves injecting the elemental mercury into the column. The reduction in gridblocks in the TOUGH2/TMOVC model causes the elemental mercury distributions to be slightly different than the STARS model. The STARS model contains 50 contaminated grid blocks in three layers. Each of the 150 grid blocks contains ten percent elemental mercury saturation for a total elemental mercury volume of 1.1 mL (15 g). 14 of the 64 grid blocks in each of the three contaminated layers do not contain elemental mercury saturation, these grid blocks allow air to flow around the contaminated section of the column (Figure 2). Elemental mercury was injected across the three contaminated grid blocks at a reduced rate of 1.00E-04 kg/s for 50 s with an enthalpy of 3.415E+04 J/kg to match the STARS simulation.

The third part of the simulation is the post injection redistribution of elemental mercury. Most of the model gridblocks are located on the top of the contaminated zone and allow for the upward movement of the elemental mercury as air is injected into the column. The grid blocks beneath the contaminated zone show the initial downward elemental mercury migration post injection. The length and placement of the uncontaminated zone within the column does not impact the remediation time for the DNAPL[1]. The contaminated zone in the TOUGH2/TMVOC model was placed in the same three layers as the STARS Simulation so that the models have similar geometries (Figure 2).

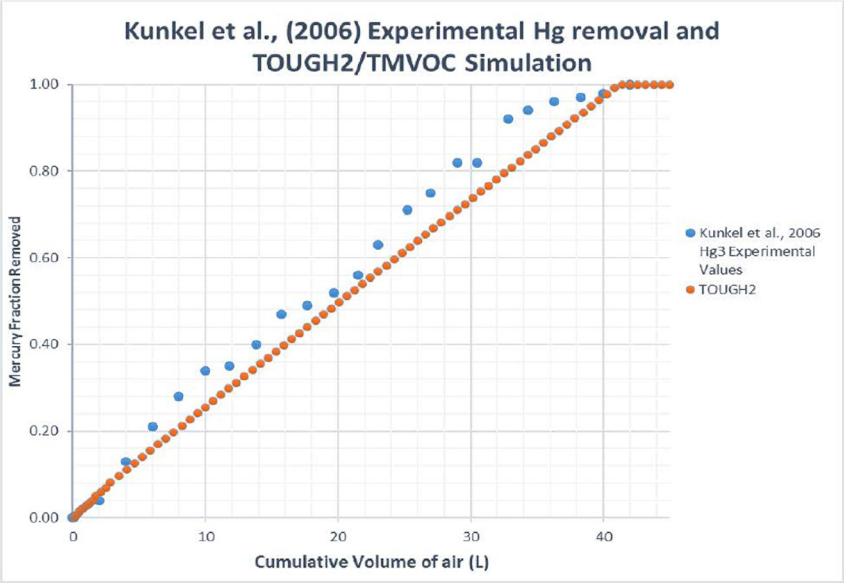

Figure 3. Verification of TOUGH/TMVOC laboratory results of Kunkel[1] with TOUGH2/TMVOC simulations. Mercury mass fraction remaining was plotted as total mercury removed from the system.

The fourth and final part of the simulation was the injection of air into the column. To match the amount of air flowing through the contaminated zone of the STARS simulation the flow of air in the TOUGH2/TMVOC simulation was reduced by 78%. The 14 uncontaminated gridblocks across the 3 layers containing elemental mercury in the STARS simulation were removed in the TOUGH2/TMVOC simulation and the air injection was reduced by the fraction of air flowing around the contaminated zone. In the TOUGH2/TMVOC simulation, air was injected into the bottom grid block of at a rate of 9.87E-07 kg/s with an enthalpy of 2.45E+05 J/kg. Water was also injected into the bottom layer of the model to account for the small fraction of water vapor in the air. The top grid block in the TOUGH2/TMVOC simulation is at fixed state so air injected in to the bottom of the column and produced from the top. The ability for the vapors to escape from the top simulates vapor extraction without the use of vacuums.

The mass fraction of elemental mercury effluent captured in Kunkel's experiment[1] was plotted along with the STARS simulation to illustrate the 48 L of flushing air necessary to remove 99.8% of the mercury. The same mass fraction of mercury effluent was plotted alongside the TOUGH2/TMVOC simulation to show that the experimental results were validated using an alternative numerical simulator (Figure 2). The TOUGH2/TMOVC numerical simulation calculates 100% elemental mercury removal after 42.61 L of air is flushed through the column (Figure 3). Reproducing the STARS simulation in TOUGH2/TMVOC was helpful in illustrating that the alternative simulator can be used to show the thermal treatments of mercury. However, the one-dimensional column only contains an initial gas phase. Gas, water and elemental mercury phases need to be added to the ex-situ simulation to simulate realistic application of thermal treatment for elemental mercury.

Application of TOUGH2/TMVOC software for Ex-Situ Simulation: The ex-situ model design is based on a container with insulated walls and intended to simulate a practical field application. The container is simulated with no flow boundaries and a lid to prevent mercury vapor from escaping the domain. The initial design of the ex-situ experiments allows material to be excavated and placed into the heated basin. The goal is to show elemental mercury remediation of consolidated fill material associated with mercury contaminated locations. The simulation was based upon a 5-m x 5-m x 2-m geometry.

The simulation contains the following saturations: water saturation 0.31, gas saturation 0.69, and elemental mercury saturation 0.000494. The small amount of elemental mercury saturation yields a total mass of mercury contamination reasonable for a control volume of 50 m^3 (2 kg/m^3 or about 100 kg total). The initial gas and water saturations are typical for coarse sand with most of the pore space occupied by air. The relative permeability and capillary pressure within the model were calculated using three phase estimation methods modified from Stone[5] and Parker[4] and the dynamic viscosity was calculated as a function of temperature using the Van Velzen et al. equation[3,6]. The permeability is homogeneous through the system and is typical of coarse sand.

Horizontal injection and deliverability wells were added to the bottom and top of the model. Air is injected into the model at a rate of 0.05 kg/s over six wells and the enthalpy of the air is defined at 200 °C. Water is injected at a rate of 1/50 of the air injection to account for the air humidity. Over time, the hot air evaporates the pore water, and the temperature increases. Energy that is delivered to the system at a specific rate has proven to be an important variable in early simulations. The rate at which hot air is injected into the system can determine how long it takes to remediate the target volume.

However, when the rate of air injection is increased the pressure within the system increases. A fine balance must be met to prevent the internal pressure from getting too high while keeping the air injection rate high enough to remove the mercury within a reasonable time. Figure 4 indicates that mercury saturations decrease from the evaporation with some localized accumulations from condensation. Condensation occurs in small areas above the initial mercury evaporation front (Figure 4) that are cool from the lack of temperature penetration in the early time steps of simulation. At the current parameters, the elemental mercury is completely removed from the system in 11.57 days with a cumulative flushing volume of greater than 200,000 m^3.

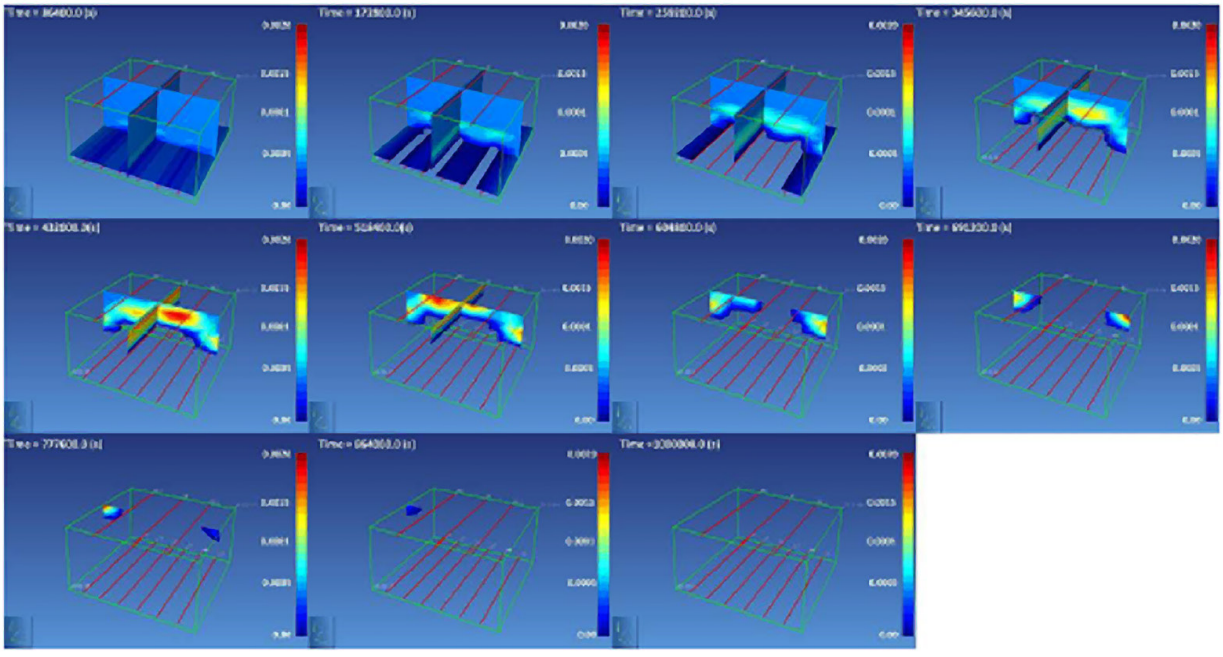

Figure 4. Three–dimensional saturations of elemental mercury taken at daily time steps. Elemental mercury is removed rapidly once most of the water has evaporated allowing the system to heat up. Some mercury condenses temporarily in the corners of the system, but all of the mercury is removed by 11.6 days.

FY2017 ACCOMPLISHMENTS

- Verified the ability of the DOE developed TOUGH2/TMVOC numerical simulator to simulate the thermal treatment of elemental mercury in porous media.
- Selected validated properties from the open literature for elemental mercury and added this data to the VOC library in the TOUGH2/TMVOC simulation.
- Performed simulations of a representative field problem to determine effect of moisture as humidity and air injection requirements to facilitate removal of elemental mercury.

FUTURE DIRECTIONS

- Seek support from DOE-EM for funds to support field-scale pilot test of the remediation technology.

PRESENTATIONS/PUBLICATIONS

Platform presentation entitled *"Stabilization of Residual Elemental Mercury Following Thermal Remediation Using Gaseous Sulfur"* at the 13th International Conference on Mercury as a Global Pollutant, SRNL-STI-2017-00434, July 2017, Providence, Rhode Island.

REFERENCES

1. Kunkel, A. M., Seibert, J. J., Elliott, L. J., Kelley, R., Katz, L. E., & Pope, G. A. (2006). *Remediation of elemental mercury using in situ thermal desorption (ISTD).* Environmental Science & Technology, 40(7), 2384-2389.
2. Reid, R. C. (1987). *The properties of gases and liquids (4th ed. ed.).* New York: McGraw-Hill.
3. Pruess, K., & Battistelli, A. (2002). *TMVOC, a numerical simulator for three-phase non-isothermal flows of multicomponent hydrocarbon mixtures in saturated-unsaturated heterogeneous media.* Report LBNL-49375 Lawrence Berkeley National Laboratory, Berkley, California.
4. Lenhard, R. J., & Parker, J. C. (1987). *Measurement and prediction of saturation-pressure relationships in three-phase porous media systems.* Journal of Contaminant Hydrology, 1(4), 407-424.
5. Stone, H. L. (1970). *Probability model for estimating three-phase relative permeability.* Journal of Petroleum Technology, 22(02), 214-218.
6. Van Velzen, D., Cardozo, R. L., & Langenkamp, H. (1972). *A liquid viscosity-temperature-chemical constitution relation for organic compounds.* Industrial & Engineering Chemistry Fundamentals, 11(1), 20-25.

ACRONYMS

DOE	Department of Energy
DOE-EM	Department of Energy - Office of Environmental Managment
SRNL	Savannah River National Laboratory
STARS	Steam and Thermal Advanced Reservoir Simulator, software developed by Computer Modeling Group Ltd.
TOUGH2/TMVOC	Transport Of Unsaturated Groundwater and Heat with non-isothermal flow of water, soil gas, and a multicomponent of volatile organic chemical module
VOC	Volatile Organic Compounds

INTELLECTUAL PROPERTY

In July of 2011 an invention disclosure for the described technology was submitted in a strategic endeavor to position SRNL in an advantageous position to garner future research funding. In July of 2014 a US Patent (#8,770,891) was issued. While the potential exists for additional intellectual property, LDRD funds are being used to develop the existing IP so that data beyond simple proof of concept is available.

SILVER-IODINE SECONDARY WASTE STABILIZATION: MULTISCALE EVALUATION

Project Team: D. I. Kaplan (Primary), M. E. Denham, D. Li, D. Diprete, D. Hobbs
Subcontractor: Texas A&M University
Thrust Area: Environmental Stewardship
Project Start Date: 10/1/16
Project End Date: 9/30/18

Iodine-129 (^{129}I) is commonly the top risk driver at low-level and high-level nuclear waste disposal sites. Objectives of this project were to quantify the effect of iodine speciation on AgI waste (the most common solid form of ^{129}I waste) stabilization and to use this information to improve wasteform formulation. Our approach was to conduct studies at varying spatial and temporal scales (molecular, laboratory, and field lysimeter). Results indicated that iodine speciation (iodide, iodate, and organo-iodine) greatly impacts the tendency for iodine to bind to cementitious waste forms and to be immobilized by silver. Both iodide and iodate existed in grout porewater, however, the proportion of each species varied with the grout formulation; slag grout contained 99% iodide and 1% iodate, whereas slag-free grout contained 39% iodide and 61% iodate. Furthermore, iodate bound more strongly to grouts than iodide. Slag-free grout bound iodide 100x more strongly than slag grout. Among the key outcomes from this research was a published manuscript, an award for user-time to conduct synchrotron-XAS measurements during FY2018 to measure solid phase iodine speciation, and a submitted proposal using seed data from this study.

FY2017 OBJECTIVES

TASK ONE
Extend our existing iodine speciation method to aqueous systems with high salt concentrations and extreme pH levels

TASK TWO
Understand and quantify the impact of iodine speciation and Ag speciation on AgI solubility under long-term waste disposal scenarios

TASK THREE
Identify appropriate wasteforms for AgI solid secondary waste. Testing reducing grout, non-reducing grout, and geopolymers under laboratory conditions.

INTRODUCTION

Significance and Motivation: ^{129}I is either the top or among the top three risk drivers (along with ^{99}Tc and ^{14}C) associated with all low-level and high level nuclear waste existing and proposed disposal sites in the U.S. **[1]**. The high risk associated with ^{129}I originates from its high inventory (high fission yield), long half-life (16 million years), high perceived environmental mobility due to its anionic character, and extremely high toxicity as a thyroid seeker. Exacerbating matters, the worldwide ^{129}I inventory is increasing rapidly. For example, U.S. nuclear power plants generate within 6 months more ^{129}I than currently exists at the Hanford Site (65.5 Ci) and SRS (26 Ci) **[1]**.

Iodine Speciation Impact on the AgI Immobilization Technology: The single most widely used technology for immobilizing radioiodine (primarily as ^{131}I or ^{129}I) from aqueous and air waste streams involves the precipitation of the sparingly soluble AgI compound. Typically the Ag^+ is attached to some solid matrix, such as various ceramics (SRS, also referred to as silver saddles), zeolites (Hanford Site used Ag-mordenite, the EU uses Ag-clinoptilolite), and granulated activated carbon (the Fukushima ALPS system used Ag-GAC). There are enormous quantities of these materials collecting throughout the world. The Hanford Site has 109 m^3 of used Ag-mordenite waste to be disposed **[2]** and the Fukushima ALPS system, being used to treat contaminated groundwater that came in contact with the exposed reactors, is expected to generate 3 m^3 of Ag-GAC waste each month of operation for several years, perhaps decades. An effective low temperature waste form is needed for the disposal of these ^{129}I secondary wastes. While the effectiveness of the Ag technology to immobilize iodine is well established **[3]**, we have not found any literature describing the desorption or dissolution of iodine from the secondary waste forms under repository conditions. At issue, is that there are several processes by which the Ag-GAC/zeolite may bind iodine (Figure 1). The iodine could be coprecipitated to Ag that is impregnated in the cracks of the GAC forming the least soluble form of AgI, nano-γAgI. It could also coprecipitate with Ag on the surfaces of the GAC/zeolite, forming a more soluble form of AgI, α-AgI. The least stable forms of iodine are those that are surface complexed or held by anion exchange.

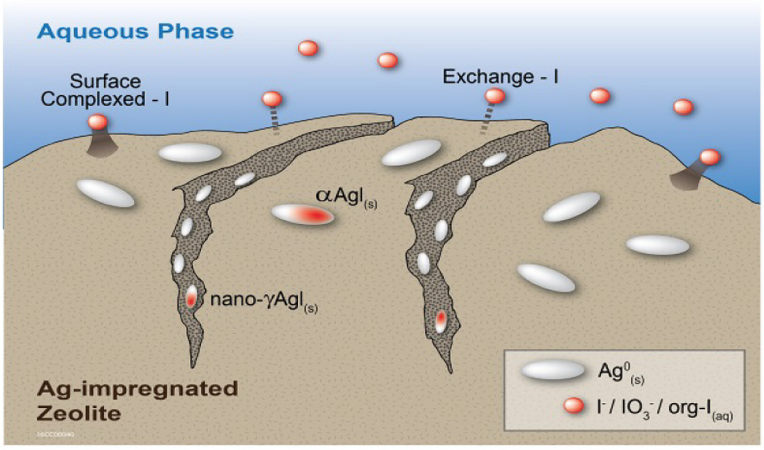

Figure 1. ^{129}I can be weakly or strongly bound to Ag-impregnated zeolites; need to quantify desorption and optimize waste form to promote strong immobilization.

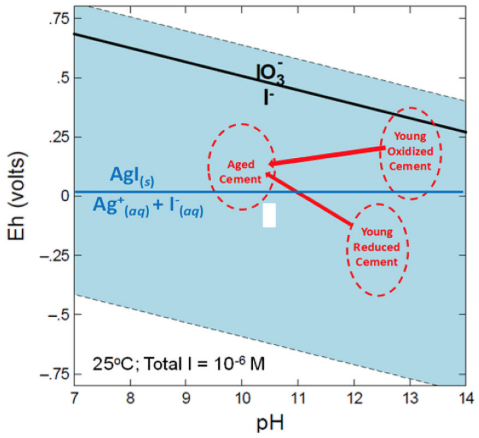

Figure 2. Ag and I speciation with respect to oxidized, reduced, and aged cementitious waste form environments; AgI may dissolve under moderately low redox conditions, thereby enhancing ^{129}I mobility

These differences, while not as important for the removal process, are extremely important for the repository waste disposal for ensuring long term stabilization. The speciation of the iodine alters the stability of the iodine-silver complex. AgI technology is designed for only I^- because its solubility as $AgI_{(s)}$ is extremely low ($k_{sp} = 10^{-17}$), whereas $AgIO_{3(s)}$ ($k_{sp} = 10^{-9}$) and AgMethyl-$I_{(s)}$ (k_{sp} is unknown) have appreciably higher solubilities.

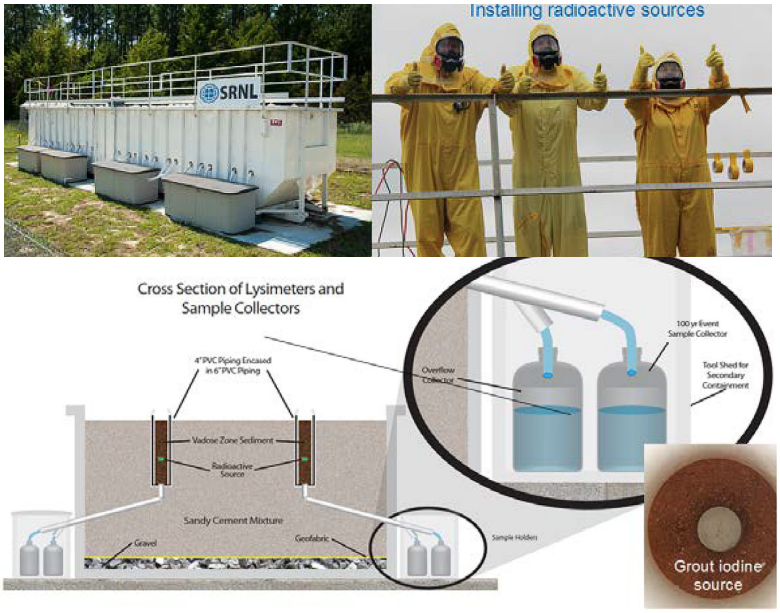

Figure 3. Clockwise starting from the top left: RadFLEx; radiation workers installing sources in RadFLEx; schematic cross-section of RadFLEx facility; and a iodine-amended grout sample in lysimeter core, prior to burying it with SRS vadose zone sediment

Waste Forms Influence Iodine Speciation: Cementitious materials are expected to be used either as waste forms or engineered barriers for low level waste and high level waste on DOE sites **[1, 4, 5]** and geopolymers or cement are expected to be used for the Ag-GAC secondary waste generated from the Fukushima ALPS system. There is some evidence that ^{129}I binds more strongly to oxidizing cements than to reducing cements. Iodine speciation has not been measured in cementitious waste forms, but is likely responsible for this observation **[6-8].** As the pH/Eh diagram presented in Figure 2 shows, the dominant iodine species is expected to be I^- (the weakly sorbing species) however the young oxidized cement is expected to have more IO_3^- than the young reduced cement. This difference is significant from the point of view of a performance assessments because iodine may have a K_d value of ~8 mL/g in slag-free grouts, compared to 0 mL/g in slag grouts (a delay in release of >1000 years from the Savannah River Site Saltstone facility) **[5].**

APPROACH

Studies were conducted at the laboratory scale and field scale at the Radionuclide Field Lysimeter Experiment, RadFLEx. (It is anticipated that studies at the molecular scale will be conducted at the Advance Photon Source using synchrotron X-ray Absorption Spectroscopy in November 2017 as part of our FY18 scope.) A cornerstone of our approach is our unique capability to measure radioiodine species at nanomolar concentrations. Importantly, the technique has been validated by accelerated mass spectroscopy, the "gold standard" **[9].** We have used this technique to analyze environmental samples at SRS, Hanford Site, Fukushima Prefecture, and in marine environments.

Testing was conducted in a manner that we added complexity to the studied system. Tests were initially conducted in simply an iodine-cementitious leachate solution, then a solid phase was added, then Ag-granular activated carbon (GAC) was added. Grout monoliths were made from ordinary Portland cement (OPC), blast furnace slag (BFS), and fly ash (FA) obtained from Lafarge North America. There were two formulations of grout, one without slag (OPC:BFS:FA = 25:0:75, at a liquid/solid ratio of 0.29) and one with slag (OPC:BFS:FA = 10:45:45, at a liquid/solid ratio of 0.45). The Ag-GAC was acquired from Calgon Carbon and contained 0, 1%, 5%, 10% and 14.1% Ag. The GAC was impregnated with Ag by Calgon Carbon (Newark, DE) by adding dissolved $AgNO_3$ to the GAC. SRNL calcined the samples for 24 hours under an inert environment at 350 °C to minimize Ag dissolution.

A silver impregnated mordenite (AgZ) amended with 37% Ag, was acquired from Sigma-Aldrich, and was also used after calcining as described above. These monoliths were not intended to simulate liquid wasteforms such as saltstone or cast stone. The liquid used to make the grout samples in this study was composed of iodide/iodate/organo-iodine water solution, rather than a high ionic strength low level waste simulate solution.

Batch adsorption and desorption tests were conducted with 1:25 solid: liquid ratios on benchtop (slag-free grout) and in inert environment glove bag (slag grout). Liquid Ag measurements were made by ICP-MS and iodine speciation by a combination of wet chemistry separation followed by ICP-MS [10]. Six grout samples (5-cm diameter x 1-cm height) were added to the Radiological Field Lysimeter Experiment (RadFLEx) (Figure 3) in March 2017. Two samples were amended with 1.9e-4 molar iodide and had identical recipes as for the slag-free and slag-containing grout samples described above. Another two samples had OPC:BFS:FA:AgZ-iodide ratios (where AgZ-iodine are silver impregnated mordenite containing an estimated 1% wt/wt bound iodide) of 8:45:27:20 %(wt/wt)and 25:0:55:20 %(wt/wt). Samples were permitted to cure for 3 months in moist conditions before deploying to the RadFLEx facility. Leachate from the lysimeters is periodically collected and analyzed for iodine. In FY18, soil concentrations in the lysimeter cores will be determined as a function of depth and the sources will be characterized via desorption experiments and s-XAS.

RESULTS/DISCUSSION

In a 1:1 solid to liquid suspension of the slag grout and slag-free grout, iodine speciation was measured (Figure 4). The iodine speciation in the slag-free grout was 39% iodide and 61% iodate. Iodide binds much less strongly to cementitious materials than iodate [11]. Another important chemical attribute is that we have measured that iodate can substitute for carbonate into calcium carbonate solids, the primary precipitate in cementitious materials as it undergoes aging.

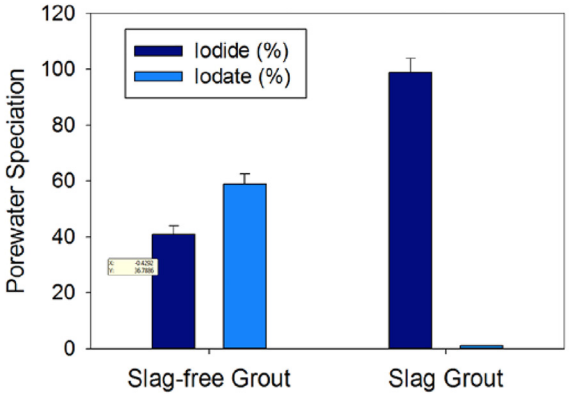

Figure 4. Porewater iodine speciation in slag and slag-free grout

Adsorption experiments with iodide demonstrated that slag-free grouts bound 100x greater concentrations of iodide than slag-containing grout (Figure 5). The distribution coefficient, K_d, is the radionuclide concentration ratio of solids:liquid, with units of (pCi/g)/(pCi/mL) or mL/g; the greater the K_d value, the greater the extent of sorption. As shown in Figure 5, the K_d value after 14 days of contact for slag-grout was approximately 0.2 mL/g, whereas for the slag-free grout, it was 20 mL/g.

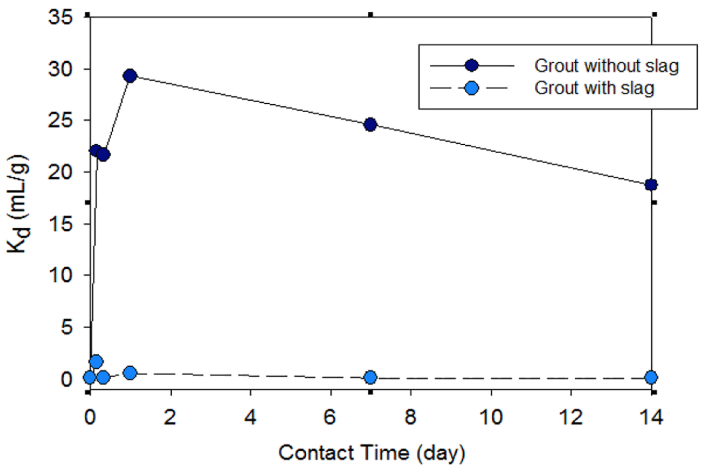

Figure 5. Iodide sorption (K_d) to grout with and without slag

Iodine sorption to Ag-GAC as a function of Ag% is presented in Figure 6. These experiments were conducted using a 1:10 grout:water leachate solution. With incremental increases in Ag concentration in the Ag-GAC, logarithmic increases in iodine K_d values were measured. It is noteworthy that a plateau of iodine sorption had not been reached therefore it is possible that even greater loadings of iodine into the GAC are possible. One environmental concern is that Ag may leach into the groundwater. An Environmental Protection Agency (EPA) limit for Ag is 100 ppb. The highest value measured in these experiments was <10 ppb, well below this EPA limit. The pH of these experiments tended to decrease with increasing additions of Ag to the GAC (pH 12.3 for 0% Ag-GAC to pH 11.3 for 14.1% Ag-GAC). Conversely, redox greatly increased with increasing Ag loadings (Eh = -52 mV for 0% Ag-GAC to 41 mV for 14.1%Ag-GAC).

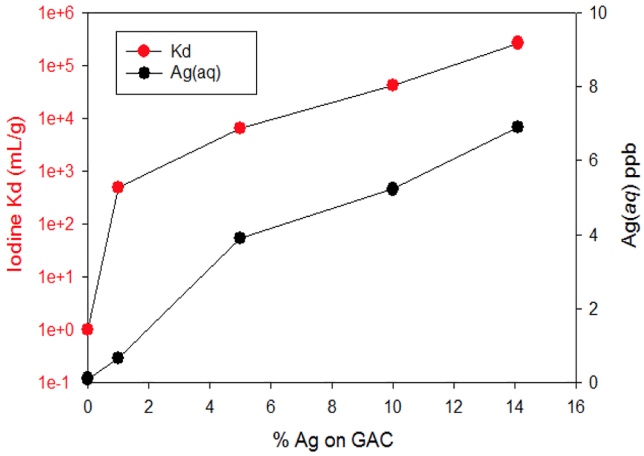

Figure 6. Iodide uptake by Ag-GAC as a function of Ag concentrations; Also shown is the concentration of Ag in the aqueous phase under steady state conditions

FY2017 ACCOMPLISHMENTS

- Iodine speciation (iodide (I^-), iodate(IO_3^-), and organo-iodine) greatly impacts the tendency for ^{129}I to bind to cementitious waste forms and to be immobilized by silver (Ag)
- Sorption to grout: IO_3^- >> I^-
- Immobilized by Ag: I^- >> IO_3^- (data not shown)
- Iodide sorption: without slag sorption 100x greater than with slag
- Porewater Iodine speciation is more favorable for immobilizinG ^{129}I in slag-free grout
- There is a logarithmic increase in iodine uptake with incremental increases in Ag loaded only Granular Activated Carbon. Iodide binds to Ag, not GAC; this is the stronger binding mechanism
- Initiated experiment at the RadFLEx facility to study iodine-Ag-Grout interactions at greater temporal (years) and spatial (meter) scales

FUTURE DIRECTIONS

- Determine redox influence (presence of slag) on Ag disposal in cementitious waste forms
- Complete s-XAS measurements to determine the oxidation state of iodine in cement and how strongly it is being bound by the cement (incorporated in minerals and electrostatically weakly bound)
- Demonstrate effect of slag on ^{129}I immobilization under field conditions

FY2017 PUBLICATIONS/PRESENTATION

- Arai, Y., Powell, B. A., and Kaplan, D. I. (2017). Sulfur Speciation in Untreated and Alkali Treated Ground-granulated Blast Furnace Slag. *Sci. Total Environ*. **589**, 117-121.

REFERENCES

1. Kaplan, D.I., et al., *Radioiodine biogeochemistry and prevalence in groundwater* Critical Reviews of Environmental Science and Technology, 2014. **44**(20): p. 2287-2337.

2. Flach, G.P., et al., *Solid Secondary Waste Data Package Supporting the Hanford Integrated Disposal Facility Performance Assessment,* 2016, Savannah River National Laboratory: Aiken, SC.

3. Patton, K., et al., *Iodine Loading of NO Aged Silver Exchanged Mordenite,* 2014, Oak Ridge National Laboratory (ORNL), Oak Ridge, TN (United States).

4. WSRC, E-*Area Low-Level Waste Facility DOE 435.1 Performance Assessment,* 2008, Washington Savannah River Company: Aiken, SC.

5. SRR, FY2013 *Special Analysis for the Saltstone Disposal Facility at the Savannah River Site,* 2013: Savannah River Remediation, Aiken, SC.

6. Wang, L., et al., *Review of sorption values for the cementitious near field of a near surface radioactive waste disposal facility,* 2009, ONDRAF/NIRAS: Mol, Brussels.

7. Westsik, J.H., et al., *Supplemental Immobilization of Hanford Low-Activity Waste: Cast Stone Screening Tests,* 2013, Pacific Northwest National Laboratory (PNNL), Richland, WA (US).

8. Kaplan, D.I., *Geochemical Data Package for Performance Assessment Calculations Related to the Savannah River Site,* 2016, Savannah River National Laboratory: Aiken, SC.

9. Schwehr, K.A., et al., *Speciation of iodine isotopes inside and outside of a contaminant plume at the Savannah River Site.* Science of the Total Environment., 2014. **497/498**: p. 671-678.

10. Zhang, S., et al., *A Novel Approach for the Simultaneous Determination of Iodide, Iodate and Organo-Iodide for I-127 and I-129 in Environmental Samples Using Gas Chromatography-Mass Spectrometry.* Environmental Science & Technology, 2010. **44**(23): p. 9042-9048.

11. Ochs, M., D. Mallants, and L. Wang, *Radionuclide and Metal Sorption on Cement and Concrete* 2016, Heidelberg: Springer.

ACRONYMS

AgZ	Silver Impregnated Zeolite
BFS	Blast Furnace Slag
EPA	Environmental Protection Agency
FA	Fly Ash
GAC	Granular Activated Carbon
I^-	Iodide
IO_3^-	Iodate
OPC	Ordinary Portland Cement
RadFLEx	Radionuclide Field Lysimeter Experiment
s-XAS	Synchrotron X-ray Absorption Spectroscopy

TOTAL NUMBER OF POST-DOCTORAL RESEARCHERS

Two at Texas A&M University

BIMETALLIC POROUS IRON (pFe) MATERIALS FOR REMEDIATION/REMOVAL OF Tc FROM AQUEOUS SYSTEMS

Project Team: Dien Li (Primary), Simona Murph, Daniel I. Kaplan, Kathryn Taylor-Pashow, Miles Denham, and John Seaman (University of Georgia)

Subcontractor: University of Georgia

Thrust Area: Environmental Stewardship

Project Start Date: 10/1/16

Project End Date: 9/30/17

Remediation of Tc remains an unresolved challenge at SRS and other DOE sites. The objective of this project was to develop novel bimetallic porous iron (pFe) materials for Tc removal from aqueous systems. We showed that the pFe is much more effective in removing TcO_4^- (×30) and ReO_4^- (×8) from artificial groundwater than granular iron. Tc K-edge XANES spectroscopy indicated that Tc speciation on the pFe was 18% adsorbed TcO_4^-, 28% Tc(IV) in Tc dioxide and 54% Tc(IV) into the structure of Fe hydroxide. A variety of catalytic metal nanoparticles (i.e., Ni, Cu, Zn, Ag, Sn and Pd) were successfully deposited on the pFe using scalable chemical reduction methods. The Zn-pFe was outstanding among the six bimetallic pFe materials, with a capacity increase of >100% for TcO_4^- removal and of 50% for ReO_4^- removal, compared to the pFe. These results provide a highly applicable platform for solving critical DOE and industrial needs related to nuclear environmental stewardship and nuclear power production.

FY2017 OBJECTIVES

TASK ONE

Prepare and characterize new bimetallic materials comprised of porous iron (pFe) modified with catalytically active metallic nanoparticles (e.g., Ni, Cu, Zn, Ag, Sn and Pd)

TASK TWO

Evaluate the novel bimetallic pFe materials for Tc removal from a wide range of aqueous media representative of: 1) groundwater conditions (e.g., pH, Eh, Fe^{2+} and humic acid or organic ligands), and 2) extreme waste stream conditions (e.g., high pH, salt concentration, NO_3^-, and CO_3^{2-})

TASK THREE

Characterize Tc binding chemistry on bimetallic pFe materials using synchrotron radiation X-ray absorption fine structure (XAFS) to provide information about its chemical speciation and bonding environment

TASK FOUR

Develop technologies to seal bound (adsorbed or reduced) Tc in the pore structures using easily injectable Na_2SiO_3 or $MnSO_4$ + $KMnO_4$

INTRODUCTION

^{99}Tc is a major long-life fission product during nuclear power generation. Over the years, Tc has been inadvertently introduced into the environment from leaks at waste storage facilities. ^{99}Tc currently is one of the key risk drivers at the Savannah River Site (SRS) and other DOE environmental management sites (most notably the Hanford Site, Paducah Gaseous Diffusion Plant, and Oak Ridge National Laboratory). The most common chemical form of Tc in liquid nuclear wastes and in the environment is anionic pertechnetate (TcO_4^-). TcO_4^- displays limited adsorption onto common sediment minerals and is highly mobile making it difficult to capture or to be immobilized.[1] As the stockpile of ^{99}Tc-bearing nuclear waste continues to increase rapidly, novel sequestration technologies are needed to reduce its potential contamination of the environmental and living organisms.

With current technologies, quaternary amine-based resins have been used to remove Tc.[2] However, these resins are expensive and have only modest TcO_4^- loading capacities from the raffinate waste streams. Chemical reductants (e.g., Fe_3S_4, soluble or structural Fe(II)[3] and some bacteria[4]) can reduce Tc(VII) to the sparingly soluble Tc(IV). However, the resulting $Tc(IV)O_2 \cdot 1.6H_2O$ has a solubility of 1.5×10^{-8} M in groundwater,[5] which greatly exceeds the EPA's maximum contaminant level of 5×10^{-10} M, and is readily re-oxidized and re-mobilized under most environmental conditions[6]. Tc reduction to form sulfides (e.g., Tc_2S_7)[7] or embedding into other sulfide phases[8] or iron oxide waste forms[9] have also been investigated. However, these methods are not practical for many applications. There are currently no demonstrated technologies that are highly efficient and cost-effective for separation of Tc-containing nuclear waste streams and remediation of aqueous Tc in the contaminated sites.

In this project, we evaluated cost-effective porous iron for TcO_4^- and ReO_4^- sequestration from artificial groundwater, and investigated the Tc speciation and removal mechanisms on the porous iron. Further, we also developed chemical reduction methods that allowed us to successfully deposit catalytic metal nanoparticles, namely Ni, Cu, Zn, Ag, Sn and Pd, on the macro-pore structure of the porous iron material. The new bimetallic pFe materials were evaluated for the sequestration of ReO_4^- and TcO_4^- from artificial groundwater.

APPROACH

The porous iron (pFe) samples were provided by our collaborator, North America Höganäs. The pFe samples were characterized by a number of analytical techniques to elucidate their morphology, size, composition, and porosity. Specifically, we used powder X-ray diffraction (XRD), scanning electron microscopy (SEM), energy dispersive X-ray spectroscopy (EDS) and BET surface area using Kr as the adsorption probe for its characterization.

pFe materials were used as templates for creation of bimetallic catalytic materials with tailored and tunable structural, optical and surface properties. Six different metallic nanoparticles, namely Ni, Cu, Zn, Ag, Sn and Pd, were grown onto porous iron by straightforward wet chemical reduction methods that are amenable for scaling up. Basically, metal salts were reduced in water under ambient conditions, with a reducing agent to yield spherical nanoparticles onto the pFe substrates. By employing these experimental conditions, one could preserve the structural integrity of porous Fe, which is critical in this study. A variety of characterization techniques including SEM and EDS mapping were used to evaluate the physico-chemical properties of these materials.

The porous iron (pFe) and six bimetallic pFe (i.e., Ni-pFe, Cu-pFe, Zn-pFe, Ag-pFe, Sn-pFe and Pd-pFe), in comparison with granular metallic iron purchased from Sigma-Aldrich, were evaluated for removal of TcO_4^- and its surrogate (ReO_4^-) from artificial groundwater under atmospheric ($P_{CO2} = 10^{-3.5}$ atm) conditions. Sorption coefficient (K_d, mL/g) and the equilibrium sorption capacity (q_e, mg/g) were calculated using formula 1 and 2, respectively:

$$K_d = \frac{C_0 - C_e}{C_e} \times \frac{V}{M} \quad (1)$$

$$q_e = \frac{(C_0 - C_e) \times V}{M} \quad (2)$$

where C_0 and Ce were Tc or Re concentrations before and after adsorption, respectively, V was the total volume of liquid phase (i.e., groundwater), and M was the mass of the solid material.

Oxidation state and chemical bonding of Tc on the porous iron materials were investigated using synchrotron radiation X-ray absorption near-edge structure (XANES) and extended X-ray absorption fine structure (EXAFS). After batch experiments, Tc K-edge XANES and EXAFS spectra of the porous iron samples were collected using the Sector 20-BM beamline at the Advanced Photon Source (APS) (Argonne National Lab, Argonne, IL). The APS sector 20-BM beam line employed a Si(111) double crystal monochromator detuned 15% for harmonic rejection. The fluorescence detector had a four-layer Al foil filter to suppress the Fe fluorescence. The Tc K-edge XANES data were processed and fitted by linear combination fit (LCF) using the software Athena.

RESULTS/DISCUSSION

Characterization of Porous Iron

The results show that the porous iron has a sponge-like porous structure (Figure 1A) with a BET surface area of 0.95 m^2/g, pore volume of 0.0068 mL/g, and average pore diameter of 364 Å. It is >92% amorphous and α-iron with small amounts of Fe and Al oxides (Figure 1C and 1D).

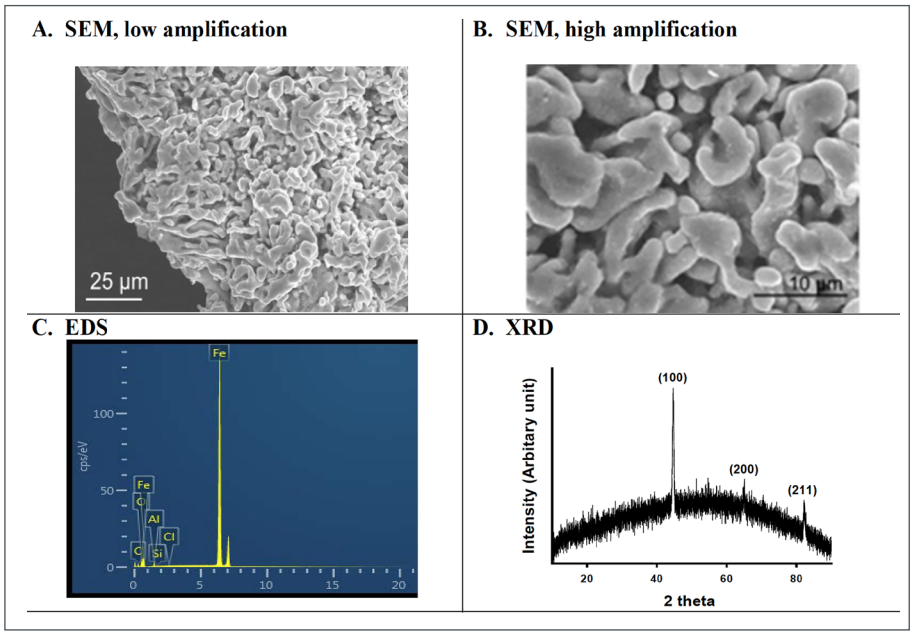

Figure 1. SEM images **(A and B),** EDS spectrum **(C)** and XRD pattern **(D)** of porous iron

Removal Capacity of Porous Iron For TcO_4^- and ReO_4^- From Artificial Groundwater

The porous iron was much more effective than granular iron for removal of both TcO_4^- and ReO_4^- from artificial groundwater. With the initial concentration of 5×10^{-5} M, the removal quantity of the porous iron was ~8 times greater for ReO_4^- and 30 times higher for TcO_4^- than the granular iron (Figure 2A). With the Tc concentration of 3.2×10^{-6} M present in artificial groundwater, the sorption coefficient of the granular iron was nearly zero for TcO_4^- removal, while the sorption coefficient of the porous iron was 2580 mL/g. Further, the removal capacity of the porous iron was demonstrated to be as high as 25 mg Tc per gram of this material (Figure 2B).

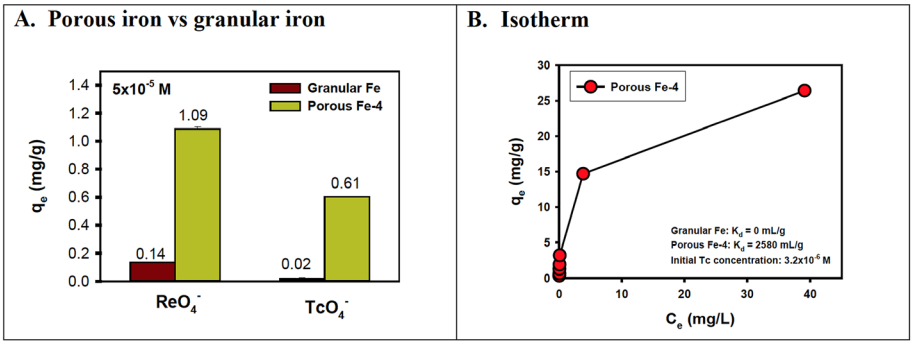

Figure 2. Removal capacity of porous iron for TcO_4^- and ReO_4^- from artificial groundwater; **(A)** Porous iron versus granular iron. **(B)** Isotherm of porous iron for TcO_4^- removal

Tc Speciation on the Porous Iron

Tc K-edge XANES spectra of two different porous iron samples are shown in Figure 3A.These spectra were compared with the spectra of ammonium pertechnetate, Tc(IV) dioxide and Tc(IV) co-precipitated goethite. The results show both oxidation state species, namely TcO_4^- and reduced Tc(IV), on the porous iron samples after exposure to TcO_4^- in artificial groundwater. Linear combination fitting (LCF) indicated that, in the case of porous iron 1, there was 44.2% Tc(VII), 24.6% Tc(IV) in Tc dioxide and 31.2% Tc(IV) in goethite, while in the case of porous iron 4, there was 18.0% Tc(VII), 28.3% Tc(IV) in Tc dioxide and 53.7% Tc(IV) in goethite (Figure 3B).

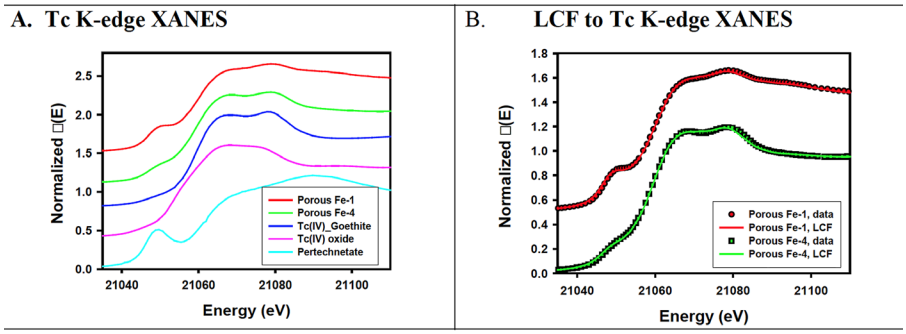

Figure 3. Tc K-edge XANES spectra of two different porous iron products in comparison with the spectra of model compounds (ammonium pertechnetate, Tc(IV) dioxide and Tc(IV) co-precipitated goethite) **(A).** The porous iron spectra were fitted through linear combination fitting (LCF) of the model compounds **(B).**

Characterization of Bimetallic Porous Iron

The six bimetallic pFe samples (i.e., Ni-pFe, Cu-pFe, Zn-pFe, Ag-pFe, Sn-pFe and Pd-pFe) were characterized by using XRD, SEM, EDS and BET surface area and pore size measurement to elucidate their morphology, size, composition, and porosity. The SEM images and EDS data of representative Zn-pFe are shown in Figure 4. After deposition of the catalytic metal nanoparticles, the pore structure of the metal-deposited porous iron was preserved (Figure 4A). Metal nanoparticles of ~50 nm (estimated media particle size) were grown on the external and pore surfaces of porous iron (Figure 4B). Zn (and other metals as well) was detected in the EDS spectrum (Figure 4C) and Zn $L\alpha_{1,2}$ face scanning overlapped on the electron image is shown in Figure 4D. The nanoparticle's loading varied for each individual metal, from 0.6 wt % to 2.0 wt %.

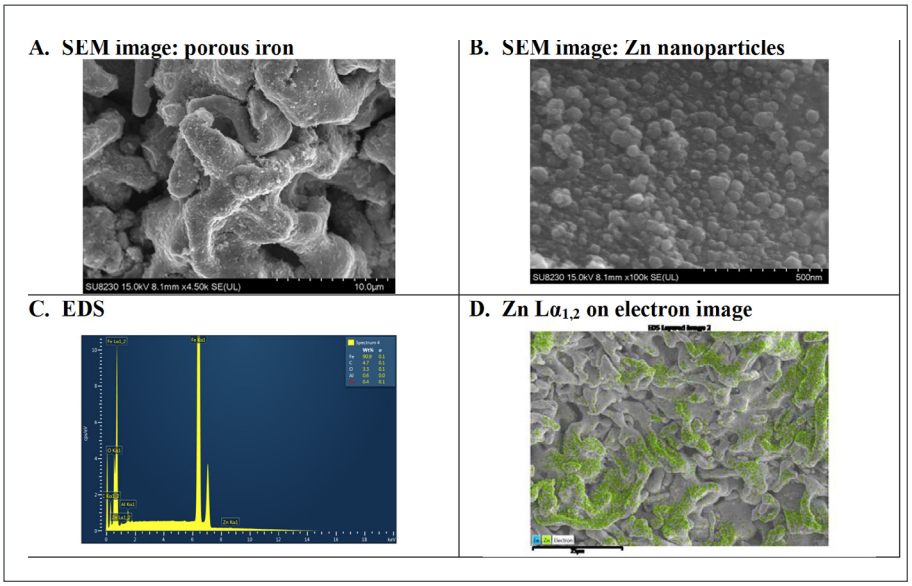

Figure 4. SEM images **(A and B),** EDS spectrum **(C)** and Zn $L\alpha_{1,2}$ on electron image **(D)** of the Zn-deposited porous iron

Removal Capacity of Bimetallic Porous Iron For ReO_4^- From Artificial Groundwater

The six metal-deposited porous iron materials were evaluated for ReO_4^- removal from artificial groundwater. Their sorption coefficient (K_d, mL/g) (A) and removal quantity (mg/g) (B), in comparison with granular and original porous iron, are shown in Figure 5. Zn-deposited porous iron was outstanding among the six metal-deposited porous iron materials for ReO_4^- removal. Data show that the Zn-pFe was more effective than original porous iron for ReO_4^- removal at three different initial concentrations of ReO_4^-. This trend was especially significant at the higher initial Re concentration. At the initial Re concentration of 5×10^{-3} M, the removal capacity of Zn-pFe increased by ~50% compared to the original porous iron.

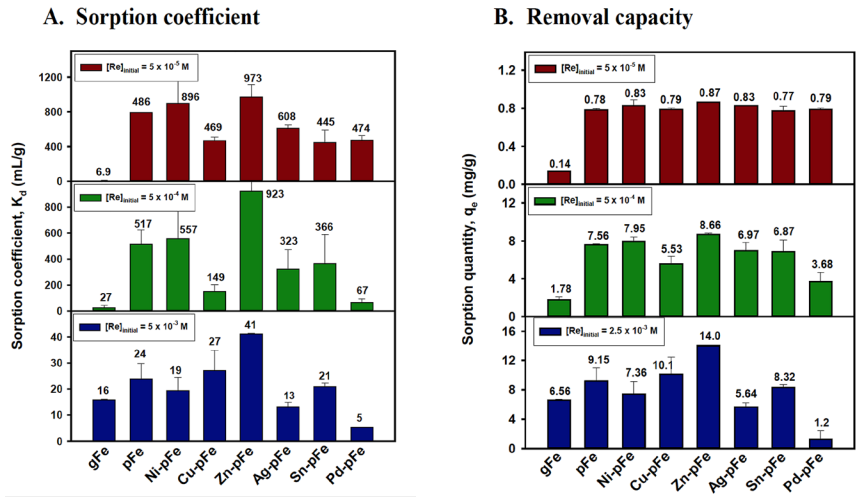

Figure 5.Sorption coefficient (K_d, mL/g) **(A)** and removal quantity (mg/g) **(B)** of six metal-deposited porous iron samples in comparison with granular and original porous iron for ReO_4^- removal from artificial groundwater (gFe = granular zero valent iron, pFe = porous iron, M-pFe = porous iron deposited with the catalytic metal nanoparticle M).

Removal Capacity of Bimetallic Porous Iron For TcO_4^- From Artificial Groundwater

Similarly, the six metal-deposited porous iron materials were evaluated for TcO_4^- removal from artificial groundwater. Their sorption coefficients (K_d, mL/g) (A) and removal quantities (mg/g) (B), in comparison with granular and original porous iron samples, are shown in Figure 6. Once again, Zn-deposited porous iron was outstanding among the six metal-deposited porous iron materials for TcO_4^- removal. Zn-pFe was more effective than original porous iron for TcO_4^- removal. Specifically, at the initial Tc concentration of 1.1×10^{-3} M and solid / liquid ratio of 2 g/L, the removal capacity of Zn-pFe for TcO_4^- removal increased by >100% when compared to the original porous iron (Figure 6B).

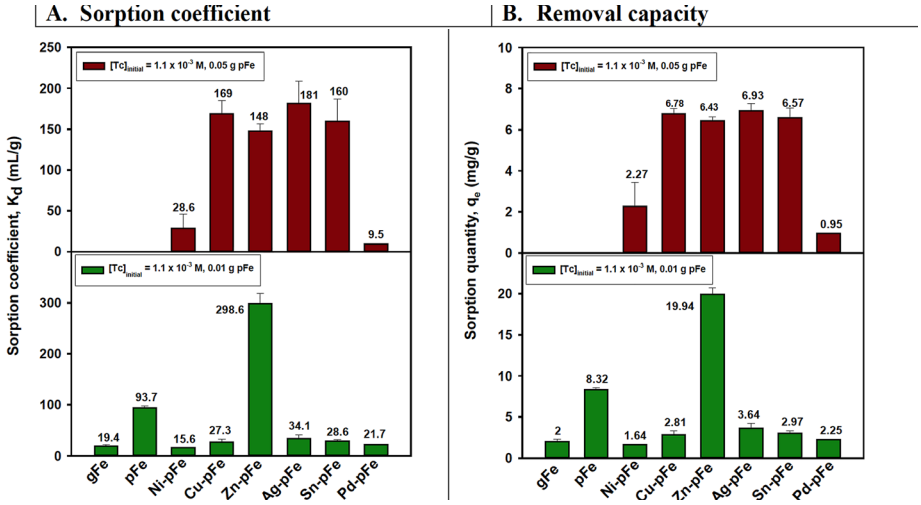

Figure 6. Sorption coefficient (K_d, mL/g) **(A)** and removal quantity (mg/g) **(B)** of the six metal-deposited porous iron samples in comparison with granular and original porous iron materials for TcO_4^- removal from artificial groundwater (gFe = granular zero valent iron, pFe = porous iron, M-pFe = porous iron deposited with the catalytic metal nanoparticle M)

FY2017 ACCOMPLISHMENTS

- Porous Fe is much more effective for removal of TcO_4^- and ReO_4^- from groundwater than granular zero valent iron. The capacity of the porous iron for TcO_4^- removal from groundwater can reach as high as 25 mg Tc/ g Fe
- Tc K-edge XAFS data indicated that Tc species on the porous iron were both reduced Tc(IV) andTcO_4^-. The percentage of the reduced Tc(IV) varied from 56% to 82%. Data show that the Tc(IV) is dominantly incorporated into the structure of Fe oxide / hydro-oxide, which are Fe corrosion products; and to lesser extent, to form Tc(IV) dioxide, which is quite beneficial as it will greatly decrease the re-oxidation and re-mobilization of Tc(IV)
- New chemical reduction methods were developed to deposit the second metal nanoparticles on porous iron and thus to make new bimetallic pFe
- Zn-pFe has been demonstrated to be outstanding among the six bimetallic pFe materials for TcO_4^- and ReO_4^- removal from groundwater. Compared to porous iron, the capacity of the Zn-pFe increased by~50% for ReO_4^- and by >100% for TcO_4^- removal from artificial groundwater

FUTURE DIRECTIONS

- Proposals to DOE EM Soil & Groundwater Remediation Program, International Program,and DOE Nuclear Energy program
- Submit a manuscript describing these results to the American Chemical Society Journal, *Environmental Science and Technology*
- Evaluate porous iron and Zn-pFe for TcO_4^- removal under different environmental and geochemical conditions (i.e., pH, Eh, solution chemistry) and for TcO_4^- separation from liquid nuclear wastes
- Field demonstration of cost-effective porous iron for Tc attenuation at SRS & other DOE contaminated sites

FY2017 PUBLICATIONS/PRESENTATIONS

1. Dien Li, Simona E. Murph, Kaitlin Coopersmith, Daniel I. Kaplan, Kathryn Taylor-Pashow,John C. Seaman, H. Chang, M. Tandukar, Pertechnetate immobilization from aqueous Media by bimetallic porous iron composites, Migration 2017, Barcelona, Spain, September 10-15, **2017.**

2. John C. Seaman, **Dien. Li,** E. Dorward, J. Cochran, H.S. Chang, M. Tandukar, F.M. Coutelot, and D. Kaplan, Immobilization of radioactive materials using porous iron composite media, Waste Management 2018, Phoenix.

3. Dien Li, Shani Egodawatte, Daniel I. Kaplan, Sarah C. Larsen, Steven M. Serkiz, John C. Seaman, Kirk G. Scheckel, Jinru Lin, Yuanming Pan, Extraction of Uranium from Seawater Simulant by Functionalized Magnetic Mesoporous Silica Nanoparticles: Capacity and Molecular Mechanisms, Submitted to *Environ. Sci. Technol.* 2017.

4. Dien Li, Daniel I. Kaplan, John C. Seaman, Brian A. Powell, Allison Sams, Steve M. Heald,Chengjun Sun, Sequestration of pertechnetate (TcO_4^-), iodide (I-) and iodate (IO3-) from groundwater by cost-effective organoclays and granular activated carbon: Capacity and chemical speciation to be submitted to: *J. Hazard. Mater,* **2017.**

5. **Dien Li,** Daniel I. Kaplan, John C. Seaman, Brian Powell, Allison Sams, Steve M. Heald,and Chengjun Sun, Effective Removal of Pertechnetate (TcO_4^-), Iodide (I-) and Iodate (IO3-)from Groundwater by Organoclays and Granular Activated Carbon, 2017 AIChE Annual Meeting, Minneapolis, Oct 29-Nov 3, 2017.

REFERENCES

1. Icenhower, J. P.; Qafoku, N. P.; Zachara, J. M.; Martin, W. J., The biogeochemistry oftechnetium: A review of the behavior of an artificial element in the natural environment. *American Journal of Science* **2010,** 310, (8), 721-752.

2. Liang, L. Y.; Gu, B. H.; Yin, X. P., Removal of technetium-99 from contaminated groundwater with sorbents and reductive materials. *Separations Technology* **1996,** 6, (2), 111-122.

3. Peretyazhko, T.; Zachara, J. M.; Heald, S. M.; Jeon, B. H.; Kukkadapu, R. K.; Liu, C.;Moore, D.; Resch, C. T., Heterogeneous reduction of Tc(VII) by Fe(II) at the solid-waterinterface. *Geochimica Et Cosmochimica Acta* **2008,** 72, (6), 1521-1539.

4. Plymale, A. E.; Fredrickson, J. K.; Zachara, J. M.; Dohnalkova, A. C.; Heald, S. M.;Moore, D. A.; Kennedy, D. W.; Marshall, M. J.; Wang, C. M.; Resch, C. T.; Nachimuthu, P.,Competitive reduction of pertechnetate (TcO_4^-) by dissimilatory metal reducing bacteria and biogenic Fe(II). *Environmental Science & Technology* **2011,** 45, (3), 951-957.

5. Li, D.; Kaplan, D. I., *Solubility of Technetium Dioxides ($TcO_{2\text{-}c}$, $TcO_2{\cdot}1.6H_2O$ and$TcO_2{\cdot}2H_2O$) in Reducing Cementitious Material Leachates: A Thermodynamic Calculation*. Savannah River National Laboratory: Aiken, SC 20908, 2013.

6. Fredrickson, J. K.; Zachara, J. M.; Plymale, A. E.; Heald, S. M.; McKinley, J. P.;Kennedy, D. W.; Liu, C. X.; Nachimuthu, P., Oxidative dissolution potential of biogenic and abiogenic TcO2 in subsurface sediments. *Geochimica Et Cosmochimica Acta* **2009**, 73, (8),2299-2313.

7. Liu, Y.; Terry, J.; Jurisson, S., Pertechnetate immobilization in aqueous media with hydrogen sulfide under anaerobic and aerobic environments. *Radiochimica Acta* **2007**, 95, (12),717-725.

8. Fan, D. M.; Anitori, R. P.; Tebo, B. M.; Tratnyek, P. G.; Pacheco, J. S. L.; Kukkadapu,R.K.; Engelhard, M. H.; Bowden, M. E.; Kovarik, L.; Arey, B. W., Reductive Sequestration of pertechnetate (TcO_4^-) by nano zerovalent iron (nZVI) transformed by abiotic sulfide. *Environmental Science & Technology* **2013**, 47, (10), 5302-5310.

9. Um, W.; Chang, H. S.; Icenhower, J. P.; Lukens, W. W.; Serne, R. J.; Qafoku, N. P.;Westsik, J. H.; Buck, E. C.; Smith, S. C., Immobilization of 99-technetium (VII) by Fe(II)-goethite and limited reoxidation. *Environmental Science & Technology* **2011,** 45, (11), 4904-4913.

ACRONYMS

APS	Advanced Photon Source
BEY	Brunauer–Emmett–Teller
DOE	Department of Energy
EDS	Energy Dispersive X-ray Spectroscopy
EXAFS	Extended X-ray Absorption Fine Structure
gFe	Granular Zero Valent Iron
LCF	Linear Combination Fit
pFe	Porous Iron
SEM	Scanning Electron Microscopy
SRS	Savannah River Site
XAFS	X-ray Adsorption Fine Structure
XANES	X-ray Absortion Near-edge Structure
XRD	X-ray Diffraction

TOTAL NUMBER OF POST-DOCTORAL RESEARCHERS

One post-doctoral researcher involved through the subcontractor

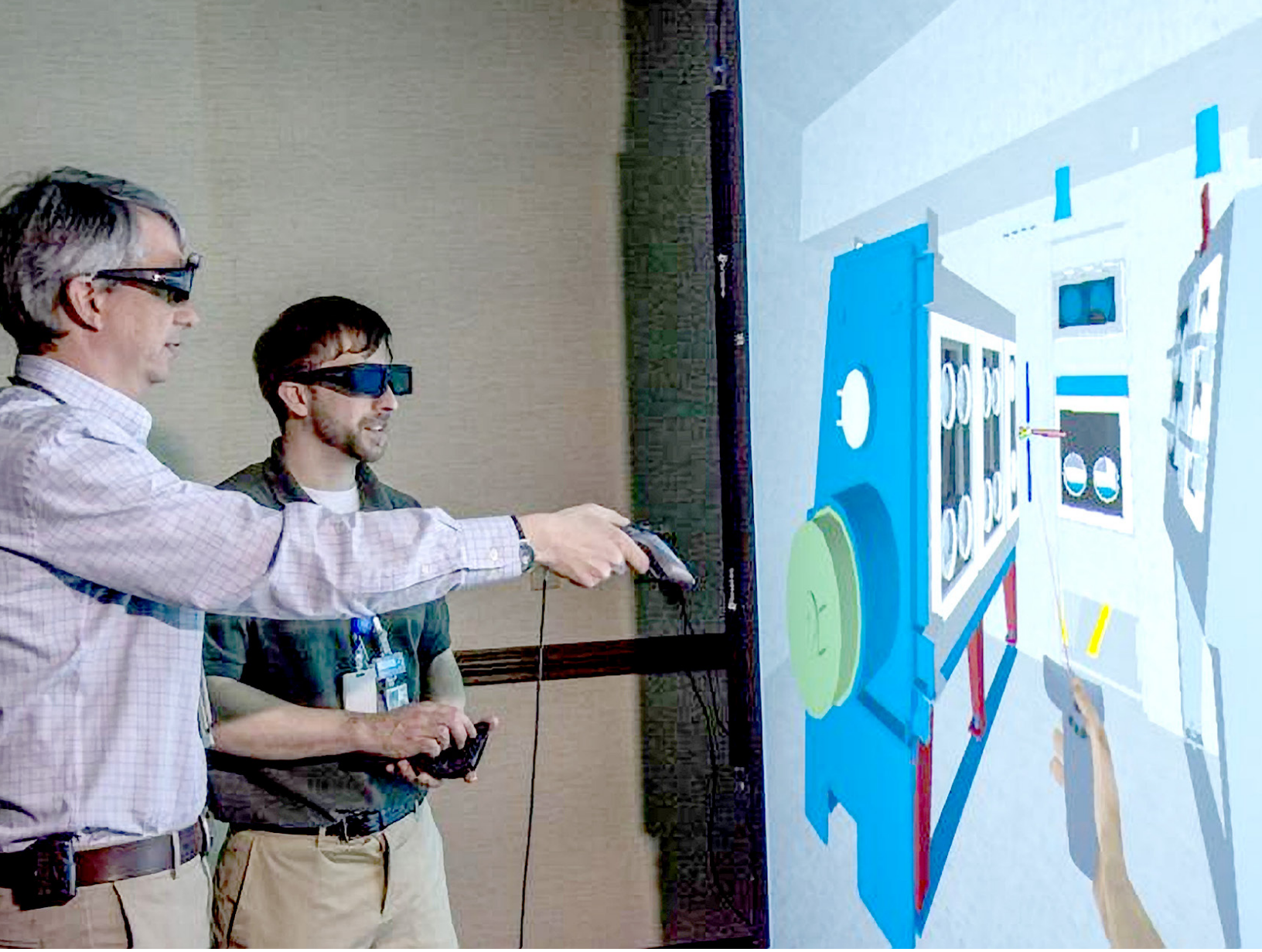

VIRTUAL/AUGMENTED REALITY ROBOTIC INTERFACE (VARRI)

Project Team: J.T. Bobbitt (PI), M.D. Folsom, and E.M. Kriikku
Thrust Area: Environmental Stewardship
Project Start Date: 10/1/16
Project End Date: 9/30/17

VARRI is a near real time virtual reality (VR) interface to allow robots to be operated with greatly enhanced situation awareness. This is accomplished by allowing the robot and environment to be viewed in VR from a third person view (TPV), in other words not just the view through a camera mounted on the robot. The VR scene allows the operator to virtually walk around the robot to understand how to navigate challenging obstacles, or to inspect features in the environment, such as concrete degradation. This interface utilizes low cost COTS scanner modules and is modular in that it can both be attached to a number of robotic platforms and can add additional sensors as required.

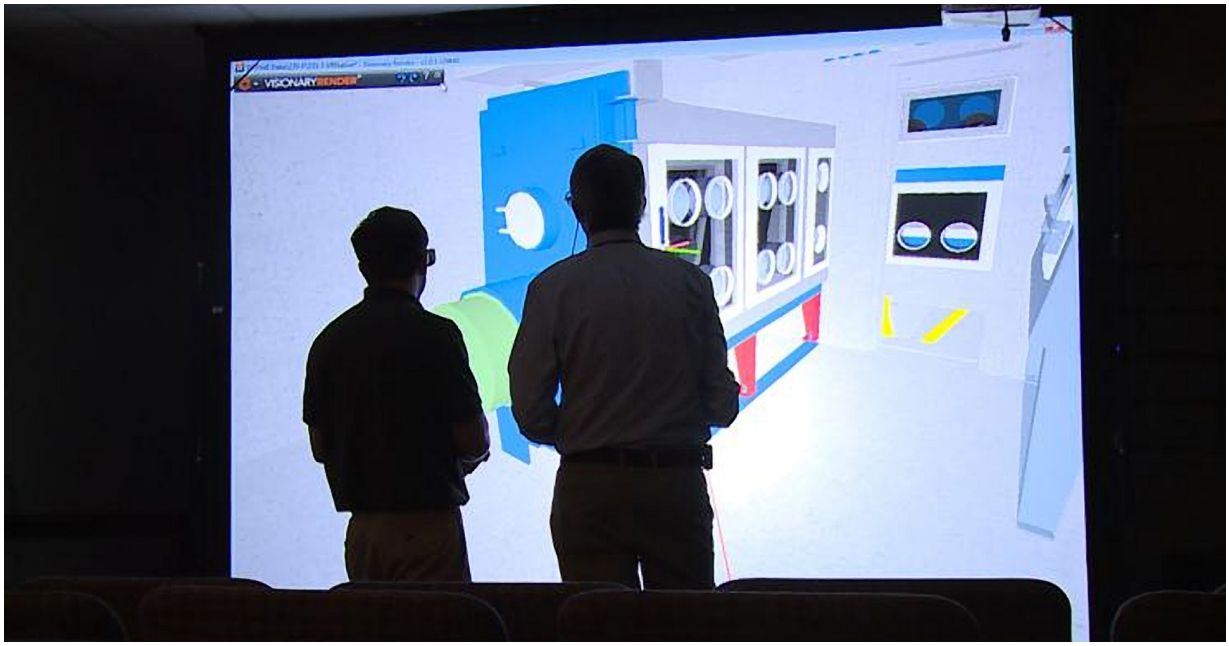

FY2017 OBJECTIVES

TASK ONE
Design and construct a modular mounting system for the system sensors

TASK TWO
Develop software to allow sensor to microcontroller communication

TASK THREE
Develop software to allow microcontroller to host computer communication

TASK FOUR
Develop software to allow sensors to be readily added to the system, calibrate their position, and merge all sensor data together

TASK FIVE
Develop software to present the data to an operator in 3D using an HTC Vive

INTRODUCTION

Savannah River National Laboratory (SRNL) has an extensive background in robotics, virtual reality, and 3D scanning. This project intended to combine those areas into a tool that could be mounted on a wide range of robots for different navigation and scanning needs. DOE's Office of Deactivation and Decommissioning (EM-13) previously funded the development of software for a 3D scanner based on low cost COTS hardware. VARRI started with the knowledge generated from that project to allow multiple scanners to network together to create a larger VR scene to be viewed by the operator. While scanning solutions are currently on the market, these are all very expensive, precluding their use in SRS's contaminated environments which often results in the equipment being disposed of after one use.

This project required a new approach to displaying VR data. In most cases, VR data is preloaded (i.e. static) or only changing slightly. However, with this system, there is a large constantly growing data set.

This provides a challenge for the hardware and software. The challenge was met with unique methods of display, updating, and creating the data. Technical limitations with the chosen display device, the HTC Vive, limited the extent of the near real time display capabilities; however the solution still performs well. The solution provides the first low cost and modular VR environment creation tool for the operation of robotics.

Figure 1. M. Folsom and J. Bobbitt with VARRI installed on a crawler robot.

APPROACH

The project had two complimentary areas—a hardware platform and a software platform. Both needed to be adaptable for a variety of deployment needs.

A hardware platform was developed with modularity in mind. The basic framework and sensor mounts were developed such they could be aimed as needed, and additional sensors added. The electronics enclosure was similarly designed to allow rapid insertion or removal of individual microcontrollers as sensors were added or removed.

The software platform interface was programmed in C++. A custom version of Point Cloud Library (PCL) was used for the alignment of individual sensor frames. A custom version of PCL was required as the open source version does not have the power or flexibility to meet the intended use of VARRI. The flow of the alignment process was changed, but not the mathematical algorithms behind PCL. Several COTS game engines were explored to handle the rendering of the VR scene. However, due to the abstraction of the rendering code, obtaining control to efficiently render the sensor data could not be obtained. VTK (Visualization Toolkit) was utilized to display the data. VTK is a visualization library built by Sandia National Laboratory and is utilized by many Lidar and medical imaging programs. A custom networking protocol was developed to allow hot plug-able sensors. A calibration program was also written to allow users to easily place sensor data in the correct pose.

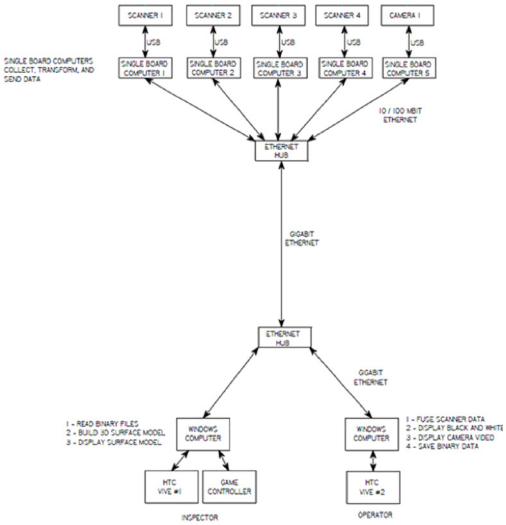

Figure 2. Block diagram showing communication path between sensors and host computer

RESULTS/DISCUSSION

The collection and combining of the scan data from five sensors has been very successful. It is easy to add a sensor and calibrate its position. Initially the robot had four structured light sensors. Due to their narrow field of view, a blind spot existed straight ahead. A fifth sensor was added to collect forward data. The underlying software strategy made that addition extremely straightforward. This demonstrates the flexibility in the base design to allow VARRI to be adapted to individual deployment needs.

The project intended to display the data in real time on the HTC Vive. This proved not to be practical due to hardware limitations of the Vive. Every time new data is pushed to the Vive, it takes approximately half a second to process the data. During the processing, the screen goes black with a loading icon. This results in a lot flashing of the screen, making it unusable. The Vive is a $600 device primarily designed for the consumer market where the data set is a complete set loaded at once, for instance from a game. It is anticipated that a much more expensive commercial device would not suffer from the same limitations; however the object of this project was to use low cost commercially available components. The hardware limitations led to a workable solution where the robot is driven via its traditional 2D camera. When an obstacle is encountered, the operator switches to the 3D view on the Vive. The image is a static 3D view, i.e., the data set does not change, but the operator can still walk around the robot in 3D.

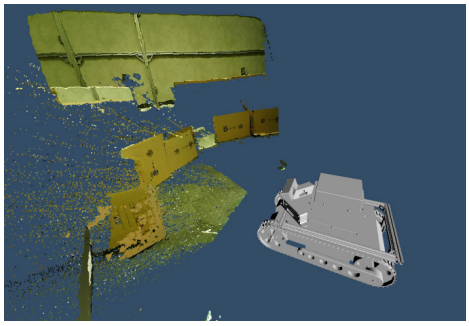

Figure 3. Scanned environment as seen on the Vive

FY2017 ACCOMPLISHMENTS

- Developed a communication protocol to allow sensors to be readily added or removed
- Software successfully written to combine a large number of sensors to create a large VR environment. Software is unlimited in the number of sensors, but network bandwidth will limit the number to approximately 20 sensors
- Developed software to mesh the data from multiple sensors into one VR environment that can be viewed in real time
- Developed a hardware package to allow sensors and microcontrollers to be readily added and removed

FUTURE DIRECTIONS

- **Janus Research Group** – Discussions are ongoing regarding pursuing DOD funding to further develop VARRI for use with military robotic operations
- **Canadian Nuclear Labs** – Discussions are ongoing regarding a collaborative effort to further develop this technology and deploy it in nuclear facility planning.
- **H Canyon Exhaust Tunnel Inspection** - Discussions will be held during the planning for the upcoming tunnel inspection to include VARRI on the robot platform chosen for the inspection
- **Hanford** – There are planned discussions with Hanford regarding deployment in the PUREX tunnel
- **DOE** – EM is interested in using VARRI to assist with small site D&D planning.

ACRONYMS

2D	Two dimensional
3D	Three dimensional
AR	Augmented Reality
COTS	Commercial Off The Shelf
D&D	Deactivation and Decommissioning
DOE	Department of Energy
FPV	First Person View
LIDAR	Light Detecting and Ranging
PCL	Point Cloud Library
SRNL	Savannah River National Laboratory
SRS	Savannah River Site
TPV	Third Person View
VARRI	Virtual/Augmented Reality Robotic Interface
VR	Virtual Reality
VTK	Visualization Tool Kit

INTELLECTUAL PROPERTY

Ongoing discussion with SRNL Technology Transfer regarding protection of the IP generated by this project. It may include patent applications or copyrights.

DESIGNING A SLAG COMPOSITION TO OPTIMIZE Tc-99 RETENTION IN OXIDIZED GROUTS

Project Team: W. P. Kubilius (Primary), F. C. Johnson, C. A. Langton, M. E. Caldwelln

Thrust Area: Environmental Stewardship

Project Start Date: 10/1/16

Project End Date: 9/30/17

Ordinary Portland Cement

Long-term retention of Tc-99 in saltstone-type grouts is problematic, because although it is insoluble under the initial reducing conditions, grout will eventually oxidize, and Tc-99 is very mobile in an oxidizing environment.

This project seeks to improve the ability of saltstone-type grouts to retain Tc-99 under oxidizing conditions, by formulating grouts engineered to contain Layered Double Hydroxides (LDHs), compounds known to be technetium getters.

Sorption experiments using perrhenate (ReO_4^-) as a surrogate for TcO_4^- showed that CuLDH, with a nominal composition of $Cu_6Al_2(NO_3)_2(OH)_{16}$, and calcined MgLDH, nominally $Mg_6Al_2O_9$, effectively sorbed perrhenate from basic solutions at pH 12. However, grout mixes made with Tank 50 simulant, and containing CuLDH or calcined MgLDH after curing, did not show significant sorption of ReO_4^-.

FY2017 OBJECTIVES

TASK ONE

Determine which LDH compositions are best at sorbing ReO_4^- in basic aqueous solutions

TASK TWO

Prepare grout mixes which crystallize or contain desired LDHs after curing

TASK THREE

Conduct ReO_4^- sorption tests on grouts, using sorption solutions representing expected pore water in aged grout

INTRODUCTION

Some low-level radioactive waste is disposed by mixing into grout wasteforms such as saltstone (SRS) or Cast Stone (Hanford), which are then placed into underground vaults. Current grout mixes include ordinary portland cement (OPC), fly ash (FA), and blast furnace slag (BFS). These wasteforms are chemically reducing when cured, so technetium occurs in the Tc(IV) oxidation state. Under these conditions, technetium is insoluble. However, after exposure to air and water over thousands of years, grout wasteforms will oxidize, and Tc-99 will convert to the oxidized form Tc(VII), which is manifested as the very soluble pertechnetate ion, TcO_4^-. Pertechnetate is expected to leach into groundwater at that time.

In order to prevent future releases of Tc-99 into the environment, it is important to identify a mechanism for immobilizing TcO_4^-, either through precipitation or sorption, within the grout matrix, after it has oxidized. Layered double hydroxides (LDHs) have potential for serving this purpose, because they have an unusual affinity for sorbing anions. LDHs have the brucite structure, $M^{2+}(OH)_2$, where M^{2+} is a metal, with Al^{3+} substituting for some M^{2+} atoms. This imparts a positive charge to the octahedral sheets, balanced by incorporation of anions (e.g. NO_3^-, OH^-, or TcO_4^-) within the interlayers. LDHs with M = Mg and Ca crystallize spontaneously in cured grouts, including saltstone. They bind anions weakly, but Krumhansl et al (2006) and Pless (2007) found that LDHs with Cu or Zn as the divalent cation (instead of Mg or Ca) can strongly bind ReO_4^-, TcO_4^-, I^-, and IO_3^-, at near-neutral pH.

APPROACH

Krumhansl and Pless investigated LDH sorption capacity in groundwater at pH 7.5, but we were interested in sorption behavior at the higher pHs representative of cementitious environments. Therefore, the first part of this work was to synthesize LDH of three compositions, where M^{2+} = Mg, Zn, and Cu. Their sorption behavior was tested, using perrhenate, ReO_4^-, as a surrogate for TcO_4^-. Perrhenate sorption behavior was tested in aqueous settings at pH 12.

The next step was to obtain saltstone-type grout mixes, which upon curing, would crystallize Mg, Zn, and Cu LDHs. This was done in two ways. First, the composition of one grout ingredient, blast furnace slag, was altered by using custom-formulated glass as a surrogate for slag. The control glass was made with the composition of normal blast furnace slag, except that reducing agents were omitted. Other test glasses substituted Zn or Cu for the Mg present in the control. The second procedure for obtaining LDH-bearing grouts was to mix prepared LDH directly into the grout.

In order to make grouts, the ingredients were mixed with solutions that simulate liquid waste. Finally, after curing, grouts were tested for their ReO_4^- sorption ability, using solutions representative of aged wasteform pore-water.

Figure 1. (top) Synthesis of CuLDH. **Figure 2. (bottom)** Glass made with composition of blast furnace slag, without reducing agents.

RESULTS/DISCUSSION

LDHs of desired compositions were easily synthesized at room temperature by mixing M^{2+} nitrate, aluminum nitrate, and sodium hydroxide dropwise over several hours. Aqueous sorption tests of synthesized LDH were conducted over 7-day periods, and found that LDHs of two compositions sorbed ReO_4^- very well at pH 12, representing the pH of aged grout. Copper LDH and calcined MgLDH showed sorption coefficients exceeding 200 mL/g (Table 1). However, sorption was reduced in the presence of 0.1 M nitrate or 0.1 M nitrite. This suggests that sorption of TcO_4^- by LDHs in grout wasteforms would be effective only after nitrate/nitrite has leached from the grout.

Slag-surrogate glasses were easily synthesized with Mg and Zn containing compositions, but in copper-containing glasses, some or most Cu^{2+} apparently was reduced to Cu^{1+} during cooling, which would not lead to CuLDH crystallizing in the grout.

Cured grouts were prepared and tested in two groups. The first group simulated fresh saltstone-type grout. These grouts were made with simulated Tank 50 waste (2.5 M NaOH, 1.7 M $NaNO_3$, 0.4 M $NaNO_2$, and lesser amounts of other solutes). After curing, they underwent sorption testing in a simulated young grout pore water, consisting of 2.5 M NaOH, 2.5 M $NaNO_3$, 0.4 M $NaNO_2$, and 0.05 M Na_2SO_4 (Table 2). The second group was intended to simulate grout from which all nitrate and nitrite had been leached—a condition expected in aged Saltstone. These grouts were made with a "zero nitrate" solution (2.5 M NaOH, 0.2 M Na_2CO_3, and 0.01 M Na_3PO_4). After curing, they underwent sorption testing in a simulated aged grout pore water, consisting of 0.01 M NaOH and 0.005 M $Ca(OH)_2$ (Table 3). Results were disappointing; all grout compositions showed little or no sorption of ReO_4^-. It is believed that the very high pH of fresh grout (14+) inhibited ReO_4^- sorption, as OH^- competes with ReO_4^- for sorption sites.

Table 1. ReO_4^- **sorption coefficients (mL/g) in aqueous solutions.**

sorption test liquid	MgLDH	ZnLDH	CuLDH	calcined MgLDH	calcined ZnLDH
0.01 M NaOH, 0.01 M $NaReO_4$	18	14	353	226	0
0.01 M NaOH, 0.0001 M $NaReO_4$			265	217	0
0.1 M NO_2, 0.01 M $NaReO_4$			44	22	
0.1 M NO_3, 0.01 M $NaReO_4$			45	23	

Table 2. ReO_4^- **sorption coefficients for LDH containing grouts in aqueous settings with nitrate.**

grout mixture		sorption liquid	Kd (mL/g)
solid	liquid		
10 OPC, 45 FA, 45 Mg-BFS	Tank 50 simulant	pore water simulant	0
10 OPC, 45 FA, 45 Zn-BFS	Tank 50 simulant	pore water simulant	1
10 OPC, 45 FA, 45 Cu-BFS	Tank 50 simulant	pore water simulant	0
9 OPC, 39 FA, 39 Mg-BFS, 13 MgLDH	Tank 50 simulant	pore water simulant	0
9 OPC, 39 FA, 39 Mg-BFS, 13 calcined MgLDH	Tank 50 simulant	pore water simulant	0
9 OPC, 39 FA, 39 Mg-BFS, 13 CuLDH	Tank 50 simulant	pore water simulant	1

Table 3. ReO_4^- **sorption coefficients for LDH containing grouts in aqueous settings without nitrate.**

grout mixture		sorption liquid	Kd (mL/g)
solid	Liquid		
10 OPC, 45 FA, 45 Mg-BFS	zero nitrate	aged pore water simulant	1
10 OPC, 45 FA, 45 Zn-BFS	zero nitrate	aged pore water simulant	1
10 OPC, 45 FA, 45 Cu-BFS	zero nitrate	aged pore water simulant	1
9 OPC, 39 FA, 39 Mg-BFS, 13 MgLDH	zero nitrate	aged pore water simulant	1
9 OPC, 39 FA, 39 Mg-BFS, 13 calcined MgLDH	zero nitrate	aged pore water simulant	1
9 OPC, 39 FA, 39 Mg-BFS, 13 CuLDH	zero nitrate	aged pore water simulant	1

It should be noted that although the second group of grouts had the low nitrate concentrations expected for aged Saltstone, their pH of 14+ is not suggestive of aged grout. Therefore the simulation was not perfect—true aged grout would have a pH less than the 14.

FY2017 ACCOMPLISHMENTS

- ✔ Identified LDHs as potential getters for Tc-99 in grout wasteforms.
- ✔ Found ReO_4^- sorption coefficients for CuLDH and calcined MgLDH to be 353 and 226 mL/g in pH 12 water (0.01 M $NaReO_4$), but reduced to 45 and 23 mL/g in 0.1 M NO_3.
- ✔ Found ReO_4^- sorption coefficients for Mg, Zn, and CuLDHs contained within grouts to be <1 mL/g in both nitrate-present and nitrate-absent mixes.

FUTURE DIRECTIONS

The strong ReO_4^- sorption abilities of CuLDH and calcined MgLDH indicate that LDHs continue to have potential as Tc-99 getters, at least in non-grout matrices. They do not sorb ReO_4^- well in fresh grouts, however, this does not necessarily preclude their use. Fresh grouts are reducing, and bind Tc-99 well. Future work will be needed to determine whether LDHs may sorb ReO_4^- or TcO_4^- in degraded grouts.

REFERENCE

1. Krumhansl JL et al, 2006. Yucca Mountain Project Getter Program Results (Year 1): I-129 and other anions of concern. SAND2006-3869, Sandia National Laboratories, July.

2. Pless JD, Chwirka JB, Krumhansl JL, 2007. Iodine sequestration using delafossites and layered hydroxides. Environmental Chemistry Letters 5:85-89.

ACRONYMS

BFS Blast Furnace Slag
FA Fly Ash
LDH Layered Double Hydroxide
OPC Ordinary Portland Cement

INTELLECTUAL PROPERTY

A prescreening invention disclosure has been submitted.

NUCLEAR MATERIALS MANAGEMENT

UNIQUE CONCEPTS THAT LEAD TO NEW APPROACHES AND OPTIONS WITH THE POTENTIAL TO ACCELERATE SAFE DISPOSITION OF NUCLEAR MATERIALS FROM AROUND SRS, THE DOE COMPLEX, AND THE WORLD.

Pu ANION EXCHANGE PROCESS INTENSIFICATION

Project Team: K. M. L. Taylor-Pashow (Primary), T. C. Shehee, D. T. Hobbs, J. G. Pribyl (Univ. of SC graduate student), B. C. Benicewicz (Univ. of SC), M. Y. Coblyn (Oregon State Univ.)

Subcontractor: University of SC

Thrust Area: Nuclear Materials Management

Project Type: Standard

Project Start Date: 10/1/15

Project End Date: 9/30/17

This research is focused on improving the efficiency of the anion exchange process for purifying plutonium. While initially focused on plutonium, the technology could also be applied to other ion-exchange processes. The technology involves the use of either open-celled polymeric foams, which have large surface areas available for solute sorption, or a microchannel array device. Both of these technologies offer the advantage of convection being the dominant mechanism by which mass transport takes place, rather than diffusion. The foam materials are prepared from a high internal phase emulsion (HIPE) process and are then functionalized with poly(4-vinylpyridine) (PVP) through either a photoinitiated or thermally initiated polymerization method. The microchannel device was prepared by etching the microchannels in stainless steel, and then functionalizing the surface of the microchannels with a nanospring coating, and subsequently PVP. These technologies provide an advantage over the typical porous resin beads by eliminating the slow diffusion through the beads. Eliminating the diffusive mass transport increases the ion-exchange rate, and also results in much sharper elution profiles.

FY2017 OBJECTIVES

TASK ONE
Optimization of poly(4-vinylpyridine) functionalization of polymeric foam materials

TASK TWO
Recycle testing of optimized polymeric foam materials

TASK THREE
Radiation stability testing of polymeric foam materials

TASK FOUR
Fabrication and testing of microchannel array prototype device

INTRODUCTION

The Pu anion-exchange process currently performed at the Savannah River Site for purification of Pu involves the use of a commercial poly(4-vinylpyridine) resin, Reillex® HPQ, in a packed bed column. This step in the Pu purification process represents a bottleneck due to the limited volume and flow rate which can be processed. Conventional ion-exchange resins are limited by mass transfer at the solution-particle interface and diffusion through the large granular resin particles. Convective mass transport through the packed bed is much faster than diffusive mass transport inside of the resin beads (Figure 1).

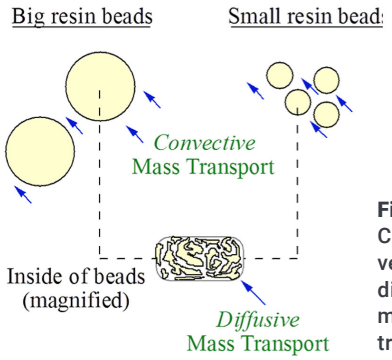

Figure 1. Convective versus diffusive mass transport

The diffusive mass transport can be somewhat reduced by reducing the size of the resin particles, however, this is limited by the increase in pressure drop across a column, which increases as the particle size of the resin decreases. This project seeks to overcome these limits through the use of a novel ion-exchange configuration, either an inverse column or a microchannel array. Both of these configurations overcome the slow diffusion through conventional granular resin particles. The inverse column, which is a porous foam monolith of material, has the advantage that it can be prepared in the appropriate size and shape to be a direct replacement for the granular resin in the current facility configuration. The microchannel arrays would allow for increased throughput by simply increasing the number of arrays deployed in order to reach the desired throughput. The initial focus of the project is on the Pu anion-exchange process, but once the technology is demonstrated for this application it is envisioned that it could be modified for other ion-exchange applications by modifying the functional groups incorporated on the materials.

SRNL established collaborations with the University of South Carolina (USC) and Oregon State University (OSU) during the course of this project. USC provided the polymer synthesis expertise, and prepared foam monoliths grafted with poly(4-vinylpyridine) (PVP) chains to introduce quaternary amine functional groups as the anion-exchange sites. In high nitric acid concentrations (i.e., 7-8 M) the Pu is present as the hexanitrato anionic complex $[Pu(NO_3)_6]^{2-}$ which binds to the quaternary amine groups on the resin. This is the same chemistry utilized by the Reillex® HPQ commercial resin, which is a PVP resin, also containing quaternary amine groups. Collaborators at the OSU Advanced Technology and Manufacturing Institute (ATAMI) provided the microchannel array expertise, and developed a prototype device for testing for this application.

APPROACH

High internal phase emulsions (HIPE) are used as templates for the formation of the porous polymeric foam monoliths. HIPEs are water-in-oil emulsions in which the water phase comprises at least 74% of the emulsion by volume. The oil phase consists of the monomers used to prepare the polymer, crosslinking agents, and a surfactant. After polymerization and drying the resulting crosslinked polymer is an open-celled isotropic foam. The foam monoliths in this work are prepared from styrene crosslinked using divinylbenzene (DVB). Varying percentages of two different co-monomers were incorporated to allow for later grafting of poly(4-vinylpyridine) chains through either a photoinitiated polymerization or a thermally initiated polymerization. For the photoinitiated polymerizations vinylbenzyl chloride was included as the co-monomer. These foams were then subsequently treated with sodium thiosulfate to introduce free-radical initiation sites on the vinylbenzyl chloride sites.[1] The 4-vinylpyridine was then polymerized from these sites upon exposure to UV light, resulting in grafted polymer chains extending into the foam. For the thermally initiated polymerizations a new monomer was prepared that contained a TEMPO (2,2,6,6-tetramethyl-1-piperidinyloxy) thermal initiating group. This new monomer (2,2,6,6-tetramethyl-1-((4-vinylbenzyl)oxy)piperidine) was then incorporated into the foam synthesis with the styrene monomer and DVB crosslinker. The TEMPO functionalized sites throughout the foam could then be used to graft the 4-vinylpyridine through thermal initiation. The final PVP content of the foams can be tuned by varying the content of the initiating co-monomer in the foam preparation (graft density) as well as by varying the reaction conditions for the PVP grafting reaction (chain length). A series of foams were prepared varying these two parameters to identify the optimal conditions for preparing the foam material with maximum Pu capacity.

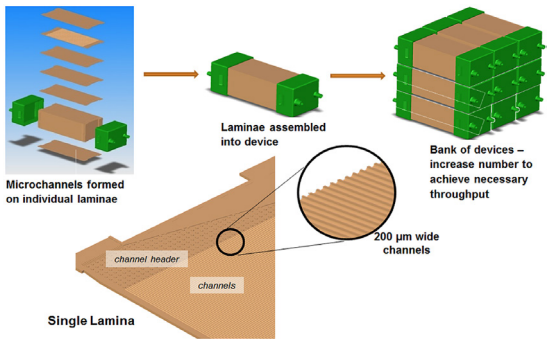

Figure 2. Example of a microchannel array device

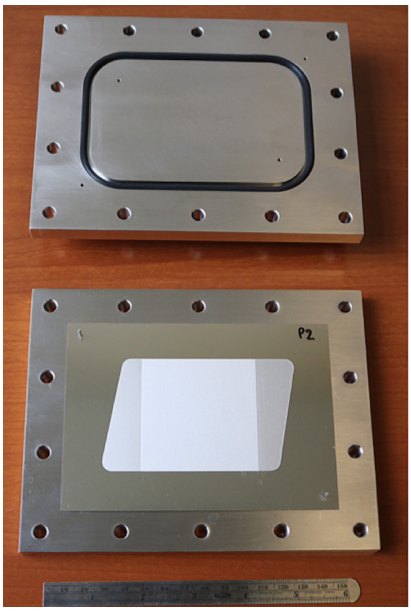

Figure 3. Microchannel plate on bottom housing plate with top housing plate top

In addition to the porous foam columns, we also prepared a microchannel array prototype device. Figure 2 provides a schematic of a microchannel array device. In FY16 we attempted unsuccessfully to prepare the individual laminae from crosslinked PVP, which would then already contain the quaternary amine functional groups necessary for the Pu anion exchange process. In FY17, we modified our approach to decouple the material of construction for fabricating the microchannel geometries from the functional material. For this approach an array of 200 microchannels was photochemically machined into a 0.02" thick 304 stainless steel plate (Figure 3). The microchannel dimensions were 75 µm deep, 200 µm wide, and 60 mm in length. The microchannels were functionalized for ion-exchange in two steps: 1) increased specific surface area with nanosprings (NS) and 2) functionalized with PVP for adsorption.

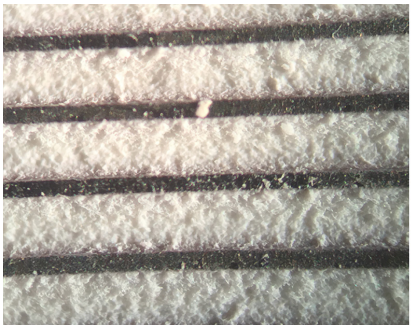

Figure 4. Nanospring mat grown and partially occupying microchannels

A SiO_2 NS mat with high porosity (up to 90%) was grown on the surface of the microchannels (Figure 4). The total surface area in the headers and microchannels was increased to approximately 15 m^2. PVP was then coated on the surface of the NS mat based on procedures from Malynych et. al.[2] The plates were treated under plasma in air for 2 minutes and then submerged in a 1% solution, by mass, of 60,000 MW PVP in ethyl alcohol for 12 hours. This was followed by annealing at 120 °C for 3 hours.

RESULTS/DISCUSSION

In FY16 we demonstrated the successful preparation of porous foam columns grafted with PVP chains using both the photoinitiated and thermally initiated grafting techniques. The thermally initiated method was found to give superior results, both in terms of PVP functionalization, which translates to increased Pu loading, as well as reproducibility of the syntheses. FY17 focused on determining the optimum graft density and chain length for the thermally initiated samples to maximize the Pu capacity. The graft density can be modified by varying the amount of TEMPO functionalized co-monomer incorporated in the initial HIPE polymerization, and the chain length varies with reaction time. A series of samples with varying graft densities and chain lengths were prepared and tested. The characterization data for this set of samples is shown in Table 1. The net N content relates directly to the amount of PVP incorporated, and as can be seen, the net N content varied from ~9.5 wt% to ~11.5 wt%. For comparison, the commercial Reillex® HPQ has a theoretical N content of 8.75 wt%. These samples were then assembled into columns using a similar procedure used in FY16, which involves encapsulating the columns in several layers of heat shrink-tubing and fitting the ends with tubing adapters. One improvement to this process made in FY17 was coating of the outside walls of the columns with a layer of epoxy, prior to the heat shrink tubing, to ensure we did not have any channeling of solution along the outside of the column.

Sample ID	Net N Content (%)	Weight Gain (%)	Graft Density	Chain Length
JP-2-36	9.57	366	Low	Med.
JP-2-110	11.16	599	High	Med.
JP-2-111	11.14	490	Med.	Med.
JP-2-112	10.46	450	Low	Med.
JP-2-113	11.47	722	High	High
JP-2-117	9.95	272	High	Low

Table 1. Summary of Foam Column Characterization Data

Figure 5 shows a representative SEM image of the porous foam columns, showing the open pore structure, and the insert shows an assembled column ready for Pu uptake testing.

The foam column samples were tested for Pu uptake and elution, and the Pu capacities were determined based on the amount of Pu that was eluted from the columns. A sample of Reillex® HPQ was also tested in FY16 as a point of comparison for this work. For the Reillex® testing, a small glass column was packed with Reillex® HPQ resin. The calculated gravimetric and volumetric Pu capacities for each of the tested columns are shown in Table 2, along with the Reillex® HPQ data for comparison. As can be seen, these columns greatly exceed the Reillex® material on a gravimetric basis, partly due to the extremely low densities of the porous foams (average of 0.091 g/cm^3 pre-functionalization). However, most of the samples also outperform on a volumetric basis, with the best performing samples having volumetric capacities approximately 1.5 times that of the Reillex®. Sample JP-2-111, with a medium graft density and medium chain length had the highest gravimetric capacity. Increasing the graft density and/or chain length did not offer much improvement in the capacity, so it appears we've reached a level of diminishing returns at the medium graft density and chain length. This formulation was selected to move forward for additional testing including radiation stability and recycle testing. Several more samples of this composition were prepared.

In addition to the high Pu capacities of the materials, another important feature, and improvement of the foams over typical resin beads, is the elution profile, which is much sharper in the foam material due to the lack of diffusion of Pu from large resin beads during elution. The elution profiles for several of the thermally initiated samples are shown in Figure 6. As can be seen in the figure, the elution is much sharper from the foam columns, as they do not exhibit the "tail" that is seen in the Reillex® HPQ elution. The elution for the foam columns spans no more than 2 bed volumes in most cases; whereas the Reillex® HPQ elution occurs over nearly 4 bed volumes, including the dilute heads and tails cuts. Several of the foam samples reached a Pu concentration of greater than 50 g/L in the hearts cut; which represents concentration by greater than 10x from the feed solution (~4.5 g/L).

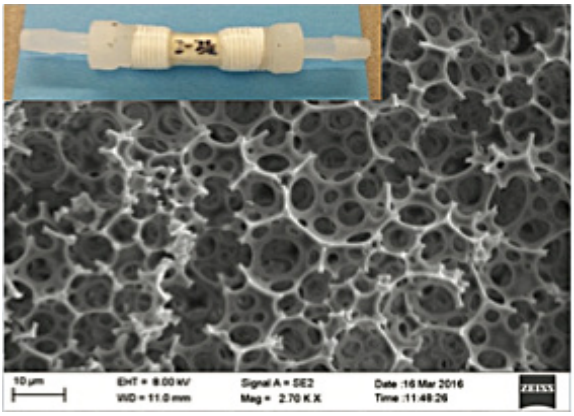

Figure 5. Photo of foam test column (inset) and SEM of foam pore structure

Sample ID	Gravimetric Pu Capacity (g Pu/g)	Volumetric Pu Capacity (g Pu/mL)
JP-2-36	0.185	0.028
JP-2-110	0.260	**0.054**
JP-2-111	**0.293**	0.052
JP-2-112	0.203	0.037
JP-2-113	0.288	0.053
JP-2-117	0.102	0.017
Reillex® HPQ	*0.038*	*0.034*

Table 2. Summary of Foam Column Pu Uptake Data

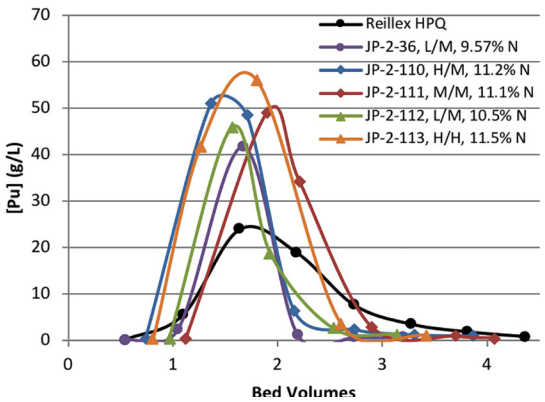

Figure 6. Elution profiles of foam column samples compared to Reillex® HPQ. The X/Y indicates graft density (X) and chain length (Y). L = low, M = medium, H = high

Additional testing of the foam column samples in FY17 focused on repeated use of the columns over an extended period of time. Several columns were prepared following the JP-2-111 formulation. Two of these samples were placed into 8 M nitric acid for a period of approximately 7 weeks. One of these samples was placed in a Co-60 irradiation source to irradiate the sample to a total dose of approximately 1 x 10^8 rads, which is the estimated maximum dose a resin column used in HB-Line would be expected to receive prior to replacement. Unfortunately, it was found that these materials were not stable to extended exposure to 8 M nitric acid. Both the irradiated and unirradiated samples were found to have decomposed at the end of the 7 week exposure; the samples were no longer solid monoliths.

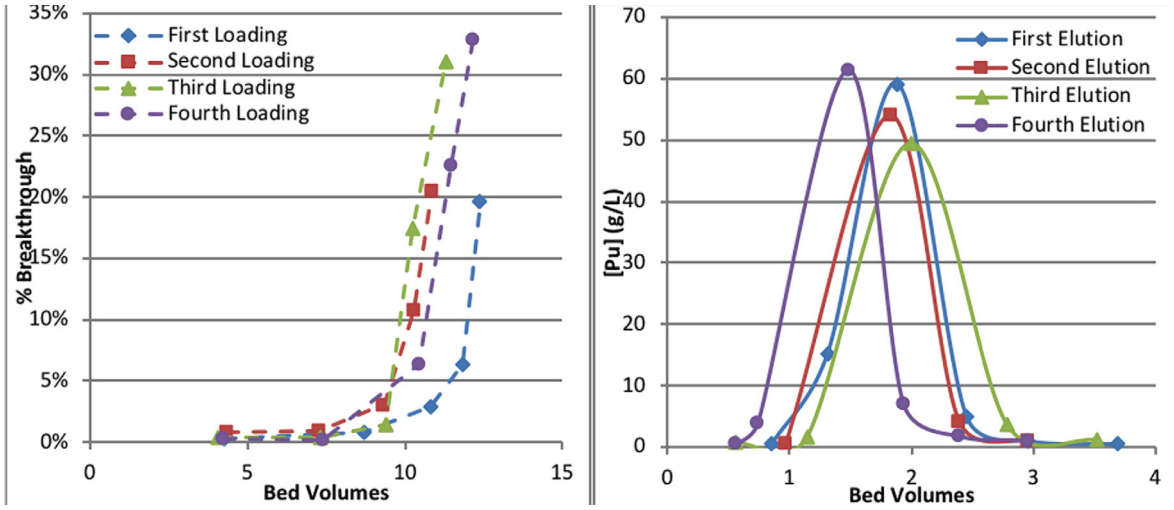

Figure 7. Loading **(left)** and elution **(right)** profiles of a single foam column sample cycled four times

An additional sample was prepared and used for recycle testing to determine the ability to load and elute the material multiple times while retaining the initial capacity. The sample used for recycle testing was loaded and eluted for a total of four times. Cycles three and four were performed approximately 3 months after cycles one and two. The column was stored during this time having last been exposed to the elution acid (0.35 M nitric acid); which indicates the column material is stable to extended exposure to dilute acid. The loading and elution profiles for the four cycles are shown in Figure 7. No loss of capacity was observed over the four cycles, indicating repeated loading and elution is possible. There did appear to be a slight increase in capacity after the first cycle; however, this increase is within the experimental and analytical error. Table 3 summarizes the capacities from the repeat cycles.

Cycle	Gravimetric Pu Capacity (g Pu/g)	% of Initial
1st	0.236	100%
2nd	0.263	111%
3rd	0.250	106%
4th	0.271	115%

Table 3. Summary of Repeat Loading/Elution Testing Results

Finally, the microchannel array prototype prepared by OSU was tested for Pu uptake. Unfortunately, the experiments indicated essentially no retention of Pu by the device. Due to limited time available after the preparation of the prototype, testing was not performed to examine the stability of the PVP coating on the NS mat in 8 M nitric acid nor was the amount of PVP immobilized on the NS mat quantified.

FY2017 ACCOMPLISHMENTS

- Demonstrated improved gravimetric and volumetric Pu capacities over the commercial Reillex® HPQ resin
- Demonstrated sharper elution profiles with the foam columns when compared to Reillex® HPQ
- Optimization of graft density and chain length showed highest gravimetric capacity with medium density and chain length
- Demonstrated reuse of the column for 4 cycles, with no loss of capacity

FUTURE DIRECTIONS

- Explore HIPE polymerization of PVP as foam backbone to increase long term stability in 8 M nitric acid.
- Explore other ion-exchange applications by identifying other functional groups that can be incorporated on the HIPE backbone for other applications.
- **For Microchannel Array:** Determine optimal NS material as well as develop more stable PVP functionalization, including incorporation of cross-linker or pre-functionalizing NS surface for end-chain attachment of PVP polymer

FY2017 PUBLICATIONS/PRESENTATIONS

1. "Porous Foam Columns for Plutonium Anion Exchange" K. M. L. Taylor-Pashow, T. C. Shehee, D. T. Hobbs, J. G. Pribyl, and B. C. Benicewicz, presented at the Nineteenth Symposium on Separation Science and Technology for Energy Applications, Gatlinburg, TN, October 11, 2016.

2. "Photoinitiated Polymerization of 4-Vinylpyridine on polyHIPE Foam Surface toward Improved Pu Separations" J. Pribyl, B. Fletcher, W. Steckle, K. Taylor-Pashow, T. Shehee, and B. Benicewicz, *Anal. Chem.,* **2017,** 89, 5174-5178.

3. "Polymeric Foams for Plutonium Anion Exchange" K. Taylor-Pashow, T. Shehee, D. Hobbs, J. Pribyl, and B. Benicewicz, presented at the 254th American Chemical Society National Meeting, Washington D.C., August 21, 2017.

REFERENCES

1. B. C. Benicewicz, G. D. Jarvinen, D. J. Kathios, and B. S. Jorgensen, *J. Radioanal. Nucl. Chem.* **1998,** 235, 31-35.

2. Malynych, S.; Luzinov, I.; Chumanov, G. *J. Phys. Chem. B* **2002**, 106 (6), 1280–1285.

ACRONYMS

DVB	divinylbenzene
HIPE	high internal phase emulsion
OSU	Oregon State University
PVP	poly(4-vinylpyridine)
TEMPO	2,2,6,6-tetramethyl-1-piperidinyloxy
USC	University of South Carolina

INTELLECTUAL PROPERTY

Invention disclosure (SRS-17-018)

Provisional patent application filed June 12, 2017.

MICROENCAPSULATION OF PuO_2 IN A LOW-WATER CEMENT-BASED WASTE FORM

Project Team: C. A. Langton, K. P. Crapse, J. M. Duffey, L. N. Oji, C. L. Crawford

Thrust Area: Nuclear Materials Management

Project Type: Standard

Project Start Date: 10/1/15

Project End Date: 9/30/17

The objective of this work was to design and test cement-based waste forms for microencapsulation of radioactive oxide waste currently stored at the SRS. The overall goal was to develop a waste form / process which supports higher waste loadings. Designing a waste form that contains moisture requires data on radiolysis of water in the waste form which results in the generation of H_2 gas. This LDRD project sought to update the H_2 G-value data currently used in engineering calculations for radiolysis of cement materials. Existing data are thought to be overly conservative and limiting because they were collected on materials which contained relatively high amounts of free water and cement systems that were not optimized for limiting radiolysis effects. To minimize hydrogen generation due to alpha radiolysis, the waste forms designed for this application contained low water to cement ratios and a novel processing technique was evaluated using resonant acoustic mixing technology. This type of mixing does not generate secondary waste, results in excellent dispersion, and supports rigorous material accountability.

FY2017 OBJECTIVES

TASK ONE
Evaluate the effect of alpha oxide loading on processing and hydrogen generation.

TASK TWO
Evaluate water sensitivity of best cement matrix: 52 X reduction in G-value for cement matrix (15.2 wt % H_2O, 5 M $NaNO_3$)

TASK THREE
Measure H_2 generation and calculate G-values for new matrices:
- Crystalline, sorbed and unbound (free) water

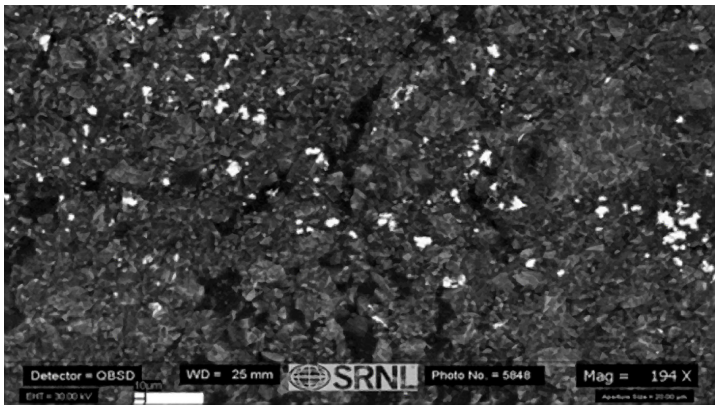

Figure 1. SEM Back Scattered Image of PuO_2 particles (~20 µm) in cement matrix at 3 wt % loading.

TASK FOUR
Evaluate scavenger effectiveness as a function of concentration and time

TASK FOUR
Determine feasibility of microencapsulation of micrometer alpha oxide particles in a cement matrix (See Figure 1)

INTRODUCTION

Alpha radiolysis of H_2O generates H_2 which can result in exceeding flammability limits. Current alpha radiolysis calculations are very conservative and limit design options for alpha material packaging, storage, transportation and disposal. Current calculations are based on data for pure water that are adjusted for mass percent of water and density of the matrix. Updated alpha radiolysis data for water and hydrated materials is needed to reduce conservatism in Safety Basis calculations.

APPROACH

The approach used to conduct this research included:

- Evaluating mixing technologies to reliable produce a low water cementitious waste form and optimizing Resonant Acoustic Mixing (RAM) which supported alpha oxide accountability requirement using HfO_2 as a surrogate for alpha oxide powder (Figure 2).
- Relocating the resonant acoustic mixer to a radiological laboratory and devising a sample preparation protocol that combined containment on bench and glovebox weighing and transfers (Figure 3).
- Designing a mixing container to fit into the pressure vessel (Figure 4).
- Measuring gas pressure in pressure vessels located in glovebox and collecting gas samples for analysis (Figure 5).
- Micro gas chromatographic analysis of gas generated by radiolysis of alpha oxide waste forms (Figure 6).

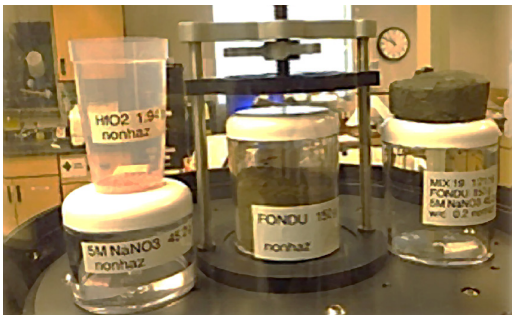

Figure 2. RAM Mixer and surrogate waste form

Figure 3. PuO_2 oxide waste form preparation

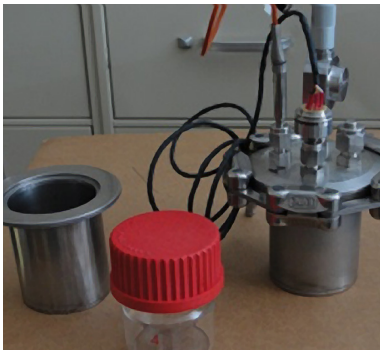

Figure 4. Pressure vessel and mixing container

Figure 5. Loading pressure vessels in glove box

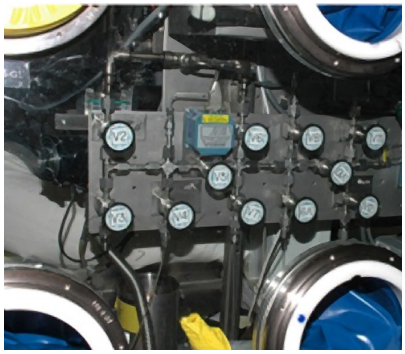

Figure 6. Gas analysis manifold with micro GC

In 2016 and 2017, methodology and test protocols were established to measure H_2 G-values for hydrated cement matrices using Pu-239 as the alpha emitter. Two concentrations of Pu-239 and two concentrations of NO_3 scavenger were evaluated.

RESULTS/DISCUSSION

Gas samples were collected in sealed vessels. Gas analyses were performed for two time intervals using micro-gas chromatography. An example of the results from the micro-gas chromatograph are shown in Figure 7. The H_2 G-values calculated for samples of hydrated cement matrices containing 5 M $NaNO_3$, a H_2 scavenger, with a total water content of 15.2 wt % were 30X to 52X lower than values calculated from literature data. See Table 1 and Figure 8. Results without the nitrate scavenger were 2.5X lower than the literature value for a sample containing 16.5 wt % water. Cement matrix mineralogy and possibly chemistry were found to affect the G-value results. This unexpected result requires further investigation. For samples containing 5 M $NaNO_3$ and 15.2 wt % water, the total alpha dose imparted to samples for 1 and 3 wt % Pu ranged from 60 to 190 kGy over times ranging from 30 to 40 days. The amounts of hydrogen generated for these samples correspond to an overall average H_2 G-value of 0.012 ± 0.001 (1 sigma for six data points).

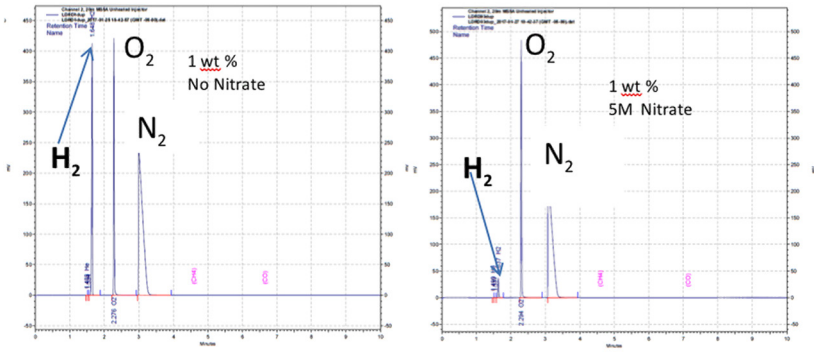

Figure 7. Micro GC data for 1 wt % oxide (water/cement = 0.2) without and with nitrate

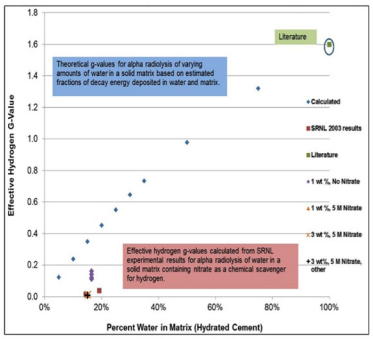

Figure 8. G-Values including updated values for 1 and 3 wt % alpha oxide

wt % α- solids	wt % water	Effective H_2 G-value for cement waste forms			G-Value Reduction
		Estimate	LDRD 2017 SRNL data	Duffey, 2003 SRNL data	
1	16.5 (water only)	0.38	0.15 ± 0.02 (0.14, 0.16), (0.12, 0.11)	--	2.5
1	15.2 (5 M $NaNO_3$)	0.36	0.012 ± 0.001 (0.012, 0.011) (0.012, 0.011)	--	30
3	15.2 (5 M $NaNO_3$)	0.36	0.012 ± 0.001 (0.013, 0.012)	--	30
3	15.2 (5 M $NaNO_3$)	0.36	0.007 (cement with more evaporable H_2O)	--	52
0.007	14.5 ($NaNO_3$ Soln)	0.34	--	0.015	23
0.008	19.5 ($NaNO_3$ Soln)	0.43	--	0.037	12

Table 1. Effective H_2 G-values for PuO_2 alpha radiolysis of cement waste forms

FY2017 ACCOMPLISHMENTS

H_2 G-value data used in engineering calculations for alpha radiolysis of cement materials were updated and H_2 scavenging by nitrate were demonstrated. RAM mixing was demonstrated as a method for (1) cement waste form preparation which results in no secondary waste and (2) excellent accountability of alpha oxide material. Results to date were presented at the Actinide Separation Conference, Argonne, IL, May 2017. This research provided an opportunity to interact with JAEA on alpha radiolysis of damp materials. In June 2017, a proposal was submitted to JAEA on Phase 1 of a collaborative 5-year research program.

FUTURE DIRECTIONS

- ✔ Complete first data set of materials with crystalline water $Ca(OH)_2$, $CaSO_4{\cdot}2H_2O$, $Fe(OH)_2$
- ✔ Optimize $NaNO_3$ scavenger loading including higher molar Na solutions and $NaNO_3$ containing slurries as the mixing water.
- ✔ Complete data set for sorbed wate
- ✔ Apply technology to demonstrating a waste form for SRS non-MOXable waste PuO_2

FY2017 PUBLICATIONS/PRESENTATIONS

1. K. Crapse, C. A. Langton, J. M. Duffey, L. N. Oji, C. L. Crawford, 2017. “Updated G-Values and Radiolysis Data for Hydrated Waste Forms Containing Alpha Oxide”, Actinide Separation Conference, Argonne, IL.

ACRONYMS

GC	Gas Chromatograph, Gas Chromatography
Gy	Gray
kGY	Kilo Gray
JAEA	Japan Atomic Energy Agency
MOX	Mixed Oxide
R&D	Research and Development
RAM	Resonant Acoustic Mixer
RPM	Revolutions Per Minute

DISSOLUTION OF USED NUCLEAR FUEL USING A TBP/N-PARAFFIN SOLVENT

Project Team: T. S. Rudisill (PI), T. C. Shehee, D. H. Jones

Unfunded Collaboration: CG. D. DelCul (Oak Ridge National Laboratory)

Thrust Area: Nuclear Materials Management

Project Start Date: 10/1/16

Project End Date: 9/30/18

The dissolution of unirradiated used nuclear fuel (UNF) pellets pretreated for tritium removal was demonstrated using a tributly phosphate (TBP) solvent. Dissolution of pretreated fuel in TBP could potentially combine dissolution with two cycles of solvent extraction required for separating the actinides and lanthanides from other fission products. Dissolutions were performed using UNF surrogates prepared from both uranyl nitrate and uranium trioxide produced from the pretreatment process by adding selected actinide and stable fission product elements. In laboratory-scale experiments, the U dissolution efficiency ranged from 80-99+% for both the nitrate and oxide surrogate fuels. On average, 80% of the Pu and 50% of the Np and Am in the nitrate surrogate dissolved; however, little of the transuranic elements dissolved in the oxide form. The majority of the 3+ lanthanide elements dissolved. Only small amounts of Sr (0-1.6%) and Mo (0.1-1.7%) and essentially no Cs, Ru, Zr, or Pd dissolved.

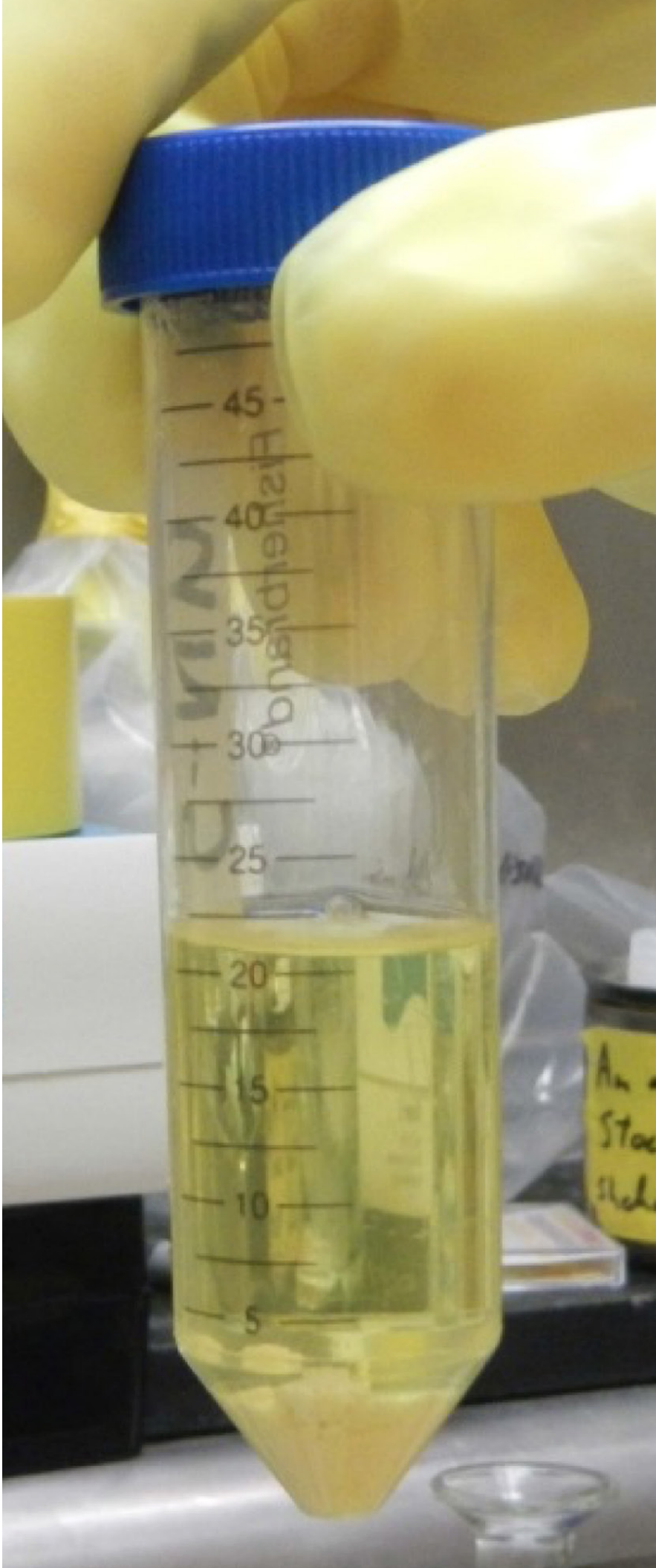

FY2017 OBJECTIVES

Demonstrate the feasibility of dissolving and purifying the actinide materials in used nuclear fuel (UNF) using a tributyl phosphate (TBP)/n-paraffin solvent following pretreatment with nitrogen dioxide gas (NO_2) to remove tritium to include the following tasks

TASK ONE

Ship uranium trioxide (UO_3) and uranyl nitrate $UO_2NO(NO_3)_2$ from Oak Ridge National Laboratory (ORNL) which was pretreated for tritium removal to the Savannah River National Laboratory (SRNL) for use in TBP dissolution studies

TASK TWO

Add Np, Pu, and Am and key fission products (as non-radioactive elements) to simulate UNF

TASK THREE

Perform dissolutions in a 30 vol % TBP/n-paraffin solvent and characterize the distribution of the actinides and fission products between the TBP and residual solids

TASK THREE

Perform optimization studies (e.g., dissolution temperature, solid-to-liquid ratio, nitric acid (HNO_3) saturation of TBP, and mixing) to maximize dissolution efficiency

INTRODUCTION

When UNF is removed from a reactor, approximately 95% of the initial U is still present in the fuel. The fuel also contains higher actinides (e.g., Np, Pu, Am, and Cm) which can be recovered, fabricated into fuels or targets, and used to generate additional energy. However, construction of a large-scale reprocessing facility with the capability to completely recycle UNF is prohibitively expensive. Simplified flowsheets which reduce the equipment footprint and facility size are needed to improve the economic viability of complete recycle. To address this issue, we have performed an initial demonstration of a hybrid process which combines the dissolution of pretreated UNF in a TBP-containing solvent with two cycles of solvent extraction required for the recovery of the actinide and lanthanide elements. A conceptual flowsheet for the headend facilities including the hybrid process is shown in Figure 1.

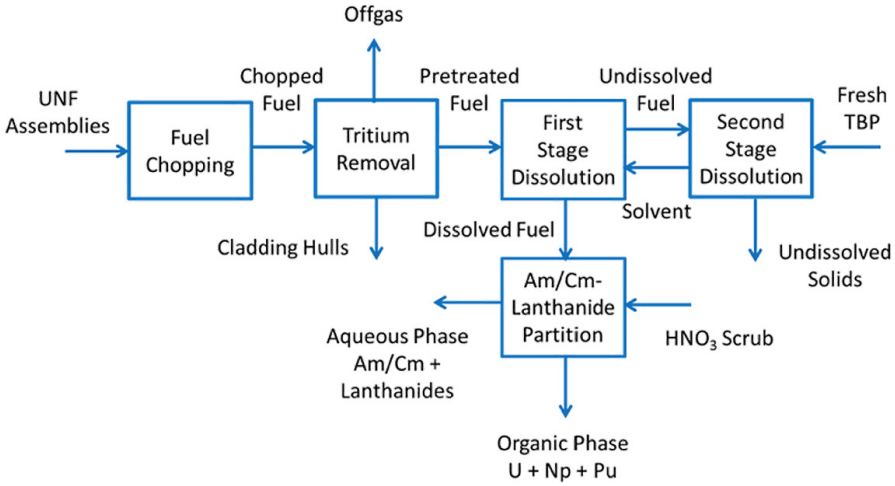

Figure 1. Conceptual Headend Process for the Recycle of UNF

A dry pretreatment process based on the oxidation of UNF is under development at ORNL for the removal of tritium (and I_2) in the headend portion of a fuel reprocessing facility. In this process, contact with a NO_2/O_2 mixture converts the fuel into a fine UO_3 powder, and with further reaction time and temperature adjustment, the UO_3 can be converted to $UO_2NO(NO_3)_2$ **[1].** In the nitrate form, U can be dissolved (extracted) directly into TBP. The direct dissolution of the UO_3 product into TBP can also be achieved by using TBP pre-equilibrated with nitric acid **[2]**. Although, the direct dissolution of both UO_3 and $UO_2NO(NO_3)_2$ into TBP has been demonstrated **[3]**, the extent of dissolution of other components of UNF into a TBP solvent has not been investigated.

To demonstrate the feasibility of the hybrid process, we prepared simulated UNF from unirradiated, depleted uranium dioxide (UO_2) fuel pellets (which were oxidized for tritium removal at ORNL) by adding selected actinide and stable fission product elements. The surrogate UNF's were subsequently used in dissolution experiments to evaluate the distribution of the actinides and fission product elements between the solid and liquid phases. The feasibility of dissolving both the UO_3 and $UO_2NO(NO_3)_2$ in TBP was investigated in three series of experiments performed with only the U compounds, the U compounds with the addition of selected stable fission products, and the U compounds with the addition of transuranic elements (e.g., Np, Pu, and Am).

APPROACH

Fourteen fission and activation products were selected to prepare the surrogate UNF's. These elements included: transuranics (Np, Pu, and Am), lanthanides (Ce, Nd, and Eu), Cs and Sr, transition metals (Mo, Zr, and Re as a surrogate for Tc), noble metals (Ru and Pd), and I_2. Generally, nitrates were added to the $UO_2NO(NO_3)_2$ and oxides were added to the UO_3. Exceptions included the addition of I_2 as cesium iodide, Mo, Ru, and Re(Tc) as oxides to both fuel surrogates, and Pd as elemental Pd. The U mass in all experiments was nominally 1 g. The non-radioactive fission products were added to the surrogates at approximately 10% of the U mass. Trace quantities (< 0.02 g) of the transuranic elements were used in the actinide only dissolution experiments. The surrogate UNF's were dissolved in 50 mL centrifuge tubes using 30 vol % TBP. For the oxide dissolutions, the TBP was equilibrated three times using a 1:1 organic to aqueous ratio with 5 or 10 M HNO_3. The solution volume was 20 mL for actinide-only dissolution and 40 mL for the surrogates containing U with the addition of the non-radioactive fission products. Dissolutions were performed at ambient (22-25 °C) and 50 °C using dissolution times of a least 2 h.

An Eppendorf Thermomixer R heating/cooling block was primarily used for temperature control and agitation. A limited number of dissolution experiments were performed using a VWR tube rotator and in a beaker with a stir bar for improved mixing. The U-loaded solvent in all experiments was initially filtered to remove solids (Figure 2). Multiple 2 mL aliquots of dodecane were used to wash the solids. Samples of the organic solvent were prepared for analysis by inductively-coupled plasma emission or mass spectroscopy (ICPES or ICPMS) by Parr bomb digestion of the TBP/dodecane. The undissolved solids (UDS) from a number of dissolution experiments were dissolved to evaluate material balance closure. The UDS were dissolved using either 8 M HNO_3 or 8 M HNO_3 containing 0.05 M potassium fluoride (KF). The small amount of UDS from the U and actinide only experiments dissolved reasonably well; however UDS from the dissolutions containing the non-radioactive fission product elements did not completely dissolve. Residual solids were characterized by X-ray diffraction analysis.

Figure 2. Filtration of Surrogate UNF Dissolved in TBP/n-paraffin solvent

RESULTS/DISCUSSION

Both U compounds began dissolving immediately upon contact with the TBP solvent. Following the dissolution cycle, a small amount of UDS was present in the centrifuge tubes. Fine white solids remained from the nitrate dissolutions and course brown solids remained from the oxide dissolutions. We also observed a small volume aqueous phase (most likely generated from water present in the TBP) which appeared to form a barrier (to dissolution) between the UDS and TBP. For this reason, dissolutions were performed using a rotary mixer and a beaker with a stir bar to increase the mixing intensity; however, results from these experiments did not show increased dissolution efficiency. Small improvements in efficiency may not have been observable based on the precision of the data. The dissolution efficiency for the U only experiments varied from 80-99+% (Table 1). The efficiency was based on the total U measured in the solvent and UDS. A small amount of hydrogen peroxide (H_2O_2) was added in several experiments to ensure the U was present as U(VI) (to increase dissolution efficiency); however, the H_2O_2 resulted in the precipitation of uranium peroxide (UO_4). The highest U recovery efficiencies were obtained at nominally 25 °C compared to experiments performed at 50 °C. This observation is consistent with U distribution coefficients between TBP and HNO_3 decreasing with increasing temperature **[4].** The material balance closures for all experiments except for ones in which H_2O_2 was added were greater than 100% due to uncertainties in the U measurements (Table 1). A limited number of two stage dissolution experiments in which most of the organic phase was removed from the centrifuge tubes and replaced with fresh solvent for a second dissolution cycle showed slight improvement in U dissolution efficiency.

Exp	Temp	Dissolved U	Undissolved U	Dissolution Efficiency	Mat Bal Closure
	(°C)	(g)	(g)	(%)	(%)
UN-1	25	1.34	0.001	99.9	123
UN-2	25	1.27	0.001	99.9	117
UO-1	25	1.14	0.163	87.5	116
UO-2	25	1.13	0.216	84.0	118
UN-3	50	1.31	0.267	83.0	144
UN-4	50	1.34	0.273	83.1	148
UO-3	50	1.44	0.135	91.4	142
UO-4	50	1.44	0.134	91.5	140
UN-5(1)	50	0.454	0.291	61.0	68.6
UN-6(1)	50	0.616	0.274	69.2	78.0
UO-5(1)	50	0.705	0.154	82.1	74.3
UO-6(1)	50	0.769	0.174	81.5	82.7

(1) H_2O_2 added to TBP/n-paraffin solvent

Table 1. Dissolution Efficiency and Material Balance Closure for U Dissolutions

Element	UN-9	UN-10	UO-9	UO-10	UN-11	UN-12	UO-11	UO-12
	(%)	(%)	(%)	(%)	(%)	(%)	(%)	(%)
U	98.2	97.5	98.3	99.5	95.2	91.8	94.1	88.3
Cs	0.0	0.0	0.0	0.0	0.1	0.0	0.0	0.0
Ce	56.8	70.5	0.0	0.0	10.8	85.5	2.2	0.2
Nd	65.8	79.4	71.2	65.1	0.7	97.8	66.4	46.0
Eu	84.5	90.3	83.1	82.7	4.8	95.3	83.9	60.4
Sr	0.7	1.0	0.0	0.0	0.2	1.6	0.1	0.0
Re(Tc)	8.8	14.8	11.2	9.2	9.6	9.4	11.1	3.3
Mo	0.1	0.2	1.7	1.2	0.2	0.2	0.5	0.6
Ru	0.0	0.0	0.0	0.0	0.0	0.0	0.0	0.0
Zr	0.0	0.0	0.0	0.0	0.0	0.0	0.0	0.0
Pd	0.0	0.0	0.0	4.5	0.0	0.0	0.0	0.0
Temp (°C)	22	22	22	22	50	50	50	50

Table 2. Dissolution Efficiencies for U + nonRad Fission Product Dissolutions

Similar U dissolution efficiencies were measured in experiments performed with UNF surrogates containing non-radioactive fission product elements compared to the U only experiments. The efficiency varied from approximately 88-99+% (Table 2). The same effect of temperature on the dissolution efficiency was observed with the highest efficiencies measured at lower temperatures. The amount of the lanthanide elements dissolved in the TBP solvent varied with oxidation state. Approximately 60-90+% of the Nd, Eu, and Ce in the 3+ oxidation state (as both nitrates and oxides) dissolved; however, little of the Ce(IV) as cerium oxide (CeO_2) was solubilized. The dissolution of the 3+ lanthanides indicates that these elements will likely exhibit the same behavior in the hybrid dissolution process as the Am and Cm present in UNF's.

A small amount of Sr dissolved (0.1-1.6%) in several experiments. Little Cs dissolved in any of the experiments. The amount of Mo dissolved varied from 0.1-1.7%. Essentially no Ru, Zr, and Pd dissolved. The concentration of I_2 in the solvent was not measured due to the complexity of the analysis; however, we recognized that I_2 was extracted due to the purple color of the solvent. It is unlikely that very much I_2 will be present in UNF pretreated for tritium removal since the pretreatment process also volatilizes I_2 as well as tritium. The material balance closures for most of the elements used in these experiments were generally very good (Table 3). Little of the Ru (added as ruthenium oxide (RuO_2) in both the nitrate and oxide surrogates) or zirconium oxide (ZrO_2) were solubilized using either the TBP solvent or during dissolution of the UDS in 8 M HNO_3 containing 0.05 M KF. X-ray diffraction analysis of the residue from the UDS dissolutions showed the presence of Ru and Zr as well as Pd. Two stage dissolution experiments were also performed with surrogates containing the non-radioactive fission product elements; however, little difference in the recovery efficiencies were observed compared to the one stage dissolutions.

Element	UN-9	UN-10	UO-9	UO-10
	(%)	(%)	(%)	(%)
U	92.6	90.8	100	98.4
Cs	91.5	96.9	85.4	92.6
Sr	86.9	93.6	71.6	67.0
Ce	101	103	91.2	98.1
Nd	103	106	99.1	99.2
Eu	98.7	100	101	102.3
Re(Tc)	87.0	87.0	83.4	88.6
Mo	93.6	93.7	84.8	88.2
Ru	0.1	0.0	0.0	0.0
Zr	85.8	85.5	2.9	2.1
Pd	85.9	84.1	86.5	96.8

Table 3. Material Balance Closure for U + nonRad Fission Product Dissolutions

Exp	Temp	Dissolution Efficiency (%)			
	(°C)	U	Np	Pu	Am
UN-21	25	98	44	83	25
UN-22	25	98	50	64	75
UN-23	50	134	55	87	50
UN-24	50	178	37	86	60
UO-21	25	113	0.3	< 0.4	0.1
UO-22	25	106	0.3	< 0.6	0.1
UO-23	50	150	2.0	12.4	4.0
UO-24	50	118	2.8	3.8	1.9

Table 4. Dissolution Efficiency for Actinide Only Dissolutions

In experiments performed with UNF surrogates containing just the actinide elements (U, Np, Pu, and Am), near complete dissolution of the U was achieved for both the nitrate and oxide compounds (Table 4). On average, approximately 80% of the Pu nitrate and half the Np and Am nitrates dissolved in the TBP solvent. However, little of the Np(IV), Pu(IV), or Am(IV) oxides dissolved which was consistent with the behavior observed for the Ce(IV) oxide. The preparation of oxide and nitrate UNF surrogates by adding individual compounds is not completely representative of real fuel. The presence of Pu and the minor actinides (Np, Am, and Cm) as solid solutions with U will almost certainly affect the dissolution rate and efficiency. Performing experiments with actual irradiated fuel pretreated for tritium removal is necessary to be certain of the actual behavior of the actinides (and fission products) during dissolution in a TBP-containing solvent. The material balance closures for the actinide only dissolutions were generally good, with closures exceeding 75% for a majority of the experiments.

FY2017 ACCOMPLISHMENTS

- ✔ Dissolution of unirradiated UO_2 fuel pellets pretreated for tritium removal in a TBP/dodecane solvent was demonstrated in laboratory-scale experiments
  - Dissolution efficiency for the U only surrogate (oxide and nitrate forms) varied from 80-99+%
  - Highest U recovery efficiency was obtained at lower temperatures (22-25 °C versus 50 °C)

FY2017 ACCOMPLISHMENTS [CONTINUED]

- ✔ Majority of U and lanthanides in UNF surrogates containing U and non-radioactive fission product elements dissolved
  - U dissolution efficiency varied from 88-99+%
  - 60-90% of the Nd(III), Eu(III), and Ce(III) dissolved (as both nitrates and oxides); little Ce(IV) (as CeO_2) was solubilized
  - Generally less than 1% of the Sr and Mo dissolved
  - Essentially no Cs, Ru, Zr, or Pd dissolved
  - I_2 extracted into the TBP solvent (not quantified)
- ✔ Dissolution of actinide only surrogates (containing U, Np, Pu, and Am) showed significantly different behavior for the transuranic nitrate and oxide compounds
  - Near complete dissolution of both U compounds
  - Observed on average, dissolution of 80% of the Pu nitrate and approximately half of the Np & Am nitrates
  - Little of the Np, Pu, and Am oxides dissolved —consistent with the behavior of the Ce(IV) oxide

FUTURE DIRECTIONS

- ✔ Demonstrate the dissolution of irradiated UNF pretreated for tritium removal in a 30 vol % TBP solvent
  - Pretreat irradiated fuel sample to prepare UO_3 and/or $UO_2NO(NO_3)_2$ for dissolution tests; previously performed for the DOE-NE Fuel Cycle Technologies Material Recovery and Waste Forms Development Campaign at ORNL
  - Ship small quantities (2-5 g) of pretreated fuel to SRNL to demonstrate dissolution process in SRNL Intermediate Level Cell
  - Demonstrate baseline dissolution process with irradiated fuel
  - Perform additional experiments to address difference in observed behavior of irradiated and unirradiated fuel
- ✔ Limited demonstration of dissolution process with irradiated fuel was funded by the SRNL FY18 LDRD program

FY2017 PUBLICATIONS/PRESENTATIONS

1. T. S. Rudisill, T. C. Shehee, D. H. Jones, and G. D. DelCul, *Dissolution of Used Nuclear Fuel using a TBP/ n-Paraffin Solvent,* SRNL-MS-2017-00067, 41st Annual Actinide Separations Conference, Argonne National Laboratory, Argonne, IL, May 23, 2017.

REFERENCES

1. G. D. DelCul, R. D. Hunt, B. B. Spencer, and R. T. Jubin, Demonstrate Complete NO2-based Tritium-Pre-Treatment Process with Simulated Fission Products at Kilogram Scale, FCRD-MRWFD-2015-000397, Oak Ridge National Laboratory, Oak Ridge, TN (September 2015).

2. F. A. Dorda, V. V. Lazarchuk, V. A. Matyukha, M. V. Sirotkina, and V. V. Tinin, Kinetics of UO_3 dissolution in nitric acid saturated 30% TBP in a hydrocarbon diluent, Radiokhimiya, Vol. 52, No. 5, p. 397-398 (2010).

3. Hiroshi Tomijima, Totsuka-ku, Yokohama, Kazushige Tsukui, Direct Dissolution of Water-insoluble Uranium Compounds by Contact with Neutral Organic Solvents Pretreated with Nitric Acid, Patent 3,288,568 (November 29, 1966).

4. M. L. Hyder , W. C. Perkins, M. C. Thompson, G. A. Burney, E. R. Russell, H. P. Holcomb, and L. F. Landon, Processing of Irradiated, Enriched Uranium Fuels at the Savannah River Plant, DP-1500, E. I. du Pont de Nemours and Co. (1979).

ACRONYMS

UNF	Used Nuclear Fuel
TBP	Tributyl Phosphate
NO_2	Nitrogen Dioxide
UO_3	Uranium Trioxide
$UO_2NO(NO_3)_2$	Uranyl Nitrate
ORNL	Oak Ridge National Laboratory
SRNL	Savannah River National Laboratory
HNO3	Nitric Acid
UO_2	Uranium Dioxide
ICPES	Inductively-coupled Plasma Emission Spectroscopy
ICPES	Inductively-coupled Plasma Mass Spectroscopy
H_2O_2	**Hydrogen Peroxide**
CeO_2	Cerium Oxide
RuO_2	Ruthenium Oxide
ZrO_2	Zirconium Oxide

SELF-PROPAGATING SOLUTION SYNTHESIS OF $Gd_2Zr_2O_7$ PYROCHLORES FOR Pu DISPOSITION

Project Team: C. S. Dandeneau, J. W. Amoroso, and T. C. Shehee (Primary)

Thrust Area: Nuclear Materials Managment

Project Start Date: 10/1/16

Project End Date: 9/30/17

The disposition of excess Pu is a high priority issue for environmental and nuclear materials management missions undertaken by the Department of Energy. As an alternative to conventional oxidation and down-blending procedures, a simple, one-step self-propagating solution method was devised to immobilize Pu in durable $Gd_2Zr_2O_7$ (GZO) lattices. Previous studies have demonstrated that the crystallinity of GZO is maintained under heavy ion bombardment, indicating that the material can withstand sustained Pu alpha decay events. Here, the generation of an exothermic redox reaction under controlled and optimized conditions led to the formation of crystalline undoped and Pu-doped GZO with no post-annealing step. The simplicity and low cost of the designed process make it highly amenable to up-scaling with minimal energy input.

FY2017 OBJECTIVES

TASK ONE

Devise a self-propagating solution-based route to fabricate undoped, crystalline $Gd_2Zr_2O_7$ with no post-annealing step

TASK TWO

Optimize fuel/oxidizer type and ratio to maximize $Gd_2Zr_2O_7$ crystallinity

TASK TWO

Fabricate Pu-doped $Gd_2Zr_2O_7$ via the devised process

INTRODUCTION

One established protocol for Pu disposition at the Savannah River Site (SRS) is oxidation and down-blending, whereby Pu is precipitated out of a nitric acid solution, oxidized by sustained heating, and then mixed with a suitable adulterant prior to disposal. However, another available option is to immobilize Pu in a durable (i.e., radiation-resistant) crystalline ceramic via elemental substitution. The resulting Pu-doped wasteform can then be safely disposed of in an appropriate manner. Among the candidates proposed for Pu immobilization is the group of ternary metal oxides known as pyrochlores, which have the general chemical formula $A_2B_2O_7$, where A represents larger, lower valence (2+ and 3+) cations (e.g. rare earth elements), while B denotes transition metals capable of octahedral coordination. The vast array of compositions possible in the pyrochlore system allows for structural flexibility and thus, a range of tri- and tetra-valent actinides may be incorporated into the ceramics.

The $Gd_2Ti_2O_7$ pyrochlore system has been extensively studied as a candidate for Pu immobilization. However, both curium doping and heavy ion bombardment experiments have shown that $Gd_2Ti_2O_7$ readily becomes amorphous due to damage by alpha decay events **[1-2].** This transition from a crystalline to amorphous state can lead to swelling, fracturing, and an increase in the actinide leach rate.

In contrast, the results of heavy ion irradiation have revealed that $Gd_2Zr_2O_7$(GZO) is more resistant to metamictization when compared to its titanate counterpart. Specifically, no amorphous regions were observed in GZO after the material was subjected to an ion fluence equivalent to 3×10^{20} alpha decay events per g, or the dose a 10 wt% Pu-doped GZO specimen would collect over 30 million years [2].

One of the characteristics that defines the structural stability of a given pyrochlore composition is the ratio of A to B cationic radii, *rA/rB,* which generally ranges from 1.46 – 1.78 **[3].** Among the known pyrochlores, GZO has the lowest cationic ratio (1.46), while $Gd_2Ti_2O_7$ has a ratio that lies at the higher end of the spectrum (1.74) **[4].** Under ion beam irradiation, pyrochlores with lower A to B radius ratios tend to maintain their crystallinity. This can be explained through the formation of anti-site defects (i.e., an A^{3+} cation at a B^{4+} site or vice versa) on the cation sub-lattice. In the case of GZO, the anti-site defect of a Gd^{3+} cation at a Zr^{4+} site would have a –1 charge. To maintain charge neutrality, this defect can be compensated by a Zr^{4+} cation at a Gd^{3+} site (+1 charge). When compared to $Gd_2Ti_2O_7$ the formation energy of anti-site defects is lower for GZO due to its smaller *rA/rB* ratio **[5].** Consequently, the energy from ion beam irradiation is dissipated via anti-site defect formation as well as through the generation of Frenkel defects (vacancy-interstitial pairs) on the oxygen sub-lattice. Such a scenario results in the transition of GZO from a more ordered pyrochlore phase to a crystalline but disordered fluorite structure (Figure 1). It is the ability of GZO to form a disordered fluorite phase that gives the compound its "radiation resistance".

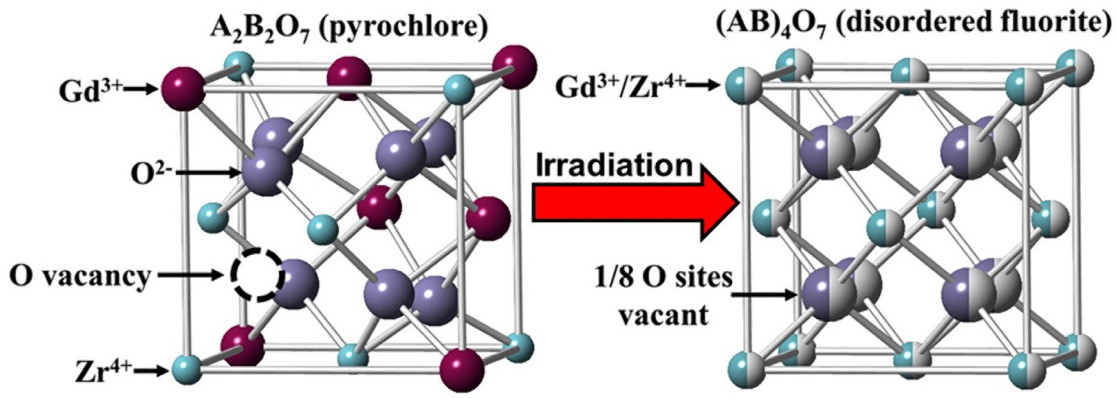

Figure 1. Under ion beam irradiation (which simulates alpha decay), the crystallinity of GZO is maintained by the formation of defects, resulting in a transition from a more ordered pyrochlore structure to a crystalline disordered fluorite phase

APPROACH

The fabrication of GZO was carried out by a self-propagating solution synthesis method. This technique involves the initiation of a thermodynamically favorable, self-sustaining redox reaction between metal nitrates and a suitable reducing agent (i.e., the fuel). The intermixing of elemental components in solution allows for excellent compositional control, while the simplicity of the process facilitates ease of scalability and the use of modular components. More importantly, the optimization of specific processing parameters can produce crystalline GZO solely from the heat generated in the exothermic redox reaction. The two primary factors of interest in this work were the fuel type and fuel:oxidizer ratio, the latter of which is commonly known as the elemental stoichiometric coefficient (ESC).

For the synthesis of undoped GZO, aqueous solutions consisting of metal nitrates and various fuels (e.g., urea, glycine, β-alanine) with different ESC values were first prepared. The precursors were subsequently placed in either a preheated muffle furnace (<600 °C) or a microwave apparatus in order to evaporate the water and initiate a self-propagating reaction. X-ray diffraction (XRD) patterns were obtained to verify the crystallinity of the as-processed powders, while differential thermal analysis (DTA) was employed to examine reaction kinetics. To fabricate Pu-doped GZO, a solution of Pu nitrate was incorporated into the optimized undoped procedure; a preheated muffle furnace contained inside a negative pressure glovebox was utilized in the Pu-doping experiments.

RESULTS/DISCUSSION

XRD patterns of undoped GZO fabricated from optimized precursor solutions under both furnace and microwave heating are shown in Figure 2; the ESC value was held constant at unity. While $ZrO(NO_3)_2$ is more commonly used as a Zr source in wet chemistry applications, enhanced crystallinity was observed when $Zr(NO_3)_4$ was employed as an oxidizer. Such a finding can be attributed to the presence of additional nitrate groups which serves to increase the exothermicity of the designed reactions. Furthermore, the utilization of amino acids (e.g., glycine, β-alanine) as fuels yielded powders with carbonaceous residue and a lower degree of crystallinity, while urea produced highly crystalline GZO. The improvement in GZO crystallinity with urea could be attributed to the dual functions of the fuel as both a reducing and complexing agent. Regarding the latter, the formation of stable metal complexes ensures sufficient solution homogeneity. However, if the stability of the metal complex is excessively high, decomposition of the solution components is hindered and incomplete combustion occurs. DTA data collected for precursor solutions containing urea, glycine, and a urea/glycine mixture confirmed that maximum exothermicity is achieved when urea is employed as a fuel.

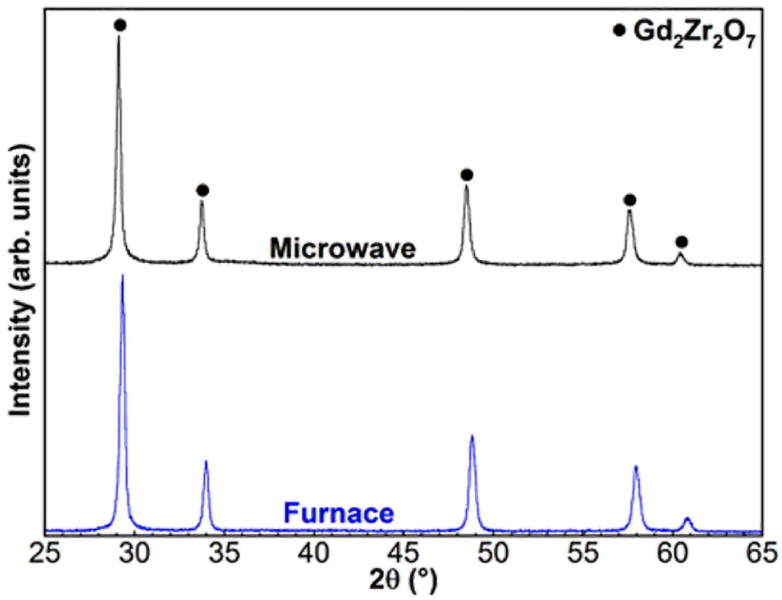

Figure 2. XRD patterns obtained with optimized GZO precursors after furnace and microwave heating.

Initial experiments designed to fabricate 5 wt% Pu-doped GZO produced powders with low crystallinity. However, subsequent variations in the ESC value (i.e., changes in the fuel content) of the precursor solutions appeared to yield single-phase Pu-doped GZO with a high degree of crystallinity. The need to adjust the ESC value may be due to the introduction of Pu nitrate solutions in the process, which alters the targeted ESC value prior to the initiation of the self-propagating reactions.

FY2017 ACCOMPLISHMENTS

- Successfully fabricated crystalline GZO via a self-propagating solution synthesis route with no post annealing; both microwave and furnace heating yielded crystalline GZO
- Optimized the solution chemistry of the undoped GZO process; maximum crystallinity was obtained with an ESC value of 1 for solutions containing $Gd(NO_3)_3$, $Zr(NO_3)_4$, and urea
- Correlations between DTA and XRD data indicate that amino acids, which are commonly employed as reducing agents in self-propagating solution synthesis methods, have a deleterious effect on crystallinity, possibly due to the formation of strong metal complexes that hinder reaction exothermicity
- Upon varying the ESC value, the fabrication of single-phase, crystalline Pu-doped GZO was successful

FUTURE DIRECTIONS

- Optimize the ESC value of Pu-doped GZO to maximize crystallinity
- Assess feasibility of an up-scaled process (cost, ease of implementation) and compare to current disposition protocols
- Investigate GZO radiation resistance via doping with shorter half-life actinides to examine the effects of alpha decay on observable time scales
- Apply developed method to other complex oxide systems (e.g., Cs-bearing hollandites)

FY 2017 PUBLICATIONS/PRESENTATIONS

1. C. S. Dandeneau, J. H. Christian, J. A. Velten, J. W. Amoroso, and T. C. Shehee, "Solution combustion synthesis of crystalline Pu-doped $Gd_2Zr_2O_7$ ceramics" (to be submitted to I*norganic Chemistr*y subsequent to filing of patent application)

FY 2017 PUBLICATIONS/PRESENTATIONS

1. S.X. Wang, B.D. Begg, L.M. Wang, R.C. Ewing, W.J. Weber, K.V.G. Kutty, *Journal of Materials Research,* 14, pp. 4470-4473 (1999).I
2. W.J. Weber, J.W. Wald, H. Matzke, *Journal of Nuclear Materials,* 138, pp. 196-209 (1986).
3. F.X. Zhang, M. Lang, R.C. Ewing, *Applied Physics Letters,* 106, 191902 (2015).
4. R.C. Ewing, W.J. Weber, J. Lian, *Journal of Applied Physics,* 95, pp. 5949-5971 (2004).
5. F.X. Zhang, J.W. Wang, J. Lian, M.K. Lang, U. Becker, R.C. Ewing, *Physical Review Letters*, 100, 045503 (2008).

ACRONYMS

SRS	Savannah River Site
GZO	$Gd_2Zr_2O_7$
ESC	Elemental Stoichiometric Coefficient
XRD	X-ray Diffraction
DTA	Differential Thermal Analysis

INTELLECTUAL PROPERTY

Invention disclosure submitted, SRS-18-003

TOTAL NUMBER OF POST-DOCTORAL RESEARCHERS

1. Christopher S. Dandeneau
2. Josef A. Velten

NATIONAL SECURITY

UNIQUE CONCEPTS THAT ADDRESS NATIONAL SECURITY MISSION AREA NEEDS THAT ARE CURRENTLY UNDERSERVED BY THE DOE LAB SYSTEM. GAME-CHANGING INNOVATIONS AND TOOLS THAT ADVANCE THE NATIONAL SECURITY AGENDA FOR THE UNITED STATES GOVERNMENT, INCLUDING MONITORING, NONPROLIFERATION, AND DETERRENCE.

ADVANCED ULTRAFAST SPECTROSCOPY FOR CHEMICAL DETECTION OF NUCLEAR FUEL CYCLE MATERIALS

Project Team: E. Villa-Aleman (Primary), A. L. Houk, and W. A. Spencer
Thrust Area: National Security
Project Type: Standard
Project Start Date: 10/1/15
Project End Date: 9/30/17

The development of new signatures and observables from processes related to proliferation activities are often related to technological advancements. In our physical world, the intensity of observables is linearly related to the input drivers (light, current, voltage, etc.). Ultrafast lasers with high peak energies, open the door to a new regime where the intensity of the observables is not necessarily linear with laser energy. Potential nonlinear spectroscopic applications include chemical detection via remote sensing, material characterization and processing, surface phenomena modifications, nuclear fusion, etc. Currently, we can achieve laser energies in the 5 nano-Joule range, preventing the study of nonlinear phenomena. To advance our nonproliferation research into the nonlinear regime we require laser pulses in the milli-Joule (mJ) energy range. We have procured and installed a 35 fs-7 mJ laser, operating at one kilohertz repetition rate, to investigate elemental and molecular detection of materials in the laboratory with potential applications in remote sensing. Advanced, nonlinear Raman techniques will be used to study materials of interest that are in a matrix of many materials and currently with these nonlinear techniques we can achieve >3 orders of magnitude signal enhancement.

FY2017 OBJECTIVES

TASK ONE
Installation of an ultrafast, femtosecond laser system and an optical parametric amplifier (OPA)

TASK TWO
Programming of a spatial light modulator (SLM) to control the phase and amplitude of laser pulses

TASK THREE
Design of microscope and optical components required to couple laser light to samples of interest

TASK FOUR
Measure various materials with different advanced Raman techniques

INTRODUCTION

The National Security Directorate (NSD) has supported the DOE NA-22 Uranium Program via characterization of UO_2F_2 particulates and aged products with Raman, luminescence and infrared spectroscopic techniques. These techniques were used to study the behavior of particulates in the laboratory under different humidity and lighting conditions. Other U-bearing compounds (UO_2, U_3O_8 and UO_3) were also studied in order to understand the oxidation process of uranyl samples in the environment. NSD has also conducted particulate matter collection campaigns from different U-based sources. Particulate collections were made during campaigns dedicated to the detonation of devices with depleted uranium, U-bearing compounds from conversion and enrichment plants and other facilities dedicated to the production of materials from the nuclear fuel cycle. Our collections have resulted in the identification of unique signatures from different processes.

Similarly, pre-screening of environmental samples for anthropogenic uranium and fluoride compounds is important in order to identify proliferation activities. The hydrolysis of UF_6 results in the formation of UO_2F_2 and its aged products. Luminescence of the environmental soil matrix overwhelms the spectroscopic signals of interest originating from the anthropogenic compounds. The weak spontaneous Raman scattering signal requires long integration times for analysis and is one of the major limiting factors of large-scale sample analysis. Ultrafast lasers have opened new doors in research to enhance detection sensitivity. The expected several orders of signal enhancement (i.e. up to 10^6 orders of magnitude)[1] with advanced, nonlinear spectroscopic techniques are a game changer for detection of chemical species related to proliferation activities.

The recent acquisition of femtosecond and picosecond lasers, a deep ultraviolet laser and an ultrafast-gated imager for picosecond Raman spectroscopy has opened the door to conduct advanced linear and nonlinear spectroscopic research. Currently, the laser systems helped to secure additional funding from DOE NA-22 to study plutonium particulates. The laser systems are also being used in different research projects funded by DOE NA-22 and LDRD programs. One goal of the current LDRD project is to demonstrate remote detection of U-bearing compounds in soil samples using Stimulated Raman Scattering (SRS) and Coherent Anti-Stokes Raman Scattering (CARS) in a standoff configuration, which has successfully been shown in literature for the detection of explosive residues.[2] Data from this project will be used to write new work with NA-22 for improved detection sensitivity for U and Pu. In another project, a gated imager will be used to gate Raman scattering from particulates generated from laser ablation of targets within a 300 picosecond window, therefore eliminating/reducing the strong luminescent background interfering with the signal of interest. We are also exploring CARS to identify microscopic particles embedded in bulk material and in airborne material. These projects are providing technological seeds to grow a core capability within the DOE weapons complex that will facilitate increased ROI through future proposals to other government agencies.

APPROACH

Our research approach for this LDRD includes completing the assembly and installation of an ultrafast Ti:Sapphire laser system with modules for an optical parametric amplifier (OPA) to access the infrared to the deep ultraviolet spectral regions. Following installation of the ultrafast laser system, advanced Raman methodologies will be developed (i.e. stimulated Raman scattering (SRS) and coherent anti-Stokes Raman scattering (CARS)) to measure and analyze samples of interest (i.e. nuclear fuel cycle materials), processes shown in Figure 1. Additionally, software will be written to manipulate the energy (spectral regime) and temporal properties of a femtosecond laser pulse with a spatial light modulator (SLM).[3] We will then demonstrate detection of particles of interest in soil samples, as well as detection of samples up to 5 meters away. Other spectroscopic and material processing applications will also be conducted and demonstrated, including surface modification through laser desorption and ablation, chemical characterization within the desorbed material pulse, hydrogen and deuterium detection, etc.

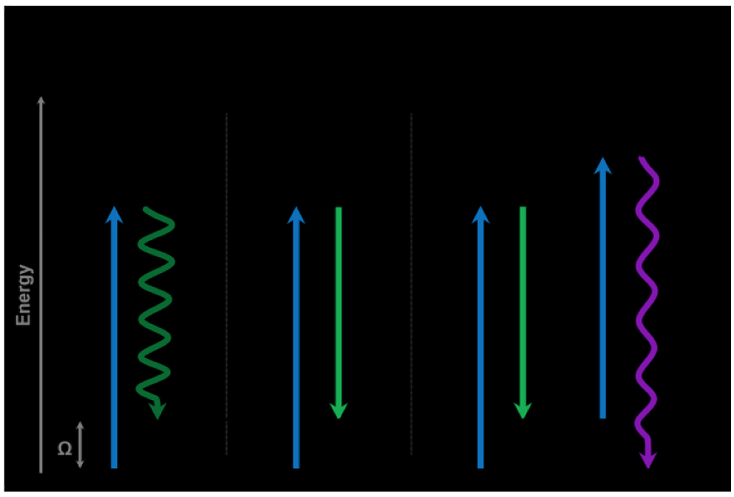

Figure 1. Schematic energy level diagrams for Raman processes

RESULTS/DISCUSSION

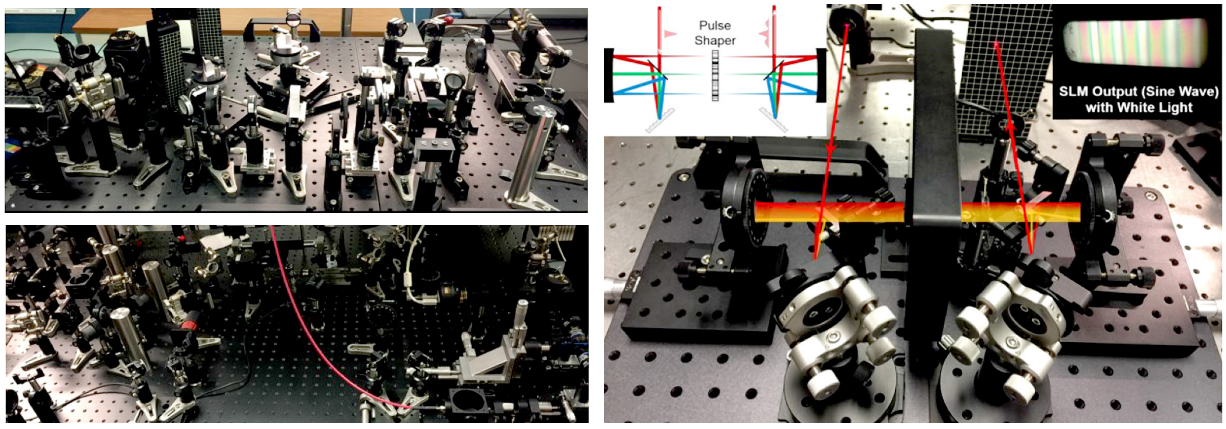

Figure 2. Experimental setups of stimulated Raman scattering **(top left)**, coherent anti-Stokes Raman scattering **(bottom left)** and quantum coherent control **(above right)**

The Astrella ultrafast Ti:Sapphire laser from Coherent that produces <35 fs pulses at >7 mJ/pulse at a repetition rate of 1 kHz and an optical parametric amplifier (OPA), the OPerA Solo from Coherent that extends the wavelength range from 190 nm to 20 μm were both installed in the National Security Directorate laser laboratory in March 2017. However, the laser system has been "down" following installation due to defective internal components of the laser system. These multiple components within the laser system need to be replaced by Coherent, but these components may not be available for installation until 2018.

Advanced, nonlinear Raman spectroscopy setups were assembled, which included coherent anti-Stokes scattering, stimulated Raman scattering and quantum coherent control, shown in Figure 2. An optical microscope setup was designed and built to couple laser light to our samples of interest. Software to control the dual-mask transmission SLM was written and tested to control both the phase and amplitude of laser pulses within the spectral range of 488-900 nm, for quantum coherent control.

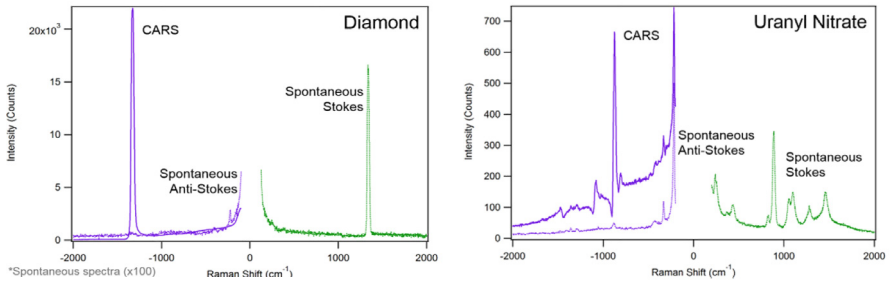

Figure 3. Coherent anti-Stokes Raman scattering, spontaneous Stokes and anti-Stokes spectra of **(adjacent left)** diamond, and **(adjacent right)** uranyl nitrate

Figure 4. (below) Coherent anti-Stokes Raman scattering and spontaneous Stokes spectra of plastic

Various liquid and solid samples were analyzed with advanced, nonlinear Raman techniques. The measured CARS and spontaneous Raman spectra of diamond and uranyl nitrate are shown in the left and right of Figure 3, respectively. Plastic was also successfully measured with CARS and spontaneous Raman in Figure 4. The signal enhancements we were able to achieve with the advanced, nonlinear Raman techniques exceeded three orders of magnitude enhancement compared to spontaneous Raman.

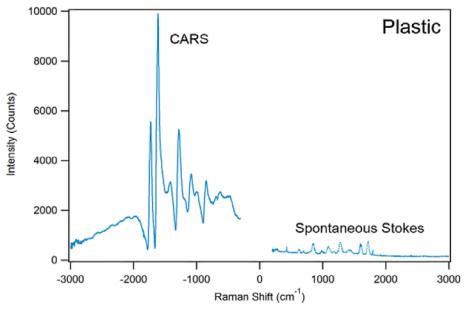

FY2017 ACCOMPLISHMENTS

- The Astrella ultrafast laser (<35 fs at >7 mJ/ pulse and 1 kHz) and an optical parametric amplifier(OPA) covering the 190 nm to 20 µm spectral range were delivered at the end of FY16 and were installed in March 2017. Following laser installation, the laser system was "down" until the end of August 2017 due to components in the system needing replacement once available from Coherent.
- Software was written and tested to control the transmission SLM (CRi SLM-128-D-VN,Meadowlark Optics) that has a dual-mask configuration for simultaneous phase and amplitudepulse shaping (spectral range of 488-900 nm).
- Completed designing and building an optical microscope setup to couple laser light to our samples of interest.
- Measured various solid and liquid samples with advanced Raman techniques, including Uranium-bearing compounds and plastics.
- Signal enhancement >3 orders of magnitude using advanced Raman techniques.

FUTURE DIRECTIONS

- Demonstrate detection of samples up to 5 meters away.
- New technologies developed during this project have the potential to lead to applications in the fields of chemical detection via remote sensing, material characterization, surface decomposition, isotropic composition, etc.

REFERENCES

1. D. W. McCamant, P. Kukura and R. A. Mathies, "Femtosecond Broadband Stimulated Raman: A NewApproach for High-Performance Vibrational Spectroscopy," *Appl. Spectrosc.,* vol. 57, pp. 1317-1323, 2003.

2. M. T. Bremer and M. Dantus, "Standoff Explosives Trace Detection and Imaging by Selective Stimulated Raman Scattering," Appl. Phys. Lett., vol. 103, pp. 061119, 2013.

3. Y. Silberberg, "Quantum Coherent Control for Nonlinear Spectroscopy and Microscopy," *Annu. Rev.Phys. Chem.,* vol. 60, pp. 277-292, 2009.

ACRONYMS

CARS	Coherent Anti-Stokes Raman Scattering
fs	femtosecond
mJ	milli-Joule
NSD	National Security Directorate
OPA	Optical Parametric Amplifier
ROI	Return on Investment
SLM	Spatial Light Modulator
SRS	Stimulated Raman Scattering
U	Uranium

CHARACTERIZATION OF ENVIRONMENTALLY INDUCED CHEMICAL TRANSFORMATIONS OF URANIUM TETRAFLUORIDE

Project Team: M.S. Wellons, M.A. DeVore II, E. Villa-Aleman, R. M. Rogers, J. T. Hewitt

Collaborators: C. Klug (NRL), J. B. Felder (USC), H. zur Loye (USC), T. L. Williamson (LANL), T. J. Tenner (LANL), L.A. Giannuzzi (L.A. Giannuzzi & Associates LLC)

Thrust Area: National Security

Project Type: Standard

Project Start Date: 10/1/15

Project End Date: 9/30/17

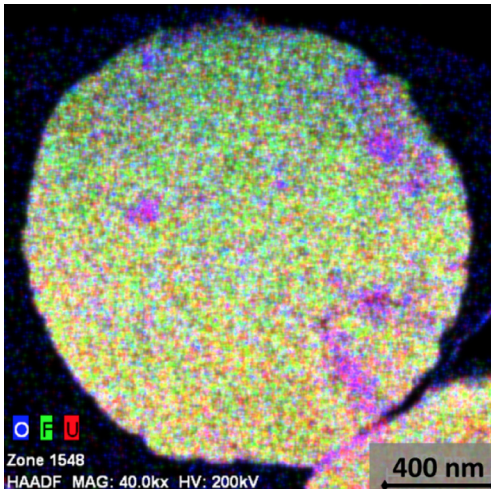

RIGHT: TEM/EDS tricolor composite elemental map of a partially hydrated UF_4 lamella specimen for U, O, and F

Advanced characterization techniques were used to probe the complex chemical and microstructural aspects of hydrolyzed uranium tetrafluoride (UF_4). The effort utilized methods such as electron energy loss spectroscopy (EELS) coupled to Transmission electron microscopy (TEM) to probe the elemental and chemical speciation of partially hydrolyzed UF_4 at the nanoscale. Micro Raman, Infrared, and fluorescence spectroscopy were utilized to characterize a series of UF_4 hydrate polymorphs to elucidate crystalline structure and spectral relationships. Solid state ^{19}F nuclear magnetic spectroscopy (NMR) was initiated to characterize the macroscale hydrolysis induced chemical changes and attempt characterization of bulk scale kinetics. The effort has resulted in an enhanced understanding of the U-F systems, their hydrolysis products, and various advanced analytical capabilities which has culminated into one accepted and two in-preparation peer-review publications.

FY2017 OBJECTIVES

TASK ONE

Demonstrate the preparation of lamella from hydrolyzed uranium fluoride specimens by focused ion beam (FIB) preparation and subsequently characterize them via TEM and EELS characterization.

TASK TWO

Characterize UF_4 hydrolysis kinetics via solid state ^{19}F NMR spectroscopy.

TASK THREE

Characterize a series of UF_4 hydrate polymorphs via Raman, Infrared, and fluorescence spectroscopy to probe chemical and structural phenomena.

TASK FOUR

Determine suitability of secondary ion mass spectrometry methods for characterization of U-O-F solids related hydrolysis products.

INTRODUCTION

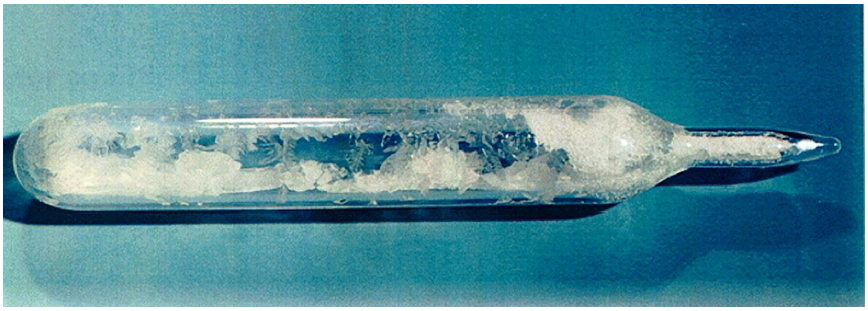

UF_6 in a glass ampoule

The chemistry of uranium fluorides is of continued interest due the relevance within chemical processing for the nuclear fuel cycle and related environmental concerns.[1-3] The two common uranium fluorides (UF_6 and UF_4) are ubiquitous within the nuclear fuel cycle as various chemical feedstocks and intermediates. However characterization of actinide fluorides has typically favored the fully oxidized +6 complex (UF_6) due to the relevance as the uranium enrichment feedstock within various nuclear enterprises.[3-5] As such UF_6 has been extensively studied both within the context of chemistry and chemical engineering; with recent focus on the hydrolysis product, uranyl fluoride, and the synthesis and characterization of various forms of uranyl fluoride hydrates.[6-12] The hydrolysis of the UF_6 is a challenging physical chemistry problem and prior research has typically focused on the reaction products (e.g. uranyl fluorides) and their respective relevance to nuclear safeguards or advanced uranium chemical processing. The corresponding tetrafluoride (U^{4+}) complex has received less study, beyond physical properties and early characterization of hydrolysis products. Uranium tetrafluoride, unlike the hexafluoride, is solid at ambient conditions and relatively chemically inert to oxygen, but does undergo reaction with atmospheric or liquid water.

A family of U^{4+} fluoride hydrates has been identified and characterized with a stoichiometric formula of $UF_4 \cdot xH_2O$; where x includes $^1/_3$, $^4/_3$, 2, and $2^1/_2$. Early efforts were reported in 1942 separately by Khlopin and Gerling, and Khlopin and Yeashenk who claimed to have isolated three U^{4+} hydrates, $UF_4 \cdot xH_2O$ (x = $^1/_2$, 1, and 2), by electrolytic reduction of uranyl fluoride in aqueous hydrofluoric acid; however it was later shown all three were actually $UF_4 \cdot 2H_2O$.[5] Prior to 1969, only three crystal UF_4 hydrates were known and included the monoclinic $UF_4 \cdot {}^4/_3H_2O$, cubic $UF_4 \cdot 2H_2O$, and orthorhombic $UF_4 \cdot 2.5H_2O$.[13] Structural data for the monoclinic $UF_4 \cdot {}^4/_3H_2O$ is not available, but the structure was determined based on powder XRD, optical methods, thermography, and NMR.[14] Structural data for the orthorhombic $UF_4 \cdot 2.5H_2O$ was obtained by single crystal X-ray diffraction but did not appear in the open literature until 1971.[15] The $UF_4 \cdot {}^1/_3H_2O$ was recently synthesized via mild hydrothermal reaction and the crystal structure was determined by single crystal X-ray diffraction.[3] Many of the UF_4 hydrates were synthesized via the reduction of U^{6+}, or suspensions of UF_4 with aqueous hydrofluoric acid.[5,16] Other methods to produce UF_4 hydrates have involved application of thermal energy to liberate structurally bound water from the 2.5 hydrate; however these methods can be complicated by the unintended production of uranyl fluorides ($UO_2F_2 \cdot xH_2O$) and/or uranium oxides (UO_2; U_3O_8).[5,17]

The primary characterization method of prior work has been single crystal and powder X-ray diffraction, although other characterization methods have been utilized, including Infrared (IR) spectroscopy and NMR, those efforts had not unambiguously identified the material crystal structure. The single prior example of IR spectroscopy published for UF_4 hydrates were derived from the thermalization of the 2.5.[17] Proton and ^{19}F NMR measurements were reported on three hydrates in 1969 ($UF_4 \cdot xH_2O$; where x includes $^4/_3$, 2, and $2^1/_2$), but none has been published since and is likely due to the challenges associated with paramagnetic U^{4+} coupling to the proton and fluorine nuclei.[13] A prior effort did attempt to characterize hydrolyzed solid UF_4 via various X-ray spectroscopic methods but due to the surface complexity uranyl fluoride was the only product identified.[18] Within our efforts the UF_4 hydrolysis chemical changes are observed as nano- and micron scale changes in chemical structure of the solids; therefore new analytical approaches are needed to characterize the system.

APPROACH

Our effort focused on both the microanalytical imaging methods and various spectroscopic techniques to characterize the complex structural phenomena with multiple chemical species simultaneously present in UF_4 hydrate systems. Raman, IR, and fluorescence spectroscopy methods were utilized as a means to characterize the bonding and chemical environment within the crystal structure of the three structurally well characterized single species uranium tetrafluoride hydrates. The advanced microanalytical technique TEM/EELS was applied to partially reacted UF_4 specimens to probe chemical-spatial qualities of the material surface and bulk ^{19}F NMR spectroscopy measurements are currently underway to qualify hydrolysis kinetics. Surrogate uranium samples were analyzed by secondary ion mass spectrometry (SIMS) techniques to assess method viability for future characterization of the U-O-F systems. Together the combination of these analytical methods have both advanced understanding of the UF_4 hydrolysis reaction and demonstrated previously untested capabilities for the characterization of uranium-based materials.

RESULTS/DISCUSSION

Prior FY16 efforts had shown multiple uranyl species were generated during the hydrolysis of UF_4; often with some dependence on relative humidity conditions. The primary characterization method used was Raman spectroscopy which identified the species as various uranyl fluorides and hydroxides, and/or uranium oxides; all often collocated within the same region of interest. Recognizing that high resolution methods capable of characterizing these specimen on the nanoscale was required, the FY17 effort prepared partially hydrolyzed UF_4 under a variety of varying humidity conditions and sent to a collaborator for TEM/EELS and TEM/EDS analyses. Test materials were mounted and then milled and polished with a FIB tool to generate thin lamella (<100 nm width) suitable for electron transmission measurements. An example lamella is shown Figure 1 along with the corresponding EELS measurement locations and spectra. The TEM image shows the partially hydrolyzed UF_4 material as a band approximately 500 nm in width at the surface interface with obvious changes in the internal material texture and image contrast consistent with a reaction region. The denoted EELS measurement locations transition from the exterior of the initial particle (#1) to the interior region (#5) and based on EDS mapping (not shown) regions #1-4 contain elevated oxygen content consistent with expected hydrolysis products. The EELS spectra in the low energy loss regime demonstrate both uranium O and P edges which are from electron beam induced electronic transitions from inelastic scattering.[19,20] Relative P_1 and P_{2-3} edged intensity variations are observed between the regions #1-4 and #5 which may be indicative of differing chemical environments for the U atoms. Data analysis is ongoing and a total of six different samples were characterized by TEM/EELS for various U, O, and F edges in the low and intermediate energy loss regimes.

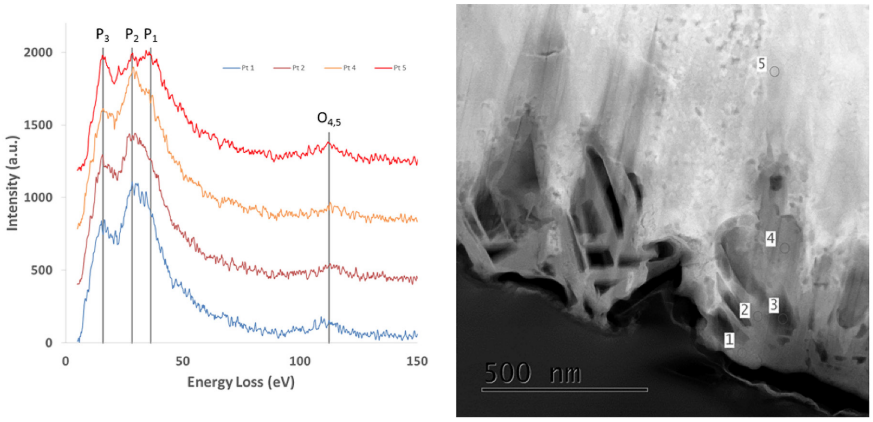

Figure 1. EELS spectra in the low energy loss region with various U transition edges denoted **(left);** TEM image of the lamella analyzed with numerical indicators for the corresponding EELS spectra, location #4 resulted in poor spectra and was omitted **(right)**

Raman, IR, and fluorescence spectra were collected for three different UF_4 hydrate polymorphs (UF_4•$2.5H_2O$, U_3F_{12}•H_2O, and UF_4•$0.33H_2O$) which share some similarities in crystalline structure and interatomic bonding with anhydrous UF_4. The blue-green crystalline UF_4•$2.5H_2O$ was prepared at SRNL via simple hydrolysis of UF_4 with neat water. Two additional hydrates, U_3F_{12}•H_2O and UF_4v$0.33H_2O$, were provide by collaborators at the University of South Carolina and although share similar stoichiometry possess different crystalline structure.[3] Spectral assignment of various vibration and fluorescence bands relied on literature and simple group theory assessments. The team attempted to model the Raman and IR spectra with conventional computational tools but these efforts were not successful; likely due to the currently unresolved theoretical challenges associated with the outer shell electrons of U^{4+}.[21,22] Regardless, some insights into the vibrionic and fluorescent structure for the family of compounds were determined. For example, Figure 2 shows an overall depiction of the 2.5 hydrate showing the interconnectivity of U-F polyhedra, interstitial water bound to the uranium as U-O/F polyhedra, and the presence of free water molecules within channels. Within the IR spectra two peaks are present in the H-O-H bending region (approximately 1600 cm^{-1}) and multiple peaks are present in the O-H stretching regions (> 3000 cm^{-1}); these are consistent with the two forms of water in the crystal structure. Similar analysis of the other hydrates and comparisons between the different crystal systems has resulted in identification of specific spectral features and their corresponding structural components.

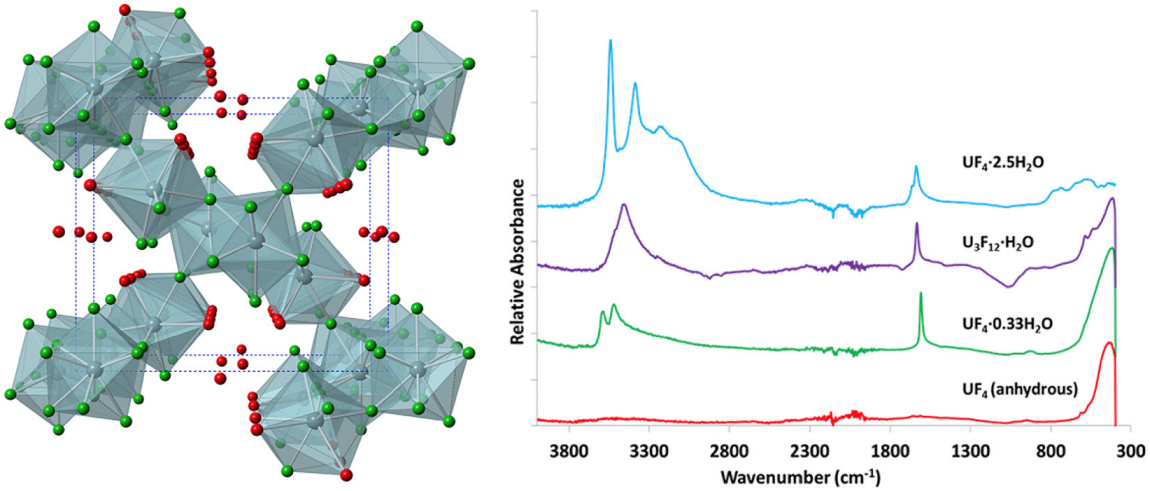

Figure 2. **An overall depiction of the 2.5 hydrate showing the interconnectivity of the chains where uranium are blue, fluorine green, and oxygen red (left); FT-IR spectra of anhydrous UF_4 and the three hydrate polymorphs (right)**

Two additional characterization methods for probing the macro scale elemental content were explored within FY17 and included SIMS and NMR spectroscopy. SRNL prepared uranyl particle test materials and shipped them to a collaborator at Los Alamos National Laboratory for a proof of concept measurement with a SIMS. Although these specimens did not contain fluorine the exercise established sample preparation technique, shipping requirements, and analysis parameters. Additionally the exercise determined that SRNL sample generation capabilities may be suitable for the generation of uranium particulate reference materials. Experiments to characterize the hydrolysis kinetics via ^{19}F NMR were designed and initiated with a collaborator at the Naval Research Laboratory. The NMR experiments were based on the Raman spectroscopy measurements of UF_4 hydrolysis conducted in FY16. The team designed and built a reaction vessel where water vapor pressure was controlled and delivered to unreacted UF_4 within the spectrometer; the equipment and UF_4 powder were delivered and setup in late FY17. Crystalline forms of UF_4•$2.5H_2O$, U_3F_{12}•H_2O, and UF_4•$0.33H_2O$ were also shipped for ^{19}F magic angle spinning (MAS) NMR characterization. Both the kinetics NMR and MAS-NMR measurements are in progress.

FY2017 ACCOMPLISHMENTS

Coupled with the prior FY16 work, this effort has successfully developed an initial chemical and structural basis for understanding UF_4 hydrolysis in the environment.

- Successful demonstration of the advanced characterization technique TEM/EELS to probe the elemental and chemical speciation of partially hydrolyzed UF_4 at the nanoscale
- Solid state ^{19}F NMR was initiated to characterize the macroscale hydrolysis induced chemical changes
- Complete Raman, IR, and fluorescence spectroscopy characterization of a series of UF_4 hydrate polymorphs and interpretation of structural, chemical, and spectral phenomena.
- Successful demonstration of SIMS methods for uranium-bearing particle analysis and a resulting peer review publication

FUTURE DIRECTIONS

Uranium tetrafluoride hydrolysis characterization has demonstrated a complex series of potential reaction pathways and numerous chemically distinct progeny species. Future work includes finalizing data analysis of photon, electron, and NMR spectroscopy measurements for a variety samples, and a new project start focused on uranium particulate reference materials.

- Measurements of UF_4 hydrolysis by ^{19}F NMR and MAS-NMR have begun; data analysis is ongoing
- TEM/EELS have been successfully utilized to characterize UF_4 hydrolysis and oxidation; data analysis is ongoing
- Two publications are currently in progress for the photon based spectroscopy of the UF_4 hydrates, and the TEM/EELS of UF_4 partially hydrated solids
- The effort to assess the applicability of SIMS methods has resulted in new FY18 project at SRNL funded by the Department of Energy, National Nuclear Security Administration

FY2017 PUBLICATIONS/PRESENTATIONS

1. Presentation: "Characterization of Hydrolyzed Uranium Tetrafluoride Solids by Raman Spectroscopy" M. DeVore II, M. Wellons, M. Summer, R. Smith, T. Daroudi, October Tech Talk, October 11, 2016w

2. Presentation: Wellons, M.S.; DeVore II, M. A.; Rogers, R. A.; Hewitt, J. T, Williamson, T. L.; Tenner, T. J.; Darroudi, T. "Practical Utilization of Uranium-Containing Particulate Test Samples for SEM/EDS and SIMS Automated Particle Analysis Method Validation", Microscopy and Microanalysis 2017 Conference, St Louis MO, August 2017

3. Publication: Wellons, M.S.; DeVore II, M. A.; Rogers, R. A.; Hewitt, J. T, Williamson, T. L.; Tenner, T. J.; Darroudi, T. "Practical Utilization of Uranium-Containing Particulate Test Samples for SEM/EDS and SIMS Automated Particle Analysis Method Validation", Microsc. Microanal. 23 (Suppl 1), Microscopy Society of America 2017

4. Publication: Wellons, M. S.; DeVore II, M. A.; Villa-Aleman, E.; zur Loye, H.; Felder, J. "The Raman and IR Spectroscopy of Uranium Tetrafluoride Hydrates", *in preparation.*

5. Publication: Wellons, M. S.; DeVore II, M. A.; Giannuzzi, G. A. "Transmission Electron Microscopy and Electron Energy Loss Spectroscopy of Partially Hydrated Uranium Tetrafluorides", *in preparation.*

REFERENCES

1. Gorden, A. E. V.; DeVore, M. A.; Maynard, B. A. Inorganic Chemistry **2013**, 52, 3445.
2. Maynard, B. A.; Lynn, K. S.; Sykora, R. E.; Gorden, A. E. V. Inorganic Chemistry **2013,** 52.
3. Yeon, J. S., Mark D.; Sefat, Athena, S.; Tran, T. Thao; Halasyamani, P. Shiv; Zur Loye, Hans-Conrad Inorganic Chemistry **2013,** 52, 8303.
4. Villa-Aleman, E., Wellons, M.S. Journal of Raman Spectroscopy **2016,** 47, 865.
5. Dawson, J. K.; D'Eye, R. W. M.; Truswell, A. E. Journal of the Chemical Society (Resumed) **1954,** 3922.
6. Stefaniak, E. A.; Darchuk, L.; Sapundjiev, D.; Kips, R.; Aregbe, Y.; Grieken, R. V. Journal of Molecular Structure **2013,** 1040, 206.
7. Kips, R.; Pidduck, A. J.; Houlton, M. R.; Leenaers, A.; Mace, J. D.; Marie, O.; Pointurier, F.; Stefaniak, E. A.; Taylor, P. D. P.; Van den Berghe, S.; Van Espen, P.; Van Grieken, R.; Wellum, R. Spectrochimica Acta Part B: Atomic Spectroscopy **2009,** 64, 199.
8. Carter, J. A.; Hembree, D. M. J.; Energy, D. o., Ed. Oak Ridge, 1998.
9. Miskowiec, A.; Anderson, B. B.; Huq, A.; Mamontov, E.; Herwig, K. W.; Trowbridge, L.; Rondinone, A. Molecular Physics **2016,** 114, 61.
10. Miskowiec, A., Kirkegaard, M.C., Herwig, K.W., Trowbridge, L., Mamontov, E., Anderson, B. Journal of Applied Physics **2016,** 119.
11. Miskowiec, A., Kirkegaard, M.C., Huq, A., Mamontov, E., Herwig, K.W., Trowbridge, L., Rondinone, A., Anderson, B. J. Phys. Chem. A. **2015,** 119, 11900.
12. Wagner, G. L., Kinkead, S.A., Paffett, M.T., Rector, K.D., Scott, B.L., Tamasi, A.L., Wilkerson, M.P. Journal of Fluorine Chemistry **2015,** 178, 107.
13. Gabuda, S. P. M., A.A.; Zadneprovskii, G.M. Zhurnal Struknumoi Khimii **1969,** 10, 1115.
14. Gagarinskii, Y. V. K., E.I.; Galkin, N.P.; Anan'eva, L.A.; Gabuda, S.P Atomnaya Energiya **1965,** 18, 40.
15. Zadneprovskii, G. M. B., S.V. Zhurnal Struknumoi Khimii **1971,** 12, 831.
16. Katz, J. J.; Rabinowitch, E. The Chemistry of Uranium; Dover Publications, Inc.: New York, **1973.**
17. Khanaev, E. I.; Teterin, E. G.; Luk'yanova, L. A. Journal of Applied Spectroscopy **1967,** 6, 533.
18. Tobin, J. G.; Duffin, A. M.; Yu, S. W.; Qiao, R.; Yang, W. L.; Booth, C. H.; Shuh, D. K. Journal of Vacuum Science & Technology A: Vacuum, Surfaces, and Films **2017,** 35, 03E108.
19. Degueldre, C.; Schaeublin, R.; Krbanjevic, J.; Minikus, E. Talanta **2013,** 106, 408.
20. Degueldre, C.; Alekseev, E. V. Radiat. Phys. Chem. **2015,** 108, 7.
21. Pantazis, D. A.; Neese, F. J. Chem. Theory Comput. **2011,** 7, 677.
22. Dolg, M.; Cao, X. Chem. Rev. (Washington, DC, U. S.) **2012,** 112, 403.

ACRONYMS

EDS	Electron Dispersive Spectroscopy
EELS	Electron Energy Loss Spectroscopy
FIB	Focused Ion Beam
MAS-NMR	Magic Angle Spinning Nuclear Magnetic Resonance
NMR	Nuclear Magnetic Resonance
XRD	X-Ray Diffraction
RH	Relative Humidity
SEM	Scanning Electron Microscopy
SIMS	Secondary Ion Mass Spectrometry
TEM	Transmission Electron Microscopy

TOTAL NUMBER OF POST-DOCTORAL RESEARCHERS

Two
1. Dr. Michael Devore II and
2. Dr. Robert Rogers

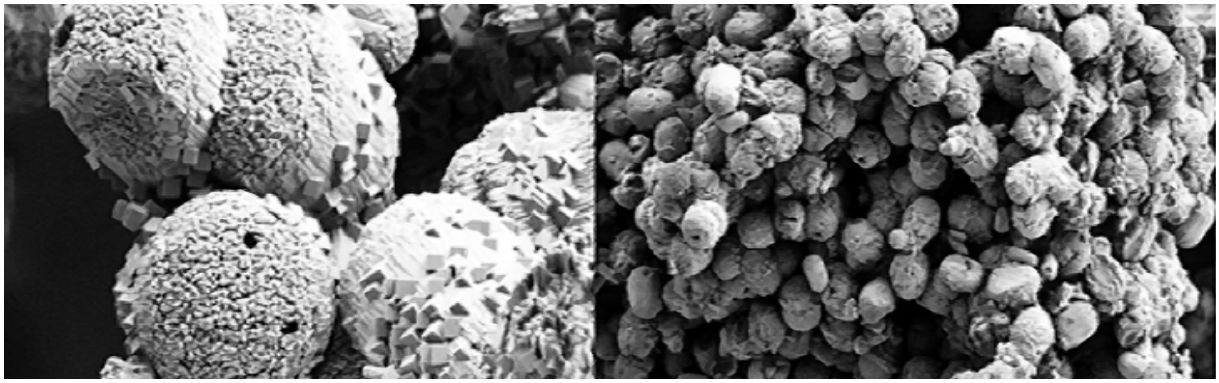

SYNTHESIS OF ZEOLITE MATERIALS FOR NOBLE GAS SEPARATION

Project Team: Randall Achey, Omar Rivera-Betancourt, Matthew Wellons, Douglas Hunter (SRNL), Christopher Klug (NRL)

Subcontractor: MPO interagency agreement (IAA) with NRL

Thrust Area: National Security

Project Type: Standard

Project Start Date: 10/1/15

Project End Date: 9/30/17

Microporous zeolite adsorbent materials are widely used as a medium for separating gases. SRNL is currently the leader in using zeolites for noble gas sampling for non-proliferation detection platforms. However, there is a constant customer need for improved noble gas sampling capabilities. The zeolites that are currently used for noble gas separation have been characterized to understand which properties are most important for noble gas separation. This knowledge was used to develop improved zeolites which will allow the building of a new generation of noble gas samplers.

FY2017 OBJECTIVES

TASK ONE
Microwave-assisted and conventional hydrothermal synthesis will be used to make a variety of zeolites tailored for noble gas separation.

TASK TWO
Boronation modifications will be tested on commercial materials and synthesized materials for fine-tuning of pore size and adsorption properties

TASK THREE
Currently used zeolites will be characterized using gas sorption analysis, SEM, XRD and NMR spectroscopy

TASK FOUR
Candidate materials will be down-selected based on highest available surface area, maximum overall capacity for gas adsorption and best selectivity for noble gases (or optimum exclusion of noble gases)

INTRODUCTION

Advances in analytical techniques and the science of zeolites since the development of zeolites that are currently used at SRNL for noble gas sampling give the opportunity to improve the understanding of how zeolites separate noble gases from air and open the door to the synthesis of better zeolites. Characterization data collected in the project has been used to help guide the synthesis of these new materials. Microwave-assisted and conventional hydrothermal synthesis has been used to make a variety of zeolites tailored for noble gas separation. Characterization data collected in the project has been used to help guide the synthesis of these new materials. A thorough understanding of the properties of the existing zeolites has been gained through characterization of the materials with XRD, SEM, and gas sorption analysis. Such characterization has revealed which properties of our zeolite materials are most important for separating noble gases from air. Custom engineered zeolites have been synthesized from raw materials with chemistry designed to give optimal adsorption characteristics and pore structure that are best for noble gas separations while maintaining robust mechanical properties and hydrothermal stability. Post-synthesis modification of the zeolites has been tested with boronation to fine tune the sorption characteristics. Full characterization of the synthesized materials has been used to determine the suitability of the synthesized zeolites for noble gas separation as well as compare their properties with the existing materials.

APPROACH

There are several zeolite materials that are currently used at SRNL for noble gas sampling. These zeolites were developed many years ago. They have a proven record of consistent and reliable performance. These zeolites are used in two different ways: one time grab sampling and continuous concentration. The grab sampling method relies on capture of the noble gas by the zeolite, while the continuous concentration method uses zeolites that exclude noble gases and adsorb the other gases in air. As part of this project, zeolites have been synthesized and/or modified to give improved performance in both sampling methods. For the continuous concentration sampling zeolite, materials were synthesized with the aim of improving size exclusion of noble gases from the pores, and the composition of the zeolite surface was designed to increase the heat of adsorption for nitrogen and oxygen to give better separation and higher capacity **(1-3).** Microwave assisted and conventional hydrothermal synthesis of zeolites from raw materials was used to prepare the materials **(4-6)** (Figure 1).

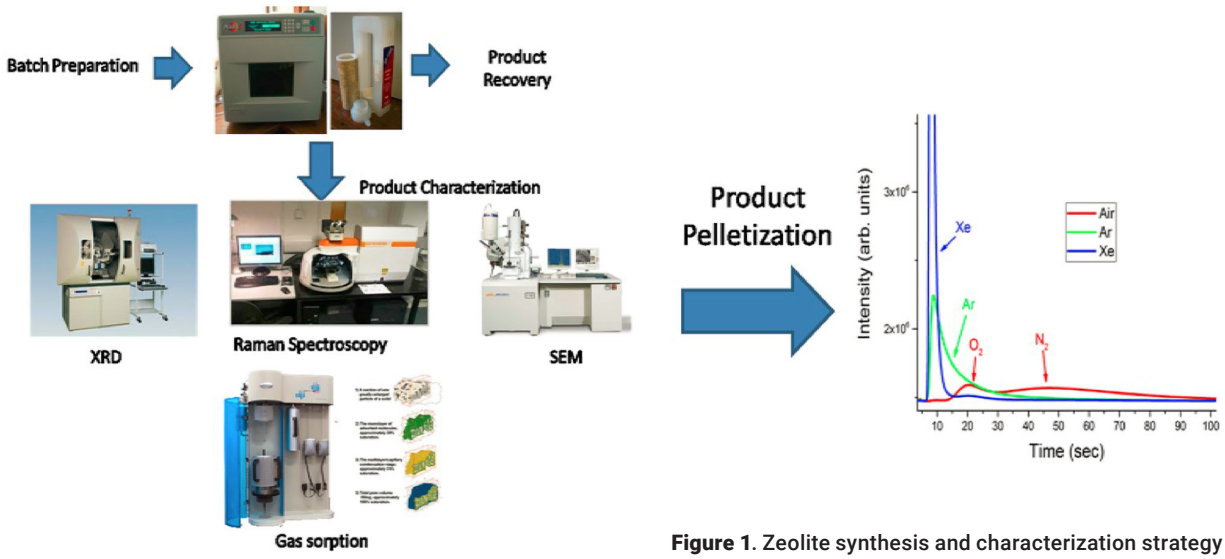

Figure 1. Zeolite synthesis and characterization strategy

Zeolite synthesis was performed at SRNL. Samples synthesized include mordenite, Linde type F, Linde type L, offretite, chabazite, faujasite and EMC-2. Powder X-ray diffraction crystallography (XRD), scanning electron microscopy (SEM), Raman spectroscopy, gas sorption analysis and nuclear magnetic resonance (NMR) spectroscopy were used for zeolite characterization. SEM has revealed crystal morphology for the different types of mordenites and offretites we have synthesized so far. XRD was used to determine the type of zeolite synthesized based on comparing the diffraction pattern of the powder sample with a reference library of diffraction patterns for known zeolite materials. Solid-state NMR analysis gave information on bonding environments of various elements in the crystal lattice. ^{27}Al and ^{29}Si NMR analysis has been performed on several custom engineered zeolites as well as commercially available products. Candidate materials have been down-selected based on highest available surface area, maximum overall capacity for gas adsorption and best selectivity for noble gases (or optimum exclusion of noble gases).

RESULTS/DISCUSSION

Currently used zeolites have been characterized using gas sorption analysis, SEM, XRD and NMR spectroscopy. Characterization and trial modifications of commercial zeolites have been performed. Syntheses of known zeolites and variations on zeolite recipes have been performed using microwave and conventional oven hydrothermal synthesis. We have performed syntheses of the following compounds: offretite, chabazite, faujasite, mordenite, Linde type F, Linde type L and EMC-2. A series of mordenite samples were sent to NRL to be analyzed through solid state NMR. All NMR spectra were obtained using a Varian NMR500 spectrometer operating at a magnetic field strength of 11.7 T where the ^{27}Al and ^{29}Si resonance frequencies were roughly 130.3 and 99.4 MHz, respectively. A 4 mm triple resonance magic angle spinning (MAS) NMR probe was used for all experiments and samples were loaded into the 4 mm rotors under ambient conditions. The typical sample mass was 50 mg. For the ^{27}Al MAS NMR spectra the spinning frequency was 12.5 kHz and a simple single-pulse excitation was used where the pulse length was 1 μs and the wait time between scans was 4 s. For the ^{29}Si MAS NMR spectra the spinning frequency was 10 kHz and rotor-synchronized Hahn spin echoes with proton decoupling were used with π/2 and π pulse lengths of 5 and 10 μs, respectively, and a delay between scans of 64 s. Chemical shifts were referenced to $AlCl_3$ (aq) and tetramethylsilane for ^{27}Al and ^{29}Si, respectively.

Initially variations on a mordenite synthesis were performed at 190 °C for five days in a Teflon lined pressure vessel within a conventional heating oven. To improve the synthesis, microwave heating was used in order to reduce the time of the reaction and increase sample purity. This reaction was performed by transferring the reaction mixture into a Teflon lined vessel and then heating in a microwave at a temperature of 220 °C. The purpose of this first set of syntheses was to study how long it takes to obtain a pure product tailored for our purposes. The microwave reactions were run at time lapses of five hours. After one lapse had passed an aliquot of the sample was removed, then the same process was repeated every five hours. The reaction concludes at the thirty hour mark. Figure 2 shows the ^{29}Si and ^{27}Al NMR spectra of the mordenite aliquots extracted every five hours (5). ^{27}Al and ^{29}Si MAS NMR spectra were obtained for mordenite samples synthesized in the microwave with reaction times of 10, 15, 20 and 30 hours. The masses of sample used for the NMR experiments were 43.6, 55.3, 66.0 and 65.7 mg, respectively. Each sample showed a single strong ^{27}Al peak around 55 ppm with spinning sidebands. The 10 hour (Figure 2A) mordenite sample showed weak spinning sidebands, which implies a high degree of amorphous environment for the ^{27}Al, while the other three mordenite samples showed strong spinning sidebands, indicating a high degree of crystallinity. The chemical shift value is consistent with tetrahedrally coordinated aluminum with four bridging bonds through oxygen to silicon, which shows that the aluminum detected is incorporated into the zeolite framework. A small peak around 0 ppm, corresponding to octahedrally coordinated aluminum, implies that there is little extra-framework aluminum, though it is possible that some extra-framework aluminum could have an NMR peak broadened so much as to escape detection.

The ^{29}Si spectra are similar for each sample, showing three overlapping peaks. The strongest peak around -112 ppm corresponds to silicon with no bridging bonds (Si-O-Al) to aluminum. The second peak around -105 ppm, roughly half the intensity of the first, is from silicon with one bridging bond through oxygen to aluminum. The weakest peak at -97 ppm is from silicon with two bridging bonds to aluminum.

A different study focused on mordenite microwave synthesis at temperatures ranging from 170-220 °C. All reactions were completed in under 3 hours. A few milligrams of mordenite powder was added as a seed, CBV10ADS from Zeolyst Corporation, to catalyze the rate of growth of the synthesized mordenite. Figure 3 shows the ^{29}Si MAS NMR spectra obtained for synthesized mordenites where there is a clear evolution from a broad peak to a spectrum dominated by peaks at -106 ppm and -112 ppm corresponding to $Si(OAl)(OSi)_3$ and $Si(OSi)_4$ respectively. The spectrum of the 180 °C sample has much broader lines, indicating a poorly crystallized sample, while there are considerably narrower peaks for the 190, 200 and 210 °C samples. The Si/Al ratio of the samples appears to increase (lower intensity of the peak at -106 ppm relative to the peak at -112 ppm) as the reaction temperature increases and the crystallinity of the sample improves, i.e. as the reaction moves further to completion. The signal as a function of delay between scans was fit to a stretched exponential indicative of a distribution: initially T_1~160 s and stretching exponent ~0.5, but gradually the T_1 shortened to ~40 s while the stretching exponential increased to ~0.7 (7-13).

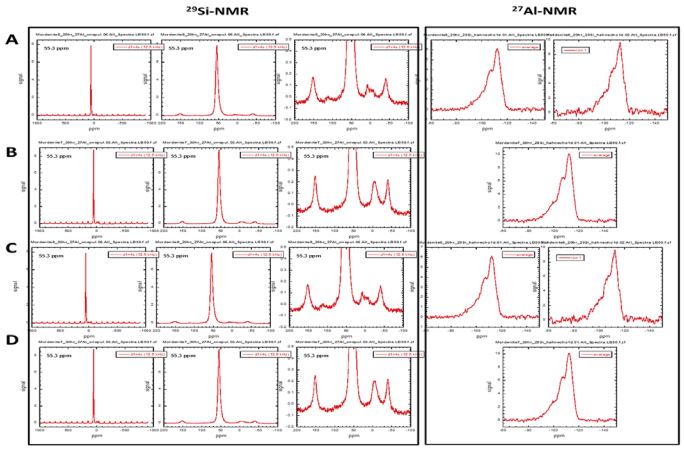

Table 2. (above) ^{29}Si MAS NMR and ^{27}Al MAS NMR spectra for mordenites synthesized for reaction times of **(A)** 10 hours, **(B)** 15 hours, **(C)** 20 hours and **(D)** 30 hours. The spectra were obtained using a spinning speed of 12.5 kHz.

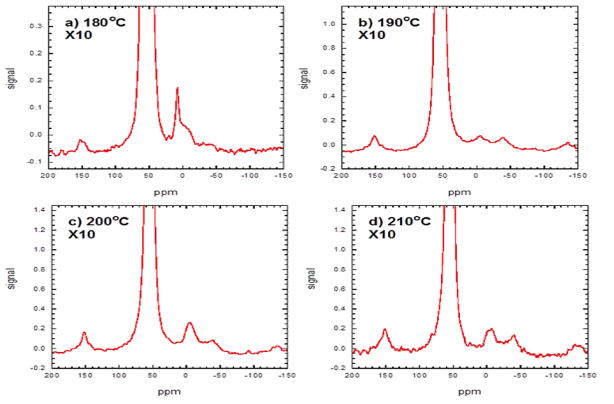

Table 3. (above left) ^{27}Al MAS NMR spectrum for synthesized mordenites with masses of **a)** 50.3 mg, **b)** 39.4 mg, **c)** 49.6 mg, **d)** 50.5 mg. The spectra were obtained using a spinning speed of 12.5 kHz. A single pulse of 0.8 s was used to excite the spins, with a wait time between scans of 2.0 s and a total of 256 scans

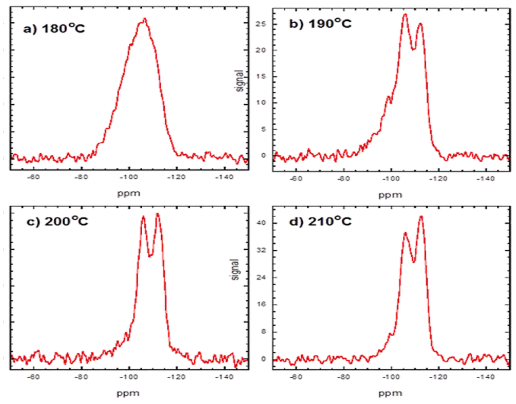

Table 4. (above right) ^{29}Si MAS NMR spectrum for synthesized mordenites with masses of **a)** 50.3 mg, **b)** 39.4 mg, **c)** 49.6 mg, **d)** 50.5 mg. The spectra were obtained using a spinning speed of 12.5 kHz. A spin echo pulse sequence with pulses of length 2.5 s and 5.0 s was used to excite the spins, with a wait time between scans of 512 s and a total of **a)** 192 scans, **b)** 96 scans, **c)** 32 scans, **d)** 96 scans

Microwave synthesis of the zeolite offretite **(14)** was performed at temperatures of 140-180 °C. Seen in Figure 5 are XRD scans and SEM micrographs of the syntheses of offretite at 160 °C. We employed microwave heating in order to reduce the time of the reaction and increase sample purity. The reaction was performed by transferring the reaction mixture into a Teflon-lined vessel and heating in a microwave to temperature for a specified reaction time. The purpose of this first set of syntheses was to study how long it takes to obtain a pure product tailored for our purposes. The microwave reactions were run at time lapses of five hours. After one lapse had passed we removed an aliquot of the sample to be characterized by XRD. As seen on the left panel of Figure 5, from the XRD, we reached the conclusion that the sample reached its highest degree of crystallinity at approximately 20 hours of the reaction. At this reaction time the diffraction pattern peaks reached maximum intensity. The XRD results obtained experimentally were compared to a database managed by the ICDD. All XRD peaks matched with those registered for offretite **(15).** The SEM images from (A) to (C) show a progression of the morphology of offretite. The structures are composed of long cylinders of porous fibrous type structures. At higher synthesis times, Figure 5 (D) and (E), we see the formation of the fibrous type structures taking more of a conglomerate dome structure with a high degree of porosity.

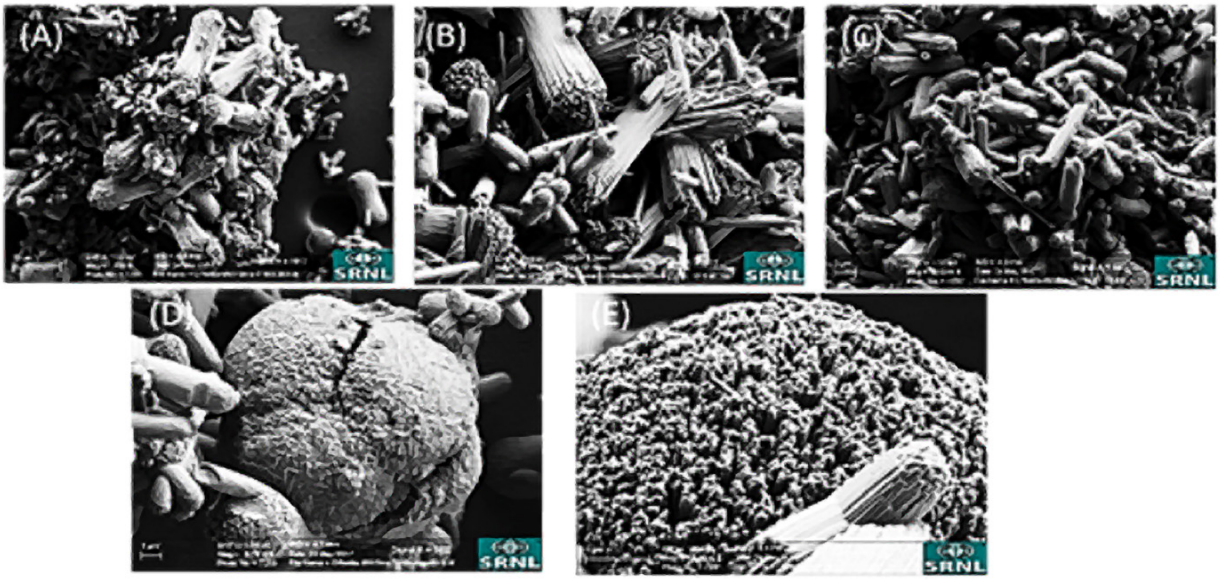

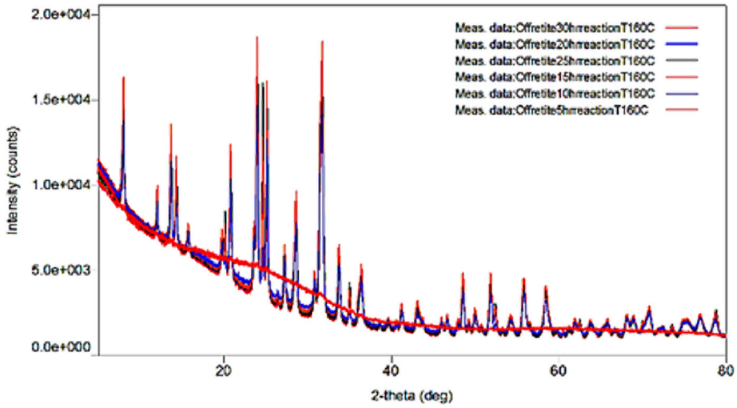

Figure 5. XRD scans of offretite (left) and SEM micrographs of offretite (right) synthesized at different reaction times. The right panel represents the SEM micrographs of offretite **(A)** 10 hours, **(B)** 15 hours, **(C)** 20 hours, **(D)** 25 hours and **(E)** 30 hours.

The nitrogen adsorption isotherms for offretite synthesized at three different times are shown in Figure 6A. Nitrogen adsorption isotherms of all the offretite samples synthesized showed type IV(b) isotherms in accordance with the latest IUPAC classification.(16) It indicates that for all samples, the initial steep increase in volume adsorbed at low relative pressure (p/p_0)<0.02 is ascribed to the monolayer-multilayer adsorption. The second uptake of nitrogen close to the saturation pressure via a multilayer adsorption indicates the presence of mesoporosity by condensation of nitrogen in the pores. Analysis of the adsorption isotherms of the offretite samples synthesized by microwave heating at treatment of 15 hours to 25 hours reveal that the surface area of the samples is 147 m^2/g, 220 m^2/g, and 410 m^2/g, respectively, as seen in Table 1. The increase of the surface area shows the increase in the number of adsorption sites and sample crystallinity when the microwave reaction time was prolonged. The enhancement of crystallinity leads to a lower probability of aggregate formation and the minimization of amorphous phases. It was noticed as well that the micropore volume increases when the samples are exposed to longer microwave reaction times, which suggests that porosity between the particles decreased at longer synthesis times (17). A separate study was performed by leaving the reaction mixture aging from one day to 5 days prior to microwave heating treatment. The best results were obtained with samples aged for one day prior to microwave heating treatment. There was an increase in surface area when the sample was aged for one day versus a reaction at the same temperature with no aging, as seen in Table 2. Offretite was also synthesized at different temperatures at a fixed reaction time with the reaction mixture aged for one day. For the samples aged one day, an increase in specific adsorption volume and microporous volume with increasing reaction time up to 20 hours was seen, as shown in Table 2. Those trends also indicate an increase in the number of adsorption sites and sample crystallinity when the microwave heating time was increased.

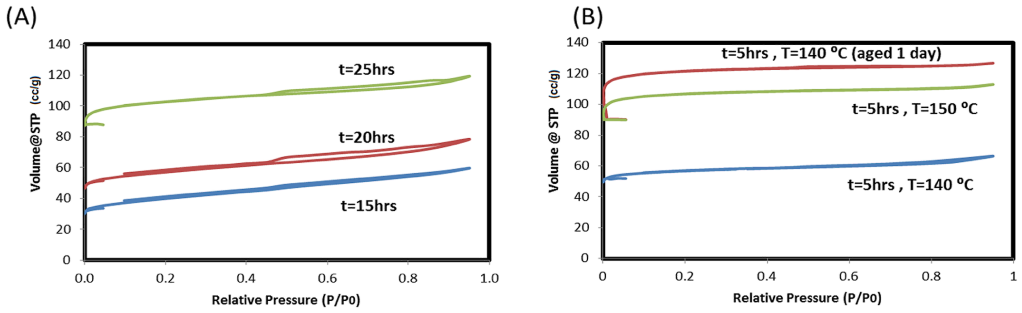

Figure 6. Gas sorption isotherms of offretite: **(A)** synthesized in the microwave at a temperature of 160 °C with varying reaction time, **(B)** reaction mixture aged for one day prior to microwave synthesis for five hours at different temperatures.

Gas Sorption Experiments-Microwave synthesis at T=160 °C			
Zeolite-Offretite	**Surface Area (m^2/g)**	**Pore Volume (cc/g)(DFT)**	**Average Pore Size (Å)**
t=15 hr	147.123	0.081	9.37
t=20 hr	219.559	0.107	8.65
t=25 hr	410.443	0.166	8.03
t=30 hr	361.799	0.142	7.96

Table 1. Gas sorption analysis results of offretite synthesized at 160 °C at different microwave heat treatment times

Gas Sorption Experiments-Microwave synthesis at T=150 °C (aged for 1 day)			
Zeolite-Offretite	**Surface Area (m^2/g)**	**Pore Volume (cc/g)(DFT)**	**Average Pore Size (Å)**
t=5 hr	433.998	0.161	7.72
t=10 hr	487.003	0.197	7.74
t=15hr	468.051	0.196	7.84
t=20hr	475.604	0.221	8.21

Table 2. Gas sorption analysis results of offretite synthesized at 150 °C, with the sample batch aged 1 day prior to microwave heating

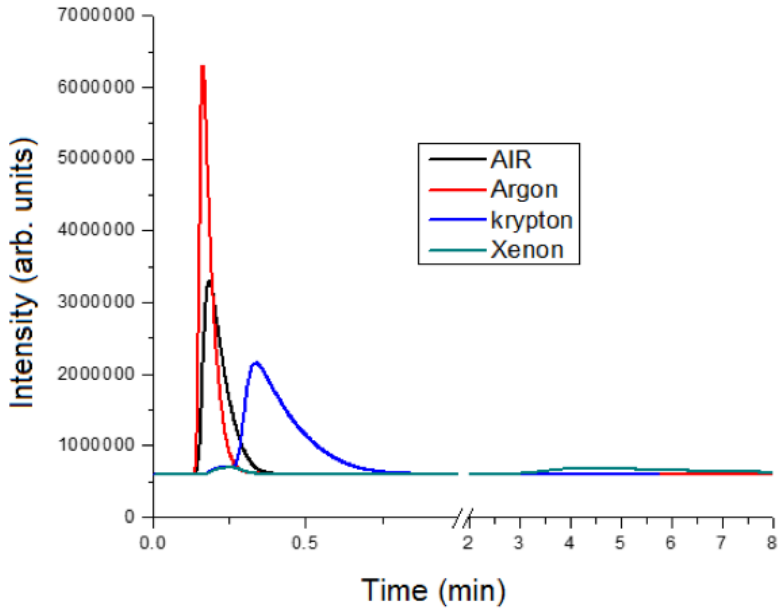

Figure 7. Chromatograms of various gases on column made with offretite 20 hr reaction at 160 °C

Chromatographic testing was performed on synthesized offretite samples. Figure 7 shows chromatograms of air, argon, krypton and xenon on a column made with an offretite sample synthesized for 20 hours at 160 °C. The offretite zeolite samples show promising separation of krypton and xenon. Based on the performance of the samples in gas sorption and gas chromatographic separation experiments, offretite samples have been selected as the best candidate for pelletization and testing in separation systems. Due to having the best crystallographic structure results from XRD analysis, as well as crystallinity and sample purity from NMR analysis, synthesized Linde Type F and mordenite samples are the next most likely candidate samples for pelletization and separation testing.

FY2017 ACCOMPLISHMENTS

- Syntheses of known zeolites have been performed using microwave and conventional oven hydro-thermal synthesis
- The following compounds have been synthesized: offretite, chabazite, faujasite, mordenite, Linde type F, Linde type L and EMC-2
- Variations in reaction conditions and recipes of offretite have been tested for improvements in separation characteristics through gas chromatography
- Currently used zeolites have been characterized using gas sorption analysis, SEM, XRD and NMR spectroscopy
- Characterization and trial modifications of commercial zeolites have been performed
- Gas chromatography screening for separation characteristics has been done on 11 commercial and natural zeolites
- Initial results of the solid state NMR experiments were obtained from NRL. Si-NMR and Al-NMR spectra were obtained of synthetically customized zeolites at SRNL

FUTURE DIRECTIONS

- Computational DFT studies can provide not only the energetics/kinetics of possible zeolite structures and chemical reactions, but can also simulate gas sorption.
- ^{11}B NMR spectra of boric acid modified Z900Na.
- ^{109}Ag NMR spectra of silver-exchanged mordenite and chabazite
- ^{29}Si and ^{27}Al NMR spectra of different batches of Ag-CHA, various sealed dry/activated samples

REFERENCES

1. Nishizawa, J., et al., "Adsorption by Zeolitic Composition", Jan 10. 1984, US Patent # 4,425,143.
2. Coe, C.G., et al., "Chabazite for Gas Separation", May 15, 1990, US Patent # 4,925,460.
3. Maroulis, P.J., "Selective Zeolitic Adsorbent and a Method for Activation Thereof" Dec. 15, 1987. US Patent # 4,713,362.
4. Meng, X., Xiao, F.S., Chem. Rev., 2014, 114, 1521-1543.
5. Aly, H.M., Moustafa, M.E., Abdelrahman, E.A., Adv. Powd. Tech., 2012, 23, 757–760.
6. Mignoni, M.L., et al., Appl. Clay Sci., 2008, 41, 99–104.
7. Li, Y., Sun, C., Fan, W., Wang, Y., Lan, A., Han, P., Li, X., Dou, T., J. Mater. Sci., 2015, 50, 5059–5067.
8. Klein, P., Pashkova, V., Thomas, H.M., Whittleton, S.R., Brus, J., Kobera, L., Dedecek, J., Sklenak, S., J. Phys. Chem. C, 2016, 120, 26, 14216–14225.
9. Zhou, D., Lu, X., Xu, J., Yu, A., Li, J., Deng, F., Xia, Q., Chem. Mater., 2012, 24, 4160–4165.
10. Lv, A., Xu, H., Wu, H., Liu, Y., Wu, P., Micr. Mes. Mater., 2011, 145, 80–86.
11. Fyfe, C.A., Thomas, J.M., Klinowski, J., Gobbi, G.C., Angew. Chem. Int. Ed. Engl., 1983, 22, 259-275.
12. Lippmaa, E., Magi, M., Samoson, A., Tarmak, M., Engelbardt, G., J. Am. Chem. Soc., 1981, 103, 4992-4996.
13. Nuclear Magnetic Resonance Studies of Zeolites, J. Klinowski, Progress in NMR Spectroscopy, 1984, Vol. 16, pp. 237-309.
14. Lechert, H., Weyda, H., Synthesis of Microporous Materials, Vol. I, M. L Occelli, H. Robson (eds.), Van Nostrand Reinhold, New York, 1992, P. 77.
15. Zhou, R., et al., Micr. Mes. Mater., 2009, 124, 117-122.
16. Thommes, M., Kaneko, K., Neimark, A.V., Olivier, J.P., Rodriguez-Reinoso, F. Rouquerol, J., Sing, K.S.W., Pure Appl. Chem., 2015, 87, 1051.
17. Jusoh, N., et al., Ultrasonics Sonochemistry, 2017, 34, 273-280.

FY2017 PUBLICATIONS/PRESENTATIONS

1. Two publications are in the preparation stages for submission to peer-reviewed journals
2. ACS Southeast Regional meeting as a poster in October 2016

ACRONYMS

DFT	Density Functional Theory
ICDD	International Centre for Diffraction Data
MAS	Magic Angle Spinning
NMR	Nuclear Magnetic Resonance
SEM	Scanning Electron Microscopy
XRD	X-ray Diffraction

ADVANCED ATMOSPHERIC ENSEMBLE MODELING TECHNIQUES

Project Team: R. L. Buckley (primary), S. R. Chiswell, R. J. Kurzeja, G. Maze, B. J. Viner, and D. W. Werth

Thrust Area: Nuclear Security

Project Type: Standard

Project Start Date: 10/20/15

Project End Date: 9/30/17

Ensemble modeling has become an essential tool for characterizing uncertainty in atmospheric model predictions. Airborne transport models are commonly driven by mesoscale atmospheric models, whose accuracy is reduced by model biases and limited available data. Ensemble modeling quantifies model uncertainty by providing a range of possible atmospheric end-states, but is still subject to underlying biases. In this extended LDRD, we have used the Diablo Canyon Tracer Experiment as a testbed to compare standard ensemble modeling with two novel techniques on a spatial scale of relevance to non-proliferation: (1) a physics-based ensemble, which adapts models to specific geographical locations and time frames, and (2) data assimilation with an Ensemble Kalman filter. This research has demonstrated that transport accuracy can be improved when a model is adapted to a particular location and time or when local data is assimilated rigorously into the simulation.

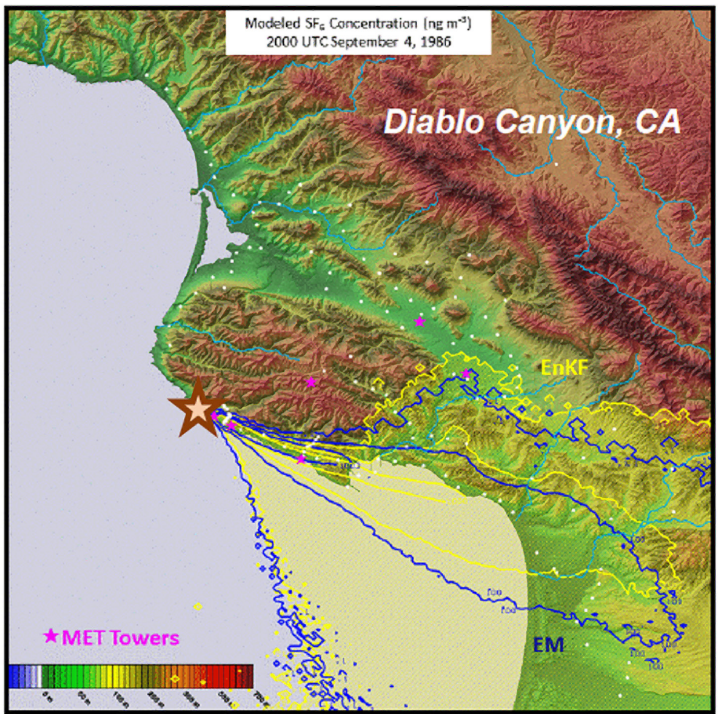

This figure illustrates improvements in coastal release (given by the large gold star) plume transport using the EnKF compared to the standard EM approach. Pink stars denote locations of Met towers providing data at 5 minute intervals. The yellow shaded area and contours represent the EnKF modeled plume 5 hours after the initial release time, while blue contours denote the EM simulation. White points show locations of tracer measurements during the experiment.

FY2017 OBJECTIVES

TASK ONE

Obtain data (meteorological and tracer) from the Diablo Canyon (DC) tracer experiment for September 04, 1986, for testing of the ensemble techniques

TASK TWO

Apply three sets of ensemble simulations to the DC tracer releases: standard ensemble, Adaptive Programming, and Ensemble Kalman-filter techniques

TASK THREE

Modify existing statistical tools to evaluate each ensemble dataset by comparing it to the DC measurements (meteorological and tracer concentration components included)

TASK FOUR

Develop adaptive grid technology to enhance transport modeling (provide better resolution in regions of interest, such as near the source, or in steep gradient topography)

INTRODUCTION

The assessment of emissions from known or suspected weapons facilities that release radionuclide, chemical, or biological materials is of great interest. Source emission estimates are often obtained by scaling downwind effluent measurements by atmospheric dilution rates estimated from airborne dispersion models. The latter are often forced by mesoscale meteorological models, which are of limited accuracy. A more robust solution is to use an 'ensemble' of model simulations, with a range of solutions. We seek to improve the standard ensemble approach through the development of two novel methods: (1) minimization of model error using adaptive (physics-based) programming techniques (AP, Roebber, 2015) and (2) application of a Kalman filter for assimilation of key local observations into the model prediction (EnKF, Evenson, 2003). Transport accuracy can be substantially improved when a model is adapted to a particular location and time and through a utilization of available local data.

Ensemble modeling (EM)—the running of multiple simulations of the same event—has become the standard for quantifying uncertainties in atmospheric forecasts (Figure 1). Typically, agreement between simulations will decrease with longer forecast times and longer downwind distance from the source. EM accounts for uncertainty due to limited input data and for non-linearities inherent in the Navier-Stokes equations, and has been shown to increase model forecast skill compared to single deterministic simulations (Galmarini et al., 2004). Unfortunately, ensembles based on a biased model will retain those biases, and the current practice is to perform EM with minimal consideration for the suitability or completeness of the ensemble (Stensrud et al., 2009).

Improvements in ensemble modeling are important in applications related to atmospheric transport and dispersion, such as emergency response and non-proliferation. In the first year of the project, focus was on simulating the European Tracer Experiment (ETEX, Girardi et al., 1998) to evaluate the quality of two novel ensemble modeling techniques. Improvement in modeling of both methods was illustrated. The current research uses meteorological and concentration data collected during the Diablo Canyon Nuclear Power Plant Tracer Experiment (DOPPTEX) at Diablo Canyon, California in September 1986 (Thuiller, 1992). The terrain is more complex and the experiment covers a much smaller spatial domain (<100 km) than ETEX (>2000 km), and is thus a more representative non-proliferation problem. The experiment also includes two different types of releases, a coastal release of SF6 over an eight hour period, and an inland release of Freon that consisted of two separate releases (two hours and three hours) separated by a three hour period.

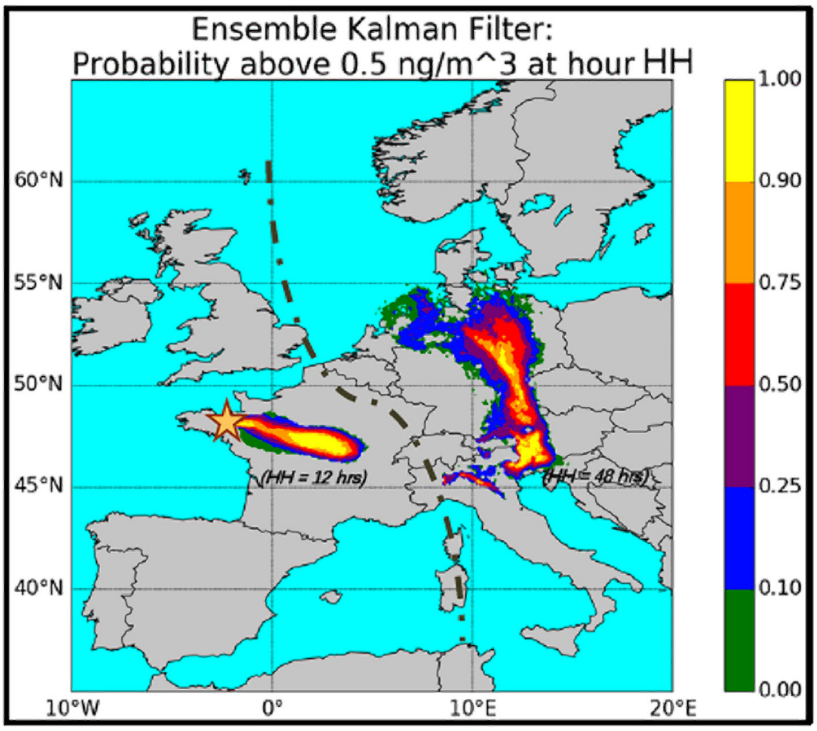

Figure 1. Confidence levels for ensembles run in Europe where contours represent the fraction of models agreeing on exceedance of a specified concentration threshold; Two times (12, 48 hrs) after release are shown

APPROACH

The approach used in this research is similar to the prior year's efforts: Select a suitable modeling scenario and compare the standard EM approach with two novel ensemble techniques. Adaptive Programming (AP) accounts for errors due to the formulation of the model physics. Mesoscale models employ parameterizations to describe unresolved physical processes such as turbulence and cloud formation. A variety of parameterization settings are possible, each with a range of plausible values. Determining the appropriate parameter set is typically performed by trial and error, which is slow and less efficient due to the many simulations required to sample the entire parameter 'space'. AP is a more robust, iterative process by which we perturb the model parameters to generate an ensemble of members. The individual ensemble members are then run, and the best performing member according to available observations is selected to serve as the 'parent' of the next generation. After a number of iterations, the simulations should converge to an ensemble that is best suited (adapted) to the prevailing atmospheric conditions. The second novel approach uses an ensemble Kalman filter (EnKF) to examine the impact of assimilating selected observations into the simulation. The EnKF improves upon existing methods of data assimilation. Standard data assimilation affords equal weight to surface and above-ground winds, but the latter are much more representative of regional air flow, and should force a much broader scale adjustment to the model fields. The EnKF technique combines the model prediction and the calculated error variance of each observation in order to determine the optimal weighting for observations at every step. Meteorological data from the ensemble techniques were ingested into the Lagrangian Particle Dispersion Model (LPDM, Uliasz 1993) to create three-dimensional, time-varying concentration fields. LPDM is also modified to use an adaptive grid (AG) technique that changes the uniform grid mesh to use finer resolution in regions of interest. Additional analysis of vertical plume structure was conducted using HYSPLIT (Draxler et al., 1998) in order to analyze performance of LPDM.

The research described here uses data from the Diablo Canyon tracer experiment (DOPPTEX) conducted in 1986 (Thuiller, 1992). Access to collections of both meteorological data and tracer measurements permits rigorous comparison of these approaches. Statistical techniques developed in the first of the study were used once again for the model evaluation (Mosca et al., 1998). Since time is critical during emergency response situations, research into use of adapted grids was also explored. The technique modifies grid spacing to provide better resolution at points of interest, and coarser resolution in less-critical areas (Srivasta et al., 2001; Khan et al., 2005). Such techniques may result in more rapid results, or provide better accuracy due to improved resolution at the source.

RESULTS/DISCUSSION

Model simulations for transport were conducted for two locations where tracers were released. The first release comprised a continuous 8 hour SF_6 release from the Diablo canyon power plant location immediately adjacent to the Pacific coast, while the second release comprised a transient release of Freon for durations of 2 and 3 hours from an interior valley location. The standard ensemble modeling (EM) approach is to perturb the initial meteorological conditions (fields of wind, temperature, etc.), assuming inherent uncertainty in the measurements used to develop them, and generate an ensemble of forecast solutions whose spread about the mean quantifies the forecast uncertainty. This is the baseline standard for comparing the two novel methods of EM. Twenty members were generated with the Weather Research and Forecast (WRF, Skamarock et al., 2008) model using a technique described in Berner et al. (2011) involving stochastic perturbation to the WRF simulations. In general, the EM runs exhibited less variation for the inland release than for the coastal location due to the observed difference of nearly 20 degrees Fahrenheit between land and ocean temperatures.

The AP ensemble technique perturbed 9 different model parameter inputs (including surface temperature, soil moisture, and turbulence length scale) of the Regional Atmospheric Modeling System (RAMS, Cotton et al., 2001). RAMS is used due to prior experience with AP at SRNL (O'Steen and Werth, 2009). The scoring of each AP ensemble member was based on tower observations at 5 locations, with the best result from a given "generation" saved for use in the next iteration. This was repeated for 40 generations. An example of improved simulation results is given in Figure 2, showing the difference in concentration between the Base Case simulation and the Generation 40 result. The AP technique showed improvements in both release cases, with more improvements showing in the inland release scenario. Although the coastal release did show an improvement in the timing of the downwind movement of the plume, the direction of plume movement was still slightly off shore. Results from the AP work from the FY16 research are the subject of a drafted peer-review journal article.

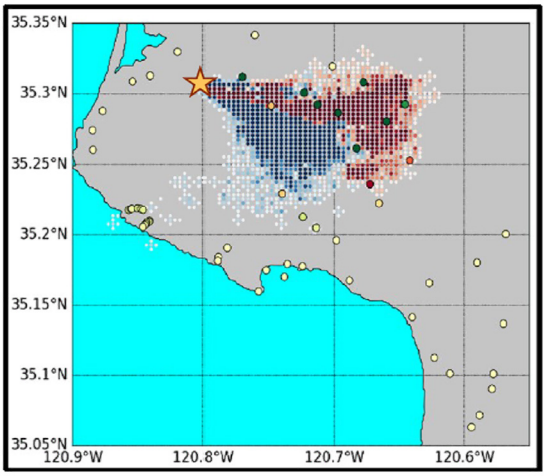

Figure 2. Diablo Canyon plume concentration difference 2 hours after release between the AP Base case and AP Generation 40. Red shading indicates a drop in concentration, while blue shading shows increased concentration. Circles denote tracer observation locations. The green circles indicate improved model results, while red circles indicate a decline in model results relative to observations.

The EnKF technique used the WRF-Data Assimilation Research Testbed (DART) software (Anderson et al., 2009) and the original EM members as the starting point. The EnKF technique showed better overall improvement than the AP technique for DOPPTEX, especially for the coastal release (Figure 1) where land and ocean temperatures provided significant spatial differences, while the diurnal warming of the interior valley induced an inland plume motion which curved around the higher coastal terrain of Diablo Canyon downwind of the release point. EnKF assimilation utilized both surface based meteorology tower measurements at 5 minute intervals and upper air measurements from SODAR at 30 minute intervals. Since the radiational heating of the interior valley demonstrated significant forcing effects on the plume motion, the surface measurements contributed most to forecast improvement.

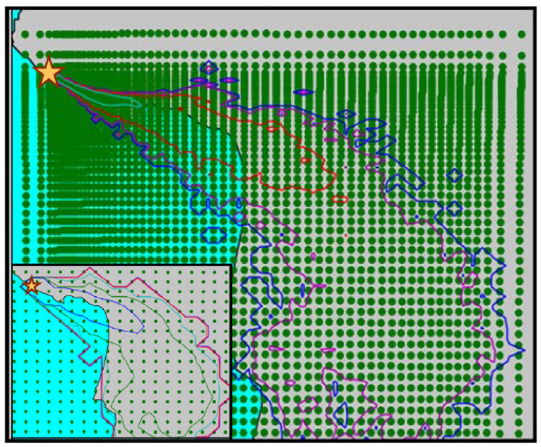

Figure 3. Modified transport grid mesh using adaptive grid (AG) technique. Note the higher density of grid points near the source location, given by the star. Inset shows an initial uniform grid mesh before application of the AG technique.

The adaptive grid technology was developed in a general sense for use at SRNL, and specifically applied to Diablo Canyon. Figure 3 shows an example of the modification to grid mesh where only 4% of the grid points were used compared to our standard modeling techniques. Due to the adaptive nature of the grid, these points were concentrated in regions of higher concentration gradients, leading to similar resolution at points of greatest interest compared to our original simulations. This technique showed better results for the coastal release. The inland release consisted of two separate releases which were both in the domain at the same time, causing some issues with the adaptive grid converging on the areas of interest. In practice, the process does not necessarily improve simulation speed as hoped, but does provide improved resolution around the regions of interest.

FY2017 ACCOMPLISHMENTS

- DOPPTEX data were collected and organized for use in the ensemble modeling. This included assembling input gridded and observed meteorological data, as well as measured tracer concentrations.
- Statistical metrics and software were modified from last year's development for ETEX and applied to DOPPTEX collections to assess ensemble model skill. Metrics can be applied to both meteorological results as well as the tracer data. However, the lack of meteorological observations for this study prevents an independent data set for statistical analysis.
- A 20-member standard ensemble (using the WRF mesoscale model and running LPDM for transport) was generated for DOPPTEX.
- A 20-member EnKF ensemble (using WRF-DART platform and running LPDM for transport) was generated for DOPPTEX. Software developed to allow for specific input of surface and upper-air meteorological data for ETEX was used here as well. The results showed improved statistics most pronounced in the flow interaction between the complex terrain and the land-ocean radiational heating differences. The close proximity of measurements provided at 5 minute intervals provided the ability to allow for local radiational forcing to impact the plume motion.
- A 10-member AP ensemble (using RAMS mesoscale model and running LPDM for transport) was generated for DOPPTEX. The results showed modest improvement in tracer plume statistics, but with a clear shift of the plume away from an area to which it did not extend based on tracer measurements.
- Adaptive grid techniques were developed with assistance from Georgia Tech and applied to DOPPTEX. Statistical improvement in simulated tracer concentrations relative to the original uniform mesh was found.

FUTURE DIRECTIONS

- Analysis of the AP parameter adjustments. Which parameter settings provide the best results?
- Further testing of the EnKF technique: What specific observations should be used? How much weight should be given to various observations?
- Further testing of the AG to transport simulations to reduce computational burden, or improve plume accuracy in regions of interest.
- Application of AG techniques for both site-related emergency response and Strategic Partnership Projects (SPP) supporting numerous intelligence community sponsors.
- Explore and explain the differences in novel ensemble technique improvement (AP, EnKF) overstandard EM as applied to large-scale problems (ETEX) versus a small-scale problem (DOPPTEX).

FY2017 PUBLICATIONS/PRESENTATIONS

1. SRNS Board of Directors poster presentation (18 October 2016).

2. Buckley, R. L., S. R. Chiswell, R. J. Kurzeja, G. M. Maze, B. J. Viner, and D. W. Werth, 2017: NovelAtmospheric Ensemble Modeling Techniques Applied to Long-Range Transport. 97th American Meteorological Society Annual Meeting, 28th Conference on Weather Analysis and Forecasting/24th Conference on Numerical Weather Prediction (Seattle, WA on 25 January,2017).

3. Buckley, R. L., S. R. Chiswell, R. J. Kurzeja, G. M. Maze, B. J. Viner, and D. W. Werth, 2017: NovelAtmospheric Ensemble Modeling Techniques Applied to Long-Range Transport, Palmetto Chapter of the American Meteorological Society 21st Annual Mini-Technical Meeting (Columbia,SC on 02 March 2017).

4. SRNL External Review Committee (08 May, 2017).

5. Buckley, R. L., S. R. Chiswell, R. J. Kurzeja, G. M. Maze, B. J. Viner, and D. W. Werth, 2017: Ensemble Atmospheric Modeling Techniques Applied to Mesoscale Dispersion. 21st Annual George Mason University Conference on Atmospheric Transport and Dispersion (Fairfax, VW on13 June, 2017).

6. Werth et al. Draft of paper discussing AP technique applied to ETEX (1st year results), to be submitted to Atmos Envir.

7. Buckley R. L., S. R. Chiswell, R. J. Kurzeja, G. M. Maze, B. J. Viner, and D. W. Werth, 2017: Advanced Atmospheric Ensemble Modeling Techniques—draft site report.

REFERENCES

1. I Anderson, J., T Hoar, K. Raeder, H. Liu, N.Collins, R. Torn, and A. Avellano, 2009: The Data Assimilation Research Testbed: A Community Facility, *Bull. Amer. Meteor. Soc.,* **90,** 1283-1296.

2. Berner, J., S.-Y. Ha, J. P. Hacker, A. Fournier, and C. Snyder, 2011: Model Uncertainty in a Mesoscale Ensemble Prediction System: Stochastic Versus Multiphysics Representations. *Monthly Weather Review,* **139,** 1972—1995.

3. Cotton W. R., R. A. Pielke Sr., R. L. Walko, G. E. Liston, C. J. Tremback, H. Jiang, R. L. McAnelly, J. Y. Harrington, M. E. Nicholls, G. G. Carrio, and J. P. McFadden, 2002: RAMS 2001: Current status and future directions. *Meteorol. Atmos. Phys*., **82,** 5-29.

4. Draxler, R.R., and G.D. Hess, 1998: An overview of the HYSPLIT_4 modeling system of trajectories, dispersion, and deposition. *Aust. Meteor. Mag.*, **47,** 295-308.

5. Evensen, G., 2003: The Ensemble Kalman Filter: theoretical formulation and practical implementation. *Ocean Dynamics,* **53,** 343-367.

6. Galmarini, S., R. Bianconi, W. Klug, T. Mikkelsen, R. Addis, S. Andronopoulos, P. Astrup, A. Baklanov, J. Bartnicki, J.C. Bartzis, R. Bellasio, F. Bompay, R. Buckley, M. Bouzom, H. Champion, R. D'Amours, E. Davakis, H. Eleveld, G. Geertsema, H. Glaab, M. Kollax, M. Ilvonen, A. Manning, U. Pechinger, C. Persson, E.Polreich, S. Potemski, M. Prodanova, J. Saltbones, H. Slaper, M. A. Sofiev, D. Syrakov, J. H. Sørenson, L.Van der Auwera, I. Valkama, R. Zelazny, 2004a: Ensemble dispersion forecasting—Part I: concept,approach and indicators. *Atmos. Envir.,* **38,** 4607-4617.

7. Girardi, F., G. Graziani, D. van Velzen, S. Galmarini, S. Mosca, R. Bianconi, R. Bellasio, W. Klug, and G. Fraser, 1998: ETEX, The European Tracer Experiment. Joint Research Centre, EC, 107 pages.

REFERENCES (CONTINUED)

8. Khan, M. N., M. T. Odman, and H. A. Karimi, 2005: Evaluation of algorithms developed for adaptive grid air quality modeling using surface elevation data. *Computers, Environment and Urban Systems,* **29,** 718-734.

9. Mosca, S., R. Bianconi, R. Bellasio, G. Graziani, and W. Klug, 1998: ATMES II – Evaluation of Long-Range Dispersion Models Using Data of the 1st ETEX Release. Joint Research Centre, European Commission. Luxembourg: Office for Official Publications of the European Communities (EUR 17756).

10. O'Steen, B.L., and D.W. Werth, 2009: The Application of an Evolutionary Algorithm to the Optimization of a Mesoscale Meteorological Model. *J. Appl. Met. and Clim.,* **48** (2), 317-329.

11. Roebber, P. J., 2015: Evolving Ensembles. *Mon. Wea. Rev.,* **143** (2), 471-490.

12. Skamarock, W. C., J. B. Klemp, J. Dudhia, D. Gill, D. Barker, W. Wang, and J. G. Powers, 2005: A description of the Advanced Research WRF Version 2. NCAR/TN-468_STR, 88 pp.

13. Srivastava, R. K., D. S. McRae, and M. T. Odman, 2001: Simulation of dispersion of a power plant plume using an adaptive grid algorithm. *Atmos. Enviro.,* **35,** 4801-4818.

14. Stensrud, D. J., N. Yussouf, D. C. Dowell, and M. C. Coniglio, 2009: Assimilating surface data into a mesoscale model ensemble: Cold pool analyses from spring 2007. *Atmos. Research,* **93,** 207-220.

15. Thuiller, R. H., 1992: Evaluation of a Puff Dispersion Model in Complex Terrain. *J. Air Waste Manage. Assoc.,* **42,** 290-297.

16. Uliasz, M. 1993: The atmospheric mesoscale dispersion modeling system. *J. Appl. Meteor.,* **32,** 139-149.

ACRONYMS

AG	Adaptive Grid
AP	Adaptive Programming
DOPPTEX	Diablo Canyon tracer Experiment
EM	Ensemble Modeling
EnKF	Ensemble Kalman Filter
ETEX	European Tracer Experiment
HYSPLIT	Hybrid Single Particle Lagrangian Trajectory Model
LDRD	Laboratory Directed Research and Development
LPDM	Lagrangian Particle Dispersion Model
RAMS	Regional Atmospheric Modeling System
SRNL	Savannah River National Laboratory
WRF	Weather Research and Forecast Model
WRF-DART	Weather Research and Forecast-Data Assimilation Research Testbed

TOTAL NUMBER OF POST-DOCTORAL RESEARCHERS

1. Dr. Grace M. Maze served as a post-doctoral researcher on this project for much of the first year (FY2016), as directed by the Oak Ridge Associated Universities (ORAU), before being hired on permanently in August 2016.

UNDERSTANDING OF LOCAL STRUCTURE/ FUNCTION RELATIONSHIPS OF ZEOLITES USED IN INDUSTRY THROUGH POLARIZED RAMAN SPECTROSCOPY

Project Team: Omar Rivera-Betancourt, Robert Lascola, Kimberly A. Fessler, Randall Achey, Douglas Hunter (SRNL)

Thrust Area: National Security

Project Start Date: 10/1/16

Project End Date: 9/30/17

The advances in zeolite developmental engineering currently employed at SRNL for noble gas samplers have provided insight as to how the zeolites separate noble gases from atmospheric matrices. Still, new characterization methods may provide additional information and guide the synthesis of materials with improved sorption properties. One such technique is polarized Raman spectroscopy. The polarization dependence of certain peaks associated with known chemical components indicates the crystallinity or amorphousness of the structure. Another technique is low frequency (THz) Raman spectroscopy, which directly probes phonon vibrations in the zeolites. By correlating these measurements with the known sorption properties of commercially available materials, we hope to establish key properties that will guide the synthesis of new zeolites. This new method of zeolite characterization should not only allow SRNL to meet customer needs in improving the materials used in noble gas samplers but also provide a better understanding of the local structure-function relationships of zeolites used in industry.

FY2017 OBJECTIVES

TASK ONE
Complete optics procurement and instrumental setup

TASK TWO
Perform polarized Raman spectroscopy experiments with around 10 different commercially and lab modified zeolites

TASK THREE
Obtain Raman spectra with different laser wavelengths to optimize experimental parameters

TASK FOUR
Set up a pressurized gas cell to allow direct spectroscopic measurements of zeolite-gas interactions.

TASK FIVE
Gain a better fundamental understanding of the site specific interaction of zeolites and non-reactive gases.

TASK SIX
Gain new insights on the differentiation of the symmetric modes of the zeolite crystals.

TASK SEVEN
Perform low wavenumber Raman spectroscopy to characterize internal metal cations found in the structural framework of the zeolite. This information and technique could be used when characterizing custom engineered zeolites.

INTRODUCTION

Zeolites are the most well-known family of microporous materials, also often referred to as molecular sieves or open-framework materials. They are a class of inorganic solids that possess regular pores or voids in the size range of 5-20 Å **(1-2)**. Zeolites are widely used in many applications, including catalysis, adsorption, molecular sieve diffusion, and nanoclusters preparation. Mesoporous and microporous zeolites have found wide applications in various refining and chemical industries due to their crystalline framework, uniform pore size, high internal surface area, and tunable acidity **(3)**.

There are several patents for the use of these materials in sampling systems which have paved the way for SRNL to develop noble gas samplers **(4-6)**. The SRNL samplers have a proven record of consistent and reliable performance, using commercially available zeolites. Nonetheless, sampler performance gains can still be realized by the development and use of more advanced materials. Rational design and synthesis of zeolites can be guided by an advanced understanding of the relationship between their structure and gas sorption properties as well as better knowledge of the crystallization process and the formation mechanism. Many techniques, such as X-ray diffraction and scattering, NMR spectroscopy, and electron microscopy have been used to study the formation mechanism of zeolites. Most studies were performed by using ex situ techniques, namely by frequently removing aliquots of the reaction mixture and analyzing the samples after quenching the reaction. However, microporous zeolite-type materials are usually synthesized under hydrothermal conditions, and the need for sample quenching and workup may cause dramatic and undeterminable structural changes.

APPROACH

A measurement technique which avoids these problems is Raman spectroscopy, which is a powerful technique for catalyst characterization and particularly for transition metal-containing microporous and mesoporous materials. Vibrational spectroscopy techniques, such as Raman scattering and infrared absorption, are extensively used in characterizing zeolites by probing the phonon vibrations of their secondary building units and identifying other dynamical features within their frameworks **(7)**.

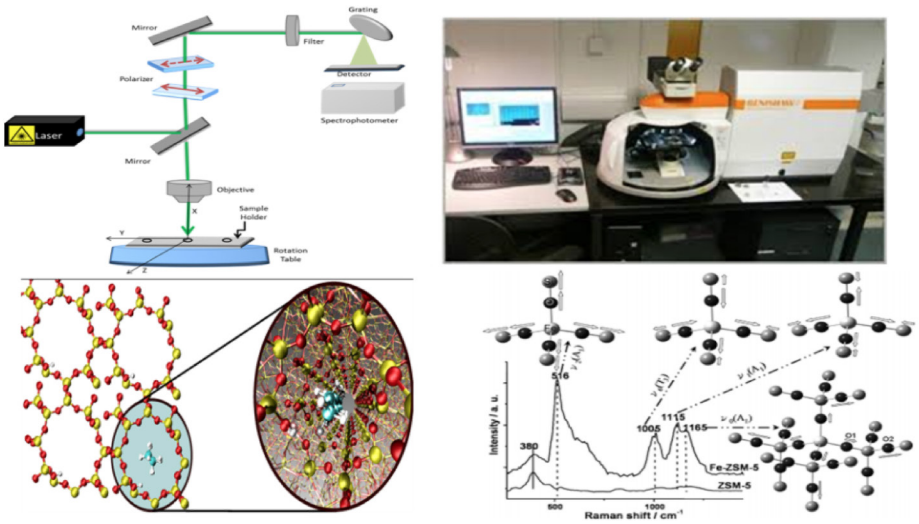

Figure 1. Experimental polarized Raman spectroscopy setup and examples of acquired Raman Spectra of structurally diverse zeolites (taken from ref.11)

In this project, we expanded the typical use of Raman by incorporating two less widely used variants of the technique—polarized Raman spectroscopy (as shown in Figure 1) and low-frequency (THz) Raman spectroscopy.

Each technique provides unique structural information about the materials. The polarization dependence of Raman scattering carries additional information about the structural symmetry of the sample being measured. Peaks for which the scattering intensity varies greatly for polarizations parallel and perpendicular to the excitation beam are indicative of symmetric vibrations and crystal structures. In contrast, a weak dependence is indicative of nonsymmetric vibrations or an amorphous or isotropic environment **(8,9)**. Obtaining this information requires filters to assure polarization purity of both the excitation and scattering. THz Raman spectroscopy is sensitive to the large-scale phonon vibrations of crystals as well as vibrations involving heavier atoms in a zeolite. Examples of such heavier atoms are transition metal ions that have undergone cation exchange for lighter Na^+ of H^+ ions at exchangeable sites created by aluminum isomorphic substitution for silicon in the framework of the zeolites that are used in the SRNL noble gas separators. Phonon and low-frequency peaks are not typically observable due to the large amount of Rayleigh scattering associated with Raman measurements. However, recent advances in filtering optics permit much more effective rejection of Rayleigh scattering and have decreased the practical limit for Raman shift frequencies from ~250 cm^{-1} to ~10 cm^{-1}.

Combined, these techniques can provide more information about the structure and orientation of molecules and clusters inside zeolite cavities. By first analyzing commercially available zeolites with known gas sorption properties, it should be possible to establish structure-function relationships that can guide synthesis of new materials. Furthermore, the ability to make Raman measurements in situ in reaction vessels suggests real time monitoring of both the synthesis process and the gas sorption process. To explore this possibility, we purchased a commercially available pressurized Raman cell. The measurements could be done at a variety of pressures and at a maximum temperature of 300 °C and as low as -60 °C. By observing zeolite structural changes as gas is absorbed, it should be possible to identify the active sites of the material and thus establish targets for synthetic modifications.

RESULTS/DISCUSSION

Mesoporous and microporous zeolites have found wide applications in various refining and chemical industries due to their crystalline framework, uniform pore size, high internal surface area and tunable acidity **(8)**. Examples of such heavier atoms are transition metal ions that have been cation exchanged for lighter Na^+ and H^+ ions at exchangeable sites created by aluminum isomorphic substitution for silicon in the framework of the zeolites that are used in the SRNL noble gas separators. Spectroscopic techniques are extensively used in characterizing zeolites by probing the phonon vibrations of their secondary building units and identifying other dynamical features within their frameworks **(9)**. Raman and IR spectroscopy are able to probe chemical entities. Raman is a powerful technique for catalyst characterization and particularly for transition metal-containing microporous and mesoporous materials. Potentially the results of these studies will allow us to modify our customized zeolites synthesized in our laboratory at SRNL. As part of another ongoing project we have already performed experiments with spatial resolution of up to 7 cm^{-1}. By analyzing the polarization dependence of the selected peaks, we can further characterize the crystal structure of the zeolites.

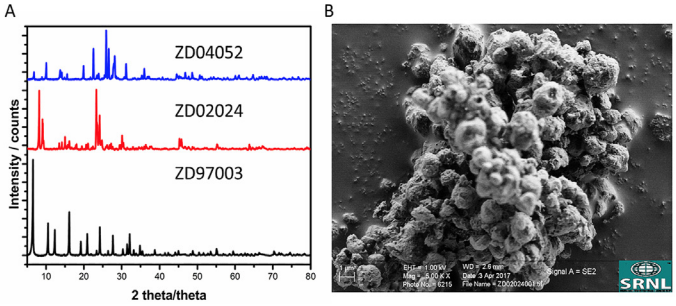

Figure 2. (A) pXRD of different commercially available zeolites, **(B)** SEM image of ZD02024

For the experiments we used a series of commercial mordenite zeolite samples. Prior to initializing the experiments we characterized the samples employing p-XRD and SEM as seen in Figure 2.

Polarized Raman spectroscopy experiments were initially performed with 532 nm excitation (Verdi; Coherent, Inc.) and a polarization-filtering fiber probe (InPhotonics). Spectra were recorded from 250-1800 cm^{-1} (Holospec; Kaiser Optical) at 7 cm^{-1} resolution, and detected with an Andor CCD camera. Samples were mounted on a xyz stage for positioning. Subsequent measurements were taken with a Jasco NRS-5100 Raman spectrometer using both 532 and 785 nm excitation. Polarization measurements on this instrument were obtained with a variety of spectral resolutions (e.g. 1 cm^{-1} to 0.4 cm^{-1}). All spectral measurement taken into consideration were acquired at a range of 100-1800 cm^{-1}. The spectra acquired with Jasco system were fluorescence and baseline corrected and smoothed using a Savitzky-Golay filter.

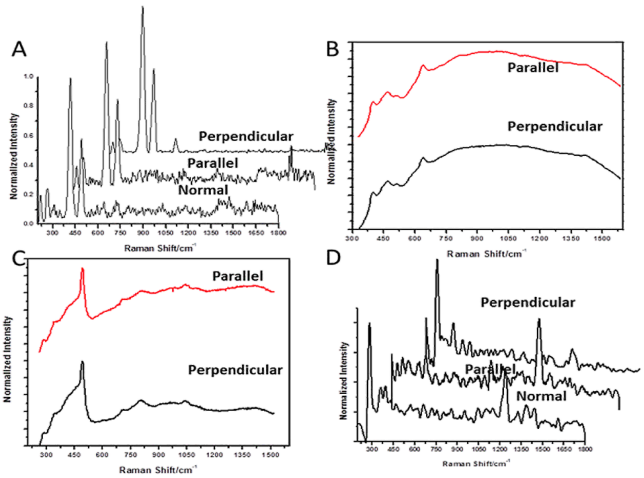

Figure 3. Polarized Raman spectra of different commercially available zeolites

Initial Raman measurements were taken of mordenite, which has unique characteristics compared to other 12-membered ring zeolites. Mordenite has a chemical formula $Na_8(H_2O)_{24}[Si_{40}Al_8O_{96}]$ with parallel 12 membered ring channels along the c-axis direction and these channels are interconnected by 8-membered rings channels along the b-axis (10). Shown in Figure 3 are a series of spectra acquired with both instruments of a series of commercially available mordenites taken at polarization angles of 0° and 90° and un-polarized Raman spectra. Figure 3A and 3D were acquired using a 785 nm laser and figures 3B and 3C with a 532 nm laser. The mordenite spectra along with the majority of the zeolite analytes present Raman shifts around 390-460 cm^{-1}. These are indicative of the formation of five membered rings of the tetrahedron interconnected with an additional tetrahedron. Bands around 490 cm^{-1} belong to Al-O-Si bending and symmetric stretching vibrations of the zeolite framework. In some cases signals were observed around 400 cm^{-1}, which are indicative of a five-fold ring stretch. Raman bands found around 950-1250 cm^{-1} belong to Si-O-Al asymmetric stretching modes. In some cases bands were found at 820 cm^{-1}. which are due to SiO_4 and AlO_4 tetrahedra. Bands below 400 cm^{-1} in general belong to lattice vibrations of the zeolitic crystalline structure, some of the specific zeolite vibrational bands belong to different point and factor groups found in the crystal **(3, 7, 11-15)**. Full details of the experimental peak positions of the observed Raman vibrational modes are found in Table 1.

Raman shift (cm^{-1}) (no polarization)	Raman shift (cm^{-1}) (0^0)	Raman shift (cm^{-1}) (90^0)	Band Assignment
158	158	158	Lattice modes
207	207	207	Lattice modes
247	247	247	Lattice modes
406	406	406	5-membered ring breathing, stretching
465	465	465	4-membered ring breathing
525	525	525	Al-O-Si bending and symmetric stretching of framework
648	648	648	8-or 10-membered ring vibration
799	799	816	Si(Al)-O symmetrical stretch
895	895		Si(Al)-O symmetrical stretch
970			Si(Al)-O asymmetrical stretch
950-1250			Si(Al)-O asymmetrical stretch

Table 1. Experimental peak positions of all the observed Raman vibrational modes of different zeolites

Raman spectroscopy is potentially a powerful technique for characterizing the microporous and mesoporous materials. Unfortunately the technique can suffer due to strong fluorescence interference caused by organic templates, impurities, and surface defect sites. This was observed for our spectra obtained at both 532 and 785 nm excitation. Fluorescence typically occurs in the range from 300 to 700 nm or longer, but can be avoided in the UV region for condensed materials. In the hopes of obtaining better spectra, we shifted the excitation line to 325 nm. The resulting Raman signal indeed had a weaker fluorescence background, as shown in Figure 4. Spectra were improved not only by the decreased background, but also by increased Raman scattering intensity associated with the shorter wavelength ($I \alpha \lambda^{-4}$) and possibly resonance enhancements. Therefore, all subsequent spectra, eventually of 11 different zeolites, were taken under these conditions. These include two natural zeolites such as chabazite and clinoptilolite, a range of commercially sold mordenites and a silver exchanged mordenite. We then purchased the necessary optics in order to perform polarization experiments on UV Raman. Unfortunately the UV laser in our facilities malfunctioned in the process of the installation of the polarization kits. The timeline to replace the laser was October 2017. This was outside of the timeframe of the fiscal year and otherwise the experiments could not be done.

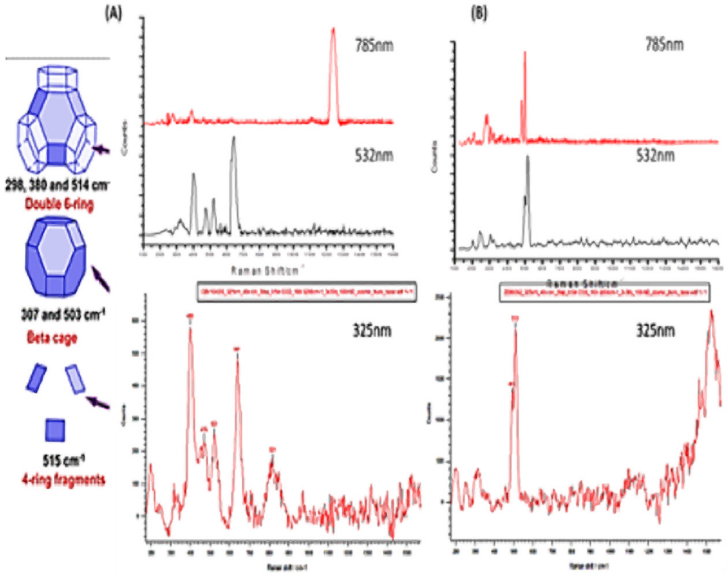

Figure 4. Raman spectra of two commercially available Mordenite zeolites taken at three different laser wavelengths

THz Raman spectroscopy was performed using a specialized fiber-based probe with high-quality filtering optics (manufactured by Ondax). The probe, designed for 532 nm excitation, permitted measurements at shifts as low as 10 cm^{-1}. We had the hopes that this technology would help identify the presence of transition metals within the structure of our custom zeolites (**11-12**). But as in the previous experiments, fluorescence interference obscured the Raman signal, as shown in Figure 5A. Figure 5B shows the original idea we proposed, the measurements of site specific interactions of commercial zeolites and non-reactive gases. Although we were able to procure the pressurized Raman cell needed for these experiments, we were not able to perform these measurements due to the problems described above.

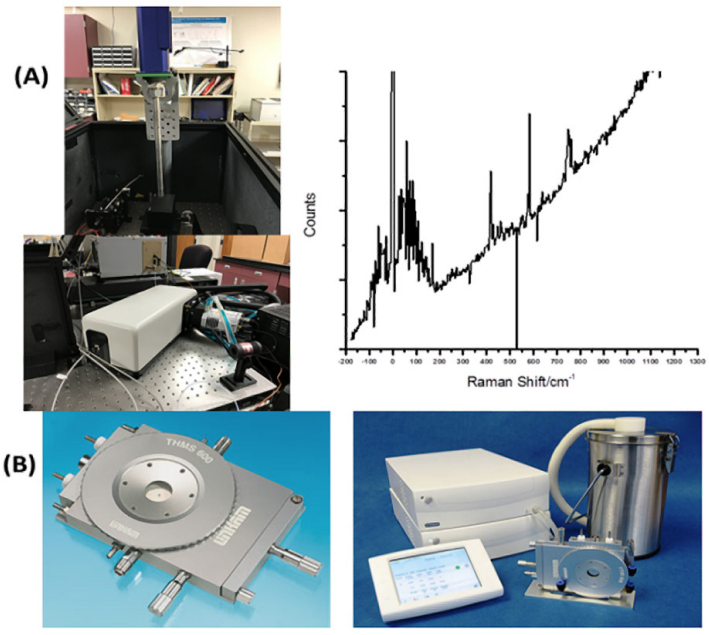

Figure 5. (A)CBV10ADS THz Raman spectra with the purchased probe and (B) specialized Raman cell for the use of zeolite-gas inteaction studies

FY2017 ACCOMPLISHMENTS

- Raman spectroscopy measurements of 11 commercially available zeolites were made at 325 nm excitation. Measurements at 532 and 785 nm excitation were largely obscured by fluorescence.
- Procurement of a THz Raman spectroscopy probe
- Improvements to the instrumentation made—purchase of a new holographic filter for the spectrograph.
- We procured and purchased a commercially available pressurized Raman cell to study zeolite-gas interactions. Experiments could be performed as well at cryogenic temperatures.

FUTURE DIRECTIONS

- We have established the necessary conditions for using Raman spectroscopy to deduce structure-property relationships in zeolites. Future work would build on this knowledge and proceed more efficiently. Such work could be enhanced by the use of density functional theory (DFT) calculations to correlate frequency and symmetry observations to chemical structure. DFT would also permit the calculation of energetics and kinetics of the structures.

FY2017 PUBLICATIONS/PRESENTATIONS

1. Referenced in the ACS Southeast Regional meeting as a poster in October 2016.

REFERENCES

1. Knops-Gerrits, P.P.; De Vos, D.E. e.t. al. Microporous Materials, 1997, 8, 3-17.
2. Fan, F., Feng, Z., Li, C; Chem. Soc. Rev., 2010, 39, 4794-4801.
3. Huang, S. et.al., Microporous Mesoporous Mater., 2014,191,18-26.
4. Nishizawa,J., et.al. , "Adsorption by Zeolitic Composition", Jan 10. 1984, Patent # 4,425,143.
5. Coe, C.G.,et. al., "Chabazite for Gas Separation", May 15, 1990, Patent # 4,925,460.
6. Maroulis, P.J., "Selective Zeolitic Adsorbent and a Method for Activation Thereof" Dec. 15, 1987. Patent # 4,713,362.
7. Fan, F., Feng, Z., Li, C; Accounts of Chem. Res.,2010, 43, 378-387.
8. Nam, D. et.al. ; Appl. Phys. Lett. ,2014,105, 173903.
9. Weisman, A.L. et al.; J. Chem. Phys., 2014, 141, 224702.
10. Khalil, U.,Muraza, O., Microporous Mesoporous Mater., 2016, 232, 211-217.
11. Sun, K. et.al. , J. Phys.Chem. C, 2008, 112,16036-16041.
12. Chen, J., Ying,P.,Li, C.,J. Phys.Chem. B, 2004, 108, 12669-12676.
13. Pechar, F., Rykl, D., Chem. Zvesti., 1981, 35, 45-50.
14. Nguyen, H.G. et.al. , J. Phys.Chem. C, 2009, 113, 12818-12825.
15. Chatterjee, A., Iwasaki, T., J. Phys.Chem. A, 103, 9857-9863.

ACRONYMS

CCD	Charged-coupled Device
DFT	Density Functional Theory
IR	Infrared
NMR	Nuclear Magnetic Resonance
THz	Terahertz
UV	Ultra-Violet
p-XRD	Powder X-ray Diffraction

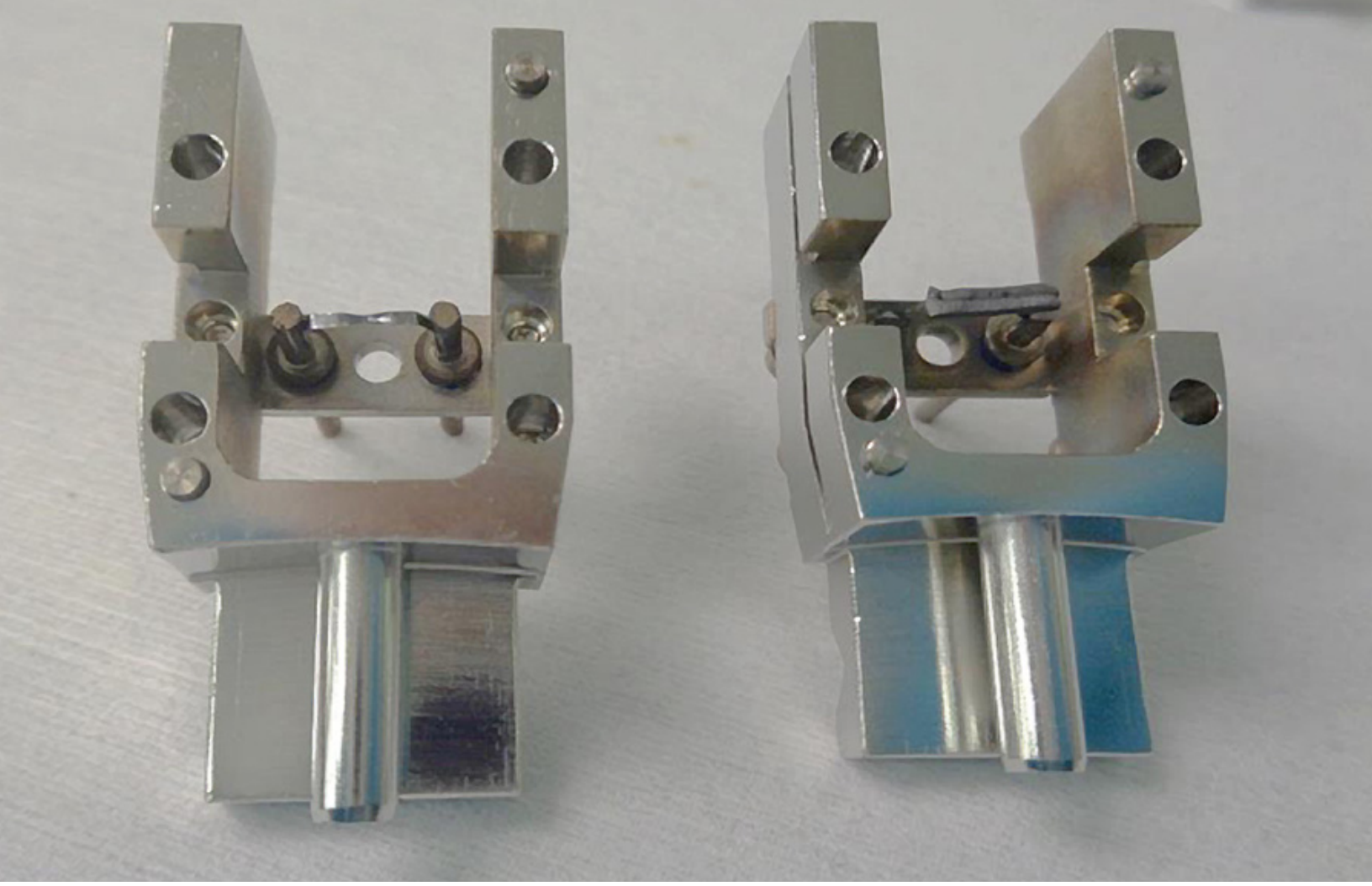

Traditional rhenium filament **(left)** and reduced graphene oxide filament **(right)**

REDUCED GRAPHENE OXIDE AS FILAMENT MATERIAL FOR THERMAL IONIZATION MASS SPECTROMETRY WITH A FOCUS ON Pu AND U ANALYSIS

Project Team: J. T. Hewitt (PI), C. R. Shick Jr., M. Siegfried, G. Hall

Thrust Area: National Security

Project Start Date: 10/1/16

Project End Date: 9/30/18

The use of graphene oxide materials for thermal ionization mass spectrometry analysis of plutonium and uranium has been investigated. Filaments made from graphene oxide slurries have been 3-D printed. A method for attaching these filaments to commercial thermal ionization post assemblies has been devised. Resistive heating of the graphene based filaments under high vacuum showed stable operation in excess of 4 hours. Plutonium ion production has been observed in an initial set of filaments spiked with the Pu 128 Certified Reference Material.

FY2017 OBJECTIVES

TASK ONE
Identify background uranium levels in commercially sourced graphene oxide material

TASK TWO
Determine impact of graphene oxide material on thermal ionization efficiency in a typical Re filament TIMS analysis

TASK THREE
3-D print small form factor graphene oxide filaments

TASK FOUR
Mate printed filaments to commercial TIMS filament assemblies

TASK FIVE
Determine durability of graphene based filaments in a TIMS source chamber when heated to greater than 1000 K

INTRODUCTION

Thermal Ionization Mass Spectrometry (TIMS) in an analytical technique that sees widespread use in the fields of nuclear safeguards,[1,2] nuclear forensics,[3,4] and environmental monitoring[5,6] for the measurement and characterization of actinide species. TIMS is currently considered the benchmark technique for determining uranium and plutonium isotopic information.[2] Sample utilization in TIMS is, however, typically quite low due to poor ionization efficiencies—normally in the range of 0.1% - 0.5% for Pu and U. Research has been done to try and increase ionization efficiencies with much of the work focused on geometry modifications of the typical rhenium filament material.[7-9] Because of thermodynamic limits related to work function of the analyte and the ionizing filament, entirely new materials (i.e. not Re or W) are needed in order to greatly improve ionization efficiency.

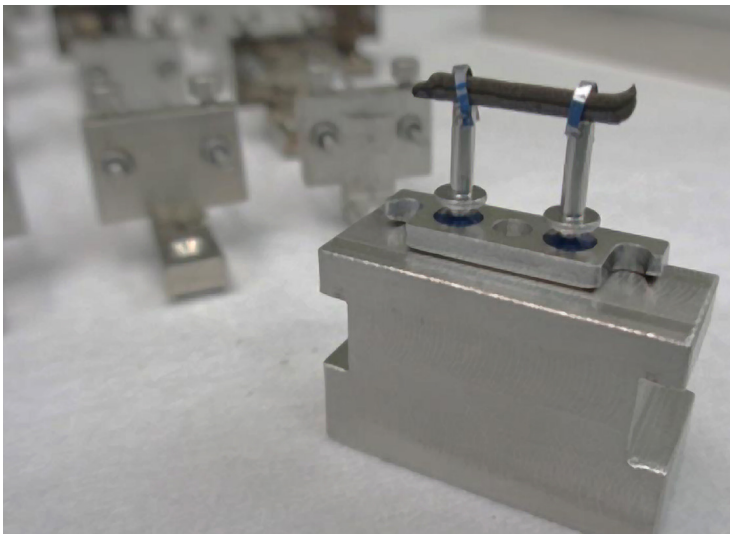

Figure 1: 3-D printed RGO filament mounted on a commercial TIMS post assemble

Developing new materials to be used as TIMS filaments is, however, non-trivial. In a typical Pu or U analysis the evaporation filament can reach temperatures in excess of 1500 K; therefore, high temperature stable materials are a must. Recent work has shown that graphene-based materials can be 3-D printed into small form factors that can be resistively heated to more than 2000 K.[10] This suggests a graphene based TIMS filament is possible and could represent an entirely new substrate material for TIMS analyses. Moreover, because the work function of graphene is tunable[11,12] the thermodynamic constraints that lead to poor ionization efficiency in Re and W based filaments could be overcome.

Orders of magnitude increases in ionization efficiency could be realized. Such improvements would directly translate into reduced sample size requirements and/or enhanced analytical capabilities which would support the nonproliferation, safeguards, and forensics communities.

The first year of this LDRD project was focused on baseline project viability studies, developing the technical knowhow to reproducibly manufacture graphene based filaments, testing different methods to mate 3-D printed filaments to commercial TIMS filament assemblies, and initial durability studies of heated filaments under high vacuum conditions. In terms of project viability, we found incorporation of graphene materials into a typical rhenium filament yields ionization efficiencies on par with that of bead loaded samples. We also found reduced graphene oxide slurries can be 3-D printed into small form factor filament shapes that can be mated with commercial TIMS filament posts. Finally, preliminary data has been collected that demonstrates pure graphene filaments can be heated in the source chamber of a commercial TIMS instrument to temperatures in excess of 1500 K with high temperature operation in excess of 4 hours.

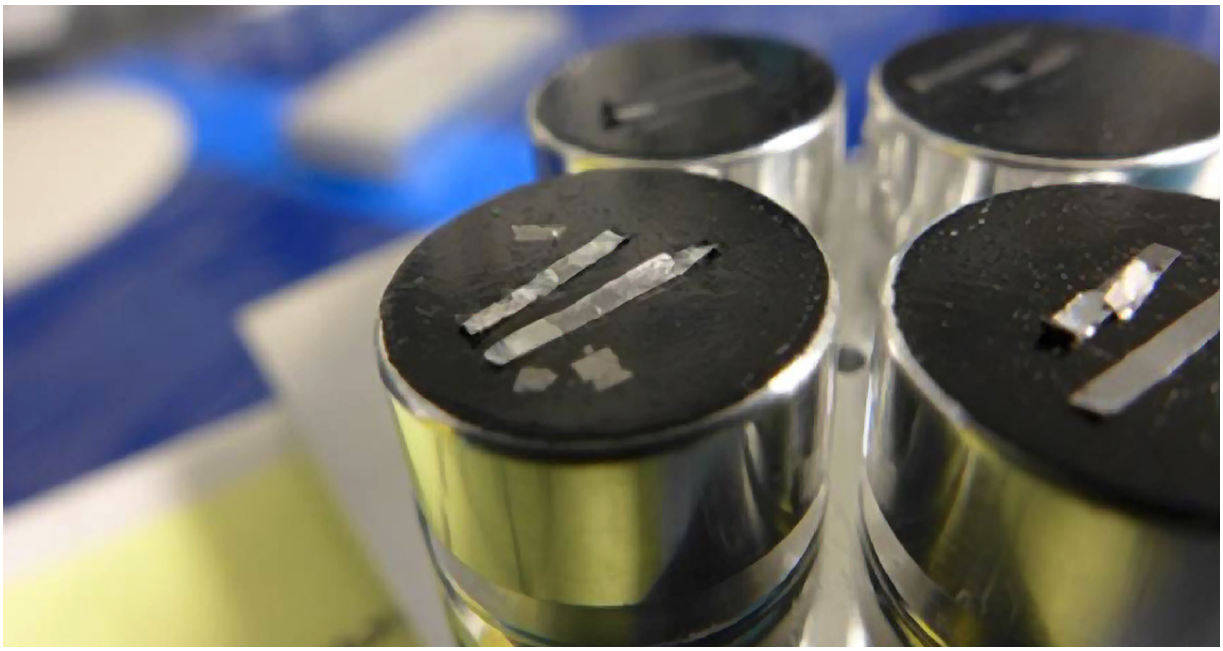

Figure 2: 3-D printed RGO filament mounted on a commercial TIMS post assemble

APPROACH

A two pronged research approach was taken in order to quickly establish project viability while also laying the ground work for slower maturing R&D goals. In regard to the former, an initial study of standard Re filaments coated with graphene oxide (GO) was undertaken to screen for potentially negative effects of GO on Pu or U ionization. Results from Pu samples directly loaded onto these hybrid filaments showed reasonably good ionization efficiencies, on par with the standard method of using bead loaded samples, and suggested filaments constructed entirely from GO or other graphene type materials would be compatible with typical TIMS analytical workflows.

With positive results from the viability study, efforts were shifted to developing the technical expertise required to reproducibly generate small form factor filaments for TIMS analysis. Multiple synthetic parameters (e.g., ink viscosity, printing speeds, drying times, pre-annealing temperature rates, etc.) were systematically varied to determine optimal filament robustness and durability. R&D associated with attachment of the 3-D printed graphene filaments to commercial TIMS filament assemblies was also conducted.

RESULTS/DISCUSSION

A commercial source of GO/water slurries was identified and initial samples were procured and analyzed. Semi-quantitative ICP-MS found trace amounts of Mn, suggesting Hummers[13] or a modified Hummers[14] method was used for GO production, as well as Na, Mg, and potentially Au. The level of uranium in the RGO slurry was found to be at the level of the blank (Figure 3), which is indicative of sub-1 ppm uranium content in the neat GO paste. This is below that of the zone refined rhenium (10 ppm) typically used in TIMS analysis. Accordingly, for ultra-trace U measurements graphene based filament materials could be superior to the more traditional Re filaments.

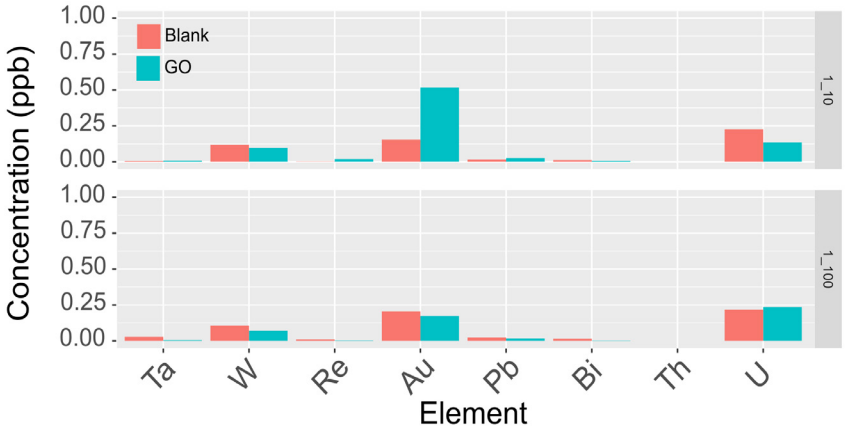

Figure 3: Select element semi-quant ICP-MS results for a 1:10 and 1:100 dilution of a 7.6 mg/mL RGO in 2% nitric acid solution

Hybrid RGO-Re filaments were characterized at the beginning of the project to assess the influence of graphene type materials on Pu ionization. In this work GO paste was applied to traditional Re filament ribbons (see Figure 2). It was found that upon heating the GO layer on top of the filament would often times delaminate exposing the Re surface. Micro-Raman characterization of the hybrid filaments after heating showed increased sp2 carbon character, which was expected[10], and is indicative of RGO formation. Small islands of sp2-like carbon were observed on areas of the Re filament where the GO/RGO film had exfoliated. The hybrid filaments were also used for Pu sample analysis. 10 pg of CRM Pu 128 was directly loaded on a small number of filaments which were then run using a typical Pu method. Ionization efficiencies for this set was approximately 0.1%, which is within the range observed for bead loaded samples. Accordingly, GO and RGO type materials seem to be compatible with TIMS analysis methodologies.

Printing of the small form factor GO filaments using commercially sourced 3-D instrumentation was found to be relatively straight forward. Difficulty was encountered trying to maintain the 3-D printed shape during the pre-annealing step. This step is required to ensure the filaments are sufficiently conductive for Joule heating in a commercial TIMS source chamber. A precise drying and thermal annealing protocol was determined that allows for filament pre-annealing with minimal loss of 3-D shape and structure. A number of different connection schemes were tested to physically and electrically attach the graphene filament to the commercial filament assembly. Three of the more successful connection motifs are shown in Figure 4. Carbon tape, copper tape, metallic paint, and Re ribbons were all tested as attachment strip materials. Re ribbons were found to be best.

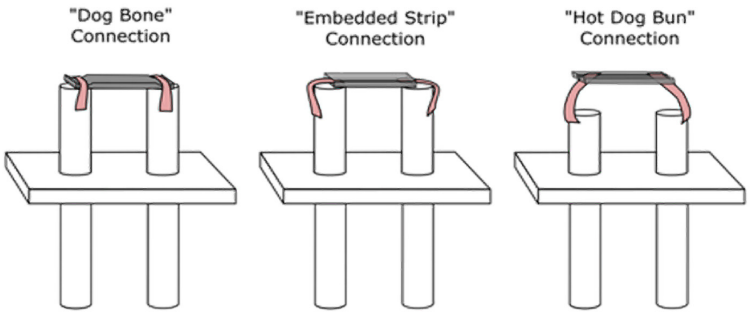

Figure 4: Three of the different connection types investigated for attaching the graphene filament to a commercial TIMS filament assembly; The pink strips are Re ribbons

FY2017 ACCOMPLISHMENTS

- Uranium content of commercial RGO found to be sub 1 ppm making it suitable substrate for ultra-trace uranium analysis.
- Ionization efficiency of hybrid Re-RGO filaments measured at approximately 0.1%
- Three different filament attachment schemes manufactured and characterized
- Graphene based filament operated in a commercial TIMS source for more than 4 hours at temperatures in excess of 1500 K
- Pu ion production observed from a 3-D printed RGO filament

FUTURE DIRECTIONS

- Iterate graphene-post attachment scheme to maximize robustness
- Injection molded filaments vs. 3-D printed
- Measure ionization efficiency of graphene based filaments for pg Pu loads
- Measure ionization efficiency of graphene based filaments for pg U loads
- Print and characterize new filament geometries (i.e. cavities)
- Develop doped/functionalized graphene materials to increase work function

REFERENCES

1. Kraiem, M.; Richter, S.; Kuhn, H.; Stefaniak, E. A.; Kerckhove, G.; Truyens, J.; Aregbe, Y. Investigation of uranium isotopic signatures in real-life particles from a nuclear facility by thermal ionization mass spectrometry. *Anal Chem* **2011,** 83, 3011-3016.

2. Boulyga, S.; Konegger-Kappel, S.; Richter, S.; Sangely, L. Mass spectrometric analysis for nuclear safeguards. *Journal of Analytical Atomic Spectrometry* **2015**, 30, 1469-1489.

3. Mayer, K.; Wallenius, M.; Varga, Z. Interviewing a Silent (Radioactive) Witness through Nuclear Forensic Analysis. *Anal Chem* **2015,** 87, 11605-11610.

4. Richter, S.; Alonso, A.; De Bolle, W.; Wellum, R.; Taylor, P. D. P. Isotopic "fingerprints" for natural uranium ore samples. *Int J Mass Spectrom* **1999,** 193, 9-14.

5. LaMont, S. P.; Shick, C. R.; Cable-Dunlap, P.; Fauth, D. J.; LaBone, T. R. Plutonium determination in bioassay samples using radiochemical thermal ionization mass spectrometry. *Journal of Radioanalytical and Nuclear Chemistry* **2005,** 263, 477-481.

6. Armstrong, C. R.; Nuessle, P. R.; Brant, H. A.; Hall, G.; Halverson, J. E.; Cadieux, J. R. Plutonium Isotopes in the Terrestrial Environment at the Savannah River Site, USA: A Long-Term Study. *Environ Sci Technol* **2015,** 49, 1286-1293.

7. Bürger, S.; Riciputi, L. R.; Turgeon, S.; Bostick, D.; McBay, E.; Lavelle, M. A high efficiency cavity ion source using TIMS for nuclear forensic analysis. *Journal of Alloys and Compounds* **2007,** 444, 660-662.

8. Duan, Y.; Danen, R. E.; Yan, X.; Steiner, R.; Cuadrado, J.; Wayne, D.; Majidi, V.; Olivares, J. A. Characterization of an improved thermal ionization cavity source for mass spectrometry. *Journal of the American Society for Mass Spectrometry* **1999,** 10, 1008-1015.

REFERENCES [CONTINUED]

9. Baruzzini, M. L.; Hall, H. L.; Watrous, M. G.; Spencer, K. J.; Stanley, F. E. Enhanced ionization efficiency in TIMS analyses of plutonium and americium using porous ion emitters. *Int J Mass Spectrom* **2017,** 412, 8-13.

10. Yao, Y.; Fu, K. K.; Yan, C.; Dai, J.; Chen, Y.; Wang, Y.; Zhang, B.; Hitz, E.; Hu, L. Three-Dimensional Printable High-Temperature and High-Rate Heaters. *ACS Nano* **2016,** 10, 5272-5279.

11.Kumar, P. V.; Bernardi, M.; Grossman, J. C. The Impact of Functionalization on the Stability, Work Function, and Photoluminescence of Reduced Graphene Oxide. *ACS Nano* **2013,** 7, 1638-1645.

12. Sygellou, L.; Paterakis, G.; Galiotis, C.; Tasis, D. Work Function Tuning of Reduced Graphene Oxide Thin Films. *The Journal of Physical Chemistry C* **2016,** 120, 281-290.

13. Hummers, W. S.; Offeman, R. E. Preparation of Graphitic Oxide. *Journal of the American Chemical Society* **1958,** 80, 1339-1339.

14. Yu, H.; Zhang, B.; Bulin, C.; Li, R.; Xing, R. High-efficient Synthesis of Graphene Oxide Based on *Improved Hummers Method.* **2016,** 6, 36143.

ACRONYMS

CRM	Certified Reference Material
GO	Graphene Oxide
ICP-MS	Inductively Coupled Plasma Mass Spectrometry
R&D	Research and Development
RGO	Reduced Graphene Oxide
TIMS	Thermal Ionization Mass Spectrometry

INTELLECTUAL PROPERTY

Invention Disclosure - SRS-16-019: *"Graphene Based Filaments for Thermal Ionization"*

Patent Application - 15/435,976: *"Graphene/Graphite-Based Filament for Thermal Ionization"*

TOTAL NUMBER OF POST-DOCTORAL RESEARCHERS

One Post-Doctoral Researcher

ROOM TEMPERATURE SIEVING OF HYDROGEN ISOTOPES USING 2-D MATERIALS

Project Team: D. Hitchcock, T. Krentz, J. Velten, H. Colon-Mercado, S. Xiao, S. Serkiz (SRNL), K. Young, E.Vogel (GA Tech), S. Creager (Clemson University)

Thrust Area: National Security

Project Start Date: 10/1/16

Project End Date: 9/30/18

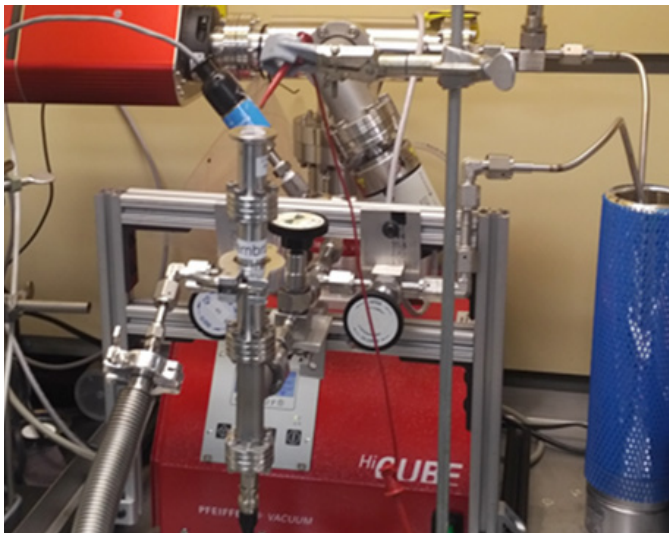

Experimental setup for isotope separation

Recent studies have shown successful separation of protium (H) and deuterium (D) in the aqueous phase using 2-D nanomaterials laminated onto proton exchange membranes (PEMs). In practice an electrochemical pump is built using the membranes where conduction is rate-limited by transport of hydrons (H+, D+, and T+) across the 2-D material. The basis for the separation is believed to be quantum tunneling through the graphene which favors the the conduction of H+ ions over D+ ions. Previous work has shown an H:D separtion factor of ~10:1 under favorable conditions and proper processing of the 2-D material.

The results of this work have shown that there is plausible merit to the claims in these previous studies with our results indicating isotope separation ratios of ~2:1 using a similar technique. Isotope separation measurements on this system are not simple due to experimental artifacts and analytical limitations. Therefore much of the effort in this FY was spent on fabricating membranes and building an apparatus for H:D separation measurements.

FY2017 OBJECTIVES

TASK ONE
Fabricate graphene coated Nafion membranes

TASK TWO
Characterize graphene films transferred to Nafion membranes by microscopy and Raman spectroscopy

TASK THREE
Build an apparatus for H/D isotope separations

TASK FOUR
Demonstrate H/D separation in an aqueous phase

TASK FIVE
Begin development of a membrane scale up approach

INTRODUCTION

Traditional techniques for hydrogen isotope separation are all based in kinetic isotope effects that are energy intensive; require low temperatures, a large footprint, or some combination of the three. Recent work has shown that 2-D materials such as graphene and hexagonal boron nitride (hBN) can act as an isotopic sieve at room temperature and, thus, provide a means of efficiently separating hydrogen isotopes. In particular one study has shown successful separation of protium (H) and deuterium (D) in the aqueous phase, with separation ratios on the order of 10:1.[1]

This process is believed to be governed by a quantum tunneling mechanism and utilizes continuous sheets of 2-D materials with no holes or defects. This is fundamentally different from the approach taken by most graphene based or intercalated separation membranes which use holes in the structure (i.e., lattice defects) or spaces between nanostructures in a composite. In the electrochemical pumping configuration, a cell is formed using a proton exchange membrane (PEM) coated with a 2-D material. A potential applied across the PEM drives ions (hydrons) to migrate across the membrane. The separation occurs as ions are then driven (quantum tunnel) across the 2-D material.

APPROACH

The goal of this project is to investigate the feasibility of 2-D materials as isotopic sieves for separation of hydrogen isotopes while simultaneously investigating the fabrication, optimization, and scale up of 2-D material Proton Exchange Membranes.

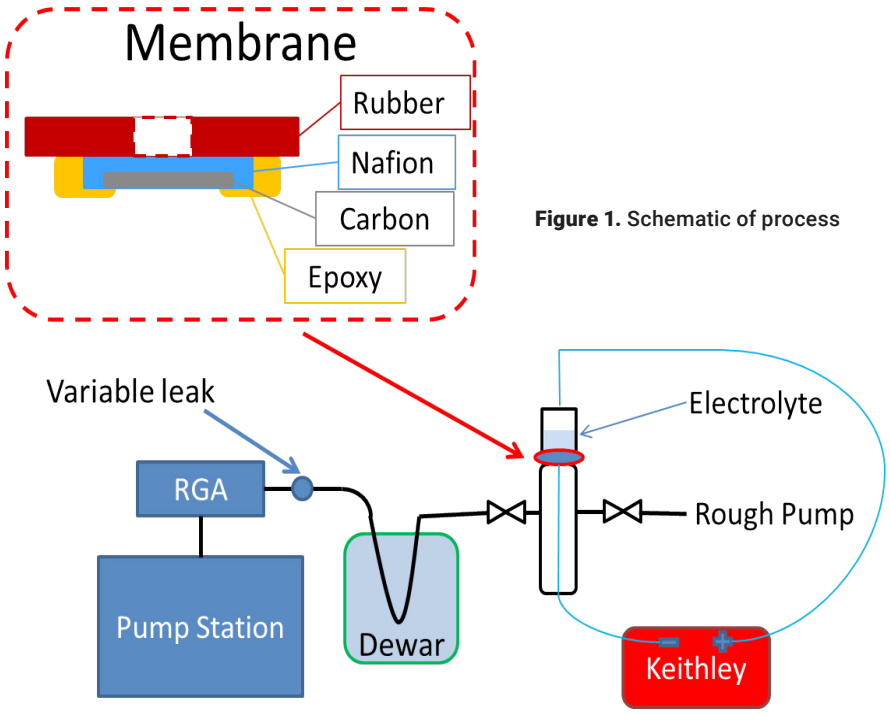

Figure 1. Schematic of process

Initial milestones were to recreate the apparatus discussed in the open literature and to develop greater understanding of the mechanism(s) governing processes described in the literature.

In this configuration hydrons are driven by a potential supplied by Keithley power supply from liquid side of the cell (0.1 M HCl/DCl electrolyte) through the membrane into the vacuum chamber. In the vacuum chamber hydrogen is detected using a quadrupole mass spectrometer (Figure 1).

In a limited scope through a Clemson University contract, research methods using graphene and related materials as isotopic sieves in water electrolysis cells have also been explored. Clemson was able to keep a graduate student employed during the summer and the feasibility, scopes, and lab setup needs were investigated for isotopic selectivity on hydrogen evolution with graphene sieving in the Membrane Electrode Assemblies (MEAs) of PEMs. The Clemson group is well known as experts on MEAs and PEMs, and SRNL has benefited from their water electrolysis cell design.

RESULTS/DISCUSSION

Graphene was grown on copper using chemical vapor deposition (CVD) and subsequently transferred to the surface of commercial Nafion membranes. Before transferring the graphene to Nafion membranes its quality and, in particular, the amount of multilayer graphene was characterized using a combination of microscopy and spectroscopy. Scanning electron microscope (SEM) images were collected before and after < 1 nm HfO_2 was deposited on top of the graphene by Atomic Layer Deposition (ALD). The deposited HfO_2 is preferentially deposited on the multilayer regions, grain boundaries, and lattice defects and thus adds contrast to SEM images for these areas. This contrast technique facilitates digital image analysis using ImageJ (Figure 2b) to quantify the high contrast area. Using this technique multilayergraphene was estimated to cover 14.2% of the sample.

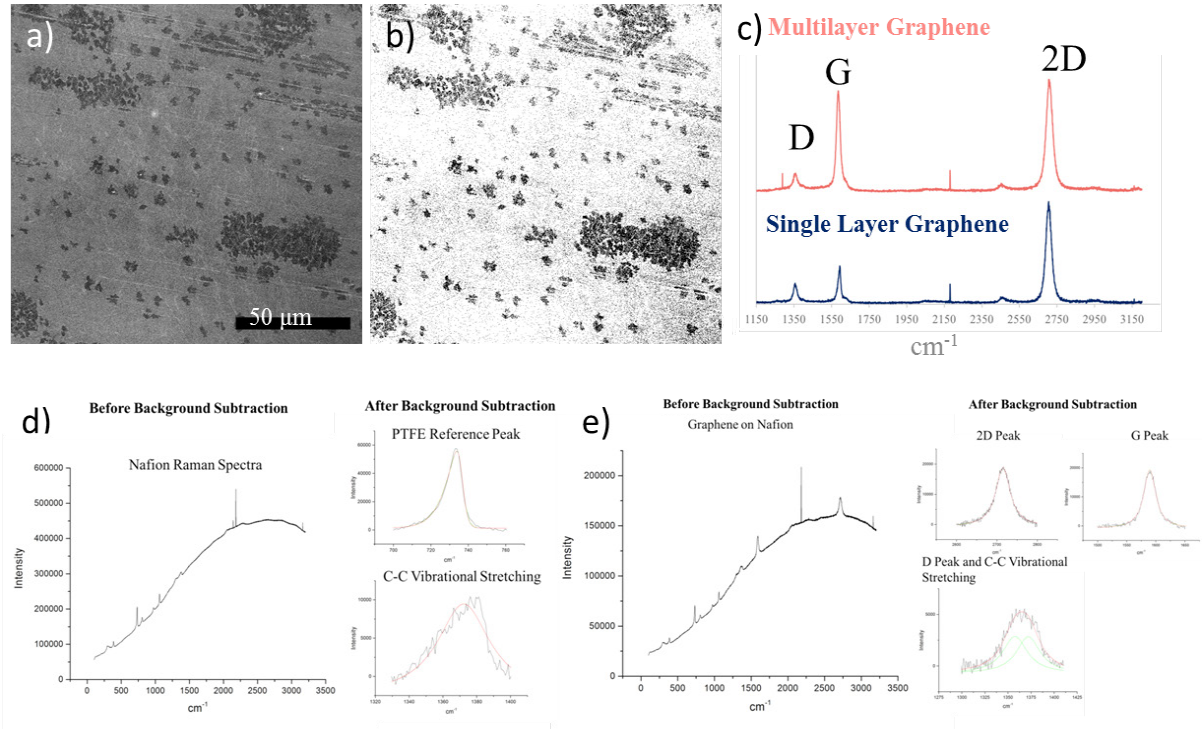

Figure 2. An ImageJ analysis (b) of SEM images (a) can quantify the density of multilayer regions and is confirmed by Raman map scans (c) Raman Maps: 14 % multilayer SEM: 14.2% multilayer (d) Raman spectra Nafion without graphene. (e) Raman spectra of graphene on Nafion

To verify the technique Raman spectra were taken and analyzed to estimate the amount of mulitilayer graphene through deconvolution of the 2-D peak. The Raman maps displayed 14% multilayer in the sample. This agreement between the techniques suggests that the ALD/SEM technique is a viable method to quantify multilayer regions in arbitrarily large graphene samples.

Generally, graphene transfer methods are optimized for hard surfaces where overall cleanliness of the final product is the governing criteria. In this case however, we had to optimize the transfer conditions to minimize stress on the graphene in order to avoid the introduction of defects into the membrane. Raman spectroscopy was used to characterize the graphene after the transfer. It is well known that graphene can be characterized using Raman spectroscopy; however, the underlying substrate plays a large role in properly measuring the characteristic peaks.[2] In the case of graphene-Nafion composites the large background signal from Nafion results in low intensity peaks and difficulty focusing both of which make measurements of the graphene quality particularly difficult.

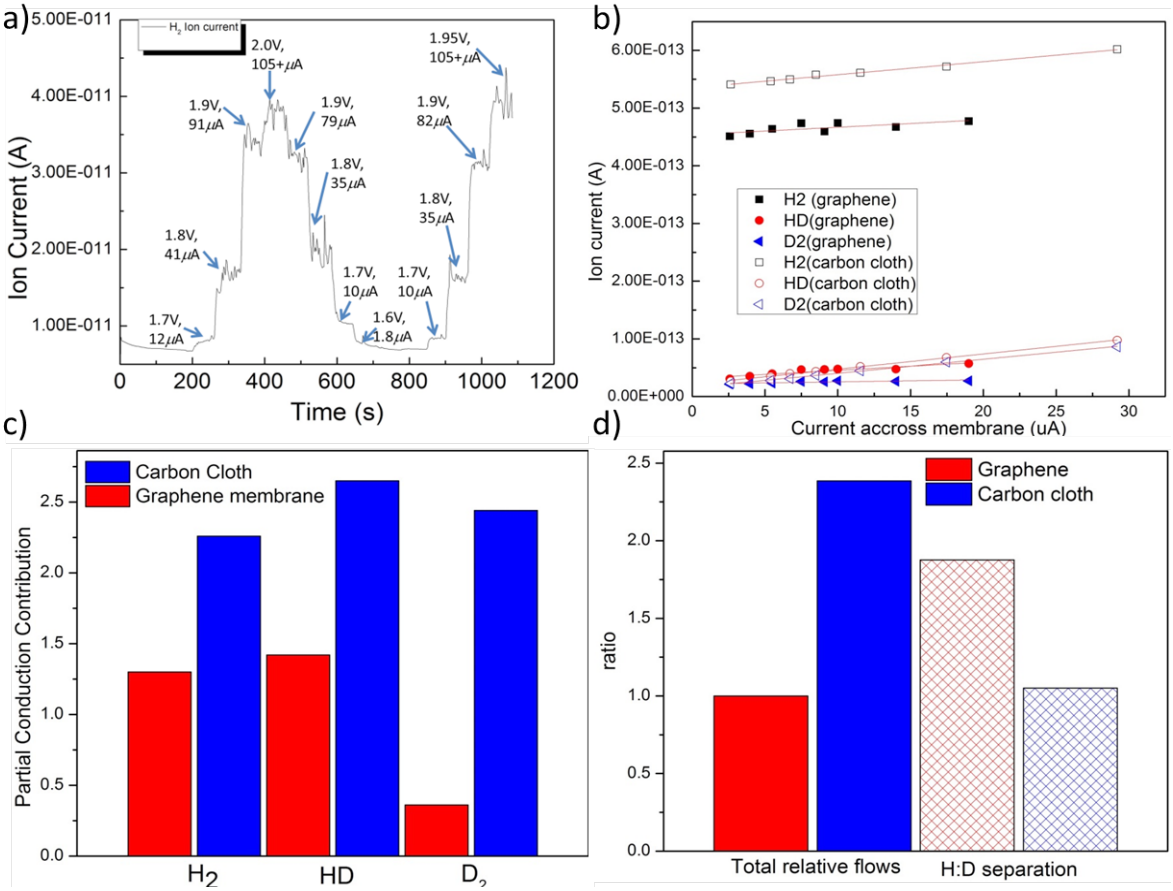

Figure 3. a) Sample raw data set **b)** Ion current as a function of cell current measured using the same solution with both carbon cloth membrane and graphene membranes **c)** Partial conduction contributions and **d)** total flow and separation ratios

Furthermore, Nafion has several characteristic Raman peaks (Figure 2d), one of which is a low intensity, broad peak found at ~1380 cm^{-1}, very close to the D peak of the graphene, thus necessitating peak fitting to resolve any usable information about the D peak (Figure 2d and e, note: the sharp lines near ~2200 cm^{-1} are an artifact of the Raman measurement).[3,4]

Figure 3a shows a sample H_2O:D_2O data set, collected with the experimental setup shown in Figure 1, where each plateau corresponds to a data point in the ion current versus membrane current plot shown in Figure 3b. Figure 3b shows the ion current as a function of cell current measured using the same solution with both a carbon cloth membrane (baseline, where no 2-D material based separation should be occurring) and a graphene membrane. Using the same solution with both a carbon cloth membrane and a graphene membrane allowed for the direct comparison ofdata without having to consider differences in detector efficiency for different isotopes in our mass spectrometer. Figure 3c shows the partial conduction contribution from different species taken as the slopes of the data in 3b to remove contributions from the chamber background, because the expected H_2 background in the chamber is an order of magnitude larger than the HD or D_2 background. Finally, Figure 3d shows the total hydron flow and separation ratios for the setup. As expected the total hydron flux across the carbon cloth membrane is significantly larger than the graphene membrane due to the increased conductivity. The measured separation factor of ~2 is significantly smaller than the 10 reported in the literature, and can most likely be attributed to imperfections in our membranes from the transfer and fabrication process.

FY2017 ACCOMPLISHMENTS

- **Synthesis**
  - Single layer graphene sheets have been synthesized via CVD
  - CVD graphene has been transferred to Nafion
- **Characterization**
  - Raman spectra collected on as-synthesized graphene, and graphene on Nafion
  - New method for estimating the amount of multilayer graphene over large areas
- **Separation Measurements**
  - Designed and built a setup to test isotope separation in the electrochemical pumping configuration
- **Membrane Scale Up**
  - Investigating direct growth of graphene on Cu coated Si-N grids
  - If successful, this route would represent a "transferless" membrane fabrication technique

FUTURE DIRECTIONS

- Optimization and scale up of the graphene transfer and membrane fabrication process
- **Characterization**
  - Continue studying Raman spectra collected on as-synthesized graphene, and graphene on Nafion
- **Separation Measurements**
  - H/D/T separation measurements

PUBLICATIONS

1. J. Velten, D. Hitchcock, T. Krentz, M. Young, and E. Vogel (September, 2017) "Two DimensionalNanomaterials for Water Detritiation and Isotope Separation" presented at the 2nd Asia-PacificSymposium on Tritium Science (APSOT-2), Livermore Valley, CA

2. K. Young, C. Joiner, D. Hitchcock, S. Serkiz, E. Vogel. (November, 2017)"A Facile Approach toMapping Graphene Grain Boundaries and Multilayer Regions on Copper" Accepted forpresentation at the fall MRS meeting, Boston, MA

REFERENCES

1. Lozada-Hidalgo *et al.,* "Sieving hydrogen isotopes through two-dimensional crystals" Science 351, 6268, 68-70 (2016)List any references used in the report.

2. Z. Ni, *et al.*, "Raman Spectroscopy and Imaging of Graphene," Nano Res. 1 (2008) 273-291.

3. A. Gruger, *et al.*, "Nanostructure of Nafion membranes at different states of hydration an IR andRaman study,", Vibrational Spectroscopy 26 (2001) 215-225.

4. J. Zeng, *et al.*, "In Situ Surface-Enhanced Raman Spectroscopic Studies of Nafion Adsorption onAu and Pt Electrodes," Langmuir 28 (2012), 957-964.study,", Vibrational Spectroscopy 26 (2001) 215-225.

ACRONYMS

ALD	Atomic Layer Deposition
CVD	Chemical Vapor Deposition
MEA	Membrane Electrode Assemblies
PEM	Proton Exchange Membrane
SEM	Scanning Electron Microscope
hBN	Hexagonal Boron Nitride

TOTAL NUMBER OF POST-DOCTORAL RESEARCHERS

1. One postdoctoral researcher (Josef Velten), and one graduate student (Katie Young, GA Tech) were involved with this project.

EVALUATION AND UNCERTAINTY OF A NEW METHOD TO DETECT SUSPECTED NUCLEAR AND WMD ACTIVITY

Project Team: R. Kurzeja, D. Werth, R. Buckley
Thrust Area: National Security
Project Type: Standard
Project Start Date: 10/1/16
Project End Date: 9/30/17

The detection of surreptitious production and testing of Weapons of Mass Destruction (WMD) is hampered by low-signal-to-noise measurements which frustrates focused analyses. The uncertainty associated with a new method to detect the development and testing of WMD from downwind chemical measurements has been calculated. The probability of origin of radioxenon from the February 2013 underground nuclear test in North Korea was calculated from an ensemble of atmospheric model simulations that captures the range of variability, i.e., uncertainty. It was found that the uncertainties in the method are low enough to yield reasonable conclusions about chemical origin, even at low signal-to-noise. Furthermore, the behavior of the method was predictable for a range of signal strengths.

FY2017 OBJECTIVES

TASK ONE
Evaluate the predicted probabilities of origin and uncertainties with an ensemble of model simulations

TASK TWO
Evaluate behavior for very low signal strength

TASK THREE
Present the method to potential users in the Intel community

TASK FOUR
Extend the presentation to a wider audience in the atmospheric science community

INTRODUCTION

The search for indications of WMD activity is difficult because small amounts of chemical are involved and the operation is concealed. This results in weak signals within a complicated background of information from upwind and global sources. The net effect is to discourage systematic analysis except for cases with a clearly detected signal. Furthermore, efforts for new measurement campaigns are poorly received because of low confidence in significant improvement.

APPROACH

SRNL's new approach is based on the assumption that atmospheric transport of a chemical from a source to a receptor produces a unique signature, which can be used as a template to analyze a data series for evidence of the source. The method can be applied to arbitrary sampling and multiple signals. The method also yields the probability of origin which is essential for weak signals. SRNL's new method was used to determine the probability that radioxenon detected in Russia originated from the February 2013 underground test in North Korea. The derived probabilities are based on the signal shape and arrival time at the receptor. This work calculates the uncertainties in these predictions from an ensemble of model simulations. Figure 1 shows measured radioxenon data and also the model prediction from which the search template is generated. The figure illustrates various signals present in the data, some of which resemble model predictions.

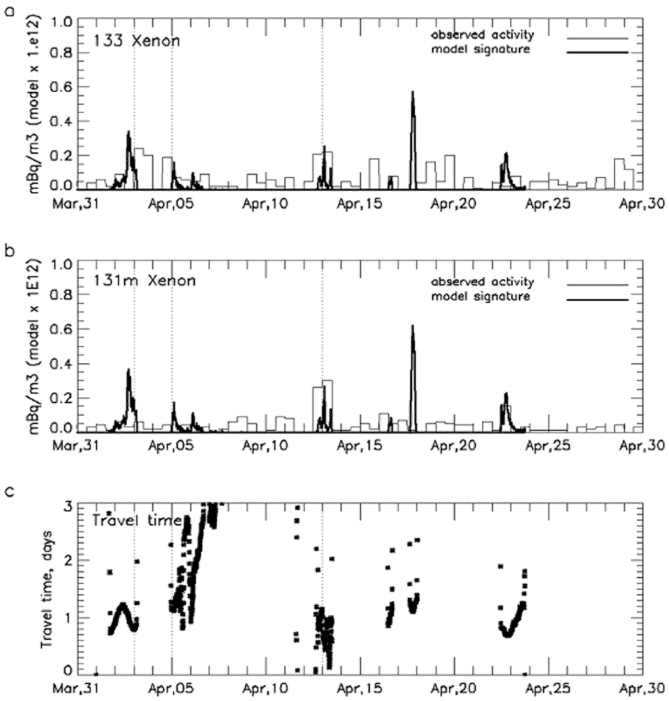

Figure 1. **(top)** Measured ^{133}Xenon activity *(thin lines)* plus model predictions *(heavy lines)* **(middle)** As above but for ^{131m}Xenon **(bottom)** Travel time in days from source to receptor

RESULTS/ DISCUSSION

The results (Figure 2) showed that the uncertainties of origin are small enough to yield confidence in the calculated probabilities. Furthermore, we showed that the method remains reliable as the signal strength is reduced to background values. This implies that results for a range of signal strengths will be interpreted with the appropriate level of confidence.

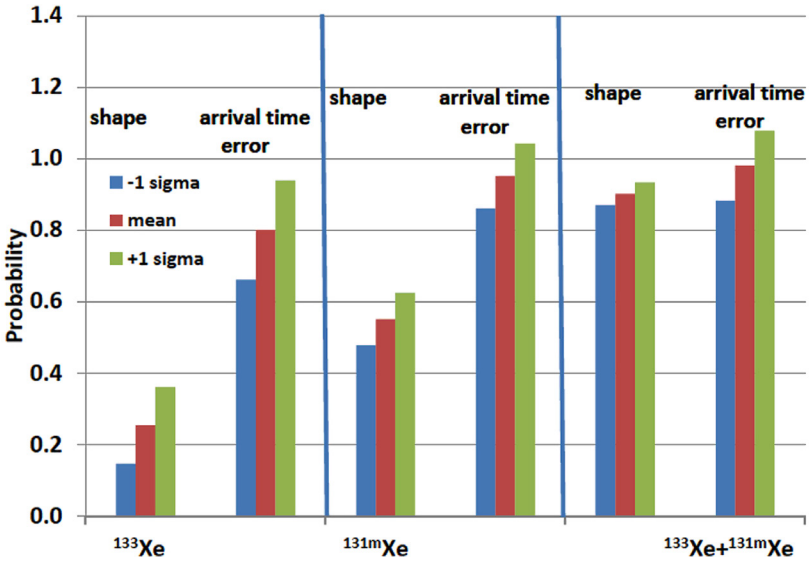

Figure 2. Probabilities plus and minus one-sigma uncertainty is shown for each isotope and both isotopes. The first probability is based on the similarity between the predicted and measured plume shapes. The second is based on the error in the predicted center of mass arrival time. The average of these two probabilities gives the net probability of origin. The two probabilities for ^{133}Xenon alone (left red bars) are 0.27 and 0.8, respectively. The net probability (right red bars) =(0.27+0.8)/2. = 0.53.

FY2017 ACCOMPLISHMENTS

- A paper describing the method has been submitted to *Atmospheric Environment*.
- **The scope of work for the project was extended to satisfy interest of the atmospheric transport community. A manuscript is in draft status and will be submitted to the** *Journal of Applied Meteorology and Climatology*.
- The method is the basis for funding requests directed to DOE's National Nuclear Security Administration and other intelligence organizations.

FUTURE DIRECTIONS

- The method should be applied to other signals of interest, e.g., optical, electromagnetic, acoustic.
- Another useful test of the method would be the detection of a weak signal added to a measured complex background, which is particularly relevant to the WMD problem.

PUBLICATIONS

1. Uncertainty in mesoscale modeling of radioxenon transport and dispersion after the Feb 2012 underground test in North Korea. To be submitted to the *Journal of Applied Meteorology and Climatology*.

2. Detection of nuclear testing from surface concentration measurements: Analysis of radioxenon from the February 2013 underground test in North Korea. Submitted to *Atmospheric Environment*.

3.A new method to detect nuclear testing with atmospheric measurements: The Feb 2013 underground test in North Korea. Presented at George Mason University, 21'st Conf. on Atmospheric Transport and Dispersion Modeling, 2017

ACRONYMS

WMD Weapons of Mass Destruction

ORGANICALLY BOUND TRITIUM BEHAVIOR IN TREES AND PLANTS

Project Team: W. Kuhne, M.Duff, A. Swindle, N. Halverson, B. Viner

Thrust Area: National Security/ Environmental Stewardship

Project Start Date: 10/1/16

Project End Date: 9/30/17

Radioactive tritium (^{3}H or T) is an isotope of hydrogen (H) associated with nuclear fuel cycle activities (i.e., reactor operation, fuel reprocessing and legacy waste). In plants and trees, the exposure to atmospheric T can result in the formation of organically bound tritium (OBT) in tissues due to normal metabolic processes. Tritiated water or HTO is also found in these tissues. An identification of the OBT accumulation behavior in these tissues could support its use as a potential signature for recent and historic nuclear activity. The focus of this work was to investigate OBT in trees and plants using a Raddec^{LTD} Pyrolyser combustion furnace and 1220 Quantulus Liquid Scintillation Counter. The fractions of HTO, exchangeable and non-exchangeable OBT in the plant and tree tissues were investigated in laboratory grown Brassica, carrots, radish, and lettuce. Cores were collected from pines, oaks, and sweet gum trees found on the Savannah River Site. Preliminary analyses of data indicate that extraction of HTO, E-OBT, and NE-OBT as independent fractions is possible with the Pyrolyser but further refinement of protocols is necessary.

FY2017 OBJECTIVES

TASK ONE

Conduct lab studies with plants to examine their ability to accumulate T as HTO and to convert it to an organically-bound form. Conversion of OBT will be examined relative to T exposure time (hours to days). Study plants will include: *Brassica napus* (mustard), carrot tops, lettuce leaves, and radish leaves. The installation and operation of the Pyrolyser which was purchased for this project was also part of this objective.

TASK TWO

Tree cores from local pines and hardwoods will be investigated for OBT accumulation and behavior within the individual tree rings of the trees growth. The newly installed Pyrolyser will be used for this purpose as well.

INTRODUCTION

Radioactive tritium (^{3}H or T) is an isotope of hydrogen (H) produced by nuclear fuel cycle activities (i.e. reactor operation, fuel reprocessing and legacy waste). Tritium found in the environment is either tritium gas (HT) or tritium bound to water (HTO). HTO can be incorporated into the tissues of an organism and quickly be used in various metabolic processes including photosynthesis. Through these metabolic processes the T becomes incorporated in organic compounds such as sugars, proteins, starches, lipids, amino acids, and other cellular structures **(1).** Incorporation into such compounds has the potential for longer retention times in the organism, however this is not well understood given that the biological half-life of HTO in living organisms is considered to be on the order of 10-14 days **(2).**

The two primary types of OBT investigated in this study are exchangeable OBT (E-OBT) which include T bound to oxygen (O), sulfur (S), or nitrogen (N) and non-exchangeable OBT (NE-OBT) where T is bound to carbon (C) **(1).** The E-OBT is thought to undergo rapid exchanges with surrounding hydrogen and has been estimated to amount to 20% of the total OBT (E-OBT + NE-OBT) in an organism. Fractionation and measurement of the E-OBT and NE-OBT has historically been a difficult process and thus most measurements found in the literature are simply a deduced calculation of E-OBT by measuring the Total OBT – NE-OBT **(3).** Recent advances in sample preparation and assay techniques utilize the isotopic exchange of hydrogen isotopes by washing the dry fraction with T-free water, then a second extraction of water to measure the E-OBT, followed by combustion of the NE-OBT.

The purchase and installation of the Pyrolyser combustion furnace and access to a Quantulus low level counting liquid scintillation counter (LSC) provide SRNL with the ability to measure the difficult fractions of E-OBT and NE-OBT in complex biological samples. The ability to grow plants in the laboratory under controlled conditions allows us to investigate the OBT behavior in several types of plant tissues and the effects T depuration on measured OBT levels. These data are needed to address the fractions of T that contribute to total T dose if these plants were to be used as an edible food source. Additionally, little information is available on the effects of chronic exposure of HTO on plant and trees. The availability of trees that have been chronically exposed to HTO through the SRS's Mixed Waste Management Facility (MWMF) phytoremediation project provides a valuable opportunity to investigate the potential for bioaccumulation of OBT and its fractions in tree tissues.

Tree rings (cores) have been pursued for their ability to be a source of historical T in the ground **(4, 5).** It is thought that cellulose as "organically-bound T" form is stable and not subject to changes over time in the tree. But not all research has come to an agreement on this. The preservation of T release levels may be species dependent. For example in 2008, OBT levels in aspen tree rings were sampled near SRB Technologies[1], Ontario, Canada and were found to reflect historic T levels in stack emissions whereas 2008 OBT levels in poplar tree rings at Darlington Nuclear Generating Station in Ontario did not **(5).** The tissue HTO and OBT levels in general vegetation were highly variable and in the few thousand to tens of thousands of pCi T L^{-1} in these studies. Love et al. 2003 **(6)** found that OBT in tree rings of pine and eucalyptus reflected atmospheric water vapor monitoring data in Berkeley, CA, USA.[2] These trees were < 100 m from the stack.[3]

APPROACH

Low level T water was collected from the MWMF retention pond. The water was mixed (50:50) with a hydroponic growth media and delivered in a known volume to growing plants. Seeds for carrots, lettuce, radish (Atlee Burpee & Co.), and Brassica (Outside Pride) were grown in pots with a 4:1 mix of Promix PGX soil (Premier Horticulture) and Perlite (Hoffman Horticultural, Good Earth). Pots (4.25" X 4.25" X 5" Kordlok, ITML Horticultural Products) were soaked in 1' deep DI water for at least 3 days (d) prior to seeding. Pots contained 100 g of soil:perlite mixture. Plants were 28 d of age prior to treatment. Plants were treated twice weekly for 3 weeks (wks) with more than 2 wks of depuration with control water. Leaf tissue was harvested and immediately frozen at -80 °C to preserve all water present in the sample. Tree cores were extracted from native grown pine, oak, and sweet gum from the MWMF.

Two cores were extracted from each tree using a Haglöf increment borer with a standard diameter 0.20" (5.15 mm). Sampling height was the standard breast-height. Cores were kept in paper straws at -80 °C until analysis.

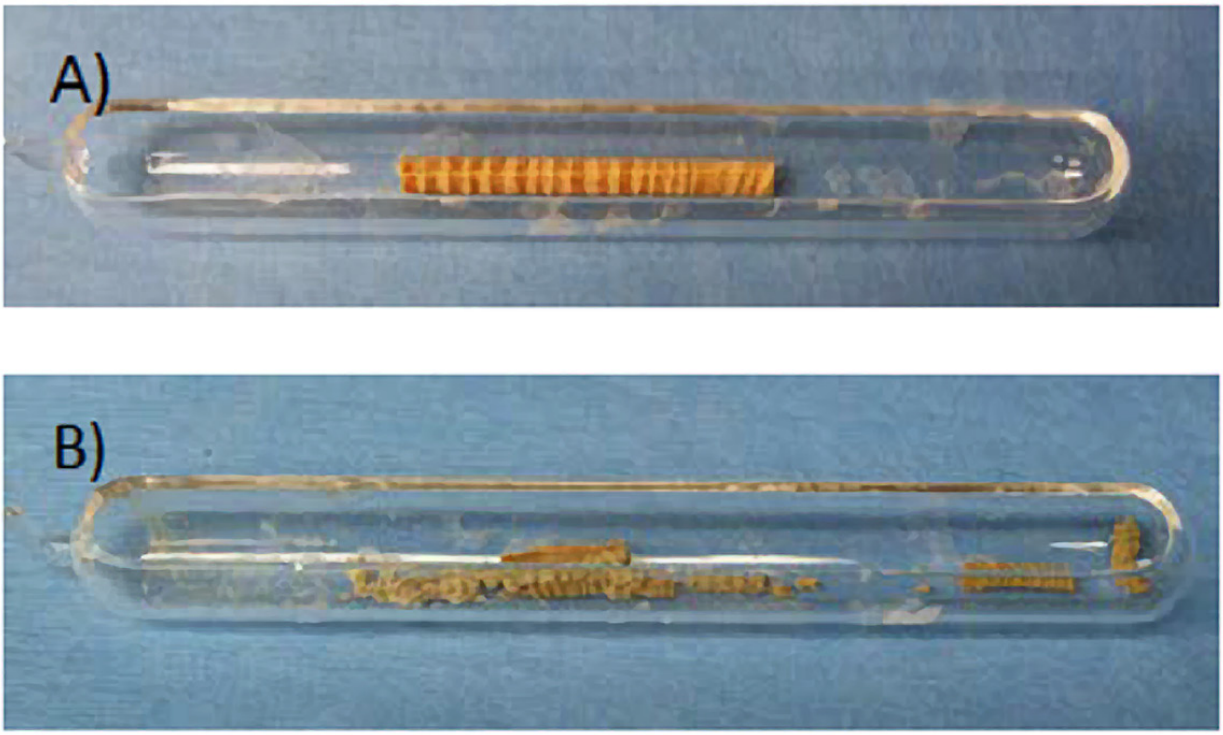

Figure 1. A) Original core just removed from the -80°C freezer B) Core dried at 150°C for 1.5 hr with HTO removed. E-OBT will be removed by rinsing the sample with T free water

For analyses a known mass (g) of tissue was placed into a sample boat and placed into an individual silica glass working tube within the sample zone of the A) Raddec Pyrolyser Trio™ System (Raddec Ltd, Southampton, UK).

Step 1 was to collect the total HTO in the sample by passing a warm stream of air (200 mL min^{-1}) over the sample while being heated at a rate of 3 °C min^{-1} to 150 °C and hold for 1.5 h (Figure 1A). During this time the water was being collected in a bubbler trap containing 10 mL of 0.1 M HNO_3.

Step 2 was to remove the E-OBT by rinsing the dried sample with T free water (~9 mL) (Figure 1B). The overlying T free water containing E-OBT was removed and placed into a liquid scintillation cocktail vial. The sample was returned to sample zone 1 in the Pyrolyser and the temperature was increased to 500 °C at a rate of 3 °C min^{-1}.

Step 3: Once the sample zone had reached 500 °C, $O_{2(g)}$ (50% in air) was introduced to accelerate oxidation of the remaining sample. The sample zone temperature was increased to 600 °C at a rate of 3 °C min^{-1} and held for 1.5 h to fully combust the remaining material. The liberated gases pass through a catalyst zone which is filled with 10 g of platinum-alumina catalyst pellets to oxidize any organic combustion products to H_2O. Any water vapor (NE-OBT) that is trapped in a bubbler trap containing 10 mL of 0.1 M HNO_3 and that prevents the co-trapping of CO_2.

RESULTS/DISCUSSION

A limited number of samples were able to be analyzed due to the time it took to procure and install the Pyrolyser in the laboratory. Preliminary results with carrot leaves indicate that plant exposure to HTO for 3 wks showed slight visual differences in mean biomass production relative to control (Figure 2). However, no statistically significant differences in fresh weight (FW) mean growth were measured between treatment and control groups. The Pyrolyser recovery efficiency for lettuce leaves was ~82% and values indicated that the levels of HTO in lettuce leaves were nearly 20X higher than control leaves after 1 wk of treatment. The E-OBT in lettuce leaves were similar to control plants for wk 1 (ratio of 1.01) and (depuration) wk 4 (ratio of 1.30). The NE-OBT in treatment lettuce leaves show slightly elevated levels in wk 1 (ratio of 2.40) and (depuration) wk 4 (ratio of 1.50) versus the controls. Ratios of the total OBT/HTO for lettuce are ~0.20 during treatment wks but they exceeded 1 after depuration. The ratios for total OBT/HTO for control lettuce leaves were >2.50.

Figure 2. Carrot biomass differences

	HTO (pCi/g)	E-OBT (pCi/g)	NE-OBT (pCi/g)	Total OBT/HTO (pCi/g)
Core A Total Core	13.55±0.18	3.00±0.09	2.28±0.07	0.39
Core B (Years 1918-1938)	2.01±0.06	0.37±0.02	0.26±0.01	0.31
Core B (Years 1939-1958)	3.82±0.09	0.52±0.02	0.46±0.02	0.26
Core B (Years 1959-1978)	1.74±0.06	0.55±0.03	0.43±0.02	0.56
Core B (Years 1979-1998)	2.07±0.06	0.54±0.03	0.46±0.02	0.48
Core B (Years 1999-2016)	2.19±0.06	0.85±0.04	0.70±0.03	0.71

Table 1. Results from loblolly pine tree (sister) cores A and B

The preliminary results from the lab studies with lettuce showed that OBT was retained after depuration and primarily HTO was lost during depuration. These findings suggest OBT (E-OBT in particular) was not highly labile in lettuce leaves during the time frame of this study.

Preliminary results for pine tree cores taken from the same tree show that analysis of a total core versus individual 20-year incremental pieces result in >80% efficiency in recovery of HTO, E-OBT, and NE-OBT (Table 1). Further work on the data is needed for decay corrections on the older years of the tree cores.

FY2017 ACCOMPLISHMENTS

- Preliminary results from lab studies with lettuce show OBT is retained after depuration and that HTO is primarily lost during depuration. These findings suggest that OBT (E-OBT in particular) is not highly labile in lettuce leaves during the timeframe of this study.
- Extraction efficiency of T from plant tissues and tree cores show >80% recovery using the Pyrolyser combustion furnace.
- Preliminary analyses of data indicate that extraction of HTO, E-OBT, and NE-OBT as independent fractions is possible with the Pyrolyser but further refinement of protocols is necessary.

FUTURE DIRECTIONS

- Installation of the Pyrolyser combustion furnace develops SRNL's expertise in extracting and measuring HTO and the OBT fractions in a wide variety of sample matrices from plants to concrete. This effort demonstrates the development of expertise that can assist in EM remediation and decommissioning projects.
- SRNL continues to partner with INL to develop additional business opportunities for T and as well as side-by-side ^{14}C analyses (as part of another INL LDRD scope).
- This work provides key data for SRNL's Atmospheric Technologies Section (through Dr. Brian Viner), who will use the product of this LDRD work to apply for additional funding from DOE for dispersion modeling of HTO plumes at SRS. The intent of this proposed collaborative work (Viner, Kuhne, Duff, et al.) is to identify a plausible deposition velocity value for T based on a request by Defense Nuclear Facility Safety Board.

REFERENCES

1. S. B. Kim, N. Baglan, P. A. Davis, Current understanding of organically bound tritium (OBT) in the environment. *Journal of Environmental Radioactivity* **126,** 83-91 (2013).

2. C. Boyer et al., Tritium in plants: A review of current knowledge. *Environmental and Experimental Botany* **67,** 34-51 (2009).

3. P. Le Goff, M. Fromm, L. Vichot, P.-M. Badot, P. Guétat, Isotopic fractionation of tritium in biological systems. *Environment Internationa*l **65**, 116-126 (2014).

4. T. Yamada, K. Yasuike, M. Itoh, N. Kiriyama, K. Komura, Temporal variation of tritium concentration in tree-ring cellulose. *Journal of Radioanalytical Nuclear Chemistry* **261,** 9-17 (2005).

5. C. N. S. Commission, "Enviornmental face of tritium in soil and vegetation. Part of the tritium studies project," (Ottawa, Canada, 2013).

6. A. H. Love, J. R. Hunt, J. P. Knezovich, Reconstructing tritium exposure using tree rings at Lawrence Berkeley National Laboratory, California. *Environmental Science and Technology* **37,** 4330-4335 (2003).

ACRONYMS

d	Day
E-OBT	Exchangeable Organically Bound Tritium
FW	Fresh weight
HT	Tritium gas
HTO	Free Tritium Water
LSC	Liquid scintillation counter
MWMF	Mixed Waste Management Facility
NE-OBT	Non-exchangeable Organically Bound Tritium
OBT	Organically Bound Tritium
SRS	Savannah River Site
T	Tritium
wk	Week

SYNCHROTRON BASED MICROSTRUCTURAL CHARACTERIZATION METHOD DEVELOPMENT FOR Pu OXIDES

Project Team: J. Venzie (Primary), M.A. DeVore II, T.C. Shehee
Collaborators: J. Fortner (ANL), B. Powell, L. Schuller-Nickels (Clemson)
Thrust Area: National Security
Project Type: Standard
Project Start Date: 10/1/16
Project End Date: 9/30/18

Advanced microstructural analysis techniques will be used to probe the internal structure of plutonium oxide particles as part of the development of new forensic signatures. Samples of plutonium oxides prepared under parametric conditions at SRNL will be shipped to Clemson University and to the Advanced Photon Source (APS) at Argonne National Laboratory for microstructural analysis using TEM (Clemson), and XRD/XRF microscopy (APS). These techniques are able to probe samples at sub-micron spectral resolution and provide information on the local crystallographic orientations, gradients, and strains.

The Advanced Photon Source currently authorizes radioactive samples in the certain beam lines of interest with appropriate double or triple containment sample holders. A significant portion of the first year of this LDRD addresses the logistical requirements at SRNL and the APS for the preparation, packaging, shipment, and residue handling of the samples. To enhance SRNL's materials characterization capabilities, the procedures, contract, and other tools will be developed in a manner that establishes a process that can be utilized by other researchers in the future.

FY2017 OBJECTIVES

FY17 efforts concentrated on the pre-experiment logistics needed to perform experiments at the Advanced Photon Source (APS) at Argonne National Laboratory (ANL).

TASK ONE
Contracts placed with Clemson and ANL

TASK TWO
Setup of shipping and receiving protocols

TASK THREE
R&D work instructions for handling at SRNL

TASK FOUR
ANL plutonium handling requirements

TASK FIVE
Consultation with beam line scientists and engagement with APS safety officers for SRNL sampleholders during visit to ANL in June 2017

TASK SIX
General user proposal (GUP) and related safety requirements/documentation for beam time experiments at APS

TASK SEVEN
Design, construct, and perform preliminary testing of a suitable Pu sample holder for shipments between laboratories.

INTRODUCTION

The pre-detonation technical nuclear forensic (TNF) community is investing in the research, development, and exploitation of new non-isotopic forensic signatures of plutonium oxide. The forensic community is interested in PuO_2 as an intermediate form in the fuel and weapons cycle, and as the most common storage form for plutonium. Isotopic signatures, while useful, only provide limited information about the provenance of plutonium oxide. The TNF community is interested in exploring chemical and morphological characteristics in order to better understand the type of flowsheet used, scale of facilities, expertise of operators, etc. Detailed material science studies of plutonium oxide are needed to advance the understanding of the crystalline properties and their relationships to macro-scale signatures.

The process by which particles grow is dependent on their crystal structures, grain size, and orientation of grains within a particle. Variations in density and microstructure of PuO_2 powder have led to differing particle sizes and morphologies (Figure 1).[1] The microstructure is controlled by calcination temperature and the physiochemical conditions of precipitation, including shape of mixing tank, valance of plutonium, mixing sequence of plutonium and oxalic acid, precipitation temperature, and molar concentrations of oxalic acid, plutonium, and nitrate.[1,2] Calcination has little effect on overall size of particle, but a great effect on surface roughness and particle morphology.

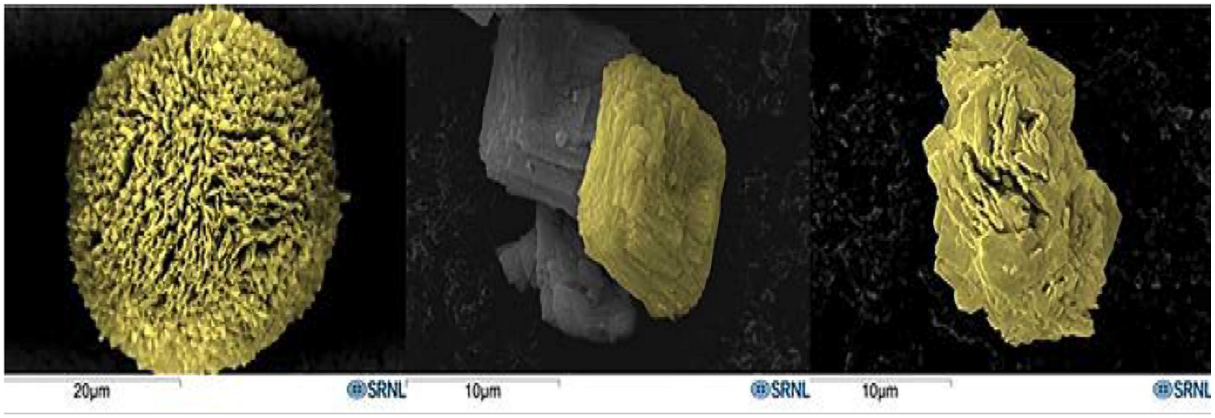

Figure 1. Three microcrystalline morphologies of PuO_2 observed in a single production batch

High sensitivity, nondestructive analysis of individual PuO_2 particles requires the use of bright sources of X-rays produced by synchrotron sources such as those produced at the APS at ANL. The light source can reveal higher resolution crystallographic mapping, more sensitive chemical analysis, and higher fidelity morphological information than any methods currently available to SRNL. APS will provide simultaneous XRD and XRF mapping of grains on a particle. These characterization techniques will provide insight into grain sizes, shapes, and orientations for further investigation. Further experiments include the use of computer-aided tomography (CAT) to provide a three-dimensional representation of each particle of interest.

APPROACH

Due to the complexity of working with plutonium samples, the administrative and procedural aspects of sending samples to APS are directly addressed and explicitly outlined in this project. The largest risk is the development of procedures, processes, and agreements necessary to prepare, package, and ship radiological plutonium samples, and are addressed in the first year of the project.

Specific activities included:

- Verification of ANL/APS radiological handling requirements.
- Selection of appropriate shipping container, generation of safety documentation, and work control documents for shipping and receiving of radiological material between laboratories.
- Developing a sample holder for use at APS that is approved both by ANL and by SRNL.
- Submission of GUP for beam time to appropriate APS review section management.
- Consultation with beamline scientists on experiments to be performed.

The second year of this project will cover execution of measurements and data analysis using open source tools developed by beamline scientists.

RESULTS/DISCUSSION

Two subcontracts were executed for work in the second year on this project. A contract to ANL was placed for consultation on experiment planning, sample holders, conversing with beamline station scientists, radioactive material shipping and handling, and laying the groundwork for future experiments. A second subcontract was awarded to Clemson to provide a preliminary data analysis utilizing TEM/EDS. They will prepare and characterize potential plutonium oxide samples to determine grain size and orientations that will be a deciding factor in the selection of plutonium oxide materials to be sent to APS. Plutonium oxide to be characterized will come from two sources: AFS-2 "clean" material with no metal contamination and lab synthesized material with trace metals added, representative of the production processes.

Figure 2. Exemption to Type A canister for shipping materials that do not meet the requirements of shipping in a Type A drum. Activity for samples must be below 2.7E-5 Ci

Normal shipments of plutonium oxide require the use of Type A or Type B drums depending on quantity and activity of the Pu isotopes. We prefer to use the Type A exemption canister, which is pictured in Figure 2, as it will make shipments to ANL easier. There are many of these containers at SRNL, therefore easier to procure and to ultimately handle with regards to shipping than Type A drums. To use this canister, the activity of the samples cannot exceed 2.7E-5 Ci. With the specific activity of weapons grade plutonium being 6.2E-2 Ci/g, samples to APS cannot exceed a total of 4.29 mg of Pu per container. The shipment to Clemson will still require a 5-gallon Type A drum as that material will exceed the exception limits so they can adequately prepare their samples for analysis.

Two sample holders were designed by SRNL engineers to provide the necessary two-layer containment required for APS. First, a backscatter sample holder was developed that would be used for XRD experiments at APS. This consists of particles placed on a carbon sticky tab on an SEM stub. The stub is then coated with epoxy (approved by APS) to fix the particles in place. A Kapton® polyimide film is placed over the top and screwed in with a metal piece to provide the first layer of containment. Then another piece of Kapton® film and metal are screwed into the first piece to provide the second layer of containment and a completed package for shipping (Figure 3).

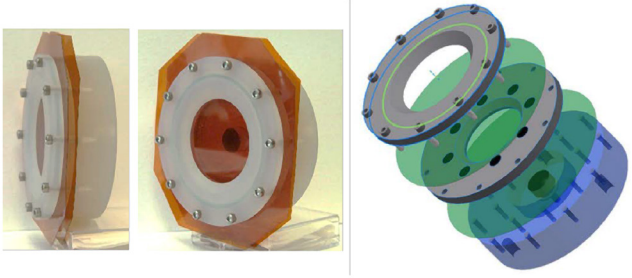

Figure 3. Diffraction sample holder developed for use at APS

After consultation with beamline scientists, a second sample holder was developed using existing design elements familiar to the scientists currently stationed at the beam line, APS radiological control, and APS safety officers. It consists of hard plastic with windows that will be attached by screws to a kinematic base plate. Inside the windows will be layers of Kapton® film and Kapton® tape. The particles will be applied to Kapton® tape with three wires acting as fiducial marks. After processing for SEM images and gamma spectroscopy for activity, a layer of Kapton® approximately 1 inch by 1 inch will be applied to the top to enclose the particles. To ensure closure, another piece of Kapton® tape will be applied to the bottom fully covering the particles. The sample can then be added to the window and held in by a second piece that screws to the main ladder, and finally attached to the kinematic base. The kinematic base has a female piece that the beamline uses and helps to position the sample(s) in front of the detectors. The samples can then be adjusted on the x-y plane until the beam is over the particle of interest for characterization and analysis.

R&D work instructions are being completed and reviewed by the appropriate safety SMEs (i.e. Radiological Protection, hazardous shipping, etc.). Currently, the work instructions are three parts; **a)** preparation of samples for the transmission sample holder, **b)** preparation of SEM stub samples for the backscatter sample holder, **c)** preparation of PuO_2 into screwcap vials for shipment in a 5 gallon Type A radiological drum. A five-gallon Type A drum will be procured to ship samples to Clemson for TEM analysis.

An APS GUP was submitted in July for free beam line time in the October to December 2017 period. The GUP has the following sections; **a)** abstract, **b)** purpose and importance of research, **c)** reason for APS, **d)** reason for beamline chosen, **e)** previous experience with synchrotron radiation and results, **f)** description of experiment(s), **g)** estimated amount of beam time. The proposal scored a 1.7 (1=best, 5=worst), but we were unable to secure availability for the upcoming cycle. The comments on our proposal were positive and we were encouraged to resubmit for the next cycle with extra shifts to complete our work.

Figure 4. Fiducial markings with three wires (Cu, Pt, Ni), and transmission sample holder ladder with pseudo sample

FY2017 ACCOMPLISHMENTS

The administrative controls and logistics were completed in FY17. These include:

- ✔ Placement of contracts to ANL and Clemson
- ✔ Documentation of safety procedures and protocols in regards to shipping plutonium oxide both at SRNL and ANL
- ✔ Safety procedures and protocols for the handling of radioactive material at APS
- ✔ Sample holders designed by SRNL were approved for use at APS
- ✔ Consultation with beamline scientists and safety officers on specific experiments to beperformed
- ✔ Submission of GUP

FUTURE DIRECTIONS

- ✔ Year 2 will include experiments at APS utilizing simultaneous XRD/XRF detectors to probe the diffraction and fluorescence data of the particles. This will allow for the mapping of grains to include sizes and orientations within the particle. Additional work at Clemson will provide data about grain structure not available at APS. Further work would be centered around computer-aided tomography that would provide a three-dimensional representation of the particles, allow for complete grain sizing, and information on the appearance of twins and cracks that could provide information about how the particle was manufactured.

FY2017 PUBLICATIONS/PRESENTATIONS

Informal presentation of sample holder design during discussions with beamline scientists and APS safety officers.

REFERENCES

1. Burney, G. A. S., P. Kent; Division, A. T., Ed.; E.I du Pont de Nemours & Co.: Aiken, SC, **1984.**
2. Machuron-Mandard, X. M., Charles *Journal of Alloys and Compounds* **1996,** 235, 216.

ACRONYMS

ANL Argonne National Laboratory
APS Advanced Photon Source
CAT Computer Aided Tomography
GUP General User Proposal
TEM Transmission Electron Microscopy
XRD X-ray Diffraction
XRF X-ray Fluorescence

TOTAL NUMBER OF POST-DOCTORAL RESEARCHERS

One postdoctoral researcher worked on the project: Dr. Michael DeVore II.

CLEAN ENERGY

ADVANCED RESEARCH IN THE DEVELOPMENT, DEMONSTRATION, AND DEPLOYMENT OF CLEAN ENERGY TECHNOLOGIES AND CLEAN ENERGY MANUFACTURING; INNOVATIVE TECHNOLOGIES TO ASSURE THE FUTURE UTILIZATION OF CLEAN, RELIABLE ENERGY OR DRAMATICALLY IMPROVE THE ENERGY EFFICIENCY OF INDUSTRIAL, MANUFACTURING, TRANSPORTATION, AND BUILDING TECHNOLOGIES, PLUS STRENGTHEN SRNL'S CORE COMPETENCIES.

NON-PGM FUEL CELL CATALYSTS

Project Team: H. Colón-Mercado (Primary, SRNL), M. Elvington (Primary, SRC) P. Ganesan (SRC)
Subcontractor: Savannah River Consulting, (SRC)
Thrust Area: Clean Energy
Project Start Date: 10/1/15
Project End Date: 9/30/17

A unique approach has been developed to probe the non-PGM catalyst active site for the Oxygen Reduction Reaction (ORR) for PEMFCs. Iron based functionalities have been engineered into a variety of catalysts to evaluate their impact on activity for the ORR. A series of high surface area catalysts were synthesized and the impact of the chemical structure on the electrochemical and electrocatalytic properties was investigated. Elemental and surface analyses of the prepared catalysts reveal the incorporation of iron in a targeted and controlled manner. A high surface area framework catalyst was prepared that shows exceptional activity, comparable to state-of-the-art materials. The results of this research project provided critical seed data for the newly awarded ElectroCat project, which focuses on rationally designed framework catalysts for the oxygen reduction reaction.

FY2017 OBJECTIVES

TASK ONE
Synthesize a series of FePhen@MOF catalysts

TASK TWO
Synthesize a series of high surface area framework catalysts

TASK THREE
Physical characterization of catalysts (bulk composition, surface composition)

TASK FOUR
Electrochemical characterization of catalysts (CV, RRDE)

INTRODUCTION

Worldwide efforts to produce durable, highly active non-PGM electrocatalysts have resulted in slow, incremental improvements in activity and an incomplete understanding of the catalytically active site. To achieve a breakthrough in activity, a greater understanding of the nature of the non-PGM ORR active site is needed. The composition of the active site is currently under debate, which has recently received heightened attention. In particular, the role of iron and/or FeN_4 complexes have in catalyzing the ORR is central to the debate. Most evidence suggests either iron has a direct role in the ORR catalysis or it influences the formation of the active site. This work focuses on developing a better catalyst while increasing the understanding of the role iron has in the ORR.

A series of high surface area catalysts were synthesized and the impact of the chemical structure on the electrochemical and electrocatalytic properties was investigated. The materials prepared within this project can be categorized as **1.)** high surface area N doped carbon; **2.)** porphyrinic MOF; **3.)** Fe-MOF; and **4.)** triazine framework. Each material type was chosen for this work because of their high surface area, nitrogen content, and electrical conductivity. Elemental and surface analyses of the prepared catalysts show the incorporation of iron in a targeted and controlled manner. A high surface area framework catalyst was prepared that shows exceptional activity, comparable to state-of-the-art materials. The results of this research project provided critical seed data for the newly awarded ElectroCat project, which focuses on rationally designed framework catalysts for the oxygen reduction reaction.

APPROACH

General catalyst preparation consisted of low temperature synthesis, metal incorporation and high temperature activation. Physical and elemental analysis were performed in-house and using an outside vendor. Materials were electrochemically characterized using rotating ring disc electrode (RRDE) in-house.

RESULTS/DISCUSSION

Elemental analysis, including inductively coupled plasma-atomic emission spectroscopy (ICP-AES) and CHN analysis, shows iron incorporation in the FePhen@MOF catalysts in a predictable and controlled manner. The table below summarizes the surface properties of the prepared materials. The materials studied show surface areas between 339 m^2/g and 3033 m^2/g. The electrochemical capacitance measured by the integration of the cyclic voltammetry (CV) curves, mirrors the trend of BET surface areas. The only exception is the porphyrinic MOF which shows no measurable electrochemical capacitance despite showing high BET surface area. This result can be explained by the lack of electrical conductivity of the 'as prepared' material. After high temperature activation, the capacitance increases. The nitrogen content was measured for most samples using CHN analysis and XPS analysis. In general, most framework samples show nitrogen content of about 3-4 at% and more than 50 at% pyridinic content. Other materials, such as high surface area nitrogen doped carbon, show nitrogen content can vary between 1 and 10 at%, depending on the synthesis conditions. These carbon sample show less than 50 at% pyridinic content.

Material	Pore Volume (mL/g)	BET (m^2/g)	Capacitance (F/g)	N At.%	Pyrollic N At.%	Pyridinic N At.%
FePhen@MOF	0.32	339	52.9	4.3	31	59
CTF	1.32	1415	43.1	3.7	32	67
Porphyrinic MOF	--	2500	0.46	--	--	--
Carbon 3000	1.56	3033	233	1.0	97	--
Carbon 900	0.49	956	11.1	10	71	29

The figure **(right)** shows the electrochemical investigation by rotating ring disk electrode (RRDE) of the most successful catalysts. The preliminary data shows the unoptimized porphyrinic MOF catalyst and the FePhen@MOF catalyst have similar performance to the state-of-the-art catalyst prepared by Los Alamos National Laboratory (LANL). It is expected that with further development, the catalyst's performance can meet or exceed the state-of-the-art.

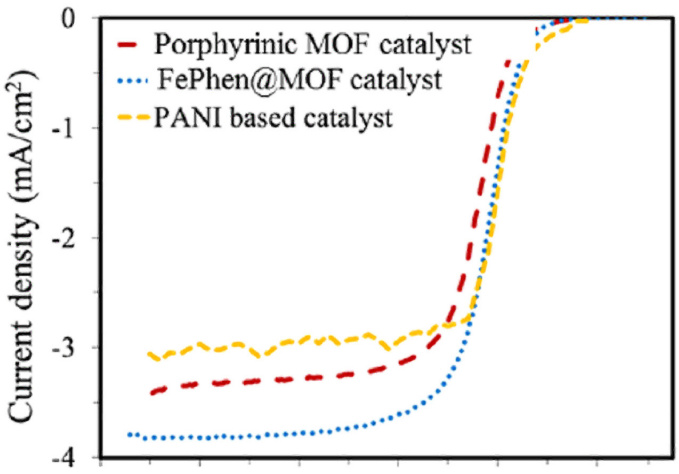

RIGHT: LSV in 0.5 M sulfuric acid saturated with O_2 and collected at a scan rate of 5 mV/s and 900 rpm.

FY2017 ACCOMPLISHMENTS

- Obtained external funding: ElectroCat project– $639k, SBIR – $40k
- Filed intellectual property: U.S. Patent Application
- Drafted peer Reviewed Paper: Joint Paper with LANL
- Synthesized a series of high surface area N doped carbon, porphyrinic MOF, Fe-MOF, and triazine framework with varying [Fe]
- Elemental analysis. Bulk compositions for nitrogen content range from 1 at% up to 10 at% with pyridinic N as high as 67at%
- FePhen@MOF and Porphyrinic MOF electrochemical activity for the ORR approaches state-of-the-art

FUTURE DIRECTIONS

- Explore additional organic frameworks in order to increase the number of active sites
- Utilize molecular modeling to explain experimental results
- Explore the use of various coordinated transition metal

PUBLICATIONS

1. P. Ganesan, M.C. Elvington, H.R. Colon-Mercado, "PGM-free Engineered Framework Nano-Structure Catalysts", ElectroCat kickoff meeting, ElectroCat awardees and DOE-EERE managers, September 2017.

ACRONYMS

BET	Brunauer–Emmett–Teller
CHN	Carbon Hydrogen Nitrogen
CTF	Covalent Triazine Framework
CV	Cyclic Voltammetry
ICP-AES	Inductively Couple Plasma Atomic Emission Spectroscopy
MOF	Metallic Organic Framework
non-PGM	Non Platinum Group Metal
ORR	Oxygen Reduction Reaction
PEMFC	Proton Exchange Membrane Fuel Cell
Phen	1,10-Phenanthroline
RRDE	Rotating Ring Disc Electrode
SRC	Savannah River Consulting
XPS	X-ray Photoelectron Spectroscopy

INTELLECTUAL PROPERTY

Patent Application Submitted

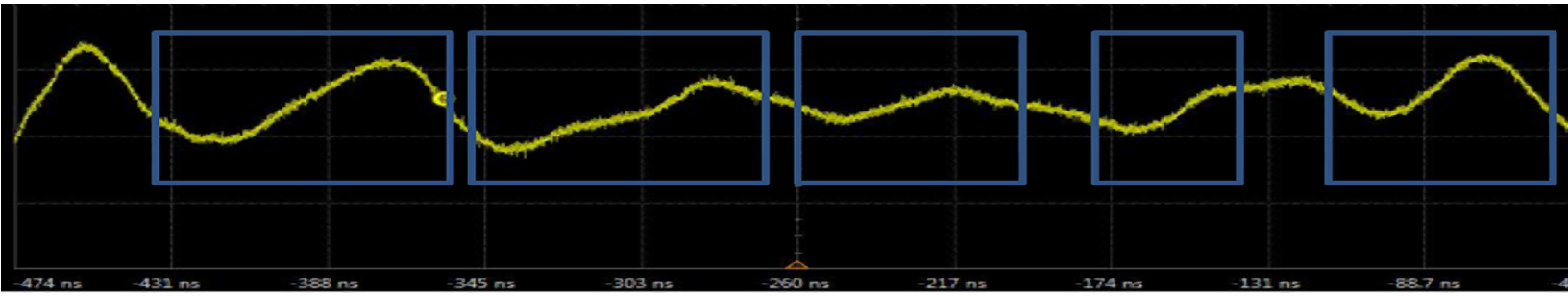

ON-LINE UNDERGROUND CABLE DIAGNOSTIC SYSTEM

Project Team: Klaehn Burkes (Primary), Nicholas Deroller, Karl Harrar

Thrust Area: Clean Energy

Project Start Date: 10/1/15

Project End Date: 9/30/17

The health of the nation's underground distribution cable network is widely unknown throughout the utility system. Typically, utility companies have policies which state that if a cable fails they can splice the failed location up to three times and then must remove the cable. The problem is this is done after the cable has caused a fault and has been de-energized. The on-line diagnostic system developed in this project can detect and monitor the degradation of the insulation in underground cables before they fail and allow for better asset management for the utility industry. During this fiscal year a prototype sensor and pulser was developed to be capable of attaching to the cable elbow, filtering off the high voltage 60 Hz power, injecting a pulse into the cable, and monitoring the reflections from the cable.

FY2017 OBJECTIVES

TASK ONE
Receive Failed Aged Cable from Santee Cooper
- Cable was aged 35 years in the field and failed due to insulation failure

TASK TWO
Analyze Cable for insulation defects

TASK THREE
Design Sensing System Within the Junction Box

TASK FOUR
Design High Voltage 60 Hz Filter
- Used to couple the sensor to the cable while cable is energized
- Physically isolates sensitive electronics from 15 kV utility voltage

TASK FIVE
Design Connecting Mechanism to Elbow

TASK SIX
Design Prototype Sensor

TASK SEVEN
Develop High Voltage Transmitter for Sensor

TASK EIGHT
Develop Low Voltage Sensing Device

TASK NINE
Test Prototype Sensor on Failed Cable

INTRODUCTION

The increasing practice of underground residential distribution (URD) cables being installed in the power system requires utility companies to know the health of these cables. Since the health of URD cables cannot be determined by visual methods like overhead lines, a better understanding of the power cable and its aging process is needed. Insulation of medium voltage URD power cables age from a phenomenon called water treeing Figure 1.

Water trees are important to utility companies because they cannot be detected using traditional protection methods. Also, they can be growing in cables without any effect on the voltage or current. They are the main reason for URD cable failures. These water trees can grow across the insulation and not cause the cable to fault **[1],** until there is enough energy supplied to it to cause a fault in the cable and vaporize the conductor Figure 2. Also, they do not produce partial discharge **[2]**, a common cable diagnostic tool. Because of these two facts detecting them becomes very difficult and expensive.

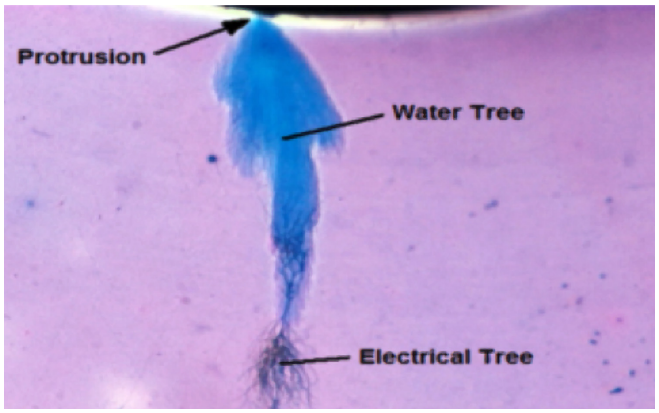

Figure 1. Water tree in Insulation

Figure 2. Damage of failed cables from water trees

APPROACH

Time Domain Reflectometry (TDR) is a traveling wave based method to determine whether water trees are present within the cable. TDR can be performed off-line or on-line. When a traveling wave is sent down a cable, it will have a reflection when it reaches the end of the cable or an element with different impedance. This can be used to locate water trees in a cable since the water treed region will change the impedance in that section. An early reflection may indicate water trees in the cable **[3].**

Current practice for detecting water trees is using TDR off-line and de-energizing the cable. This requires the cable to be disconnected from the network and then very expensive equipment checks each individual cable. This is very expensive and costly. This LDRD focused on developing a device and method for testing TDR in energized cables without the need for human interaction. The system developed functions as in Figure 3, with a sensor on each cable within a junction box. Each sensor would communicate to a National Instruments CompactRIO Platform that will determine if there is a damage on the cables.

Within the network, a system in one junction box can inject a pulse onto the cables. Junction boxes close to this injection site can then monitor the cables within their box and perform leading/lagging cable reference. For example, in Figure 4, sensor 2 (yellow) would see an input pulse before sensors 1 (blue) and 3 (green), which will see it around the same time (depends on the bus work configuration, but both will be after 2). This allows the CompactRIO Platform to start monitoring sensors 1 and 3 and disregard sensor 2 because another junction box system will be monitoring it. Then sensors 1 and 3 record data until they receive a reflection. This reflection measured in sensors 1 and 3 is then compared and there will be a time delay between the two measured reflections. This is because the reflection is coming from the shorter cable and will therefore have to travel past that sensor, in this case 3 (green), and then into the other cables, 1 and 2. This allows for the system to understand that that reflection was from sensor 3 and can be removed through software in other cables. The same can be done for cable 1 (blue) for the second termination reflection. This was also done with coaxial cables with no damages. Therefore, as can be seen in-between terminations there are no reflections just noise.

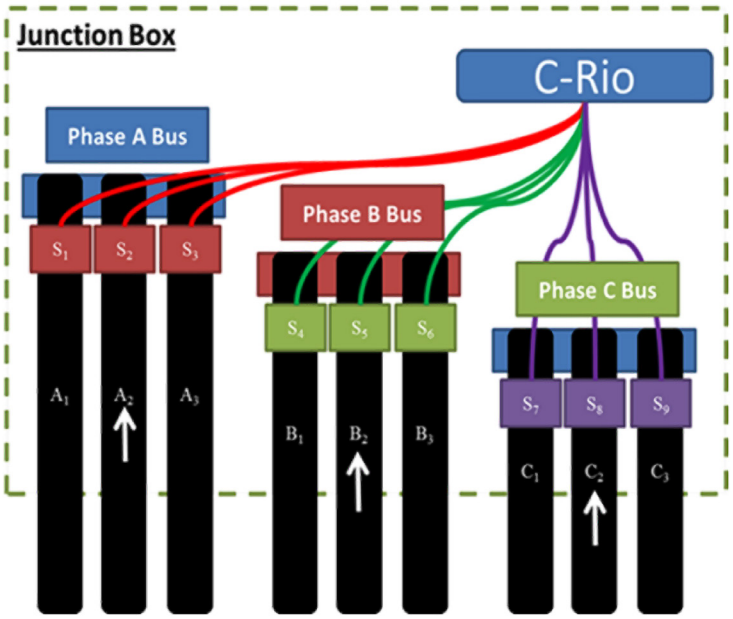

Figure 3. SST system block diagram

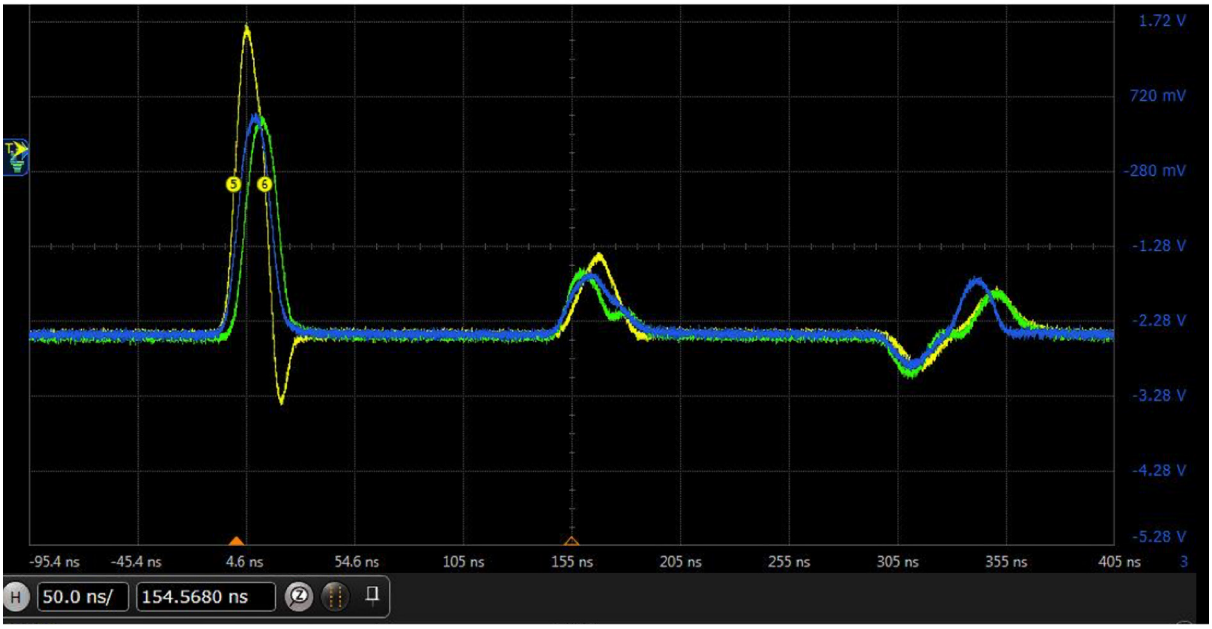

Figure 4. Coaxial Demonstration of Operation in Junction Box

RESULTS/DISCUSSION

A prototype sensor was developed to perform the above approach of monitoring energized underground cables. An enclosure was developed with SRNL's 3-D printing capability to house the electronics and connect them to the cable elbow shown in Figure 5. The circuit for the porotype is represented in the 3-D rendering in Figure 6. The high voltage is connected to the sensor through the spring attached to the bottom of the board. The circuit board is used as isolation capacitance to filter off the high voltage 60 Hz power from the high frequency pulse being injected or measured. This device sits inside the enclosure and connects to the cable to monitor.

Figure 5. Enclosure for connecting high frequency sensor to underground cable elbow

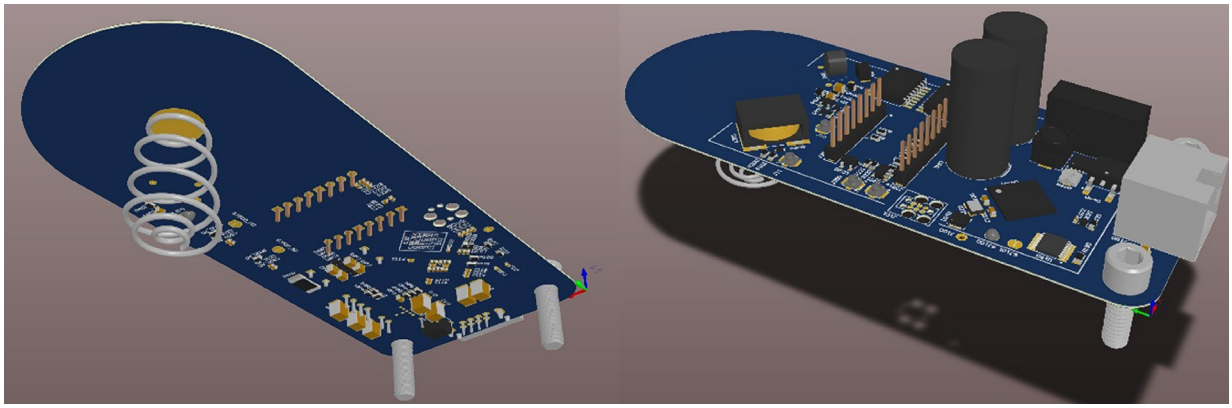

Figure 6. 3-D Rendering of Prototype Sensor

Failed cable was provided by Santee Cooper shown in Figure 2. This failed cable was analyzed for water trees and several were detected. Because the high frequency pulse is a much higher voltage a transmit receive switch was used to switch between the lower voltage measured pulse and the higher voltage transmit pulse. Therefore, better resolution is given to detect water trees. Because the cable was so old and with no outer jacket many large and small water treed regions were found as shown in Figure 7.

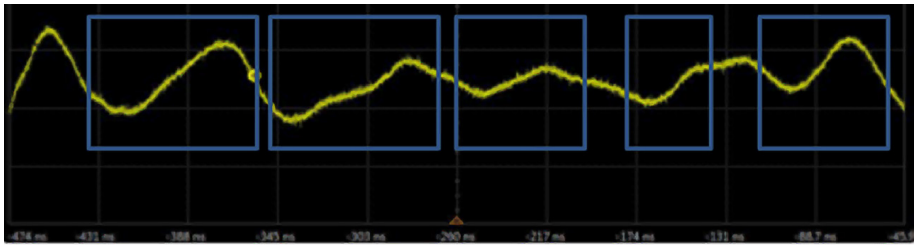

Figure 7. Multiple Water Tree Reflections in Santee Cooper Failed Cable

FY2017 ACCOMPLISHMENTS

Developed a prototype pulser and sensor that can connect to the underground cable and monitor the insulation health of the underground cable while energized.

- ✔ Utilized PCB board as spacing for capacitive filter to isolate high voltage power from low voltage circuit components
- ✔ Created advanced circuit design to perform high frequency data acquisition with medium voltage pulses
- ✔ Prototype is basically a specialized function generator and oscilloscope for under $100 per unit.
- ✔ Detected water trees in failed underground cable from Santee Cooper.

REFERENCES

1. W. A. Thue, "Treeing," in *Electric Power Cable Engineering,* Boca Ranton, FL, Taylor & Rancis Group, 2012, pp. 367-384.

2. J. Densley, "Ageing mechanisms and diagnostics for power cables—an overview," *IEEE Electrical Insulation Mag.* Vol. 17, pp. 14-22, Jan/Feb 2001.

3. V. Dubickas, *On-Line time domain reflectometry diagnostic of medium voltage XPE power cables,* Stockholm, Sweeden: Royal Institute of Technology, 2006.

ACRONYMS

PCB	Printed Circuit Board
TDR	Time Domain Reflectometry
URD	Underground Residential Distribution

INTELLECTUAL PROPERTY

1. Invention Disclosure titled “Leading/Lagging Cable Referencing Platform for Monitoring the Health of Underground Cable Networks”

METAL HYDRIDE THERMAL ENERGY STORAGE MATERIAL DEVELOPMENT FOR DISH-STIRLING SYSTEMS

Project Team: Ragaiy Zidan (PI), Patrick Ward

Subcontractor: Savannah River Consulting, Ted Motyka, Claudio Corgnale

Thrust Area: Clean Energy

Project Start Date: 10/1/15

Project End Date: 9/30/17

Concentrated solar power (CSP) has been gaining significant attention as a method to produce electricity, but requires a thermal energy storage (TES) system for continuous operation when the sun is unavailable. Thermochemical energy storage systems based on metal hydrides have advantages due to their high energy densities, potential for cost reductions, and higher operating conditions versus commonly used molten salts. Higher operational temperatures in CSP power plants are desired to achieve higher efficiencies and lower costs. This requires the TES system to operate at higher temperatures as well. We demonstrate the feasibility of $CaAl_2$ as a high temperature thermal energy storage material for concentrated solar power applications. Herin, $CaAl_2$ has been demonstrated to have excellent reversibility, high thermal conductivity, and is comprised of low cost elements. These qualities have made this material the best known candidate for TES systems operating at 600 °C.

FY2017 OBJECTIVES

TASK ONE
Develop high temperature metal hydride based thermal energy storage materials from low-cost materials

TASK TWO
Demonstrate cycle stability of the material over extended cycling

TASK THREE
Measure thermodynamic properties of the developed material

TASK FOUR
Demonstrate a low-cost method for the large scale production of the material

INTRODUCTION

As global energy demands have increased, concerns of diminishing fossil fuel supplies and the adverse effects of their combustion products on the global climate has inspired a significant amount of research in renewable energy technologies. Solar energy represents the largest source of sustainable energy available on our planet. Concentrated solar power (CSP) is positioned to provide a large contribution of the future solar energy supply due to its scalability and potential for providing low cost electricity. Since solar irradiance is only available in the day, continuous operation of the power block is only feasible when interfaced with an appropriate thermal energy storage (TES) system. These types of systems typically utilize one of three different methods of storing heat: (1) materials which store latent heat, (2) sensible heat, or (3) thermochemical heat. While sensible heat materials, namely molten salts, are the current state-of-the-art TES, the achievable energy densities and heat storage periods are far less than thermochemical energy storage systems **[1].** Solar salt, the most commonly utilized TES molten salt, faces challenges of high rates of corrosion and decomposition at temperatures above 600 °C **[2].** Thermochemical energy storage materials based on metal hydrides have the potential to store large energy densities of heat and operate at high temperatures.

Numerous types of chemical systems can be utilized to store thermochemical energy. These systems include metal hydrides, carbonates, hydroxides, peroxides, ammonia decomposition systems, and various organic systems **[3-9].** Metal hydrides have a distinct advantage due to the significant amount of research which has been conducted on the cycle stability of hydrogen storage materials, and the ability to provide a self-regulating system when an appropriate metal hydride pair is selected **[9,10].** The light weight of hydrogen typically leads to a higher gravimetric energy density for metal hydride based TES systems depending on the enthalpy of the reaction and the hydrogen gravimetric capacity.

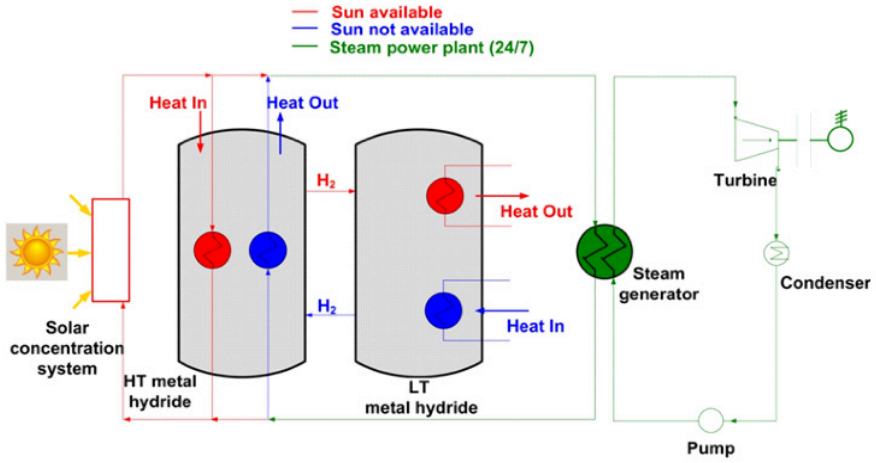

Figure 1. Diagram illustrating the concept of a metal hydride based thermal energy storage system

Recently, there has been a significant push to operate next generation CSP power plants at temperatures of 600 °C and above due to the higher efficiencies which can be achieved. The use of MgH_2 to store thermochemical energy was evaluated in the early 1990s by Bogdanovic´ et al. **[11,12].** Unfortunately, the high equilibrium pressures at higher temperatures and significant vapor pressure of magnesium at temperatures greater than 500 °C hinder the use of MgH_2 in next generation TES systems. The push for higher operational temperature creates a variety of technical and material challenges to overcome for these systems **[13,14].** The enthalpy of the reaction of $CaAl_2$ with H_2 to produce CaH_2 and Al has been predicted by DFT calculations to be -72 kJ/mol [15]. Experimental measurements of the reaction of $CaAl_2$ with H_2 have measured this enthalpy to be -83.1 kJ/mol [16]. Using the experimentally measured value, this material can theoretically store 865 kJ per kilogram of $CaAl_2$. Herein, we demonstrate that this material is reversible with very little capacity degradation and possesses a reasonably high thermal conductivity. The cycle stability and thermal conductivity of $CaAl_2$ reported herein are two essential aspects necessary for the development of an economically feasible thermal energy storage system.

APPROACH

The reaction of hydrogen with calcium metal to form CaH_2 has and enthalpy of -181.5 kJ/mol. While this is an incredibly high heat of reaction, the equilibrium pressures of CaH_2 are quite low (~ 1 bar) even at very high temperatures (750 °C). Furthermore, CaH_2 is highly corrosive in the molten state (813 °C) which creates significant challenges and increased cost in the construction of containment vessels for this material. In this work, we utilize additives which alloy with Ca during dehydrogenation to alter the thermodynamic properties of the material and prevent corrosion associated with molten CaH_2. The addition of Si or Al to the material results in the formation of Ca_xSi_y and Ca_xAl_y alloys upon dehydrogenation. This year's focus lied mainly with a particular formulation: $CaAl_2$. This material possesses desirable equilibrium pressures, high operational temperatures, excellent cycle stability, reversibility with no undesirable side products, and suitable thermal conductivities. Once this material was determined to have the highest chance for being commercially viable for TES applications, an enhanced effort to fully characterize and test the material was carried out.

RESULTS/DISCUSSION

For a practical thermal energy storage system, the material must be able to be cycled thousands of times with very little loss in capacity. The $CaAl_2$ system was cycled 100 times at 600 °C with starting absorption pressures between 22 and 24 bar H_2 for 3 hour periods. Desorption of the material was carried out at 2 bar H_2 over 3 hours. A helium calibration curve for the pressure drop in the reaction vessel during cycling was obtained and used to calibrate the hydrogen uptake measurements. The slight differences in the starting pressures during hydrogenation are due to the slight differences in the starting reservoir pressure set by the software before each absorption cycle. Figure 2 illustrates some variation in capacity between 2.0 and 1.9 wt. % H_2 during the first 20 cycles. This is typically observed in metal hydride materials and is a result of the material reaching an equilibrium state with respect to particle proximity for dissociation and recombination. Once equilibrium was reached (cycle ~ 20), the capacity demonstrates only a very slight degradation from ~1.9 wt. % to ~1.85 wt. %. The temperature of the material was also monitored during absorption/desorption of H_2. The thermal profile of the material, given in Figure 3, shows a large temperature spike of ~ 80 °C during the hydrogenation and clearly illustrates the large amount of heat that can be rapidly generated and extracted from the system to facilitate 24 hour operation of a future CSP plant.

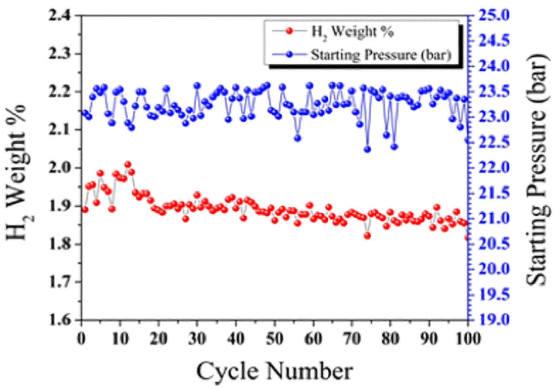

Figure 2. Hydrogen capacity of $CaAl_2$ at 600 °C over 100 cycles (red) and the starting pressure

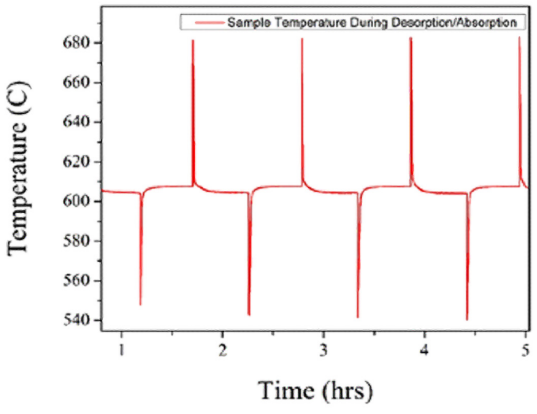

Figure 3. Temperature profile of $CaAl_2$ during hydrogenation and dehydrogenation starting at ~600 °C

We also believe that this may be responsible for the slight degradation observed in the material. In a real system, this heat would be extracted to maintain an operational temperature of 600 °C and pressure would be altered very slowly in a controlled fashion. In our cycling reaction, no such heat extraction mechanism is possible and high pressure above both equilibrium pressure plateaus is given instantaneously. Therefore, the material exceeds 660 °C, which is the melting point of aluminum. Since the hydrogenated state of this material consists of CaH_2 and Al, it is quite possible that a small amount of phase segregation of the powdered material is responsible for the slight capacity loss observed. After hydrogenation of $CaAl_2$ for 2 hours at 600 °C and 25 bar H_2, the crystalline species observed were CaH_2 and Al. Subsequent dehydrogenation of the material resulted in the formation of $CaAl_2$ once again as shown in Figure 4.

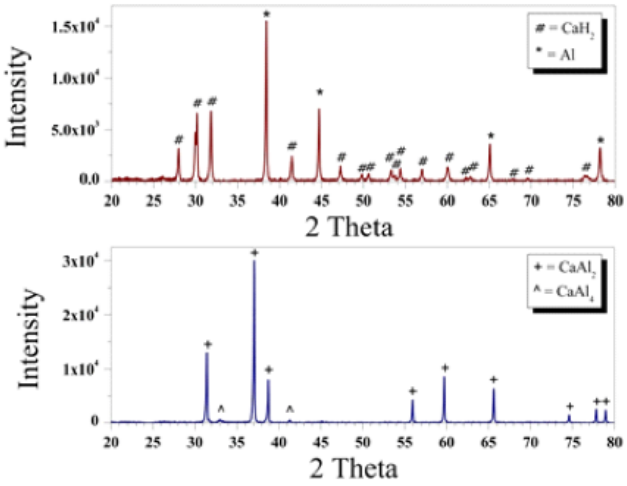

Figure 4. XRD patterns of $CaAl_2$ in the hydrogenated **(top)** and dehydrogenated state **(bottom)**

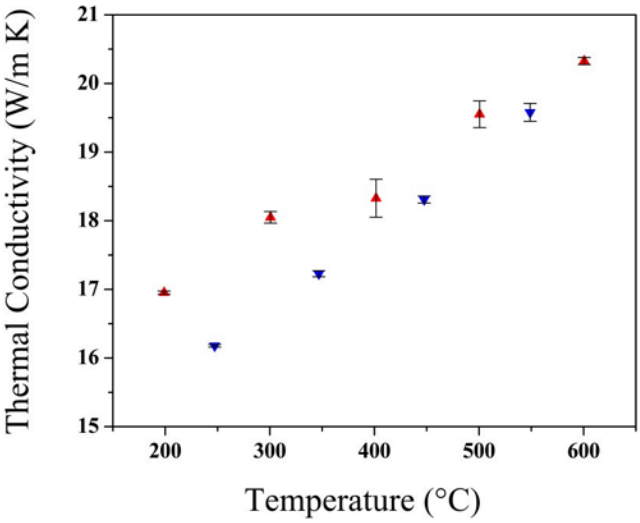

Figure 5. Thermal conductivity of $CaAl_2$ from 200 °C to 600 °C. The red up arrows show measurements acquired during the heating ramp and blue down arrows show measurements acquired during the cooling ramp.

Figure 5 shows the thermal conductivity of the as prepared $CaAl_2$ from 200 °C to 600 °C. The thermal conductivity at the desired operational temperature (600 °C) was determined to be 20.3 W/m K. While this value is not as high as most metals (i.e. aluminum 205 W/m K at 25 °C), it is exceptionally high for most metal hydrides given that the measured pellet is only 80% of the theoretical crystal density of $CaAl_2$. It is well-known that the thermal diffusivity strongly depends on the packing density and inter-grain connectivity, hence further improvement in thermal diffusivity is expected upon increasing the cold-pressing pressure and/or further sintering the pellet. Obtaining thermal conductivities for the hydrogenated samples at 600 °C was not possible with the current instrumental setup due to hydrogen release at elevated temperatures without having the appropriate hydrogen overpressure. Therefore, the thermal conductivities for the hydrogenated materials were measured from 80 °C to 200 °C to ensure no hydrogen evolution.

Figure 6 shows that the thermal conductivity of the hydrogenated material falls within the range of 6.8 W/m K to 7.9 W/m K from 80 °C to 200 °C. This value still far exceeds the thermal conductivities of most metal hydrides and molten salts (usually less than 2 W/m K) that would be used for TES applications. Lastly, a pressure composition isotherm (PCI) was measured at 600 °C to determine the equilibrium pressure of the reactions associated with the hydrogenation of $CaAl_2$. Figure 7 demonstrates that the equilibrium pressure plateaus at 600 °C are approximately 8 bar and 19 bar for the first reaction step and the second reaction step.

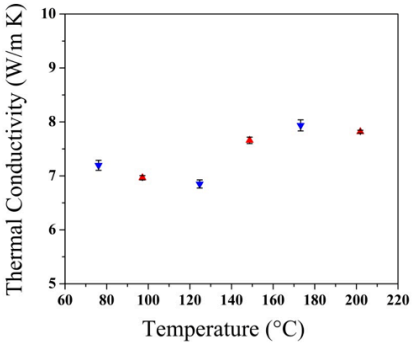

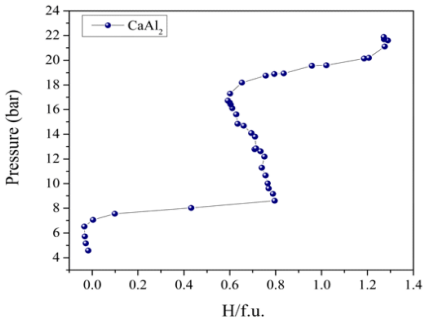

Figure 6. (above left) Thermal conductivity of $CaAl_2$ (hydrogenated to CaH_2 + Al) from 80 °C to 200 °C. Red up arrows depict measurements acquired during the heating ramp and blue down arrows depict measurements acquired during the cooling ramp. **Figure 7. (above right)** PCI data for $CaAl_2$ at 600 °C. A temperature correction is required to adjust the slight backwards drift observed. This data is presented to demonstrate the equilibrium pressures of the two absorption steps as ~ 8 bar and ~ 19 bar.

FY2017 ACCOMPLISHMENTS

- Developed a material which represents the most commercially viable high temperature metal hydride for TES applications
- Demonstrated excellent cycle stability of the $CaAl_2$ material
- Measured an array of thermodynamic properties of the $CaAl_2$ material which demonstrate the feasibility of this material for TES applications
- Published 4 peer reviewed journal articles
- Submitted 1 patent application
- Presented 3 invited lectures based on the work conducted for this LDRD

FUTURE DIRECTIONS

- Conduct long term cycling of the $CaAl_2$ materials
- Investigate additives to increase operational temperatures
- Demonstrate pairing of $CaAl_2$ with a suitable low temperature metal hydride
- Obtain DOE SunShot funding for further research

FY2017 PUBLICATIONS/PRESENTATION

1. Ward, P.A., Corgnale, C., Teprovich, J.A., Moytka, T., Hardy, B., Sheppard, D., Buckely, C., Zidan, R. Technical challenges and future direction for high efficiency metal hydride thermal energy storage systems. *Appl. Phys. A,* **2016,** 122, 462.

2. D. A. Sheppard, M. Paskevicius, T. D. Humphries, M. Felderhoff, G. Capurso, J. Bellosta von Colbe, M. Dornheim, T. Klassen, P. A. Ward, J. A. Teprovich Jr., C. Corgnale, R. Zidan, D. M. Grant, C. E. Buckley. Metal hydrides for concentrating solar power energy storage. *Appl. Phys. A,* **2016,** 122, 395.

FY2017 PUBLICATIONS/PRESENTATION [CONTINUED]

3. C. Corgnale, B. Hardy, T. Motyka, R. Zidan. Metal hydride based thermal energy storage system requirements for high performance concentrating solar power plants. *Int J Hydrogen Energy,* **2016,** 41, 20217-20230.

4. Ward, P. A.; Teprovich, J. A. Jr.; Lu, Y.; He, J.; Zidan, R. High Temperature Thermal Energy Storage in the $CaAl_2$ System. *Journal of Alloys and Compounds*, **2017,** in press.

5. Ward, P.; Zidan, R.; Teprovich, J.; Corgnale, C.; Hardy, B. Thermal Energy Storage in Calcium Aluminum Alloys European Materials Research Society 09/20/2016 **Invited Presentation**

6. Ward, P. Zidan, R.; Teprovich, J.; Corgnale, C.; Motyka, T. Temperature Thermal Energy Storage in Calcium Aluminum Gordon Research Conference (Hydrogen-Metal Systems) 07/17/2017 **Invited Presentation**

7. Ward, P. Zidan, R. Teprovich, J. Corgnale, C., Motyka, T. High Temperature Thermal Energy Storage in the $CaAl_2$ System. Gordon Research Seminar (Hydrogen-Metal Systems) 07/17/2017 **Invited Presentation**

8. Ward, P.; Zidan, R.; Teprovich, J.; Corgnale, C.; Motyka, T. High Temperature Thermal Energy Storage in the CaAl2 System. Gordon Research Conference (Hydrogen-Metal Systems) 07/18/2017 **Poster**

REFERENCES

1. Pardo, P.; Deydier, A.; Anxionnaz-Minvielle, Z.; Rouge, S.; Cabassud, M.; Cognet, P. *Renew. Sust. Energ. Rev.* **2014,** 32, 591-610.
2. Liu, M.; Tay, N. H. S.; Bell, S.; Belusko, M.; Jacob, R.; Will, G.; Saman, W.; Bruno, F. *Renew. Sust. Energ. Rev.* **2016,** 53, 1411-1432.
3. Barker, R. J. *Appl. Chem. Biotechn.* **1974,** 24, 221-227.
4. Ervin. G. J. *Solid State Chem.* **1977,** 22, 51-61.
5. Wentworth, W.E.; Chen, E. *Sol. Energy* **1976,** 18, 201-214.
6. Garg, H.P.; Mullick, S.C.; Bhargara, A.K. Solar thermal energy storage. Dordrecht, Holland: D. Reidel Publishing Company; **1985.**
7. Sheppard, D. A.; Corgnale, C.; Hardy, B.; Motyka, T.; Zidan, R.; Paskevicius, M.; Buckley, C. E. RSC *Adv.* **2014**, 4, 26552-26562.
8. Corgnale, C.; Hardy, B.; Motyka, T.; Zidan, R.; Teprovich, J.; Peters, B. Renew. *Sust. Energ. Rev.* **2014,** 38, 821-833.
9. Aswin, N.; Dutta, P.; Murthy, S. S. *Appl. Therm. Eng.* **2016,** 109, 949-957.
10. Harries, D. N.; Paskevicius, M.; Sheppard, D. A.; Price, T. E. C.; Buckley, C. E. *Proceedings of the IEEE* **2012,** 100 (2), 539-549.
11. Bogdanovic´, B.;Ritter, A.; Spliethoff B. Angew. *Chem. Int. Edit.* **1990,** 29, 223–234.
12. 12. Bogdanovic, B.; Hartwig, T. H.; Spliethoff, B. *Int. J. Hydrogen Energ.* **1993,** 18, 575–589.
13. 13. Ward, P.; Corgnale, C.; Teprovich, J. A.; Motyka, T.; Hardy, B.; Sheppard, D. et al. *Appl. Phys. A-Mater.* **2016,** 122 (4), 462.
14. 14. Sheppard, D. A.; Paskevicius, M.; Humphries, T. D.; Felderhoff, M.; Capurso, G.; Bellosta vol Colbe, J. et al. *Appl. Phys. A-Mater.* **2016,** 122, 395.

ACRONYMS

CSP	Concentrated Solar Power
DFT	Density Functional Theory
PCI	Pressure Composition Isotherm
TES	Thermal Energy Storage
XRD	X-ray Diffraction

INTELLECTUAL PROPERTY

1. R. Zidan, "High Performance Metal Hydride Based Thermal Energy Storage Systems for Concentrating Solar Power", U.S. Patent Application Nos. 62/087,939 and 14/961,087.

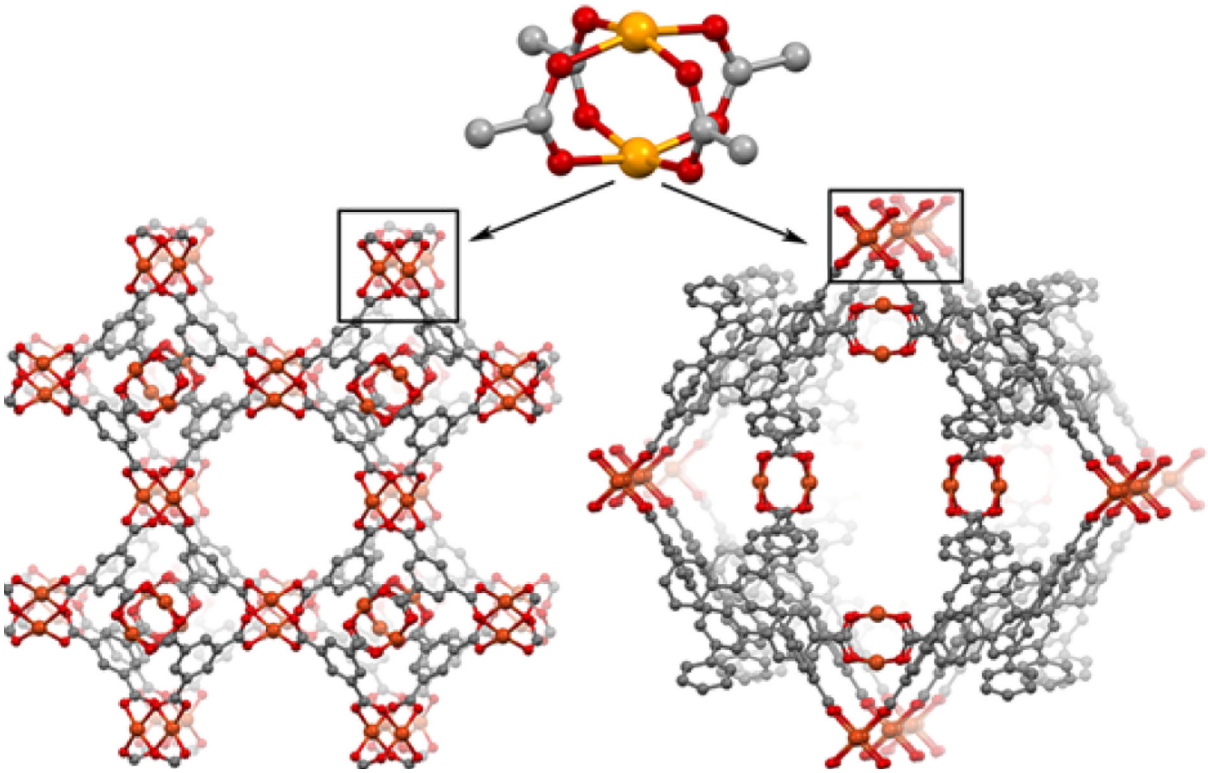

The crystal structures of MxM'1-x(BTC) (left) and $M_xM'_{1-x}$(BTB) **(right)** systems. In both structures, the secondary building unit, shown on top, is a paddle-wheel, $M_2(O_2C–)_4$. Orange, gray, and red spheres representcopper, carbon, and oxygen atoms, respectively.

SELECTIVE ADSORPTION /PURIFICATION OF NATURAL GAS USING TUNABLE ADSORBENTS

Project Team: Bruce Hardy-PI (SRNL), Anna d'Entremont (SRNL), Martin Sulic (SRC), Claudio Corgnale (SRC), Theodore Motyka (SRC), Natalia Shustova (USC), Donna Chen (USC))

Subcontractor: Savannah River Consulting, University of SC

Thrust Area: Clean Energy

Project Start Date: 10/1/15

Project End Date: 9/30/17

The research effort consisted of the development of methodologies for the systematic design and evaluation of adsorbent based natural gas purification systems. The project focused on metal organic frameworks (MOFs), but can readily be extended to gas separation processes and adsorbents. The effort was distinct from prior work in that it evaluated adsorbent based separation from fundamental adsorbent properties and synthesis to performance of the MOFs in a separation system. MOFs were selected as candidate adsorbents because they can be designed to have separation factors and distribution coefficients suitable for removal of commonly occurring impurities in natural gas. Selectivity can be engineered into a MOF by using techniques established at USC for producing "tunable" surface properties. MOFs were synthesized and characterized for selectivity via analytical methods that examine the in situ binding energies of the adsorption sites. Multicomponent isotherm models, that utilized single component data, were incorporated into mathematical simulations for adsorbent based separation on a system level. The system models can be used to design large-scale separation processes and evaluate them in terms of economic and exergetic efficiency.

FY2017 OBJECTIVES

TASK ONE
Complete isotherm models describing multicomponent selective adsorption.
- Multicomponent models must use single component isotherm data to predict multicomponent adsorption.
- Validate models against binary data.

TASK TWO
For existing adsorbents, use the isotherm models to demonstrate proof of concept for pressure swing separation.

TASK THREE
Implement multicomponent isotherms in preliminary system models for industrial scale separation.

TASK FOUR
Simultaneously, USC was to design, synthesize and evaluate new selective adsorbents for target gas species.

TASK FIVE
Adsorbents developed by USC to be sent to SRNL for isotherm measurement (along with other required properties).

INTRODUCTION

Worldwide, there are significant reserves of sub-quality natural gas, defined as containing >2% CO_2, >4% N_2, >4 ppm H_2S. It is estimated that 50% of known reserves have > 2% CO_2. Adsorption-based purification processes have high potential for energy and capital investment savings over conventional CO_2 amine scrubbing and cryogenic distillation N_2 rejection unit technologies. This LDRD project, which comprises the second year of a 2 year effort, consists of the systematic development methodologies and materials for adsorbent based natural gas purification systems. Funding in the second year was reduced which resulted in a corresponding reduction from the original scope of work. Reduced funding manifested itself as the termination of advanced MOF development by the University of South Carolina (USC), beyond that initiated in the first year of the project and as completion of adsorption system models without application to design and evaluation at SRNL.

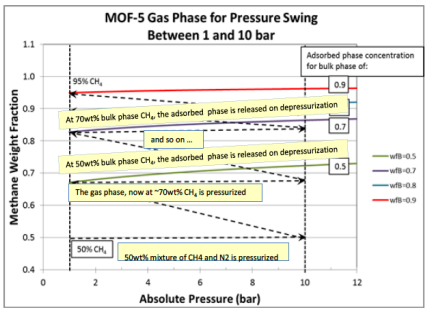

Methane/nitrogen separation with MOF-5

As originally proposed, the project focuses on the use of metal organic frameworks (MOFs), which are a new class of adsorbent materials that can be designed to selectively bind to specific gases. In partnership with USC, MOFs were engineered and synthesized to have "tunable" surface properties suitable for removal of commonly occurring impurities in natural gas. As such, MOF based purification processes, designed to specifically take advantage of the performance of these adsorbents, have the potential for significant improvement over currently used adsorbents. In this effort, adsorbent based gas separation was evaluated from fundamental adsorbent properties and synthesis to the performance of MOFs in a separation system. Although this effort is applied to separation of methane from wellhead natural gas, the underlying methodology can be readily applied to other adsorbent based gas purification processes.

A new generation of MOF's was synthesized and delivered to SRNL to be characterized for its selectivity. The characterization data is for use in mathematical models, developed by SRNL, that predict the performance of process systems. The models can be used to design large-scale separation systems and evaluate them in terms of economic and exergetic efficiency. The MOFs were synthesized and then characterized for selectivity via unique analytical methods that examine the in-situ binding energies of the adsorption sites. The models can be used to identify needed improvements in MOF performance to guide the design and synthesis of successive, improved generations of MOFs for separation systems.

APPROACH

At the current level of funding, the goal of this LDRD was the development of models suitable for the design and techno-economic evaluation of adsorbent based separation systems for natural gas; this part of the effort was conducted by SRNL. The basis of the separation process is MOF adsorbents, synthesized by USC, to have high affinity for gas species comprising wellhead natural gas. For tractability within the timeframe of the LDRD, the focus was restricted to MOFs. To achieve practical cycling rates, the system operates as a pressure swing adsorption (PSA) process. System design thus focused on PSA, although the operating temperature was allowed to vary within practical limits, to achieve optimal conditions for performance.

A combination of high surface area and high adsorption selectivity is necessary for an adsorbent to have high gas separation factors. MOFs are a class of crystalline hybrid materials that satisfy both criteria. MOFs also offer unprecedented tunability, thereby enabling very high adsorption selectivity based on: pore aperture or geometry, composition, and ensemble sizes of the metal active sites. Enhanced selectivity for gas separation and adsorption is achieved by systematic alteration of the metal sites and variation of MOF surface area through design of ligand in the coordination complex. Moreover, MOF metal nodes can include a least two distinct metals, which provides a pathway for tandem selectivity (i.e., increased selectivity for a particular adsorbate).

RESULTS/DISCUSSION

The technical approach to this project entailed two requirements: One was the development of mathematical models that accurately described the behavior of the adsorbent in a pressure swing system. The other was the design and synthesis of species selective MOFs that were durable in the presence of gases in the process stream.

Multicomponent isotherm models that determine the degree of separation have been developed and tested against known MOFs; namely MOF-5 and UiO-66. With SRNL characterization data for MOFs provided by USC, the models can be used for general MOF/gas compositions.

Starting from Cu_3BTC_2 (HKUST), which is a known and durable MOF, USC has designed and synthesized “first generation” selective MOFs. Following this, USC successfully synthesized 10 "second generation" MOFs; more syntheses were attempted. Two generalized synthesis methods were developed. USC evaluated MOFs it produced for suitable properties and selectivity by using: X-ray photoelectron spectroscopy (XPS) for surface elemental composition; powder X-ray diffraction (PXRD) for phase transitions and crystallinity; Fourier transform-infrared (FT-IR) spectroscopy to identify chemical compounds and molecular bonds; energy dispersive X-ray spectroscopy (EDX) with a scanning electron microscope for elemental analysis; and inductively coupled plasma-mass spectrometry (ICP-MS) which detects very low concentrations of metal and non-metal elements. MOFs were delivered to SRNL for measurement of properties required for the adsorption system models.

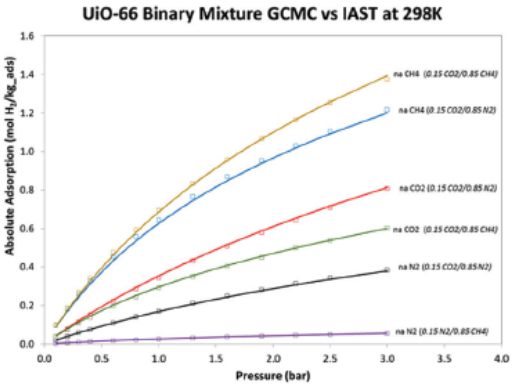

IAST vs GCMC

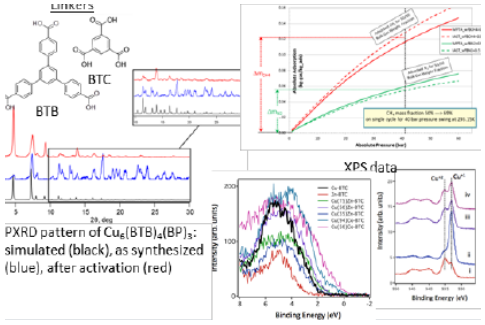

Multi-curve Chart: Top 2 curves represent increasing substitution of Co with respect to Cu. XPS analysis indicates electronic properties similar to semi-conductors, perhaps implying increased thermal conductivity.

FY2017 ACCOMPLISHMENTS

- SRNL has refined and customized specialized experimental apparatus for measuring single & multicomponent isotherms as adsorbents become available (future capability for SRNL).
- SRNL has developed the modeling framework for multicomponent isotherms
  - Theoretical and numerical formulation of models was developed.
  - Isotherm models using MPTA and IAST were developed for system models.
- Isotherm models were used with MOF-5 and UiO-66, as test, to demonstrate that the pressure swing concept is viable for N_2/CH_4 separation
  - Isotherm measurements were performed at SRNL
- System (global) models for large-scale gas purification are in piecewise functional form
  - Can be used for design of separation systems, scale-up, optimization and evaluation of concepts
  - Can be used to determine economic and exergetic efficiency
- USC has designed and synthesized "first and second generation" selective MOFs.
  - MOFs were evaluated at USC using PXRD, FT-IR, ICP-MS, EDX and XPS.
  - MOFs were delivered to SRNL for measurement of isotherms and other properties required for separation system design.

FUTURE DIRECTIONS

- Secure funding to further PSA system evaluation and development using technology developed in this LDRD.
- Extend adsorption separation to processes other than methane purification. Methodology is applicable to general adsorbent based gas separation—not just natural gas. Can be used to design and assess other multicomponent gas separation processes.
- Publish the SRNL models as application for methane separation from wellhead natural gas.
- Use the models to identify needed improvements in MOF performance to guide the design and synthesis of future generations of MOFs.

FY2017 PUBLICATIONS/PRESENTATIONS

1. Preparations for papers and presentations are in progress.

REFERENCES

1. *The removal of CO2 and N2 from natural gas: A review of conventional and emerging process technologies.* **Rufford, T E,** et al., et al. 94-95, s.l. : Elsevier, 2012, Journal of Petroleum Science and Engineering, pp. 123-154.
2. *Thermodynamics of Mixed-Gas Adsorption.* **Myers, A L and Prausnitz, J M.** 1, 1965, AIChEJournal, Vol. 11, pp. 121-127.
3. *Gas Separation by Adsorption Processes.* **Yang, Ralph T**. ISBN-10 1-86094-047-1. 1987 (Repr2008).

ACRONYMS

EDX	Energy Dispersive X-ray Spectroscopy
FT-IR	Fourier Transform-infrared Spectroscopy
GCMC	Grand Canonical Monte Carlo
IAST	Ideal Adsorbed Solution Theory
ICP-MS	Inductively Coupled Plasma Mass Spectrometry
MOF	Metal Organic Framework
MPTA	Multicomponent Potential Theory of Adsorption
PSA	Pressure Swing Adsorption
PXRD	Powder X-ray Diffraction
XPS	X-ray Photoelectron Spectroscopy

EXPLORE INNOVATIVE CHEMISTRY OF NATURAL GAS CONVERSION TO DME

Project Team: Steve Xiao (PI) A.B. Thompson, P. Ward, M. Sulic, D. Anton

Subcontractor: University of SC (Frank Chen, Andreas Heyden, Donna Chen, Salai Ammal, Libin Lei), Greenway Energy (Martin Sulic)

Thrust Area: Clean Energy

Project Start Date: 10/1/15

Project End Date: 9/30/17

In collaboration with University of South Carolina (USC), an innovative electrochemical pathway using catalyst/membrane assembly was investigated to efficiently convert natural gas to dimethyl ether (DME), a future diesel fuel component. This novel and unique process combines multiple chemical reactions/separations into a one-step reactor design. In year 2 we demonstrated success with 4 individual elementary reactions involved in the proposed membrane process using traditional catalyst testing techniques. Concurrently, SRNL has discovered independently an efficient biomass conversion pathway while investigating DME synthesis. This 2-year LDRD project has led to 1 invention disclosure, 2 RAPID proposals and 1 hiring of postdoc to SRNL.

FY2017 OBJECTIVES

TASK ONE
Develop an efficient chemical conversion pathway from natural gas to liquids

TASK TWO
Design, build, and characterize the performance of a solid oxide membrane catalyst assembly for natural gas conversion into DME

TASK THREE
Create a new set of original work for publications and external funding proposals

INTRODUCTION

Abundant production of low-cost natural gas has changed the energy landscape in the United States. Domestic natural gas (NG) costs only 1/7th as much as petroleum crude on an energy-content basis. The rapid advances in shale gas technology and hydraulic fracturing have also led to increased emissions and flaring associated with production, which is usually located in remote areas. Worldwide, over 150 billion m^3/year of natural gas is wasted **[1],** which is equivalent to emissions of an additional 1 million cars on America's roadways **[2].** Dimethyl ether (DME) is an excellent diesel fuel additive **[3-7],** having a cetane number of 55, while regular diesel is in the low 40s. Because of the absence of a carbon-carbon bond, combustion of DME produces no soot, thus eliminating or greatly reducing particulate emissions from diesel engine exhaust.

There is significant economic and environmental incentive for developing new technologies to efficiently convert natural gas into DME. Methane conversion has been well studied for decades. Its conversion to syngas followed by Fischer–Tropsch or methanol synthesis is known, but not economical. Direct conversion of methane without the syngas step is attractive, but the yield is poor. Methane's reaction with oxygen is difficult, but its reaction with halogens (Cl_2, Br_2) can occur at moderate or even room temperature under UV light irradiation. This makes methane activation by oxidative coupling with HCl or HBr very promising. An innovative catalyst/membrane system and three additional chemical reactions have been investigated to carry out methane conversion into DME in a single step. Membrane (Ba, Ce, Zr, Y, Yb oxide based perovskites) and catalyst (LaOCl, LaOBr) assemblies are designed to convert methane while keeping oxygen separate from the reaction mixture, thus avoiding the complete combustion to CO_2. Once methyl chloride or bromide is formed, its hydrolysis to methanol and conversion to DME are also combined to improve efficiency. In the overall reaction, HCl or HBr originates from the catalyst such that the halogen participates in the reaction but is not consumed. After coupling this chemistry the net transformation would be methane and oxygen yields DME and water.

APPROACH

This project has developed, designed, built, and characterized the solid oxide membrane catalyst assembly for natural gas conversion into DME, in collaboration with University of South Carolina. The goal is to create a new set of chemical pathways more efficient than the existing methane conversion technologies.

- Membrane is used innovatively to avoid methane oxidation while still keeping intended chemical reactions
- Methane is activated at mild temperature by heterogeneous catalysis involving a labile halogen species
- Complex chemical reaction is broken down into stepwise reactions using membrane/catalyst design

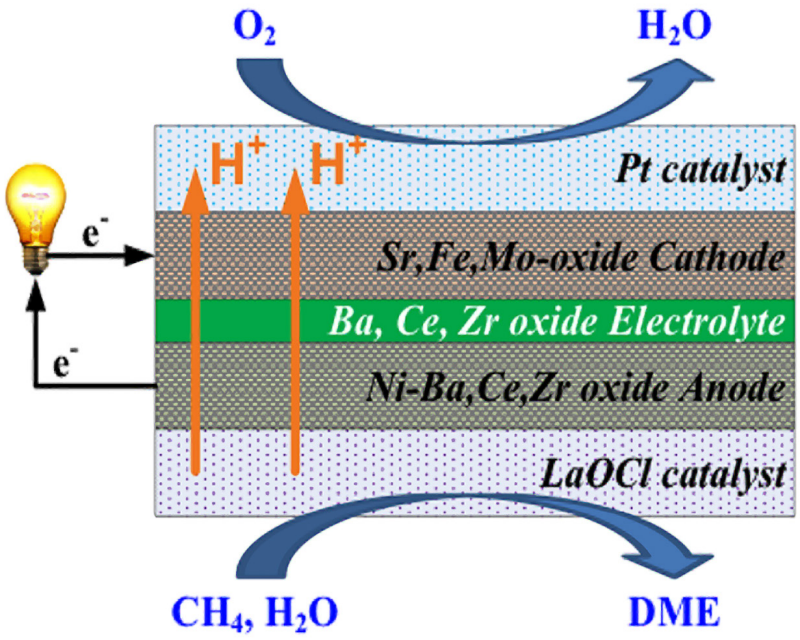

Figure 1. Illustration of methane conversion principle over membrane catalyst assembly

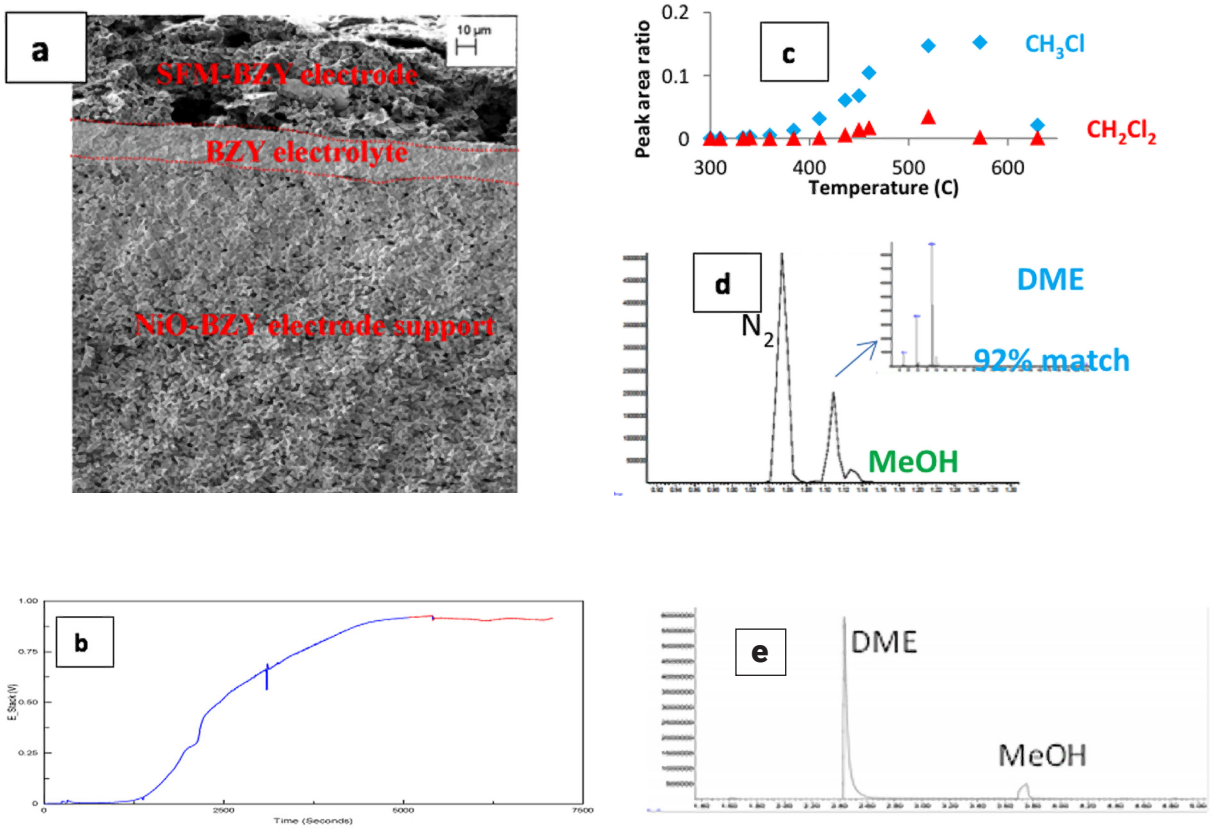

Figure 2. a) SEM of 15 µm proton conducting membrane on substrate **b)** membrane performance verified with open circuit voltage (during activation) **c)** methane activation to CH_3Cl; d) $CH_3Cl + H_2O$ to DME over γ-Al_2O_3 catalyst **e)** methanol to DME conversion over KOH catalyst

RESULTS/DISCUSSION

The complex chemical reaction is broken down into stepwise reactions leading to the production of DME. Existing experimental data, shown in Figure 2, have demonstrated the high performance of solid oxide proton conducting membrane that is only 15 µm in thickness (a-b); methane activation over LaOCl catalyst (c); and hydrolysis of chloromethane to methanol and DME at high yield (d-e).

USC has provided SRNL their membrane reactor design and necessary assistance. SRNL has implemented this testing technology successfully. Figure 3 shows the membrane reactor constructed at SRNL per USC design.

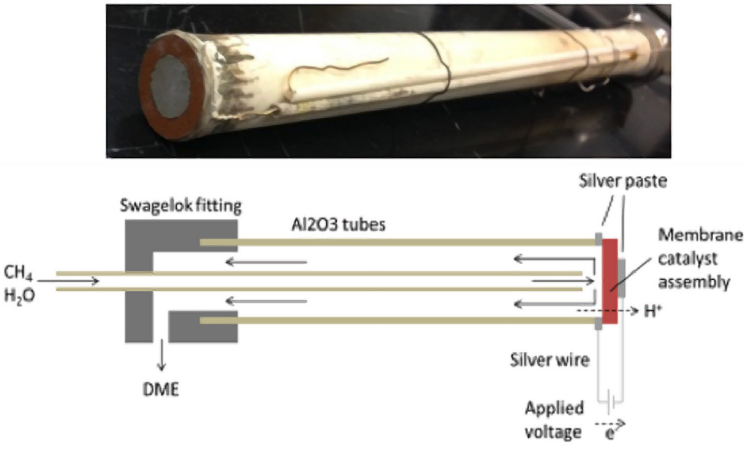

Figure 3. Membrane reactor constructed at SRNL (above) and membrane reactor design (per USC)

FY2017 ACCOMPLISHMENTS

- Developed an effective catalyst that activates methane even at ambient temperature to form chloromethane, with optimum temperature 450-500 °C matching membrane operation (Figure 2c)
- Constructed membrane reactors and successfully reduced membrane electrolyte layer from 500 to 15 μm (Figure 2a, Figure 2b)
  - Facilitate proton flux through the membrane to increase reaction rates
- SRNL implemented membrane testing technology from USC (Figure 3)
- Proof-of-concept DME synthesis (CH_3OCH_3) from CH_3Cl over Al_2O_3 catalyst (Fig. 2d)
- DME synthesis from methanol over KOH catalyst (Fig. 2e)
- Submitted a proposal to AIChE RAPID Institute based on this LDRD development
- Made a biomass conversion discovery during investigation of methanol to DME reaction
- Submitted a proposal to AIChE RAPID Institute based on the biomass conversion discovery

FUTURE DIRECTIONS

- System integration of these reaction steps enables the overall electrochemical reaction to convert methane to DME, and allows for further optimization by adjusting membrane composition, reaction conditions, and applied voltage.
- Further development of this novel biomass conversion process on process optimization, product separation, material balance and yields.

FY2017 PUBLICATIONS/PRESENTATIONS

1. http://www.worldbank.org/en/programs/gasflaringreduction
2. R. Salmon, A. Logan, Ceres "Up: North Dakota natural Gas Flaring More than Doubles in Two years", Ceres, July 2013
3. A. S. Ramadhas, *Alternative Fuels for Transportation,* CRC Press, Oct 9, 2012
4. P. Kapus, W.Cartellieri, "ULEV Potential of a DI/TCI Diesel Passenger Car Engine Operated on Dimethyl Ether," SAE Technical Paper 952754, 1995, doi:10.4271/952754
5. J. McCandless, S. Li, "Development of a Novel Fuel Injection System (NFIS) for Dimethyl Ether-and Other Clean Alternative Fuels," SAE Technical Paper 970220, 1997, doi:10.4271/970220
6. R. Verbeek, J. Van der Weide, "Global Assessment of Dimethyl-Ether: Comparison with Other Fuels," SAE Technical Paper 971607, 1997, doi:10.4271/971607
7. J. Dong, Q. Pan, Z. Pan, D. Yang, "Design of DME-Diesel Fuel Supply System for Non-Gasification," SAE Technical Paper 2013-01-1152, 2013, doi:10.4271/2013-01-1152

ACRONYMS

DME	Dimethylether
NG	Natural Gas
SEM	Scanning Electron Microscope
SRNL	Savannah River National Laboratory
USC	University of South Carolina
UV	Ultraviolet

TOTAL NUMBER OF POST-DOCTORAL RESEARCHERS

2 (A. Boone Thompson joined this project as postdoc, and has been hired as SRNL employee during this LDRD performance period, Xiaomin Wang postdoc at Univ. of SC)

LOCATION AUTHENTICATION PLATFORM TO INCREASE DEFENSE-IN-DEPTH OF WIRELESS NETWORKS

Project Team: R. B. Barnett (PI), D. Gobin, K. Burkes

Thrust Area: Clean Energy

Project Start Date: 10/1/16

Project End Date: 9/30/17

Current standards for wireless network security utilize IEEE 802.11i which makes use of encrypted block ciphers and four way handshakes. If this security is compromised a cyber intruder could spoof the wireless network devices' traffic to confuse the central controller or remote terminal units (RTUs) within the system. We intend to develop a static network location authentication platform that will be integrated into current interoperability platforms for wireless networks. Our method will utilize the wireless signal strength of RTUs to develop a pseudo grid geography of the system. This will inform a control center when there is a spoofing attempt on an RTU from an unexpected location. An artificial learning algorithm will be implemented to compensate for typical fluctuations in signal strength due to factors such as weather. We successfully developed the mathematical algorithm necessary for the pseudo-grid development, and constructed a working prototype of the hardware.

FY2017 OBJECTIVES

TASK ONE

Hardware/Software Prototype Design for Location Authentication System

- Select hardware for WSN and Setup Test Bed hardware for WSN

TASK TWO

Develop Location Authentication System

- Analyze effectiveness of Triangulation vs Multilateration

TASK THREE

Develop Hardware for Location Authentication Platform Prototype

- Firmware modification
- Network Architecture
- Signal Strength Acquisition

INTRODUCTION

Wireless communication is continuously developing into a more viable technology for communication of control systems because of the increasing signal range available, and because it requires less capital investment. It is also being integrated into nearly every commercial product sold on the market. Therefore, secure communications for these wireless networks are becoming a big concern for critical systems within the manufacturing, electric power, and military sectors. The current standard for Wi-Fi (IEEE 802.11i) uses Advanced Encryption Standard (AES) for securing the communication packets and can operate with a range of 100 ~ 500 m. However, the security of critical systems can be increased by integrating a location factor for stationary systems. This location authentication factor will be used to keep cyber intruders from maliciously controlling a wireless control system by increasing the defense-in-depth of the static network.

A specific application for the electric grid is transactive controlling of buildings to increase efficiency. Transactive control is an important function of Grid Modernization, and allows for the transactions of energy between buildings and campuses. This requires the communication and control of RTUs from a central command center in order to balance PV, batteries, and load in a cost effective manner. If one of these platforms becomes compromised or circumvented a cyber intruder could spoof these devices' packets to maliciously confuse the central controller and cause large scale blackouts. Another potential layer of security is to take advantage of the stationary aspect of the RTUs, as well as the fact they are largely physically protected. The vulnerability of these wifi systems is an attack where they are spoofed, but the attacker must physically be at another location than where the real RTU is located. The good RTUs, which act as bridges between end devices and higher level controllers, should always be stationary. This stationary aspect, combined with many RTUs within close enough proximity to detect each other's beacons, creates a constellation or pseudo-grid of points for this network. The ability to compromise the network from a spoofed RTU can be defeated by baselining this pseudo-grid, and detecting when an RTU is out of position within the pseudo-grid.

Most wireless intrusion detection systems focus on finding rogue access points within a wireless network. The assumption is that the rogue can already be identified, and only its location needs to be known. This approach is novel in that it is attempting to secure the space a wireless network occupies, by taking a super position of signal strengths to determine the correct geometry of the wifi space. This method would achieve our goal of defeating spoofed RTU signals within the network, but would also provide a reference system to locate signals within and around the pseudo-grid.

APPROACH

The location authentication platform uses information already available to the RTUs: the signal strength of surrounding RTUs and time of flight of packets. Each RTU in the network will record the signal strength from the surrounding RTUs communicating back to the central server. This information will be sent to the central server. With all this information the server can form a matrix containing the magnitude of distance between each point in the network. This matrix can be transformed into a pseudo-grid, using a law of cosines algorithm, of the network containing magnitude and angle for each RTU in the network with reference to the server through trigonometric functions (Figure 1). The system is a pseudo-grid because there is no reference zero location with the physical grid.

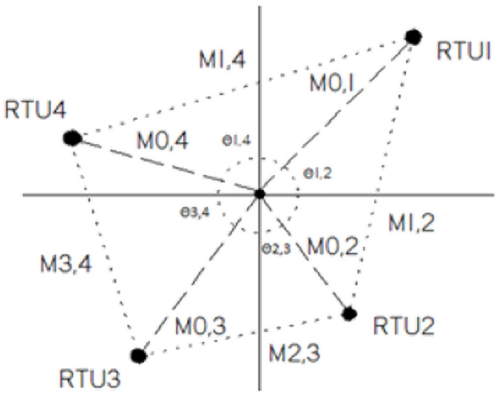

Figure 1. An illustration of the calculation method for determining pseudo-grid topology

This initial pseudo-grid can be baselined to determine the normal configuration of the network. If a hostile actor is attempting to spoof an RTU, the surrounding RTUs will see a change in signal strength due to the intruder being at a different location. When these RTUs report their neighbors' locations to the server the calculated pseudo-grid will have changed and the server can determine which RTU was reported in a different location and can raise an alert. In order to increase the accuracy of the system an artificial learning algorithm is used in order to account for normal fluctuations in signal strength. One example of a normal cause of signal fluctuation can come from changes in weather. If the weather is clear the signal strength at all clients will be stronger, making the network appear relatively constricted. If the weather is very dense the signal strength is weaker, making the network look more spread out. The artificial learning algorithm will learn how the network as a whole expands and contracts due to weather and will compensate the location authentication accordingly.

The prototype for this system involves the development of a hardware prototype that can handle the measurement of received signal strengths from the environment, a database to collect and handle this measured data, and another algorithm to do the detecting. Once this prototype system is established, it can be scaled up and deployed to a testbed location to begin development of the detection AI, as well as tuning the sensitivity of the detection algorithm to environmental factors.

RESULTS/DISCUSSION

We successfully developed the pseudo-grid algorithm and developed a hardware prototype for the RTU access point unit. The back-end networking to communicate the received signal strength data was also developed.

To further develop this system, a test bed would be necessary to scale up the number of RTU units and sensors in order to collect data with the signal strengths being modified by the environment. This step was not accomplished this FY and is essential to the development and tuning of both the detection algorithm and the artificial intelligence. Reprogramming firmware for wireless routers was a non-trivial task and took longer than expected. Despite this, the prototype development for the RTU/access point went well, and was ready to be scaled up for a test bed. In the process of developing this system, several points for improvement were identified, and future iterations would result in a smaller footprint for the prototype with better processing capabilities.

FY2017 ACCOMPLISHMENTS

- ✔ Hardware/Software Selection and Modification for Prototype
  - Wireless routers selected for AP and Node points
  - Open Source Firmware modified to allow received signal strength measurement and database communication
- ✔ LAP Systems Development
  - Algorithm for pseudo-grid generation
  - Back-end networking for node data and data storage

FUTURE DIRECTIONS

- ✔ LAP Systems Development
  - Move prototype to smaller platform
  - Scale up and deploy test bed
  - Develop Detection Algorithm
  - Develop AI
  - Tune detection algorithm and Train AI (Data collection dependent)
- ✔ Data Collection
  - Without AI to gather detection algorithm tuning data
  - Generate AI training set from detection algorithm tuning data
  - Train AI from collected empirical data
- ✔ Volttron Agent and Final Report
  - Agent developed and report on overall findings

ACRONYMS

AES	Advanced Encryption Standard
AI	Artificial Intelligence
AP	Access Point
LAP	Location Authentication Platform
PV	Photovoltaics
RTU	Remote Terminal Unit
WSN	Wireless Sensor Network

POWER HARDWARE-IN-THE-LOOP TESTING OF DISTRIBUTION SOLID STATE TRANSFORMERS

Project Team: John McIntosh (Primary), Klaehn Burkes

Subcontractor: Resilient Power System and Clemson University

Thrust Area: Clean Energy

Project Start Date: 10/1/16

Project End Date: 9/30/18

Savannah River National Laboratory and Resilient Power Systems have developed a utility grade solid state transformer (SST) and are planning on deploying it for testing in January 2018. The SST is the next generation solution to implementation of distributed energy resources such as solar and batteries. The SST can revolutionize current grid modernization initiatives by supplying grid support and building support services at the edge of the grid. For this fiscal year in this project the SST was designed and built to prepare for testing next fiscal year. Also, a battery system was purchased to compare the performance of lithium ion and lead acid batteries abilities to mitigate solar fluctuation and demand response. Next year the SST and battery system will be tested at Clemson University's Duke eGRID.

FY2017 OBJECTIVES

TASK ONE
Determine specifications for Solid State Transformer

TASK TWO
Determine specification for Energy Storage System

TASK THREE
Purchase Solid State Transformer

TASK FOUR
Receive Distribution SST at eGRID

INTRODUCTION

The electric grid is changing rapidly through the integration of distributed energy resources (DER) that consist of intermittent renewable energy sources, battery energy storage systems (BESS), and other advanced technologies. DERs require higher levels of control from power electronic inverters and rectifiers to convert the DC power consumed or produced into AC power to connect to the electric grid. To fully leverage DER penetration, passive elements such as a traditional transformers and passive inverters and rectifiers need to be replaced with equivalent active elements like a solid state transformer (SST). With SSTs integrated into the electric grid more functionalities become readily available at the grid edge to perform grid and building support functions such as control of power flow on multiple ports, reactive power support, power factor correction, integration of renewables and BESS on DC buses, fault isolation, advanced metering, load shaping, demand side management, and transactive control.

Renewable sources are being integrated into the electric grid at alarming amount and not only in the California region. North Carolina has the second highest integration of photovoltaic (PV) energy in the country (Figure 1). One problem seen by this large amount of PV integration is that generation peak and load peak don't occur at the same time. This is because the largest power demand is at the end of the day, when people are returning home from work. PV systems peak power supply is in the middle of the day. Late in the day, since PV's supplied power is falling off when the load is increasing, utilities must keep a larger amount of spinning reserve and use generators with a fast ramp rate to supply power. This is inefficient and wastes money to support the loss of PV energy. The problem can be solved by integrating a BESS controlled by a distribution scale SST to absorb the PV energy during the peak and supply it back into the system as PV energy lessens and load is ramping up.

APPROACH

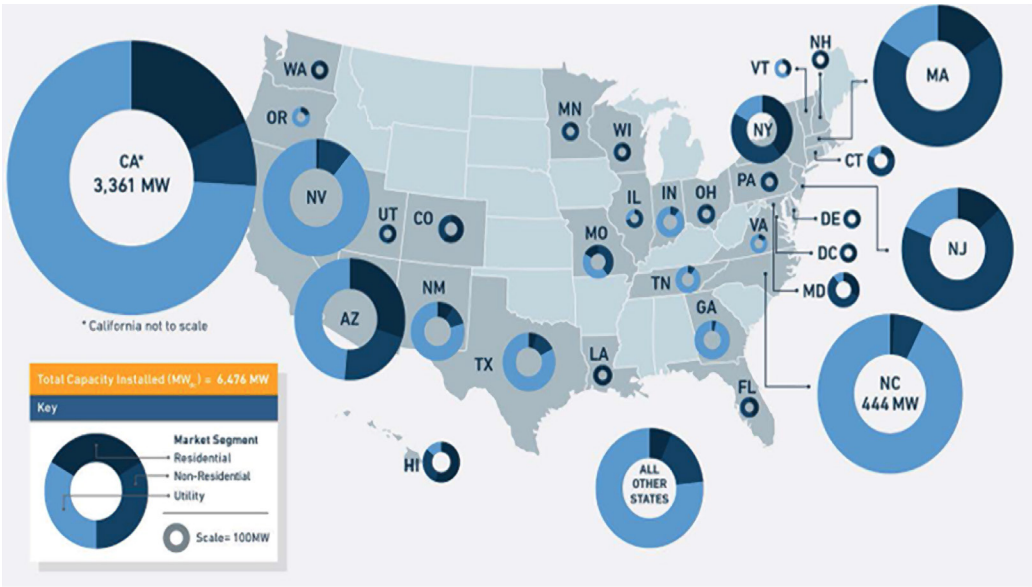

Figure 1. PV installations in the US by state in 2014 [1]

SRNL worked with Resilient Power Systems (RPS) to develop a solid state transformer. Together SRNL and RPS determined the parameters for the SST, what type of functionality the SST would be capable of performing, how many ports the SST contains, and how the SST will operate above that of a traditional transformer. Together SRNL and RPS have developed a utility grade SST that is not a research project but ready to deploy to utility companies.

The solid state transformer consists of power electronics that convert the AC power delivered by the electric grid to a high frequency AC power. This high frequency allows for a smaller transformer to be used to isolate the primary from the secondary. The high frequency transformer is a 1 to 1 transformer and only performs isolation. The power electronics on the secondary are configured in a way to which they drop the voltage down to the secondary voltage level. A block diagram of the system is shown in Figure 2. The primary and secondary power electronics are utilizing multiple modules that consist of active h-bridge architectures to control power flow bi-directionally. This allows for power to be routed through any port in the transformer in any direction. To increase power and voltage the modules are cascaded to reach desired levels, and the modules utilize silicon IGBTs and not wide band gap devise. This allows for reduced losses and costs because the power is being distributed throughout many modules, and the costs of wide band gap devises would make the system astronomically expensive and not cost competitive with current installed technologies.

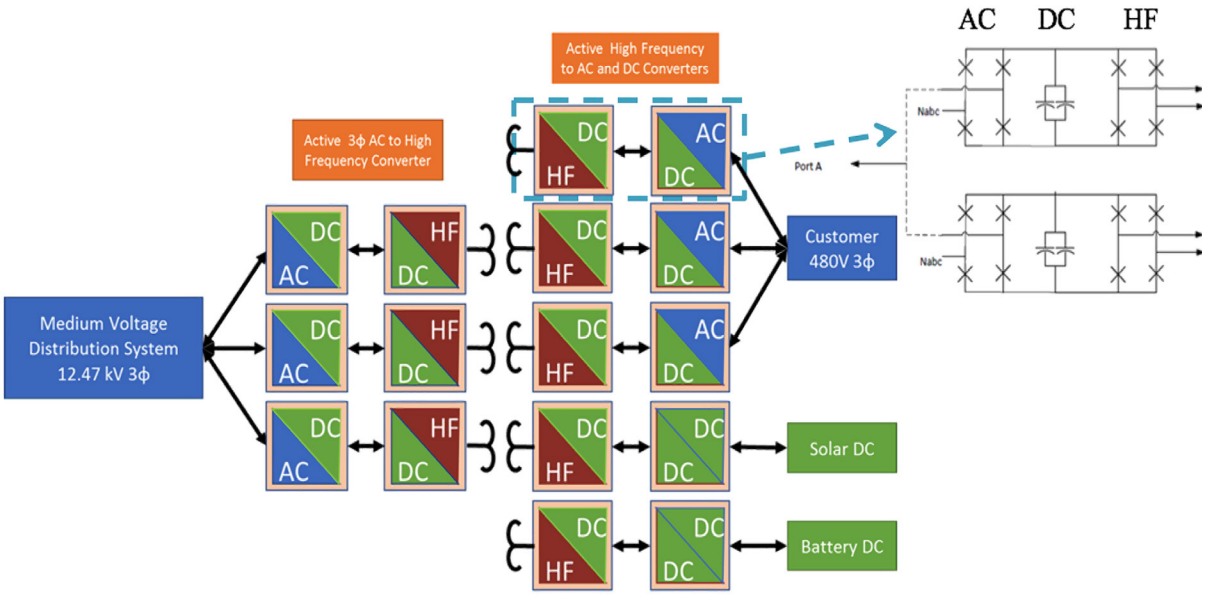

Figure 2. SST system block diagram

RESULTS/DISCUSSION

SRNL, in collaboration with RPS, has developed a commercial ready solid state transformer that is cost competitive per kVA with current technologies that perform the same functionality. However, the SST is directly connected to the electric grid, while current technologies are coupled through a step down transformer. The prototype SST with 2 extra DC ports is $340/kVA, but it is expected that a production SST would be around $200/kVA. This is not directly cost competitive with iron and copper which for the same power transformer with only AC connections is $20-30/kVA. However, the cost for a static synchronous compensator (STATCOM) is $200-500/kVAR. The SST performs the same functions as a STATCOM but in the distribution system, which is increasingly needed for more grid support functions because of the increasing penetration of DER on the distribution system. Therefore, the SST is competitive with current grid devices that perform similar functionality, but has the potential to penetrate a larger market in the distribution system versus the transmission system.

FY2017 ACCOMPLISHMENTS

- ✔ Distribution Scale SST was purchased from Resilient Power Systems
  - It is a 3 phase 500 kVA 15kV/480V distribution transformer
  - Replicates distribution transformer SRNL is planning on purchasing for the GMLC Efficient Transformer Project
  - Has 2 750V DC ports for integrating solar and battery systems
- ✔ Toshiba Battery System specified and purchased to provide "real-world" test system for SST evaluation
  - 200 kVA power rating
  - 1 100 kVA Lead Acid Battery for constant load supply
  - 1 100 kVA Lithium Ion Battery for solar mitigation (Delayed due to Hurricane Harvey)
  - Batteries could be used in parallel to supply a constant source for traditional loads and a variable source for solar fluctuations
- ✔ National Instruments Data Acquisition system for controlling SST was purchased

FUTURE DIRECTIONS

SRNL will be working with Clemson University and Resilient Power Systems to develop the hardware-in-the-loop control needed to perform the SST functionality. This work will be done at Clemson University's Duke Energy eGRID (Electric Grid Research Innovation and Development). The eGRID is a 15 MW hardware-in-the-loop grid simulator. This simulator will simulate the electric grid by controlling the input voltage and current to the SST to simulate grid conditions. The battery system will be connected to the DC port and a DC PAU from the eGRID to simulate solar fluctuations.

- ✔ Develop Control Strategy for Lithium Ion Battery systems
- ✔ Perform Load Profile Shaping at eGRID
- ✔ Develop Control Strategy for Lead Acid and Lithium Ion Dual Battery Systems
- ✔ Perform SST Functionality
  - Controlling power flow, reactive power support, power factor correction, integration of renewables and BESS, fault isolation, advanced metering, load shaping, and transactive control

REFERENCES

1. "Solar Market Insight Report 2014 Q4" Solar Energy Industries Association, 2014. (Accessed 9/20/2017) https://www.seia.org/research-resources/solar-market-insight-report-2014-q4

ACRONYMS

AC	Alternating Current
BESS	Battery Energy Storage Systems
DC	Direct Current
DER	Distributed Energy Resources
eGRID	Electric Grid Research Innovation and Development
GMLC	Grid Modernization Laboratory Consortium
IGBT	Insulated-Gate Bipolar Transistor
PV	Photovoltaic
PAU	Power Amplifier Unit
RPS	Resilient Power System
STATCOM	Static Synchronous Compensator
SST	Solid State Transformer

WIRE ARC ADDITIVE MANUFACTURING

Project Team: P. Korinko & A. Duncan (Co-PIs), J. Bobbitt, E. Kriikku, D. Gobin, PS Lam, A. d'Entremont, M. Folsom, & W. Housley

Subcontractor: A. Reynolds (USC)

Thrust Area: Clean Energy

Project Start Date: 10/1/16

Project End Date: 9/30/18

This project develops and deploys a wire arc additive manufacturing (WAAM) capability for SRNL. To better understand and predict Process-Structure-Property-Performance interrelationships, modeling will be conducted a-priori and will be validated experimentally. WAAM materials and components will be tested and evaluated. This project positions SRNL as a technical leader in WAAM. This project redeploys a gantry robot with a state of the art aluminum welder, develops the software needed to drive the robot and weld system, and develops microstructure, thermal, and residual stress predictive tools to enable SRNL and USC to improve/optimize the manufacturing processes.

FY2017 OBJECTIVES

TASK ONE
Procure Fronius CMT Weld System

TASK TWO
Place subcontract with University of South Carolina Professor Anthony Reynolds for WAAM and wire fabrication

TASK THREE
Integrate Fronius CMT with robot and conduct initial trials

TASK FOUR
Initiate WAAM trials with USC using Al 2319

TASK FIVE
Develop microstructural model correlating secondary dendrite arm spacing (SDAS) with cooling rate

TASK SIX
Implement beta version of Abaqus Welding Interface (AWI) for multi-pass additive processing

INTRODUCTION

Additive Manufacturing (AM) has the capability to make components of almost infinite complexity using one of several different technologies. These technologies include directed energy approaches such as laser engineered net shape (LENS) or powder bed laser or electron beam processes. The powder processes work well and have dimensional limits of about 75 µm. However, the build rate is slow with layer thicknesses of about 50 µm each, requiring over 4000 layers to build a 200 mm tall component over a time of approximately 45 hours with a single heat source. The powder processes also have a potential fire concern, especially for reactive metals like aluminum and fine titanium. The fire hazard may be mitigated by using passivated powders, thus reducing their pyrophoric nature by slightly oxidizing the surfaces or by adding other reaction products, but this treatment degrades the powder purity which will compromise the material performance. The reaction products could also prevent melting and inhibit the incorporation of the particles into an integral part of the component. Alternative AM methods such as the currently proposed Wire Arc Additive Manufacturing (WAAM) can alleviate these anticipated concerns.

WAAM uses either cold or hot wire feed Gas Tungsten Arc Welding (GTAW), Plasma Arc Welding (PAW), or Gas Metal Arc Welding (GMAW) technology to deposit metal layer by layer. The use of wire as the source material enables significantly higher build rates, e.g., 1 kg/h for WAAM vs. 0.2 kg/h for powder bed processes, reported for titanium alloys **(1).** In contrast to fine unpassivated powders **(2),** wires are generally not considered pyrophoric. As a result, WAAM eliminates the fire hazard without introducing impurities (e.g., oxides) into the product. Finally, WAAM reduces the materials costs, since it costs less to make wire than powder.

WAAM is being rediscovered as an approach for freeform fabrication or three dimensional printing for large net shape components. Unlike many of the powder-based processes that produce net or near net shapes, WAAM is generally considered an additive manufacturing process that can be coupled directly with a subtractive process. The subtractive element is required due to the higher volume deposition rate and coarse deposit scale that requires machining of the excess material to meet final dimensions. This allows WAAM to produce complex parts with machined surfaces. Despite the need for subtractive manufacturing, WAAM provides tremendous cost and material savings over conventional subtractive processes. For example, the "buy-to-fly" ratio, i.e., the material required to make a component vs. the material remaining after final machining, can be 10:1 for conventional processing of titanium alloys in the aerospace industry while the buy-to-fly for WAAM can be as low as 1.2:1. WAAM does have the shortcoming that parts must be slightly oversized to accommodate the machining allowance; this gives rise to new design terminologies such as total wall width (TWW) and effective wall width (EWW) where TWW includes the weld bead scallops on the surface which need to be machined away and EWW is the final dimension of the post-machining wall. See Figure 1 for illustration of these terms. The difference in TWW and EWW gives rise to the buy-to-fly ratio that is attributed to WAAM.

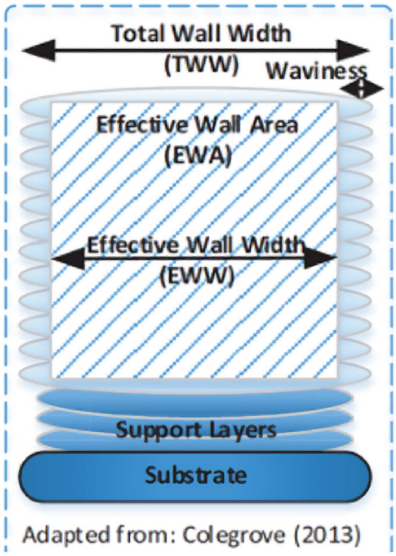

Figure 1. Definitions for TWW and EWW for WAAM processes showing the required overbuild

APPROACH

This project has two primary drivers: first, establishing a WAAM capability and, second, establishing a modeling capability based on commercial software evolution. WAAM has been established as a viable technology for titanium-based alloys **(3, 4, & 5)** and has been suggested as a feasible technology for aluminum as well **(3)**. Aluminum is best deposited using GMAW and either spray or dip transfer modes. The benefit of using dip transfer is that it minimizes the spatter associated with spray transfer for GMAW. Ultimately, an existing SRNL gantry robot will be fitted with a Fronius Perfect Weld system GMAW weld torch head that uses the dip transfer mechanism (Figure 2). The software and hardware will be integrated with open source code with open architecture to allow both simple and more complex 3D shapes to be printed. A rotating table will also be incorporated to allow printing of cylindrical components.

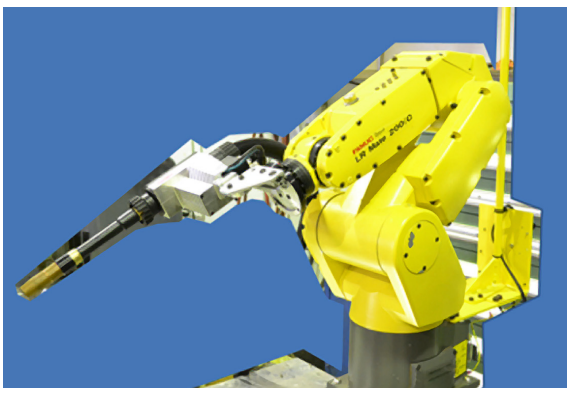

Figure 2. Fronius Robotic Weld torch temporarily mounted on a SRNL Fanuc robot to be used for fabricating coupons and small test articles

Tne major hurdle for AM is to close the gap between the as-designed and the as-manufactured configurations. For WAAM, this includes minimizing the difference between TWW and EWW as well as controlling distortion and residual stresses in the printed part. This optimization can be facilitated by computer modeling or simulation of the WAAM process. Therefore, in parallel to fabricating the SRNL WAAM system, coupled microstructural, thermal, and stress modeling will be conducted. The following three-step approach is proposed. Step 1 – Simulate WAAM by predicting the as-manufactured part based on the as-designed specifications. The multi-purpose commercial finite element code Abaqus available at SRNL will be utilized along with its welding-interface plugin. The 2017 Abaqus Welding Interface (AWI), which SRNL currently has access to in beta version, has the capability to account for gradual addition of material to the workpiece over the course of the simulation (vital for simulation of WAAM), coupled with a heat source model well-established for representing welding heat inputs. The AWI also enables specification of weld geometric features, temperature-dependent material properties, bead/chunk specification, multiple weld passes, and thermal and structural boundary conditions. The final shape of the product, distortion, and residual stress will be calculated both before and after "unclamping" of the mechanical constraints, fracture and damage can be assessed, and optimization of the WAAM process will be conducted by varying the operating parameters and the material properties (Figure 3). Step 2 – To close the gap between as-designed and as-manufactured, it may be necessary to fully capture the material properties using multi-scale technology because the AM process will impact the material properties. Important metal phase transformations occur during melting and re-solidification that affect tensile strength and fracture toughness, but most currently available property data corresponds to temperatures well below the solidus temperature. This can be resolved by benchmarking the test data, or by acquiring multiscale computer software for materials modeling. Step 3 – Conduct optimization of process parameters to match the as-manufactured to the as-designed configurations (or minimize the gap between TWW and EWW). The process-specific considerations include deposition path data, heat source characteristics, multi-scale scope, and the model size.

RESULTS/DISCUSSION

Due to slow procurements and long lead items required to develop and deploy the WAAM equipment and facility, not as much progress was accomplished for this period as planned. The Fronius CMT welder was installed on a Fanuc multi-axis robot and the site acceptance testing was completed. These samples were metallographically characterized.

The beta version of the AWI was successfully implemented and improved in conjunction with Abaqus South. The temperature, distortion, and stresses during the welding process and cooldown period have been successfully simulated for both single-pass welds (Figure 3) and for multi-pass blades. The distortion caused by the same weld on several different substrate thicknesses was calculated and compared. These calculations can be used to select substrates to minimize distortion in fabricated components. A method to extract cooling rates and thermal gradients from the AWI thermal model was developed and used to implement a microstructural model to predict the SDAS at each location within the weld. The resulting three-dimensional SDAS map will be validated against experimental test specimens produced at USC and SRNL.

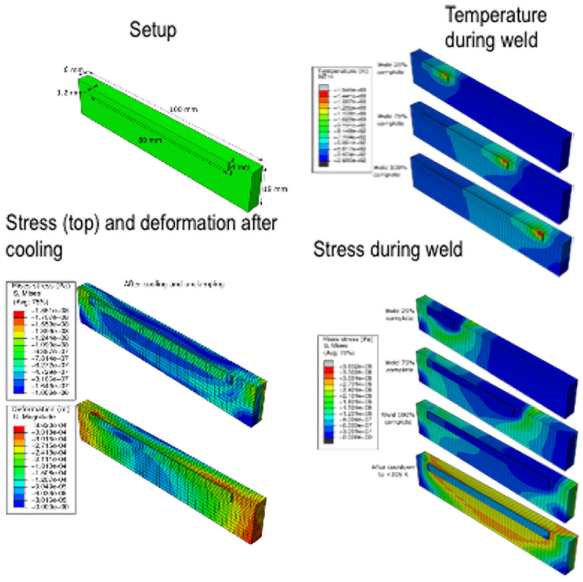

Figure 3. AWI modeling results for a single-pass weld showing stress and distortion on cooling

During the site acceptance testing and installation of the Fronius CMT, three single pass bead layups were made (Figure 4) using each control mode: pulse, CMT, and combined pulse and CMT. These samples were examined microstructurally. The size of the heat-affected zone in the Al6061 decreased from pulse, to CMT, to pulsed + CMT. The WAAM parameters need to be optimized to produce a higher quality deposit, since pores and cracks were visible in the metallographic cross-sections.

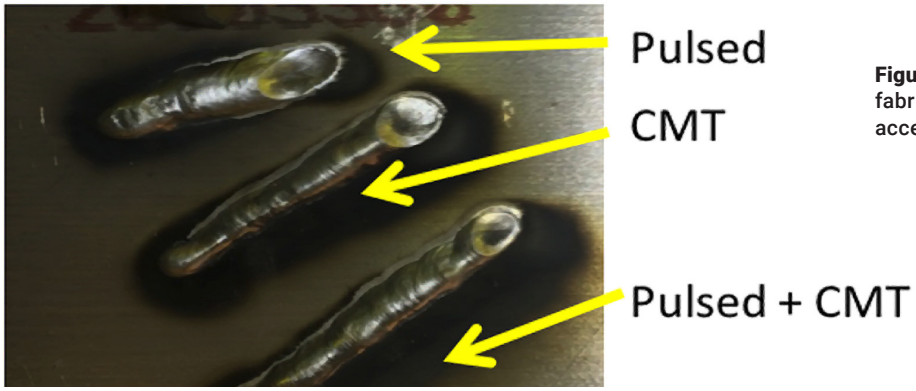

Figure 4. Single pass WAAM fabricated during site acceptance testing.

FY2017 ACCOMPLISHMENTS

- Integrated Fronius CMT weld system with Fanuc robot to provide automated movement of the weld torch in multiple axes
- Initiated Virtual Reality software development for tool path characterization to decrease likelihood of tool crashes with welding torch
- Performed initial WAAM trial during site acceptance testing and characterized microstructure
- Modeled single and multi-pass welds using AWI and extracted cooling rate data to correlate with SDAS and microstructure model
- Collaborated with USC and their GTAW WAAM system

FUTURE DIRECTIONS

- Fabricate fully dense simple blade structures for mechanical and microstructural characterization using Al6061 substrates and Al4043 initially
- Measure SDAS to validate the cooling rate calculations from the AWI model predictions
- Compare the microstructure and properties of GTAW and CMT based WAAM components
- Measure the mechanical properties as a function of temperature of the alloys of interest to provide fundamental data for the materials databases used for modeling

FY2017 PUBLICATIONS/PRESENTATIONS

1. SRNL-STI-2017-00333 SRNL Metal Additive Manufacturing Capabilities, Wire Additive Manufacturing Focused Exchange, Atomic Weapons Establishment, June 5-9, 2017, Presentation

2. SRNL-STI-2017-00158, Development and Deployment of a Wire Arc Additive Manufacturing Capability, Anna d'Entremont, Andrew Duncan, Poh-Sang Lam, John Bobbitt, Eric Kriikku, Derek Gobin, Matthew Folsom, Paul Korinko, Anthony Reynolds (USC), JOWOG 28 Main Meeting, Atomic Weapons Establishment, August 29- Sept. 1, 2017, Poster

2. SRNL-STI-2017-00594, Development and Deployment of a Wire Arc Additive Manufacturing Capability, Anna d'Entremont, Andrew Duncan, Poh-Sang Lam, John Bobbitt, Eric Kriikku, Derek Gobin, Matthew Folsom, Paul Korinko, Anthony Reynolds (USC), to be presented at MS&T17, Oct. 8-12, 2017 Pittsburgh, PA, Presentation

REFERENCES

1. Busachi, A., et. al, "Designing a WAAM Based Manufacturing System for Defence Applications", Procedia CIRP (2015), 48-53.

2. Kwon, Y.S. et. al, "Passivation process for superfine aluminum powders obtained by electrical explosion of wires", Applied Surface Science 211 (2003) 57–67.

3. Williams, S.W, et. al "Wire + Arc Additive Manufacturing", Materials Science and Technology, 32:7, 641-647, DOI:10.1179/1743284715Y.0000000073

4. Szost, B.A., et. al, "A comparative study of additive manufacturing techniques: Residual stress and microstructural analysis of CLAD and WAAM printed Ti–6Al–4V components, Materials and Design 89 (2016) 559–567.

5. Berminham, M.J., et. al, "Controlling the Microstructure and Properties of Wire Arc Additive Manufactured Ti-6Al-4V with Trace Boron Additions", Acta Materialia 91 (2015) 289-303.

ACRONYMS

Al4043	Aluminum welding Alloy 4043
Al6061	Aluminum Alloy 6061
AM	Additive Manufacturing
AWI	Abaqus Welding Interface
CMT	Cold Metal Transfer
EWW	Effective Wall Width
GMAW	Gas Metal Arc Welding
GTAW	Gas Tungsten Arc Welding
LENS	Laser Engineered Net Shape
PAW	Plasma Arc Welding
SDAS	Secondary Dendrite Arm Spacing
SRNL	Savannah River National Laboratory
TWW	Total Wall Width
USC	University of South Carolina
WAAM	Wire Arc Additive Manufacturing

TOTAL NUMBER OF POST-DOCTORAL RESEARCHERS

One post-doctoral researcher was supported on this contract and one MS student was supported through a subcontract with University of South Carolina

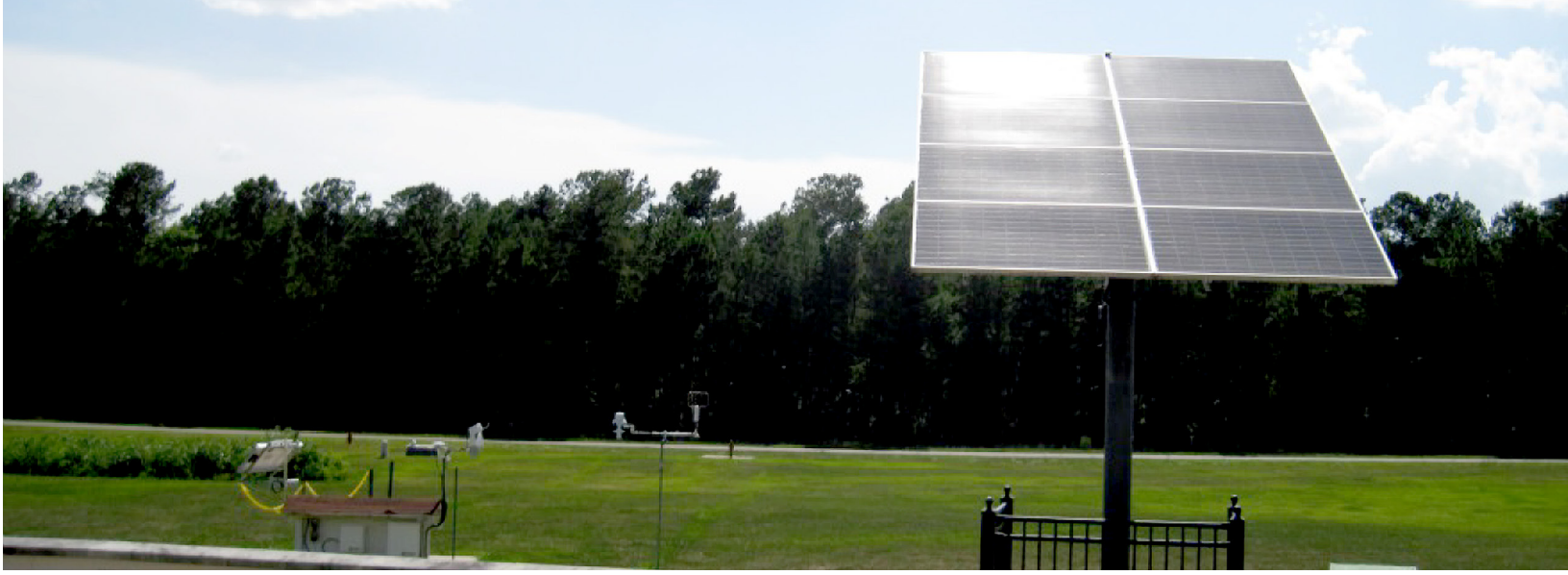

Solar monitoring station installed at the ARC

ADVANCED CLOUD FORECASTING FOR SOLAR ENERGY'S IMPACT ON GRID MODERNIZATION

Project Team: M. J. Parker, D. Werth, and R. Nicholss
Thrust Area: Clean Energy
Project Start Date: 10/1/16
Project End Date: 9/30/17

Given that today's electrical grid was not designed to accommodate variable power sources, the growth of solar energy in the Southeast poses a difficult challenge. Energy forecasts in the one-to-five day range are critical for managing diversified energy portfolios and energy trading floor transactions, and meteorological forecasts play a large role in deciding how much projected electrical demand to allocate to solar panels.

This LDRD focuses on 1) establishing a unique irradiance/cloud and photovoltaic power measurement system at the Applied Research Center and assembling a valuable dataset to characterize the relationships between cloud types and power output, and 2) applying an analog method to improve forecasts in the one-to-five day period. By investing in this project, ATG, with utility partners from the region, will become a leading research group in forecasting solar power production.

FY2017 OBJECTIVES

TASK ONE

Create a dataset of solar irradiance, cloud properties, and photovoltaic (PV) power output

- Establish a solar research station at the Applied Research Center
- Develop relationships between cloud and aerosol properties, solar irradiance, and solar power output
- Analyze the timescales of solar variability

TASK TWO

Apply analog modeling techniques to create forecast ensembles and improve one-to-five day solar forecasts

- Develop a scheme for the application of analog forecasting to predicting solar energy, and test it against existing forecasting tools.
- Install it to produce daily solar forecasts at SRS

INTRODUCTION

Distributed solar energy systems in the Southeastern United States have exceeded thousands of megawatts[1] (MW) and continue to grow[2]. Utilities often assume that roughly 25% of the potential solar resource can be used to meet the projected demand. This conservative estimate is due to the uncertainty in weather forecasts and the consequent uncertainty in projected photovoltaic (PV) power output. If this percentage could be significantly increased through improved confidence in the meteorological forecast, utility grid managers could more confidently allocate more future demand to solar panels and reduce production from conventional sources of energy within their portfolio. According to internal utility estimates, an improvement in forecast accuracy can result in a $20/MWh savings with an additional 80 MW available for power production on a 1000 MW system.

Clouds and aerosols affect solar energy production not only by reflecting incoming solar radiation back into space, but also by partitioning it into direct normal irradiance and diffuse irradiance, which can alter the solar yield in different ways. The impact of clouds on the solar resource is not well understood, and atmospheric modeling techniques to predict these relationships have not been developed.

The overarching goal of the proposed work is to develop improved methods of forecasting the solar energy resource in the U.S. through an advanced understanding of the impacts of cloud type, and translating this understanding into improved meteorological modeling techniques. This proposal focuses on 1) utilizing a unique irradiance/cloud measurement system in conjunction with measurements of PV power to characterize solar variability and the relationships between irradiance and solar power output, and 2) developing an 'analog' forecasting system to produce forecasts in the 24-48 hour "day ahead" period.

APPROACH

The plan is to establish a solar monitoring site at the Applied Research Center, which is to include: 1) a solar panel, which records the generated voltage and current, 2) a shadowband radiometer (Fig. 1), to record global, direct and diffuse solar irradiance (Myers, 2005), 3) a sonic anemometer, to record wind speed and direction, and 4) sensors for 2 m temperature and relative humidity.

We will analyze the data to learn what leads to variability in solar power, including using data to estimate cloud properties, relating these to the partitioning of solar radiation into its direct and diffuse components, determining how the two components affect power output, and determining the timescales on which solar irradiance varies.

Figure 1. Shadowband radiometer installed at the ARC

We will also develop and evaluate an analog forecasting system by which a set of weather patterns from the past that resemble that of today (the 'analogs') will be selected, and the observations of solar irradiance subsequent to those analogs are then used to get a forecast of today's solar irradiance.

RESULTS/DISCUSSION

The solar monitoring station at SRS is operational, and we have started looking at the data to explore how changes in solar radiation affect changes in solar power. A power utility must constantly shift the ever-changing demand among its various sources, and this must often be done on short timescales. Clouds induce very short-term changes in solar irradiance (Hinkelman, 2013), and we are therefore interested to learn how likely is it we will see a particular change in solar irradiance in a brief period. For a period from the summer of 2017, we created a probabilistic distribution function (PDF) of change in solar power over a 5 minute period (Fig. 2).

This analysis included only fair weather cumulus days (no overcast or cloudless days) during mid-day hours (eliminating changes due to sunrise or sunset). Generally, the changes were between 0-7.5 Watts/5 minutes, though one change reached as high as 56.8 Watts.

We have developed an analog system for forecasting solar radiation, similar to that outlined by Hall et al. (2010) and Inman et al. (2013), and tested it at SRS. The system acts by comparing the weather pattern of today (the target) with patterns of the past to find the 5 best matches (the 'analogs'). For example, assume we wish to forecast the next day's solar irradiance at SRS on January 1st, 2007. The surface pressure pattern on that day resembles that of January 9th, 2000 (Fig. 3), so we select the latter as an analog of the former. The solar irradiance subsequent to the analog (that is, on January 10th, 2000) measured at SRS is then considered one possibility of what will occur following the target date (January 2nd, 2007).

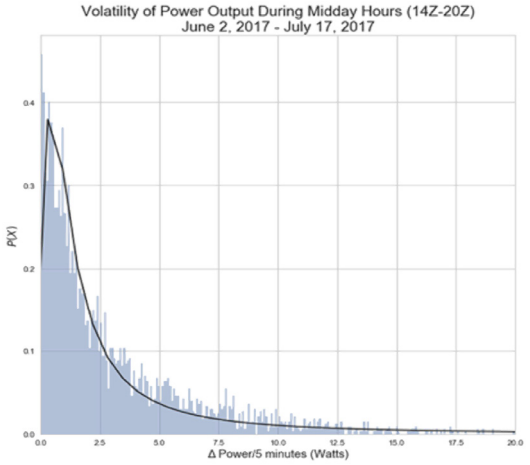

Figure 2. PDF of 5-minute changes in solar power (W)

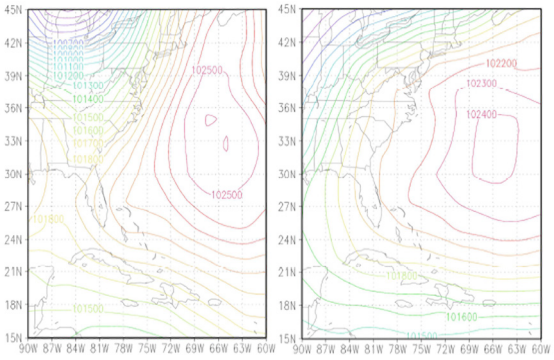

Figure 3. Surface Pressure (Pa) **(left)** January 1, 2007 (the Target Date) , **(right)** January 9, 2000 (the First Analog)

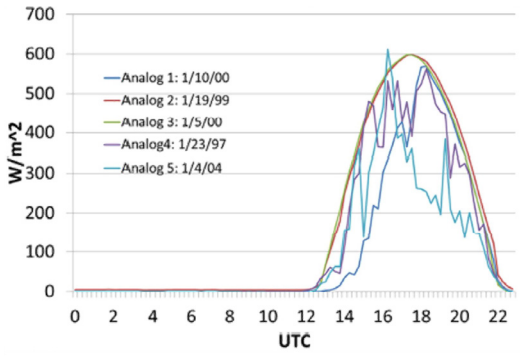

Figure 4. Solar irradiance at SRS corresponding to each analog

The time series of solar radiation at SRS for the day following each of the five analog days (Fig. 4) is then used to get the forecast range for the target date. A wide range of forecasts generally indicates greater uncertainty than a narrow range.

The system was first tested for the month of July, 2017 – each day was forecasted using the analog method, and the forecasts were scored according to how closely they resembled observations. The system was seen to do well when compared to solar forecasts from the National Weather Service's North American model (NAM), which ATG currently uses.

The system was then designed to run operationally—producing a new forecast each morning for solar irradiance for that day. The forecast for September 25th, 2017 (Fig. 5) does not capture the solar variability perfectly – it is too high early on, and misses the drop at 1600 UTC, but it does indicate that we may expect periods of mostly sunny skies occasionally interrupted by clouds, similar to what was observed.

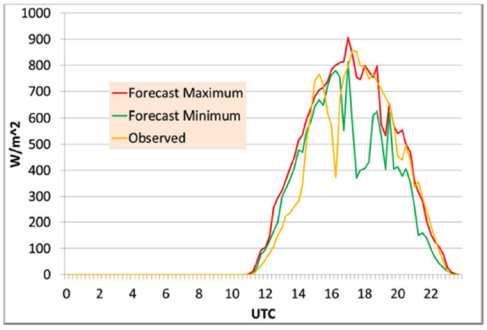

Figure 5. Solar irradiance forecast at SRS for Sept. 25th, 2017, along with the observed irradiance.

FY2017 ACCOMPLISHMENTS

- Developed a solar monitoring station at SRS and are now creating a long-term database of variables associated with solar energy production
- Began an analysis of relationships between cloud and aerosol properties vs solar power production
- Developed and installed an analog solar forecasting system
- Awaiting a funding decision from EERE on a proposal that will leverage these developments

FUTURE DIRECTIONS

- Run analog forecasting system operationally, and determine its value
- Complete analysis of 1) cloud/power relationship and 2) relationship between timescale and variability
- Collect long-term data from solar site, and make use of aerosol data

FY2017 PUBLICATIONS/PRESENTATIONS

1. Submitted for presentation at the 2017 American Geophysical Union Fall meeting in New Orleans (December, 2017).
2. Presented at the 2017 Mini-Tech conference of the Palmetto Chapter of the American Meteorological Society

REFERENCES

1. Hall, T., R. Thessin, G. Bloy, and C. Mutchler, 2010: Analog sky condition forecasting based on a k-nn algorithm. Wea. Forecasting, 25, 1463-1478, doi:10.1175/2010WAF2222372.1.
2. Hinkelman, L., 2013: Differences between along-wind and cross-wind solar irradiance variability on small spatial scales, Solar Energy, 88, 192-203, doi: http://dx.doi.org/10.1016/j.solener.2012.11.011
3. Inman, R., H. Pedro, and C. Coimbra, 2013: Solar forecasting methods for renewable energy integration. Progress in Energy and Combustion Science, 39, 535-576, doi:10.1016/j.pecs.2013.06.002.
4. Myers, D., 2005: Solar radiation modeling and measurements for renewable energy applications: data and model quality. Energy, 30, 1517-1531, http://dx.doi.org/10.1016/j.energy.2004.04.034

ACRONYMS

ARC	Applied Research Center	**PDF**	Probabilistic Distribution Function
ATG	Atmospheric Technologies Group	**PV**	Photovoltaic
NAM	North American Model	**SRS**	Savannah River Site

CROSS-CUTTING HIGH SURFACE AREA GRAPHENE-BASED FRAMEWORKS WITH CONTROLLED PORE STRUCTURE/DOPANTS

Project Team: Jay Gaillard (primary), J. Teprovich, S. Tinkey, J. Weeks, L. Olson, H. Colon-Mercado, L. Angelette, S. Xiao (SRNL); M. Sulic, M. Elvington, A. Wilber, J. Smith (Savannah River Consulting); R. Czerw (NanoTechLabs, Inc.); R. Baughman's team (University of Texas at Dallas, NanoTech Insitute)

Subcontractor: University of Texas at Dallas, NanoTechLabs, Inc.

Thrust Area: Clean Energy

Project Start Date: 10/1/16

Project End Date: 9/30/18

The proposed research seeks to enhance SRNL's materials innovation portfolio by developing novel 3D graphene-based frameworks that apply to applications in process intensification, advanced manufacturing, and clean energy with a specific focus on hydrogen storage. Our objective is to enhance the hydrogen adsorption properties of graphene and graphene nanoribbons (GNR) by optimizing pore structure and increasing hydrogen binding energy at adsorption sites. Initial activated graphene has reached specific surface area (SSA) values of 2600 m^2/g with a pore volume of 1.88 cm^3/g and hydrogen uptake (77 K) of 5.3 wt%. Similar experiments have been performed on GNRs with comparable results. Our goal at project end is to achieve SSAs >3400 m^2/g and >9 wt% H_2 uptake at 77 K and >3 wt% near room temperature for GNRs

FY2017 OBJECTIVES

TASK ONE

Prepare High Surface Area 3D Graphene Structures

- **Prepare 3D graphene frameworks with a high surface area (>2500 m^2/g) and > 5 wt% H_2 uptake.**
- **Develop methods for the microwave/ thermal exfoliation of graphene that is activated either by chemical (KOH) or gas phase activation (CO_2).**

TASK TWO

Prepare High Surface Area GNRs doped with Heteroatoms

- **Prepare high surface area (>2500 m^2/g) GNRs with substitutional doping.**
- **Synthesize GNRs with varied geometric architecture (UTD)**
- **Measure hydrogen uptake of high surface area activated GNRs.**

INTRODUCTION

DOE's Fuel Cell Technologies Office (FCTO) has set a goal to enable widespread commercialization of hydrogen, which requires adequate hydrogen storage media for onboard vehicles and portable power applications. Graphene-based framework's multifunctional properties provide potential to meet all DOE targets for hydrogen storage. SRNL is teaming with the University of Texas at Dallas (UTD) to use a facile rationally designed approach to enhance the hydrogen adsorption properties of high-aspect ratio graphene nanoribbons (GNRs), which contain remarkably high graphene-edge content and more easily accessible basal planes than its competitor, graphene.

A few material development approaches essential for the advancement of graphene-based H_2 adsorbents have been suggested: optimize pore structure[5], increase binding energy[5] with substitutional atoms and localized curvature, and high-density edge decoration[6]. The addition of heteroatom dopants to the graphene planar surface has been shown[7] to increase localized binding energy (Figure 1). Recent models on edge decoration have shown promise as a means to meet DOE H_2 storage targets[8], but that success applies more for GNRs due to their inherently high edge content. The outcome of this work is to prove feasibility of the synthesis of a carbon-based hydrogen adsorbent that stores hydrogen at higher loadings than predicted by the Chahine rule[9] in which a linear dependence of the hydrogen uptake is related directly to surface area. Our proposed design will increase the hydrogen affinity relative to surface area and seek to obtain uptake values that are ~2X the storage based on the Chahine rule alone.

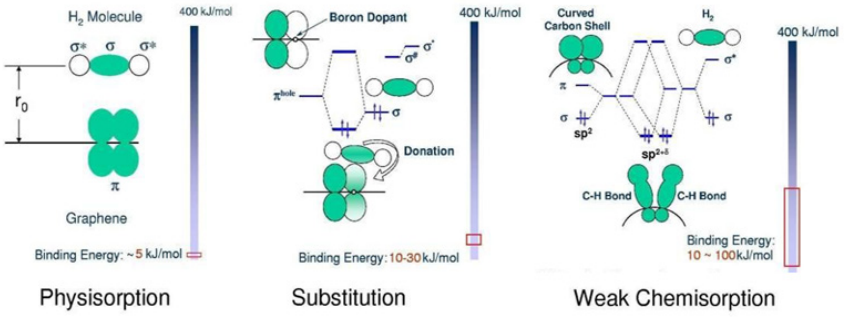

Figure 1. Illustration of three types of sorbent binding mechanisms: the two on the right enhance dihydrogen binding via substitution and curvature[8].

APPROACH

In a 3-phase, 2-year research approach, the GNRs will be constructed into macroscopic functional 3D architectures followed by perforation, corrugation and heteroatom (i.e., B, N) doping on the graphitic planar surfaces in order to significantly increase surface area (>3300 m^2/g) and hydrogen binding energy (>10 kJ/mol), to increase uptake at room temperature. The objective is to optimize the adsorbents with a ~9 wt% gravimetric and 40 g/liter volumetric capacity at 77 K with a subsequent primary objective of increasing H_2 uptake near room temperature.

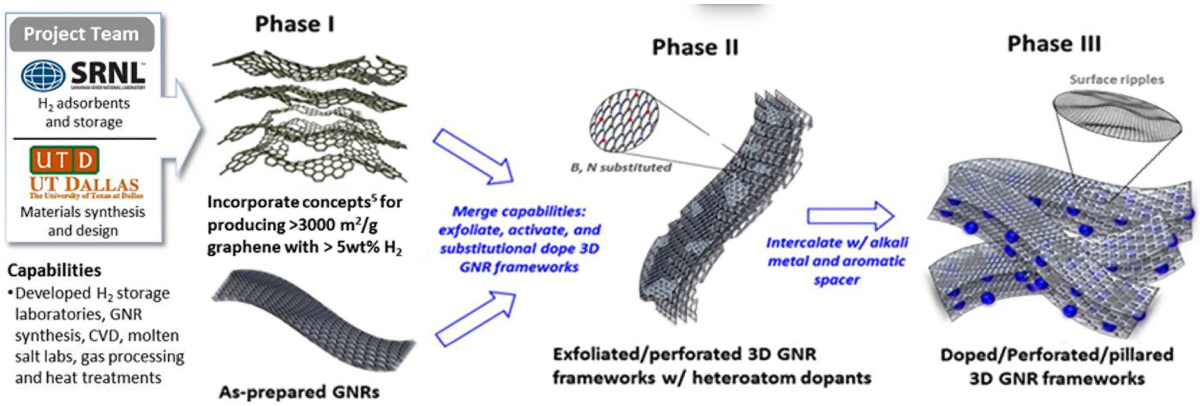

Figure 2. Flow schematic of material development shown in three phases. **(From left to right)** Phase I) development of capabilities to produce high surface area 3D graphene frameworks and parallel synthesis of GNRs, Phase II) exfoliation, activation, and substitutional B, N doping, and Phase III) plane separation with alkali metals and aromatic spacers in addition to imparting surface ripples for increased binding energy.

The specific scientific approach is to produce:

- 3D graphene nanoribbon frameworks with high surface area and optimal binding energies due to the heteroatom doping of narrow, high aspect ratio GNR structures with optimized and accessible pore structure (0.6-1.3 nm interplane)
- Corrugation and plane separation that provides additional enhancement to H_2 adsorption capacity and performance due to curvature induced binding sites, accessible interplanes, and metal induced charge gradients.

SRNL's proposed multiple post-treatment steps are necessary to meet DOE performance targets where application of only one approach (i.e., perforation, substitution, plane separation) would fall short. The innovation of the approach comes from first developing scientific principles for GNR base materials with: 1) ribbons of various dimensions (i.e., widths and lengths controlled by CNT starting material) where SRNL currently, in collaboration with NanoTechLabs, can synthesize CNTs with incremental diameters and lengths by carefully controlling growth parameters, and 2) controlling stacked (unzipped, but not fully exfoliated) and single layer architectures while understanding their role in hydrogen adsorption. The developed base materials will be thermal or microwave exfoliated and perforated using recently improved KOH activation[1] to significantly increase surface area near or above 3000 m^2/g. As mentioned, further innovation is expected from taking advantage of the high graphene edge content.

RESULTS/DISCUSSION

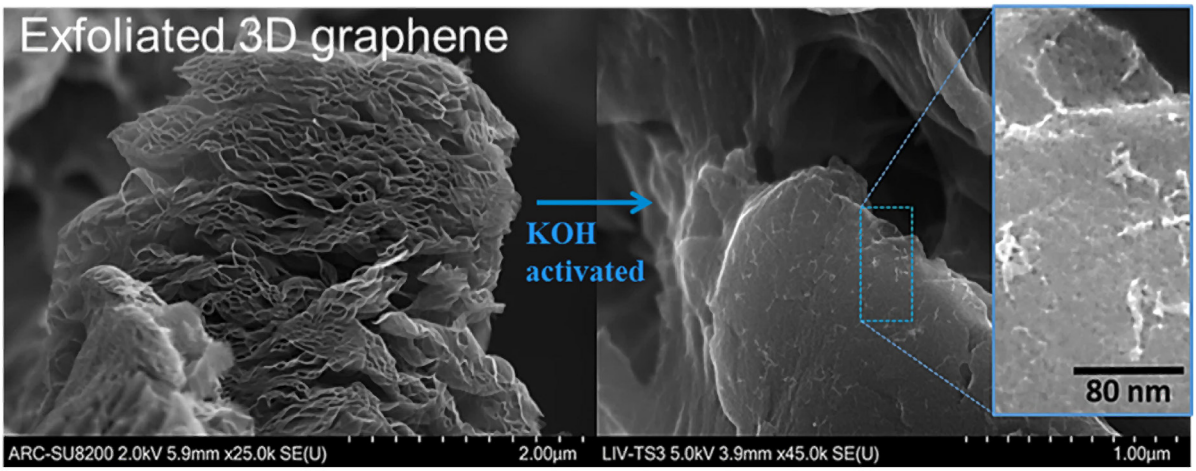

Figure 3. (Left) Thermally exfoliated GO and thus rGO produced at SRNL. (right) KOH activated rGO that exhibits higher density and typical perforation on the surface

To establish a greater than 3000 m^2/g surface area with > 6 wt% hydrogen uptake at 77 K, we have produced scaffolded[2] graphene using thermal exfoliation to produce reduce graphene oxide (rGO) followed by KOH activation. Graphene oxide is produced by chemically oxidizing graphite using the Hummers[10] method. Briefly, graphite flakes, $NaNO_3$, H_2SO_4 (98%) are mixed in an ice bath to prevent premature reaction, stirred for 2 hours followed by slow addition of $KMnO_4$. After stirring for 2 days at 35 °C, The suspension is heated to 98 °C with effervescence for 10 minutes. As shown in Figure 3, the graphene forms a highly porous structure after thermal exfoliation. It then densifies after a KOH/methanol solution is mixed with the thermally exfoliated GO, vacuum dried, and heated at 800 °C for 1 hour. Initial activated graphene reached specific surface area (SSA) values of 2600 m^2/g with a pore volume of 1.88 cm^3/g and hydrogen uptake (77 K) of 5.3 wt%. The thermally exfoliated GO yielded a SSA of 250 m^2/g before the activation. Several factors that need further development to increase surface area are:

1) Using thermal exfoliation versus microwave exfoliation is crucial to creating a chemically compatible surface for KOH wetting and reaching high surface areas after KOH activation.

2) A surface area after thermal exfoliation is needed above 350 m^2/g, but too high can lead to lower surface areas following KOH activation.

3) The optimal thermal exfoliation temperature[11] is 70-90 °C above the first mass loss measured by thermogravimetric analysis (typical at ~225 °C). These values change for graphene nanoribbons.

To these points, we have used several approaches to optimize thermal exfoliation to reach >350 m^2/g: 1) ball milling the graphite before oxidation to impart defects, 2) HCl acid incorporation into the graphene oxide step to increase interlaminate pressure, and 3) increasing the effervescent reaction time at the end of the oxidation step. Methods 1 and 2 failed to provide sufficient final high SSAs, but method 3 was successful in increasing the SSA after thermal exfoliation to ~380 m^2/g for graphene. We have KOH activated these materials and are currently in process of measuring the final SSA and performing hydrogen uptake measurements.

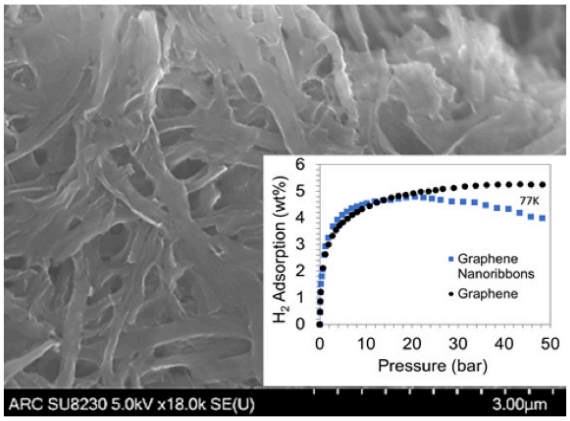

Figure 4. SEM image of large-width GNRs. Insert shows hydrogen uptake at 77 K of graphene and LWGNRs with ~2400 m^2/g SSAs

For graphene nanoribbons, we produce large width (~800 nm) and small width (~150 nm) GNRs (LWGNRs and SWGNRs, respectively) by chemically oxidizing carbon nanotubes with different diameters using the Tour[12] method. The LWGNRs (shown in Figure 4) were found to fully unzip as discerned from the XRD data in Figure 5a. Following the unzipping, thermal exfoliation easily occurred with a complete disappearance of the graphene oxide peak seen in the XRD data. EDS and FTIR also confirmed reduction of the oxygen functionalities. The thermal exfoliation step was found to produce an SSA of 485 m^2/g followed by KOH activation SSA of 2726 m^2/g with a total pore volume of 2.07 mL/g. Half of the original sample was sonicated during the KOH activation step. This sample gave an SSA of 2465 m^2/g with a 1.66 mL/g total pore volume. The smaller surface area sample was activated first and subsequently tested for hydrogen uptake which showed ~4.8 wt% (insert, Figure 4). Testing of the larger SSA sample is in progress in addition to further increasing the final surface area. The SWGNRs were difficult to thermally exfoliate which led to a study shown in Figure 5b, which involves an oxidation reaction time study versus XRD peak shift. The material produced after a 1.5 hr reaction was successfully thermally exfoliated as shown in Figure 5c; however, the SSA was low due to a needed longer exfoliation time. The further exfoliation and subsequent KOH activation is in progress.

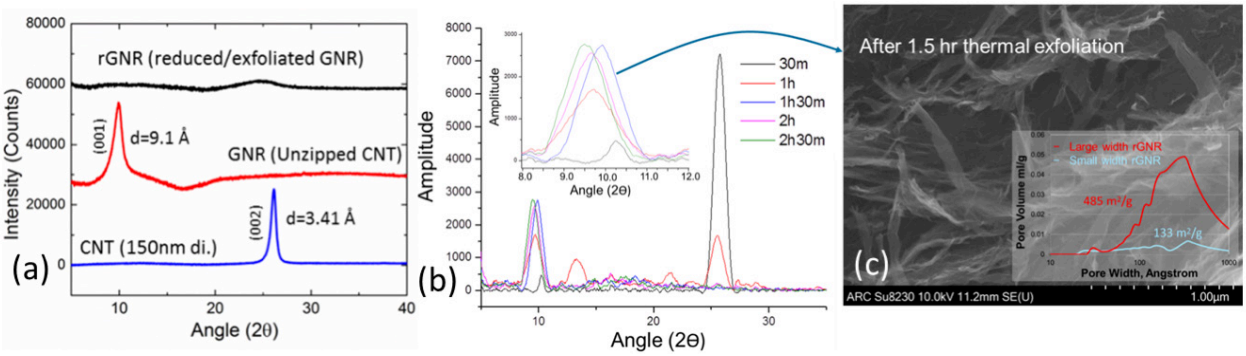

Figure 5. (a) Results show the loss of the large diameter CNT peak (26°) and the appearance of the LWGNR oxidation peak (9.1 Å). **(b)** The disappearance of the small diameter CNT peak (26°) occurs 1st at 1.5 hrs and shows a significant SWGNR oxidation peak (~9.5°) indicating full unzipping without over oxidation. **(c)** A larger batch of the 1.5 hr recipe was produced and thermally exfoliated to produce well-structure SWGNRs, as seen in the SEM image. The insert compares the pore structure of the LWGNR to the SWGNR. The small SSA for the SWGNR is likely due to incomplete exfoliation.

FY2017 ACCOMPLISHMENTS

- Graphene and graphene nanoribbon adsorbents with an average SSA of 2400 m^2/g had ~5.0 wt% H_2 uptake. The graphene and graphene nanoribbons have been further optimized, with measurements pending. Initial boron and nitrogen doping has proven successful up to full conversion of the carbon to BN. This research is ongoing for controlling the dopant content.
- XRD analysis showed the 100% conversion from carbon nanotube to GNRs.
- Small diameter GNRs were difficult to thermally exfoliate, but after an XRD aliquot study versus reaction time, optimized structures did thermally exfoliate.
- The hydrogen test cell was modified to be able to measure reduced sample sizes (from 200 mg to 100 mg) to help reduce the need for large sample batches.Submitted a proposal to AIChE RAPID Institute based on the biomass conversion discovery

FUTURE DIRECTIONS

- Utilize the expertise at UTD to develop new techniques to increase hydrogen uptake at room temperature for the GNRs.
- Focus on pore structure, volumetric capacity, and increasing binding energy (increase uptake temperature)
- Publish work in collaboration with UTD. The work for the two different sized GNRs will be finished and published in FY18

REFERENCES

1. *Ind. Eng. Chem. Res.,* 55 (29), pp 7906–7916 (2016).
2. *Scientific Reports 6,* Article number: 19367 (2016).
3. Zhu et al., *Nature Communications*. 6: 6962 (2015).
4. *Chem. Commun.*, 51, 15280 (2015).
5. Klechikov et al., *Chem. Commun.,* 51, 15280 (2015).
6. M. Wu, Y. Gao, Z. Zhang, and X. C. Zeng, *Nanoscale,* 4, 915-920 (2012).
7. JNREL/PR-590-41726, DOE Annual Merit Review in Washington, D.C., May 16-19 (2006).
8. L. Simpson, DOE EERE Fuel Cell Technologies Program, HSCoE Final Rep. Exec. Summ. (2010).
9. B. Panella, et al, *Carbon,* 43, 2209, (2005).
10. W. Hummers and Jr., R. E. Offeman, *J. Am. Chem.* Soc., 80 (6), pp 1339–1339 (1958).
11. A.G. Klechikov et al., *Microporous and Mesoporous Materials* 210 (2015).
12. Kosynkin, et al., *Nature,* 458, 872 (2009).

ACRONYMS

CNT	Carbon Nanotubes
EDS	Energy Dispersive X-ray Spectroscopy
FCTO	Fuel Cell Technologies Office
FTIR	Fourier Transform Infrared Spectroscopy
GNR	Graphene Nanoribbon
GO	Graphene Oxide
rGO	reduced Graphene Oxide
LWGNR	Large Width Graphene Nanoribbon
SRNL	Savannah River National Laboratory
SEM	Scanning Electron Microscopy
SSA	Specific Surface Area
SWGNR	Small Width Graphene Nanoribbon
UTD	University of Texas at Dallas
XRD	X-ray Diffraction